ISBN 978-82-326-1840-8 (printed version)
ISBN 978-82-326-1841-5 (electronic version)
ISSN 1503-8181

Doctoral Thesis

Xingbo Wang

Doctoral theses at NTNU, 2016:251

Xingbo Wang

Filter array based spectral imaging

Demosaicking and design considerations

Xingbo Wang

Doctoral theses at NTNU, 2016:251

NTNU
Norwegian University of
Science and Technology
Faculty of Computer Science and Media Technology

NTNU
Norwegian University of
Science and Technology

UNIVERSITÉ DE BOURGOGNE

NTNU
Norwegian University of
Science and Technology

UNIVERSITÉ DE BOURGOGNE

Xingbo Wang

Filter array based spectral imaging

Demosaicking and design considerations

Thesis for the degree of Philosophiae Doctor

Gjøvik, September 2016

Norwegian University of Science and Technology
Faculty of Computer Science and Media Technology

École Doctorale SPIM - Sciences Pour l'Ingénieur et Microtechniques
Université de Bourgogne

NTNU
Norwegian University of
Science and Technology

UNIVERSITÉ DE BOURGOGNE

Thesis for the degree of Philosophiae Doctor

Joint degree between:

Norwegian University of Science and Technology,
Faculty of Computer Science and Media Technology

Université de Bourgogne,
Faculty of Mathematics and Natural Sciences,
École Doctorale SPIM - Sciences Pour l'Ingénieur
et Microtechniques

ISBN 978-82-326-1840-8 (printed version)

ISBN 978-82-326-1841-5 (electronic version) ISSN
1503-8181

Doctoral theses at NTNU, 2016:251

Printed by Skipnes Kommunikasjon as

Dedicated to my loving parents
and
my uncle who introduced me to the compelling world of imaging.

Contents

*

Abstract

Spectral imaging apparatus in current use are often cumbersome, costly and slow in operation, which becomes a major obstacle to extensive use of spectral imaging in several application areas. In recent years, the technical and commercial success of color filter array (CFA) based imaging systems has motivated researchers to generalise and expand the concept of CFA to achieve efficient spectral imaging through the use of the spectral filter array (SFA). This dissertation expounds the research into the filter array approach to spectral imaging based on a simulation framework, from the development of demosaicking methods to the design and evaluation at the system level.

The dissertation first presents the development of the field of spectral imaging from its roots in spectroscopy and imaging, and explores the state-of-the-art solutions based on SFA from design to realisation. It then proposes a simulation framework composed of the major parts in a typical imaging pipeline. Based on this, the influence of chromatic aberration on CFA demosaicking and the impact of filter bandwidth on spectral reconstruction were evaluated. The results helped to better understand the delicate interactions between the components in the pipeline and verify the validity of the simulation framework. On the basis of the framework, three novel SFA demosaicking methods were developed and evaluated. The methods differ fundamentally and thus featuring distinct properties, as confirmed by the experimental results. The key to understanding the differences lies in the way demosaicking methods deal with the spatial and spectral correlation between pixels in a mosaicked image. An evaluation of the colorimetric performance shows that a properly designed SFA-based imaging system may also be useful for colour image acquisition. Lastly, performance of the proposed and conventional demosaicking methods were scrutinised, given the characteristics and parameters of a real-world SFA sensor design.

We conclude that, for a successful SFA-based spectral imaging system design, it is important to consider carefully the joint influence of all the involved modules as well as the requirements and constraints of applications. And we hope that the use of SFA based spectral imaging is expected to be wider in the foreseeable future in the light of technological advances and market demand.

Acknowledgments

Spectral imaging is such a wide ranging subject, covering so many disciplines of science and engineering, that no one person could give an adequate account without help from many quarters. My own indebtedness extends to a wide circle of colleagues and friends, and I am particularly grateful to the following for their assistance.

It was the group of doctoral advisers, Dr Jean-Baptiste Thomas, Professor Jon Yngve Hardeberg and Professor Pierre Gouton, who introduced me to the academia; their painstaking work, their kindness and assistance, and above all their insights to the topic, have all been a source of real inspiration.

Amongst my colleagues who were a great help, I am fortunate to be able to include those with the Norwegian Colour and Visual Computing Laboratory at NTNU Gjøvik, Ivar Farup, Marius Pedersen, Faouzi Alaya Cheikh, Philip John Green, Congcong Wang, Peter Nussbaum, Aditya Suneel Sole, Raju Shrestha, and, among those with the Laboratoire Electronique, Informatique et Image at Université de Bourgogne, Samuel Chef, Jacques Matanga and Pierre-Jean Lapray. I am also grateful to the administration of the faculties, the labs and the doctoral schools of both universities for their kind support.

I have also benefited from my associations with those in the sphere of colour and spectral imaging, including Joyce Farrell of Stanford University, Ronnier Luo of Zhejiang University and Michael Sterling of the Academy of Motion Picture Arts and Sciences.

My thanks are due to the following organisations for the permission to reproduce the texts and figures in our previously published papers: SPIE, IEEE, Springer and AIC.

the texts and figures in our previously published papers: SPIE, IEEE, Springer and AIC.

The regional council of Bourgogne in France and NTNU Gjøvik (formerly Gjøvik University College) in Norway are gratefully acknowledged for jointly funding the research work.

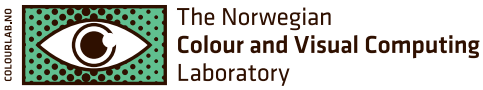

List of notations

λ	wavelength
$\phi(\lambda)$	relative colour stimulus function
Φ_e	radiant flux or radiant power
$\phi_\lambda(\lambda)$	colour stimulus function
$\tau(\lambda)$	spectral transmittance of an object
θ	angle
D	defocus
E_e	irradiance
H	system responsivity
I	radiant intensity
k	normalising constant
L_e	radiance
m, n, c	number of rows, columns and planes of a matrix
M	radiant existence
$n(\lambda)$	refractive index at certain wavelength

P system response

Q_e radiant energy

$R(\lambda)$ spectral reflectance/radiance of an object

r spectral reflectance at a point

r_c corneal radius

R_E dioptre

$S(\lambda)$ relative spectral power distribution of illuminant

T transmittance of a lens

$x(\lambda)$, $y(\lambda)$, $z(\lambda)$ colour-matching functions of a standard colorimetric observer

X, Y, Z CIE tristimulus values

Chapter 1

Introduction

This chapter presents the motivation, methodology, contribution of the research work, and illustrates the organisation of the dissertation.

1.1 Motivation

Spectral imaging, to wit the acquisition of spectral images, has its roots in both spectroscopy and imaging. It provides not only spatial distribution of light of a scene, but also its spectral composition, which are valuable to various applications including astronomical observation, earth remote sensing, preservation of cultural heritage, chemical analysis, military object recognition, etc.

Conceptually a spectral image is often characterised by a higher number of spectral bands than its trichromatic counterpart. In practice, this often results in spectral imaging systems of considerable size, weight and cost, as well as complex, time-consuming and inconvenient operation. For instance, the filter wheel is a typical approach to spectral imaging using a rotatory filter wheel placed in front of a monochromatic image sensor, whereas airborne and spaceborne remote sensing systems often rely on push-broom scanning whilst flying. In the former case, one exposure produces an image of a spectral band, and in the latter, one exposure corresponds to a line-scan of the object. Clearly both techniques require a sequence of exposures in order to capture a complete spectral image, and mechanical movement of the filters and/or sensor results in blur. Characters of such techniques, i.e., dimensions, complexity and cost, therefore become a major obstacle to a wider range of practical uses for spectral imaging, such as on-site real-time imaging ap-

plications.

The ubiquity of the digital still and video cameras owes much to the origination of solid-state image sensor and CFA (colour filter array) in mid-1970s [13]. Essentially an arrangement of colour filter tiles, CFAs enable an instantaneous acquisition of trichromatic images with a single sensor, at the expense of reduce spatial resolution. In practice, CFA based colour cameras are usually compact, lightweight and easy to operate.

The technological and commercial success of CFAs has aroused academic and industrial interest in extending the simultaneous and in-plane spatio-spectral sampling capability of CFAs into the spectral realm [148, 20]. The term SFA (spectral filter array) may be coined to describe a generic filter array integrating certain types of filter elements for the purpose of spectral image acquisition. To the best of our knowledge, few, if any, SFA based spectral imaging system were commercially available when the research commenced. We believe SFA is a viable solution to spectral imaging for certain applications.

1.2 Contribution

Due to the practical and economical difficulties in engineering an imaging system using filter array, the experiments and analyses are performed through computer simulation on the implicit assumption that the simulation model represents the rationale of a real system to a certain extent. In essence, the filter array is a spatio-spectral sampling mechanism that works on the assumption that there exist spatial or spectral correlations between samples. In other words, images sampled presumably bear a continuous tone. This hypothesis allows us to utilise and extend the CFA imaging pipeline [111, p. 7], which forms the basis of this study.

Based on general concepts of spectral imaging systems and empirical knowledge of the CFA/SFA-based colour imaging pipeline, we establish a simulation framework as a modular toolbox composed of a scene module (see Section 4.1), an image taking module (see Section 4.2), an image processing module (see Section 4.3) as well as an evaluation module (see Section 4.4), as depicted in Fig. 4.1. Each module is defined by a set of parameters and/or routines, with standardised interfaces between the modules in connection. This not only allows flexible design and adjustments of the system components, but also permits an efficient and intuitive means of evaluation. Also analyses are carried out to ensure the radiometric validity. Modules are developed with parameters determined quantitatively on a combined empirical and theoretical basis. Limitations of the simulation are also

discussed in detail (see Section 4.5). Subsequent examinations are carried out in order to verify the predictions, and explore the influence of one factor on another.

As the foremost element of an optical imaging system, the imaging optics affects the formation of optical images, thus influencing the input to the subsequent modules, in particular, the intra-band and inter-band correlation. And demosaicking works on the assumption of intra-band and inter-band correlations. To our knowledge, little is known about the influence of chromatic aberration, a prominent optical aberration, on CFA employed colour imaging, as it is normally considered in lens design and largely compensated by lenses. Therefore we simulate chromatic aberration in the image taking module, and studied how it affects the resultant image quality and the system performance (see Chapter 6). The use of spectral images as virtual scenes permits a sufficiently realistic simulation of both types of chromatic aberration, namely axial and transverse. Thanks to the flexibility of the simulation framework, we also conduct a survey on the impact of filter bandwidth on the accuracy of spectral reconstruction (see Chapter 5). A varying number of filters of a wide variety of bandwidths are simulated to mimic characteristics of various practical filters, coupled with three spectral reconstruction techniques. These two studies helped to examine the validity and practicability of the simulation framework, and investigate the role of these two key elements in the pipeline. This paved the way for the development of SFA demosaicking methods.

Rather than developing entirely new techniques, we focus primarily on extending potential interpolation techniques for the purpose of SFA demosaicking. The emphasis is therefore placed on the scalability of approaches to CFA demosaicking. Eventually three demosaicking methods on the basis of vector median filtering (see Chapter 7), discrete wavelet transform (see Chapter 8), and linear minimum mean square error estimation (see Chapter 9) respectively, are considered and selected for extension. The application of vector median filtering to demosaicking relies on pseudo-pixels artificially formed by a few adjacent pixels in the vicinity of the pixel in question. As a result, the size of the neighbourhood plays a role in both the demosaicking results and the computational complexity. Discrete wavelet transform may decompose an image into multiple frequency bands. When the high-frequency components in an image, i.e., edges and fine details, are highly correlated, they can be estimated with ease. Low-frequency components can be estimated by low-pass filtering. A combination of the resulting high- and low-frequency components may give rise to a reasonable demosaicked image. Unlike the two aforementioned heuristic approaches, the last technique, a.k.a. linear minimum mean square error, is a computational method that treats demosaicking as image

restoration. This linear operation applies a priori information obtained through training to demosaicking, with the aim of resulting in minimum mean square error between the full resolution image and the demosaicked image.

As a spatio-spectral sampling apparatus, filter array can be considered as a compromise between spectral and spatial sampling rate. Thus a SFA sacrifices spatial sampling rate for higher spectral sampling rate. In this case, would SFA be beneficial to colour image acquisition? To answer the question, we placed the CFA and SFAs in the pipeline, and evaluated the colorimetric performance of both respectively (see Chapter 10). For the purpose of a comparative analysis of SFA demosaicking, three proposed methods are compared with three representative methods given parameters of a real-world SFA based system design that covers both visible and IR bands (see Chapter 11).

1.3 List of publications

The research work connected with this dissertation has by far resulted in 8 conference and journal publications. The interconnections between the chapters and the publications are illustrated in Figure 1.4.

Conference publications

(I) **Xingbo Wang**, Jean-Baptiste Thomas, Jon Yngve Hardeberg, and Pierre Gouton. Median filtering in multispectral filter array demosaicking. In *Digital Photography IX*, volume 8660 of *Proc. SPIE*, pages 86600E–86600E–10. SPIE, February 2013. [176]

(II) **Xingbo Wang**, Jean-Baptiste Thomas, Jon Yngve Hardeberg, and Pierre Gouton. A study on the impact of spectral characteristics of filters on multispectral image acquisition. In *Proceedings of 12th Congress of the International Colour Association*, volume 4, pages 1765–1768, July 2013. [177]

(III) **Xingbo Wang**, Jean-Baptiste Thomas, Jon Yngve Hardeberg, and Pierre Gouton. Discrete wavelet transform based multispectral filter array demosaicking. In *Proceedings of Colour and Visual Computing Symposium (CVCS), 2013*, pages 1–6, September 2013. [175]

(IV) Congcong Wang, **Xingbo Wang**, and Jon Yngve Hardeberg. A linear interpolation algorithm for spectral filter array demosaicking. In Abderrahim Elmoataz, Olivier Lezoray, Fathallah Nouboud, and Driss Mammass, editors, *Image and Signal Processing*, volume 8509 of *Lecture Notes in Computer*

Science, pages 151–160. Springer International Publishing, July 2014. [170]

(V) **Xingbo Wang**, Marius Pedersen, and Jean-Baptiste Thomas. The influence of chromatic aberration on demosaicking. In *5th European Workshop on Visual Information Processing (EUVIP)*, pages 1–6. IEEE, December 2014. [174]

(VI) **Xingbo Wang**, Philip John Green, Jean-Baptiste Thomas, Jon Yngve Hardeberg, and Pierre Gouton. Evaluation of the colorimetric performance of single-sensor image acquisition systems employing colour and multispectral filter array. In Alain Trémeau, Raimondo Schettini, and Shoji Tominaga, editors, *Computational Color Imaging*, volume 9016 of *Lecture Notes in Computer Science*, pages 181–191. Springer International Publishing, March 2015. [173]

Journal publications

(VII) **Xingbo Wang**, Jean-Baptiste Thomas, Jon Yngve Hardeberg, and Pierre Gouton. Multispectral imaging: narrow or wide band filters? *Journal of the International Colour Association*, 12(1):44–51, July 2014. [178]

(VIII) Pierre-Jean Lapray, **Xingbo Wang**, Jean-Baptiste Thomas, and Pierre Gouton. Multispectral filter arrays: Recent advances and practical implementation. *Sensors*, 14(11):21626–21659, November 2014. [100]

1.4 Organisation of the dissertation

The dissertation comprises four parts, as illustrated in Figure 1.1.

Part I presents background information in connection with the research. As an introductory chapter, Chapter 1 outlines the research question, motivation and methodology, presents the contribution and a list of associated publications, and describes the organisation of this dissertation. Chapter 2 locates the research work in the scientific enterprise in an evolutionary point of view by illustrating the historical development of spectroscopy and imaging, the emergence of spectral imaging, and then demonstrates a list of approaches to spectral imaging including the SFA based techniques. Publication VI is connected with this chapter. Chapter 3 reviews literature in regard to the design, development and realisation of SFA based systems.

Part II describes the construction of the simulation framework and gives results on the interactions between the components. Details, assumptions and limitations of the simulation framework are presented in Chapter 4. Chapter 5 shows how bandwidths of filters affects the accuracy of spectral reconstruction by coupling filters of various bandwidths and linear reconstruction techniques selected from the state-of-the-art methods. Publication II and IV concern the bandwidth of filters and its influence on reconstruction. Chapter 6 investigates the influence of chromatic aberration on demosaicking, which is also covered by Publication VII.

Part III concerns methods for SFA demosaicking based on vector media filtering in Chapter 7 and Publication I, discrete wavelet transform in Chapter 8 and Publication III, and linear minimum mean square error estimation in Chapter 9 and Publication V respectively.

Part IV evaluates the system performance of a SFA based imaging system. Chapter 10 focuses on the colorimetric performance and the balance between spatial and spectral resolution of SFA in comparison with that of CFA, which leads to publication VIII. Chapter 11 studies the performance of the proposed SFA demosaicking methods given the characteristics and parameters of a real-world SFA based system design.

Chapter 12 summaries the dissertation, presents the major findings, discusses relevant issues and put forward a few suggestions for future work.

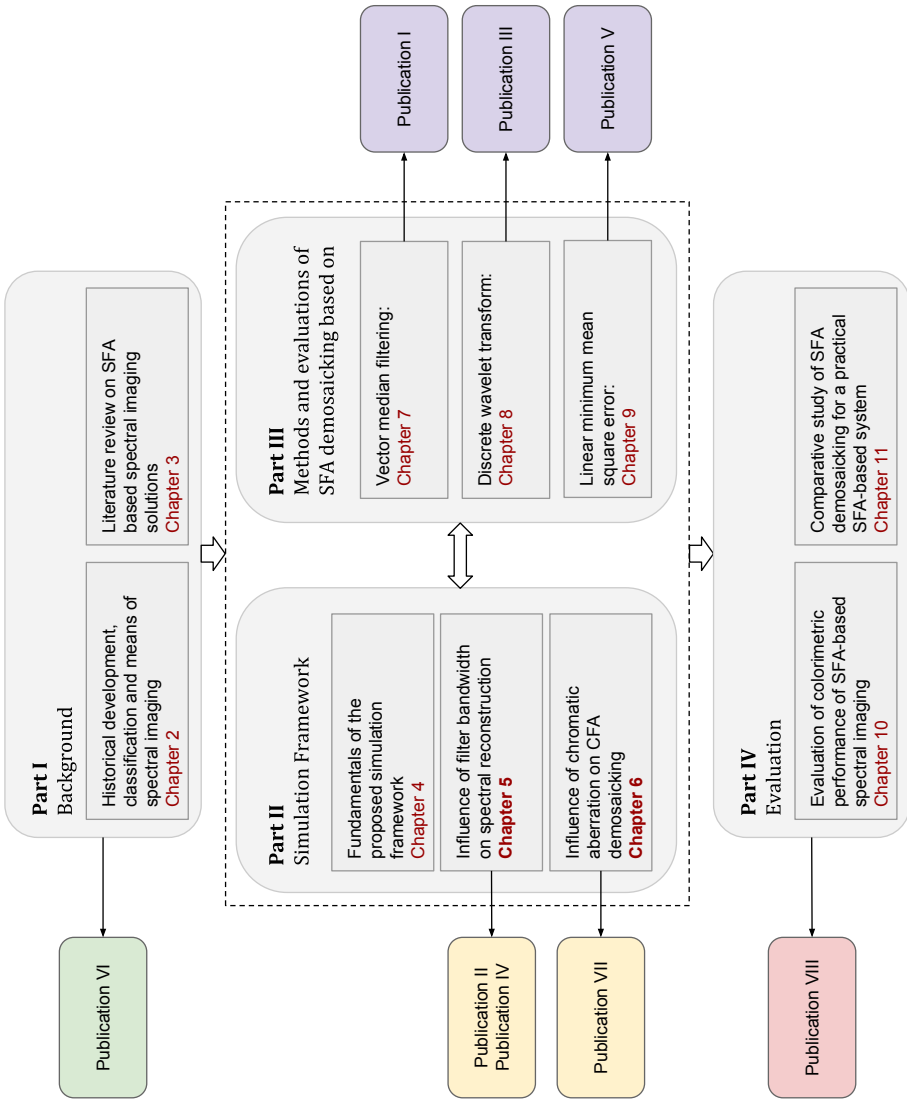

Figure 1.1: Contributions and organisation.
The dissertation is composed of four parts. Part I provides the background to the dissertation which supports the two following chapters. Part II describes the design and verification of the simulation framework. Part III brings forward three SFA demosaicking proposals on the basis of Part II. Part IV evaluates the colorimetric performance and studies the performance of the SFA demosaicking techniques in a practical system.

Part I

Background

Chapter 2

Overview of spectral imaging techniques

Solar radiation is the main source of energy on which nearly all life on earth survive. Direct and indirect sunlight also enables most animals to perceive the environment visually. From the viewpoint of evolutionary theory, the human eye is the optimal sense organ that allows human beings that allows vision. The unfailing interest of humans in exploring the nature and bettering their life, however, often requires vision systems beyond the capability of the HVS (human visual system) in terms of acuity, distance, precision, sensitivity, field of view, spectral range and resolution, dynamic range, non-volatile recording, quantifiability, etc. This leads to the development of optical devices and systems.

Light is considered as rays in geometrical optics, and waves in physical optics, which are collectively known as classical optics. As a ray, light obeys the rules of reflection and refraction. As waves, light has properties such as wavelength and frequency, which explains phenomena like diffraction. Later study of quantum mechanics reveals that light possesses both wave and particle properties, known as wave-particle duality. In quantum optics, light, therefore, comprises photons that may be absorbed and emitted by atoms or molecules in association with variations in the energy levels. These theories lay the foundation and pave the way for the measurement of light, and foster the development of measuring systems and techniques for various purposes.

2.1 Measurement of power of radiation in space

Among various quantities of light, or in general optical radiation, that can be measured, energy is perhaps the most frequently used one. This is covered by the subject of radiometry, a technical subject concerning the measurement of optical radiant energy [141]. The study of radiometry begins with fundamental units. Apart from radiant energy (Q_e) and radiant flux or radiant power (Φ_e), radiance (L_e), the elementary quantity of radiometry is defined by radiant power per unit area per projected solid angle. Integration of radiance over solid angle yields radiant existence (M) or irradiance (E_e), and integration over area yields radiant intensity (I). An associated subject, photometry, deals with the response of human eyes to visible light by incorporating the luminous efficiency function defined by the CIE into radiometric measurements [25]. Radiometry and photometry are the roots in light measurement, and all measuring instruments of light should be calibrated accordingly. The units in both disciplines are summarised in Table 2.1.

Table 2.1: Basic quantities, units and symbols used in radiometry and photometry.

Radiometric quantity	Unit	Photometric quantity	Unit
radiant flux (Φ_e)	watt (W)	luminous flux (Φ_v)	lumen (lm)
radiant intensity (I_e)	watt per steradian ($W \cdot sr^{-1}$)	luminous intensity (I_v)	candela (cd)
radiance (L_e)	watt per square metre and per steradian ($W \cdot m^{-2} \cdot sr^{-1}$)	luminance (L_v)	candela per square metre ($cd \cdot m^{-2}$)
irradiance (E_e)	watt per square metre ($W \cdot m^{-2}$)	illuminance (E_v)	lumen per square metre ($lm \cdot m^{-2}$), lux (lx)

2.2 Spectral measurement of light

In comparison with photometry, colorimetry can be seen as an extension of light measurement to spectrum. Distinct from photometers that determine an photometric quantity of light, colorimeters measure a set of three quantities, known as tristimulus values, in accordance with the CIE colorimetry [27], as described below:

$$
\begin{aligned}
X &= k \sum_{\lambda} \phi_{\lambda}(\lambda)\bar{x}(\lambda)\Delta\lambda \\
Y &= k \sum_{\lambda} \phi_{\lambda}(\lambda)\bar{y}(\lambda)\Delta\lambda \\
Z &= k \sum_{\lambda} \phi_{\lambda}(\lambda)\bar{z}(\lambda)\Delta\lambda
\end{aligned}
\tag{2.1}
$$

In the above equations $\phi_{\lambda}(\lambda)$ denotes the spectral distribution of the colour stimulus function (see CIE International Lighting Vocabulary item 845-01-17 [26]). X, Y, Z are tristimulus values, $x(\lambda)$, $y(\lambda)$, $z(\lambda)$ are colour-matching functions of a standard colorimetric observer, and k is a normalising constant. For reflecting or transmitting object colours, the colour stimulus function, $\phi_{\lambda}(\lambda)$, is replaced by the relative colour stimulus function, $\phi(\lambda)$, evaluated as $\phi(\lambda) = R(\lambda) \cdot S(\lambda)$ or $\phi(\lambda) = \tau(\lambda) \cdot S(\lambda)$ where: $R(\lambda)$ is the spectral reflectance/radiance of the object colour. $\tau(\lambda)$ is the spectral transmittance of the object colour. $S(\lambda)$ is the relative spectral power distribution of the illuminant. In this case, the constants, k is chosen so that $Y = 100$ for objects for which $R(\lambda)$, or $\tau(\lambda) = 1$ for all wavelengths, and hence $k = 100/\sum_{\lambda} S(\lambda)\bar{y}(\lambda)\Delta\lambda$.

In fact, when light interacts with matter, absorption, emission and scattering of light follow a specific pattern. Thus a measurement of transmittance, reflectance or emissivity at one or more specific wavelengths may assist in determining the composition of materials, identifying matter of interest, analysing certain properties of objects, etc. This is known as spectroscopy, according to a strict definition, the branch of science which involves the use of spectroscope, or in modern use, the investigation of spectra by any of various instruments. The first use of spectroscopy is attributed to Joseph von Fraunhofer who discovered in 1918 black lines in the spectrum of sunlight with what he called a spectroscope [137, p. 24]. A wide variety of measuring devices has since been realised under the umbrella of spectroscopy, notably for chemistry, physics and astronomy.

In fact, spectroscopy may denote a few distinct principles [52], such as optical spectroscopy, nuclear magnetic resonance spectroscopy, mass spectrometry, etc. In this dissertation, spectroscopy denotes optical spectroscopy and refers to all techniques that use non-ionising radiation. This covers the spectral range from the 200 nm far ultraviolet (UV) all the way to the 500 μm far infrared (IR).

Common spectroscopic instruments include spectrometer, spectroscope, spectrograph, spectroradiometer and spectrophotometer. What they share in common is the ability to measure a specific quantity of light, i.e., intensity or polarization, as a function of its wavelength(s), albeit with literally different etymologies. Similarly, there are corresponding words referring to the subject where these instruments are used. In practice, these are often used interchangeably, and it is not the intention of the dissertation to distinguish one from another. And the term, *spectrometer*, is used to refer to spectral measuring instruments hereinafter, unless otherwise indicated.

In modern use, spectrometer refers to any of a wide range of instruments for producing spectra and measuring the positions, etc., of spectral features [161]. Such an instrument typically employs basic wavelength selective devices such as monochromators, interferometers and polychromators.

2.2.1 Monochromators

Monochromators may be based on the following architectures.

Prism Prism is a transmitting optical component that has three major spectroscopic functions: dispersion, reflection, or polarisation. A dispersing prism separates light into its constituent wavelengths, because the refractive index of the prism's material varies with wavelength. If the two interfaces of the prism are non-parallel, the outgoing light rays of differing wavelength will travel in slightly different directions, becoming dispersed by wavelength.

Gratings Gratings work in reflection or transmission mode, use of reflective is quite common spectroscopy. A reflection grating is a surface that has been lined with closely spaced grooves. Upon reflection of a collimated incoming broadband light source, each groove acts as an independent slit. Reflections from multiple slits constructively and destructively interfere so that light of a particular wavelength constructively interferes at a particular angle. As such, the broadband incoming light becomes angularly diffracted.

Filters Filters come in two types. A bandpass filter allows a range of wavelengths to pass, while a cut-off filter only allows light above or below a certain wavelength to pass. Most filters use either absorption or interference to eliminate all but the desired regions of light. An absorption filter contains a pigment that absorbs all but a range (or ranges) of light. For a band-pass filter, the range $\Delta\lambda$ is expressed by the wavelengths at which the transmission is

half the maximum transmission for the full width of the range (abbreviated "full width at half maximum,", or FWHM). A filter with an exceptionally narrow $\Delta\lambda$ is a notch filter. Cut-off filters are either short-wavelength cut-off or long-wavelength cut-off, depending on whether they absorb all light below or above a specified wavelength.

Interference filter An interference filter uses destructive interferences of most light to isolate and transmit a narrow range of wavelengths of light. One type of interference filter is the Fabry-Pérot filter. It is a thin layer (several hundred nanometers) of low refractive index, usually mounted between glass sheets. Incoming polychromatic light experiences some internal reflection and mostly undergoes destructive interference. However, light of a particular wavelength undergoes constructive interference and passes through the filter. Interference filters are tunable, the exact wavelength that passes can be varied by changing the characteristics of the filter, typically the angle of incidence or the thickness.

2.2.2 Interferometer

In addition to monochromator, interferometer is also widely used in spectral measurement where high spectral resolution is desired. Common types include Fabry-Pérot interferometer and Michelson interferometer. Similar to a Fabry-Pérot filter, a Fabry-Pérot interferometer employs two pieces of highly reflective mirrors separated by an air gap. Optical radiation of a certain wavelength constructively interfere and thus passes through the interferometer. This wavelength and the exit angle varies depending on the width of the gap and the index of refraction. A Michelson interferometer consists of a beamsplitter, a fixed mirror and a movable mirror [128]. The input polychromatic light is separated by the beamsplitter into two beams, which are then reflected by the two mirrors respectively. Adjusting the position of the moving mirror results in path difference. When recombined, the two beams carrying all wavelengths interfere constructively or destructively depending on the path difference. A plot of light intensity against the mirror position, an interference pattern, is termed interferogram. In 1892, Rayleigh discovered that a spectrum was related to its interferogram through Fourier transform, which was first implemented by Fellgett in 1949 [11]. As a result, such an instrument is also termed Fourier transform spectrometer (FTS).

Parameters developed to evaluate performance of spectrometers include spectral resolution, spectral range, resolving power, throughput, signal-to-noise ratio, etc.

2.3 Spatial measurement of light

The HVS is a stereoscopic system on the basis of two eyes that project the three-dimensional world on the two-dimensional retina, as a result, acquisition of two-dimensional images are expected. Technically, the group of techniques of forming two-dimensional images is named imaging. An early attempt and illustrative example of imaging is known as film photography thanks to photochemical process. Nevertheless, it is the discovery of photoelectric effect that opens the door to electronic imaging and later digital imaging, which makes possible the applications like television, fax, digital photography, digital cinematography, etc. The basis of imaging lies in the form of the image sensor, also known as the imager, and the means of scanning that arranges the spatial information on the imager. Nowadays the majority of images is trichromatic due to the wide use of colour imaging devices. Colour imaging makes use of the principle of colorimetry and metameric colour reproduction, and interprets the spectrum of light with tristimulus values in association with the cone fundamentals of human eyes.

Common image sensors are designed to discretise a one- or two-dimensional optical image and convert it to an electronic representation by means of optoelectronic conversion, namely an integration of incident power over the photosensitive area, the spectral responsive range as well as the exposure time.

Spatial shape of an imager decides the way of image acquisition. Whisk broom or zig-zag scan is required to capture a two-dimensional image when an individual photodiode is used, and a historic example is Nipkow disk used in early TV production. As linear (1-D) scanner becomes available, push broom or line scan appears, and a notable example is flatbed desktop scanner. A large number of imagers, seen in most digital still or video cameras, are solid-state area image sensors, also known as staring array or focal plane array.

Parameters developed to evaluate performance of an image sensor include spatial resolution, sensitivity, dynamic range, signal-to-noise ratio, uniformity, field-of-view, etc.

2.4 Spatio-spectral measurement of light

Radiometry and photometry are not spatial, nor is spectroscopy. Likewise, imaging lacks the ability to capture spectrum, although colour imaging can be regarded loosely as spectral acquisition. Nevertheless the study of astronomy and in particular astrophysics in the nineteenth century was in need of a class of instruments

that combines spectral and spatial measurement of light, thus measuring the spectrum at every point in an image. This leads to the development of various spectral imagers and accordingly the discipline of spectral imaging.

Similar to trichromatic images used extensively in our daily life, spectral images also take the form of a three-dimensional data matrix consisting of three image variables. More specifically, a discrete image is an array of m rows, n columns and c spectral channels. An image where $c \geq 3$ is generally called a spectral image. In other words, a trichromatic image can be regarded as a particular instance of spectral images where $c = 3$.

Spectral imaging, as its name implies, refers to the discipline in which a spatio-spectral representation of a scene is formed and recorded. That is, each pixel in a discrete spectral image represents a sampled spectrum. From technological and historical points of view, spectral imaging has its root in and evolved from both spectroscopy and imaging, both of which concern the measurement of light, albeit purposed differently. In other words, spectral imaging can be intuitively seen either as a spatial extension of spectroscopy, or as a spectral extension of imaging. Figure 2.1 shows a concept of spectral imaging.

The first attempt to obtain a spectral image may date back to 1869 when the French astronomer Pierre Jules César Janssen observed the solar corona with a spectroscope. A narrow-band spectral image was formed with the persistence of vision by spinning the device rapidly, and adjustments could be made for viewing other wavelengths [80, 81]. The evident pioneers who invented spectroheliograph, an instrument that captures a monochromatic photographic image of the sun at a single wavelength, are American astronomer, George Ellery Hale, and French physicist, Henri Alexandre Deslandres [19]. Hale designed and built a spectroheliograph for a telescope in 1892 with which he discovered solar vortices, and a similar development by Deslandres to record monochromatic images of the solar chromosphere commenced at about the same time as Hale [71, p. 105]. The spectroheliograph mentioned is essentially an imaging capable spectrograph, which can be regarded as early efforts towards spectral imaging.

In addition to planetary science, there were concomitant demands for, and development of, imaging spectrometers in remote earth sensing in 1980s. As technology advances, such instruments were soon introduced to many applications which helped to shape today's spectral imaging.

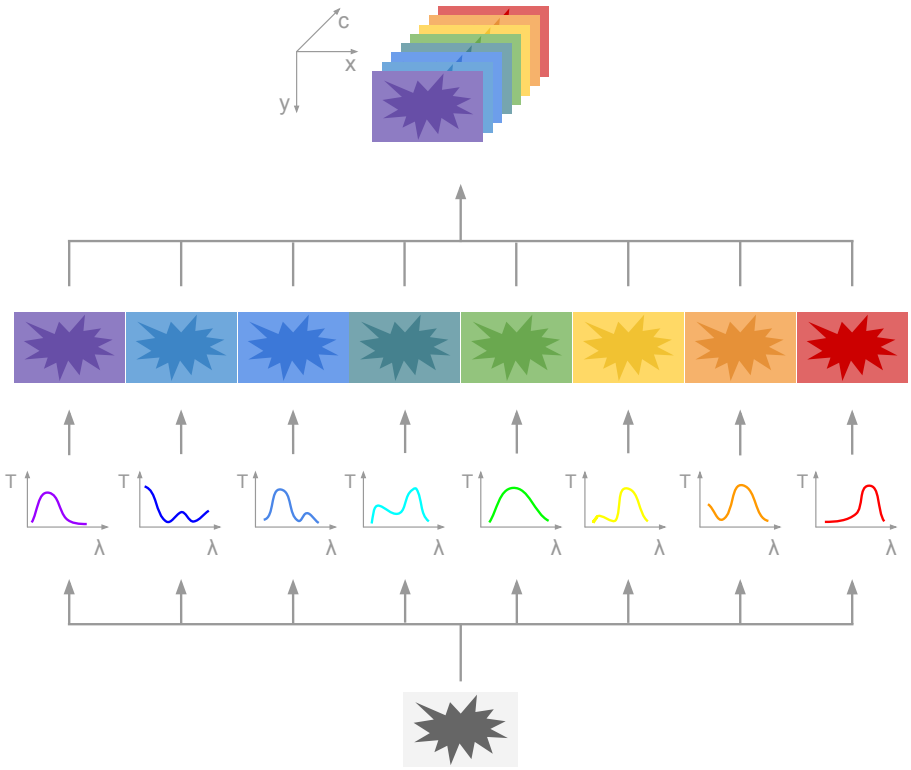

Figure 2.1: Concept of spectral imaging. The radiation emitted, reflected or transmitted by an object passes through 8 arbitrary absorptive filters resulting in an 8-band spectral image.

2.4.1 Multispectral, hyperspectral or ultraspectral?

The wide variety of spectral imaging devices may be classified into multispectral, hyperspectral and ultraspectral according to their spectral characteristics. Breckinrige provides the following definitions within the framework of remote sensing [18].

Though it is not straightforward to find out the origin of “multispectral”, the term appearing in 1960s stemmed probably from “multiband spectral reconnaissance”. In Colwell’s work [31], an example is illustrated where four surfaces, e.g., grass, cement, asphalt, and soil, are distinguished solely from an examination of their

Table 2.2: Definition of multispectral, hyperspectral and ultraspectral imaging.

Category	Spectral resolution $\Delta\lambda/\lambda$	Number of bands	Examples	Application
Multispectral	≈ 0.1	10-20	LANDSAT	maximises the contrast of the object space irradiance distribution
Hyperspectral	≈ 0.01	100-200	AVIRIS, HYDICE	reveals chemical composition of solids and liquids
Ultraspectral	≤ 0.001	1000-10000	ATMOS, AES, TES	reveals chemical composition of gases

images as seen on aerial photographs taken at high altitude. Two types of photographic films and two filters are combined to take two photographs by comparing both so that all four surfaces become distinguishable. Later the author examines the uses and limitations of multispectral remote sensing through specific examples including forestry, agriculture, geology, oceanography, meteorology, hydrology and geography [33, 32]. The launch of the Landsat 1, the first Earth-observing satellite, by NASA in 1972 opens the door to space-borne multispectral remote sensing with the Multispectral Scanner System (MSS) it carries [135]. The MSS responds to Earth-reflected sunlight in four spectral bands covering the spectrum between 0.5 μm and 1.1 μm [136, 99]. As can be seen, multispectral imaging, in a broad sense, can be any system capable of capturing images in multiple discrete bands that may go well beyond the visible range of the electromagnetic spectrum.

As geologists found it difficult to discriminate among minerals on the earth's surface on MSS images, it became necessary to measure spectral reflectance and emittance [58]. Hyperspectral imaging, first coined by Goetz *et al.* in 1985, refers to the "acquisition of images in hundreds of contiguous, registered, spectral bands such that for each pixel a radiance spectrum can be derived" [60]. In fact, few materials, if any, require hundreds of spectral bands spread over several octaves of the spectrum to be identified uniquely. However it turns complicated when the region of interest is mixed with other surfaces viewed remotely through the uncontrolled atmosphere [59]. To that end, the Jet Propulsion Laboratory started developing the first imaging spectrometer for earth observation in 1980, which leads to the implementation of the Airborne Imaging Spectrometer (AIS) and the Airborne Visible/Infrared Imaging Spectrometer (AVIRIS) that first flew in 1982 and 1986 respectively [63]. The AIS covers the 1.2-2.4 μm region with 128 spectral

bands, while the AVIRIS covers 0.4-2.45 μm with 224 spectral bands [58]. Unlike multispectral imaging, hyperspectral imaging requires the continuity of bands and often a higher number of bands.

In comparison with hyperspectral imaging that produces contiguously sampled spectra, multispectral imaging systems typically acquires images over a lower number of broader bands that carry useful information in themselves and may cover both visible and invisible portions of the spectrum. The so-called ultraspectral imaging is not much different from hyperspectral imaging, yet involves even higher spectral resolution, thus yielding more bands and shorter intervals. The increase in spectral resolution and hence the data rate makes real-time data processing and data storage two practical issues.

As seen, hyper- and ultra-spectral imaging systems sample the spectral domain at a "rate" usually sufficient to develop unique spectral signatures capable for use in direct surface materials identification on a pixel-by-pixel basis as well as providing detailed information, e.g., for study of geophysical and biophysical processes [157].

In spite of the discrepancies in spectral capabilities and characteristics, all of the three types of systems mentioned above may be considered collectively as spectral imaging techniques. In this dissertation, we focus on multispectral imaging.

2.4.2 Scanning spectral imaging devices

Thanks to the spatio-spectral essence, spectral imaging devices may be categorised in a more systematic way by the methods they obtain information spatially and spectrally.

Table 2.3: Classification of scanning spectral imaging devices by signal collection method.

		Spatial		
		whiskbroom	pushbroom	staring
Spectral	Filtering			tunable filter
	Dispersive	grating/prism	grating/prism	tomographic
	Interferometric		Sagnac	Michelson

Table 2.3 shows a few examples of spectral imaging devices commonly used. What is common to these types of instruments is the need for scanning, i.e., a series of exposures. Whiskbroom scanning works with 1-D (linear) detectors, whereas

pushroom scanning and staring (focal plane array) function with 2-D (area) detectors. In consequence, spectral scanning is necessary in the filtering class, and spatial scanning is needed in the dispersive and interferometric classes, in order that these devices may acquire 3-D spectral images with 1-D or 2-D sensors. Scanning decomposes complicated 3-D imaging into viable 2-D image acquisition, since the overwhelming majority of human made detectors till now are of up to 2-D.

It is not hard to imagine that the variety of scanning spectral imagers lies in the way a 3-D spectral image is decomposed into a sequence of 2-D slices (and rarely 1-D slices in case of whiskbroom scanning). Consequently a scanning spectral imager may be considered as a straightforward generalisation of non-imaging spectrometers or photographic imagers, predominantly driven by the maturity of 2-D detectors in 1980s. The examples appearing in Section 2.4.2 are described below respectively.

Filtering

Perhaps the most intuitive example of spectral scanning techniques is so-called tunable filters. By capturing an image of one spectral band at a time with a staring detector, a complete spectral image is produced after a sequence of exposures.

A common and illustrative instance is filter wheel where a series of desired optical filters are installed [49]. When integrated with a monochromatic camera, and typically inserted in the optical path, such a rotatory filter wheel may work in a synchronised way with the camera, so that one exposure corresponds to a certain type of filter, which yields an image at a certain spectral band. An illustrative example of a filter wheel based spectral imaging system is outlined in Figure 2.2.

The rotatory speed of such filter turrets are limited by its mechanical nature, therefore tunable filters whose spectral properties can be controlled electronically are developed [51]. Refractive indices of some materials vary in the presence of electrical fields, magnetic fields or sound fields, which result in electro-optical, magneto-optical and acousto-optical modulators. These principles are further utilised in electronically tunable filters, among which the two most used ones are LCTF (Liquid Crystal Tunable Filter) and AOTF (Acousto-Optical Tunable Filter). In fact, both of them provide notch pass-bands, but they differ in the principles [132]. The LCTF incorporates liquid crystal waveplate retarders tuned by applying electronic voltage within a Lyot birefringent filter, whereas AOTFs are solid-state birefringent crystals that vary in response to an applied acoustic field [70]. The transition of these filters are much faster in comparison with the

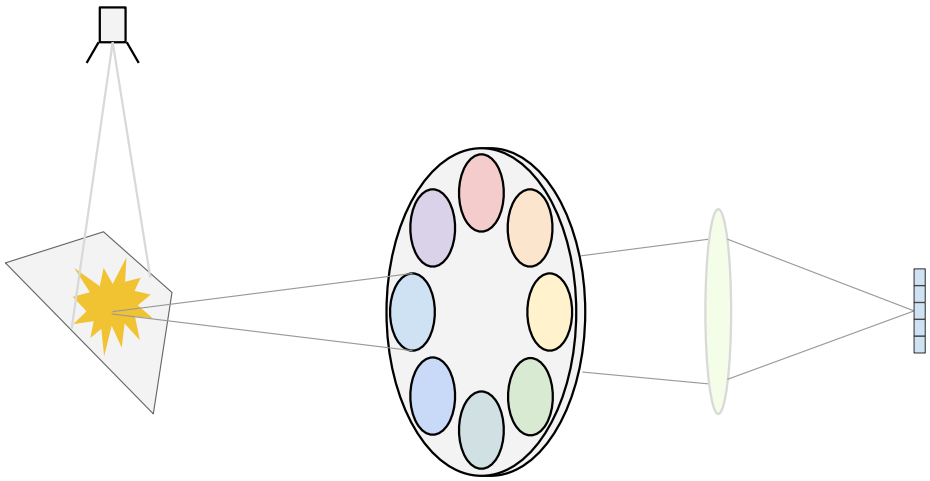

Figure 2.2: Illustration of a filter wheel based spectral imaging system. Inserted into the optical path of a normal imaging system, the turret holds multiple absorptive filters. When rotating, the scene is scanned spectrally and recorded by the image sensor synchronising with the filters.

filter wheel solution. As an example, a multispectral imaging spectrometer with millisecond resolution has been developed based on the use of an AOTF for spectral filtering and a progressive scan camera capable of snapshot operation for recording [88]. The use of LCTF is common in the multispectral imaging of cultural heritage in the museums [76].

A typical scenario where spectral images are taken comprises a light source, an object and an imaging device. The methods mentioned above depend passively on filters integrated with the imaging device, and certainly they can be inserted anywhere in the optical path, such as at the illumination end (see Figure 2.3). This set up is widely used in cultural heritage [114] and medical imaging [84], although it is usually customised and thus lacks scalability. To change the spectrum of an illumination, however, filtering is not the only solution. Bouchard *et al.* present a new LED-based system capable of high-resolution multispectral imaging at frame rates exceeding 220 Hz [15]. Other examples of tunable illumination can be seen in [114, 84].

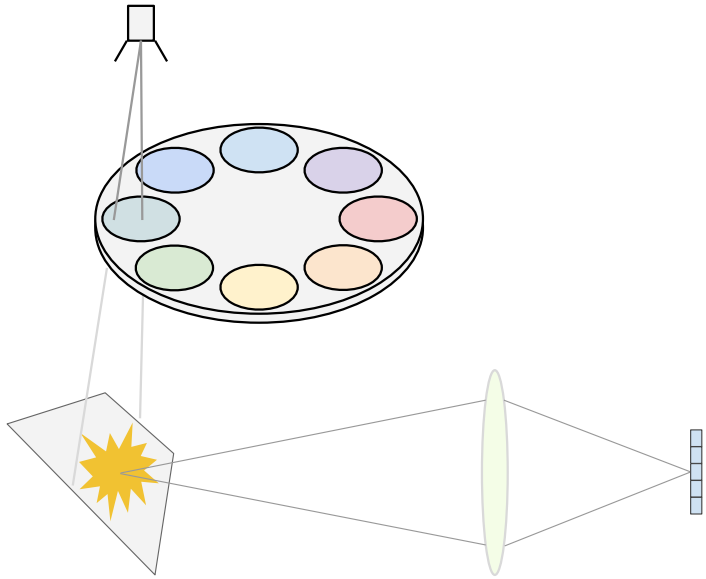

Figure 2.3: Illustration of tunable illumination. Dissimilar to filter wheels inserted in the imaging device, they can also be placed at the illumination end which modulates the light actively.

Dispersive

Non-imaging spectrometers employing gratings and prisms may easily be extended as imaging spectrometers by introducing a spatial scanning component and a corresponding image detector. For instance, a point-scan spectrometer with two scan mirrors oscillating in two orthogonal directions, when coupled with a linear image sensor, scans the scene, disperses each spatial element into a spectrum and projects it on the sensor. Similarly one oscillating mirror is sufficient when there is relative movement between the instrument and the scene. This is known as whiskbroom scan in remote sensing. Alternatively a slit-shaped input aperture, when accompanied by an area image sensor, allows an acquisition of the spectrum of the image of the slit at one exposure, which is figuratively named pushbroom scan.

Prisms make use of refraction while gratings take advantage of diffraction. Both are capable of spectral dispersion, yet none of them is fully superior to the other.

Though simpler, prisms are limited by non-linear and relatively low dispersion as well as light absorption due to the substrate and refractions. Gratings outperform prisms in the mentioned aspects, however they suffer from multiple order effects in case a wide range of spectrum is required, and they exhibit polarisation effects that are wavelength dependent. In practice, therefore, combinations of both of prisms and gratings may avoid some of the drawbacks [8].

Motivated by the fact that the scan that slices a 3-D spectral image datacube into a sequence of 2-D images is actually a tomographic process, Mooney discusses a technique, that angularly multiplexes spectral and spatial information on the image plane by a rotatory direct vision prism [131]. As the prism rotates along the optical axis, the resulting imagery, a slant stack of chromatic images resulting from dispersion of the prism, also rotates. That is, the image of each spectral band moves following a circular path and the radius is determined by the prism dispersion as well as the focal length of the image taking lens. Accordingly, a sequence of images is formed by recording the images with an area image sensor. In subsequent processing, a 3-D date cube can be restored by demultiplexing the resultant imagery in tomographic manner, which is in general computationally expensive.

Interferometric

Interferometers play an important role in spectroscopy because of its high spectral resolution and high light collection efficiency. There are various types of interferometers, two of which broadly used in imaging spectrometers are Michelson interferometers and Sagnac interferometers.

In a non-imaging FTS, a single detector is sufficient to scan the interferogram, and each scan represents a linear combination of amplitudes at all wavelengths. Similarly an imaging FTS, named FTIS, may be realised by introducing an area image sensor to FTS [145, 181]. As the range of movement of the movable mirror is normally very short, the scan can be very fast. Such scans resembles spectral scanning of tunable filters. Thanks to its multiplex advantage and therefore high signal-to-noise ratio, use of FTS and FTIS is very common in infrared region where signal is often weak, e.g., in astronomy.

To eliminate the movable mirror in the FTIS, Meigs *et al.* present a FTIS employing a Sagnac interferometer for deployment in a light aircraft [119]. This is an instrument of pushbroom type that records the interferogram of a slit-shaped aperture in a stationary configuration. Sagnac interferometer is a type of common path interferometer in which the two beams travel along the same path in opposite dir-

ections. In this instrument, the interferometer is implemented as a pentaprism-like solid block with a beamsplitting layer built inside.

2.4.3 Snapshot spectral imaging devices

The examples illustrated in Section 2.4.2 are all based on scanning, either spectral or spatial, due to the insufficient dimensionality of modern image sensors in comparison with 3-D spectral image data cubes. It is not hard to imagine that there are important limiting factors to both of these two approaches. Spectral scanning works properly only when there is no relative motion between the imager and the scene. Similarly spatial scanning works on the assumption that the spectral properties of the object does not change in the course of scanning. In nature and human activities, however, some very fast changing phenomena or fast moving objects are of interest, for instance missile exhaust plumes, missile intercept events, and lightning strikes, hypervelocity impacts, etc. In such cases, scanning operation, i.e., multiple exposures, often yields motion artefacts. In addition, the operation of scanning naturally weakens the light collection efficiency, thus not favourable in sensor-noise-limited conditions, e.g., astronomical observation of remote planets.

Therefore a non-scanning approach to spectral imaging is preferable, which leads to snapshot spectral imagers capable of acquiring a complete spectral image data cube in a single integration period of a focal plane array. Though snapshot does not necessarily mean shorter integration time than its scanning counterpart and may still cause blur, it is easier to correct blur than dealing with motion artefacts due to multiple exposures [68]. Further, non-scanning techniques do not rely on moving parts and thereby in general leading to simpler and cost-effective design of higher portability, accuracy and robustness. A comparison between these two is demonstrated in Figure 2.4.

Snapshot spectral imagers make use of focal plane arrays, which implies that a 3-D data cube must be encoded and arranged in 2-D format. Inevitably subsequent data processing is often of necessity to reconstruct the 3-D spectral image. And most of them rely on a large detector array.

Hagen and Kudenov present a comprehensive review of 13 types of snapshot spectral imaging technologies [68], listed in Table 2.4. As can be seen, most of the technologies employ both spectral dispersing devices and beam splitting or image slicing components. This is not unexpected, as a snapshot spectral imager is expected to multiplex spatial and spectral information on a single detector array. To better understand the principles and characteristics of these methods, we shall here

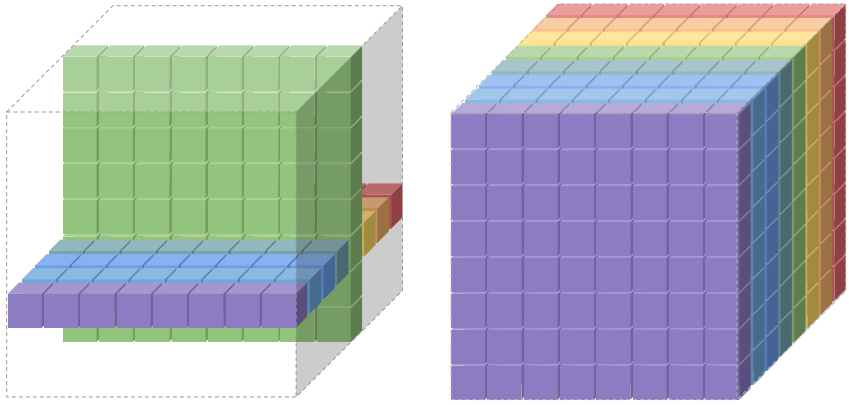

(a) Scanning spectral imaging **(b)** Non-scanning spectral imaging

Figure 2.4: Illustration of scanning and non-scanning spectral imaging. In a scanning system, one exposure may form an image at a spectral band or a slice of the image at all bands. In a non-scanning system, one exposure captures necessary information sufficient to reproduce/estimate a full spectral image.

follow their numbering and nomenclature, and re-group the instruments into fewer classes by the similarities in the principles.

Beamsplitting

The use of beamsplitters in television cameras dates back to 1950s when RCA introduced its massive 3-tube colour camera consisting of a configuration of three dichroic mirrors that direct incoming light into red, green and blue beams each of which is projected through a lens onto a camera tube individually [74, p. 45]. To reduce the complexity and the dimensions of a colour camera, Lang and Bouwhuis propose a prism assembly for Plumbicon® camera in 1965 [37], which comprises three prism blocks and makes use of total internal reflection and dichroic filters.

Intuitively the technique of beamsplitting may generate more than three beams (See Figure 2.5). A general multispectral beamsplitter is introduced in [159] where a three-band example is presented. Later a similar approach is developed that employs a stack of dichroic filters, thus reducing the dimensions and enabling a single-sensor system [12]. Like previous configurations, the number of beams is still limited due to the cumulative transmission losses. As the system described

Table 2.4: Comparison of snapshot spectral imaging technologies.

	1	2	3	4	5	6	7	8	9	10	11	12	13
re-imaging lens		×	×		×		×		×	×	×		×
grating		×	×	o	×		×			×			×
prism				o							×	×	
filter				o									
interferomter							×						×
filter array						×		o					
stacked/tunable sensor								o					
image slicer/mapper	×										×		
lenslet array			×			×					×	×	
coded aperture										×			
polariser/waveplate									×			×	
optical reformatter				×									
no. of detector arrays	w	1	1	w	1	1	1	1	1	1	1	1	1

Please note that in the table above "×" indicates compulsory components, "o" denotes selective components, and "w" denotes number of spectral bands. The numbering of spectral technologies is consistent with that given by Hagen and Kudenov [68] for ease of comparison. The corresponding full names represented by the numbers are listed below.

1 Integral Field Spectrometry with Faceted Mirrors (IFS-M)
2 Integral Field Spectrometry with Coherent Fibre (IFS-M)
3 Integral Field Spectrometry with Lenslet Arrays (IFS-L)
4 Multispectral Beamsplitting (MSBS)
5 Computed tomography Imaging Spectrometry
6 Multiaperture Filtered Camera (MAFC)
7 Tunable Echelle Imager (TEI)
8 Spectrally Resolving Detector Arrays (SRDA)
9 Image-Replicating Imaging Spectrometer (IRIS)
10 Coded Aperture Snapshot Spectral Imager (CASSI)
11 Image Mapping Spectrometry (IMS)
12 Snapshot Hyperspectral Imaging Fourier Transform Spectrometer (SHIFT)
13 Multispectral Sagnac Interferometer (MSI)

in [12] require some lenses to disperse and direct the beams, a stack of tilted filters can eliminate the dispersive lenses and further reduce the size as illustrated in [140]. However, the filters operate in double-pass mode and therefore prevents the increase of number of bands. A somewhat different strategy takes advantage of multiplexed volume holographic gratings written in a thermally stable photosensitive glass [116]. A 12-channel beam splitter is prototyped by multiplexing three volume holograms in a 2×2 array, and another prototype is planned to cover

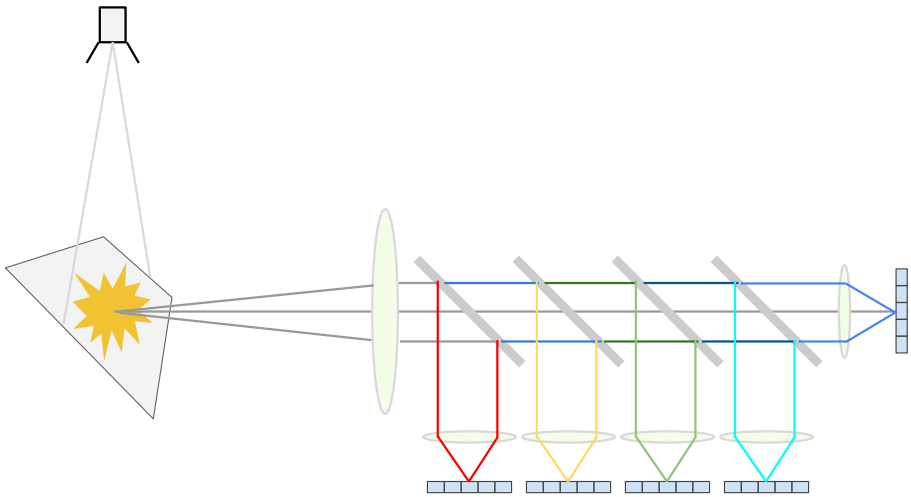

Figure 2.5: Illustration of a 5-band beamsplitting spectral imaging system. Four dichroic mirrors split the incoming beam into five, each projected to a separate image sensor, resulting in five bands.

both visible and SWIR (short wave infra-red) region. These are termed MSBS in [68].

Another approach to beamsplitting, named IRIS [68] (see Figure 2.6), makes use of beamsplitting polarisers. Gorman *et al.* [62] describe a generalised Lyot filter that employs multiple cascaded birefringent interferometers to simultaneously spectrally filter and demultiplex multiple spectral images onto a single detector array. An example of an eight-band multispectral movie sequence is obtained without further processing, as demonstrated in Figure 2.6. More spectral channels, however, requires larger polarisers and may be affected by chromatic aberrations, which may limit this approach to 16 spectral bands [68].

Although beamsplitting enables a snapshot solution, there are a few limiting factors, such as the number of bands and the incident angle, apart from the space requirement and the manufacturing cost, due partly to the necessity of multiple sensors and partly to the beamsplitter.

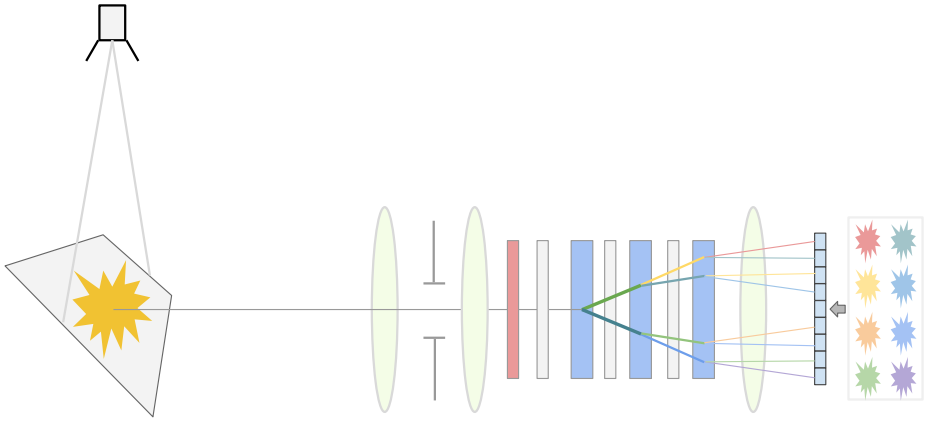

Figure 2.6: Illustration of 8-band beamsplitting system incorporating generalised Lyot filters. As a means of beamsplitting, a generalised Lyot filter splits the incoming beam spatially and filters it spectrally. The use of a stack of them therefore produces a set of spectral slices illustrated at the output.

Image mapping

Beamsplitters project an image into multiple ones, each corresponding to a spectral band, which may be considered as spectral mapping. Similarly it is also intuitive to map the image spatially by means of slicing or reformatting.

In astronomy spectral imaging is usually known as integral field spectrometry, which varies in principle. One common method, labelled IFS-M in [68], is based on image slicer, e.g., multifaceted mirrors, that slice an image into thin stripes and translate each stripe to form a slit, which can then be measured by a slit spectrometer. This originates in Bowen's image slicer based on a series of tilted mirrors [16] and may also be realised by a piezo-driven multifaceted mirror [180] or multifaceted mirrors. Although commonly seen in astronomy, this approach suffers from relatively low spatial resolution due to the limited number of manufacturable facets. Also the preparation of the image mapper of high precision is challenging.

Another astronomical way of snapshot spectral imaging transforms the 3-D input into 2-D output by physically rearranging a bundle of fibres [86]. Described as IFS-F in [68], this technique relies on a coherent fibre bundle. At the image plane,

the bundle is organised so that the end of the bundle forms a sampler. The other end, however, is reformatted into a thin line, which can then utilised as inputs to a slit spectrometer. One of the first implementation of this concept appears 1980 to extract spectroscopic information in nebulosities of quasars [167]. Later similar systems for non-astronomical applications is developed [117]. Performance of IFS-F solutions is affected by issues specific to optical fibres, such as lower F-number at exit face than input face, broken fibres, and modal noise, etc.

Both of IFS-M and IFS-F techniques provide much higher spectral resolution than spatial resolution. For applications where spatial resolution is more important, such as microscopy, a solution termed IMS [68] is more appropriate. What IMS and IFS-M share in common is a faceted mirror as an image mapper, whereas IMS differs from IFS-M in that multiple facets may face the same angle. As a result, multiple slices of images may be mapped to each individual pupil through which each sub-image projected on the detector array. The final pattern incident on the sensor is therefore an array of sub-images, each of which consists of spectra of multiple dispersed image slices. An early implementation is realised by Gao for microscopic applications [50]. Like IFS-M, the difficulty with IMS lies in its dependence on highly precise image mapper.

Division of aperture

Apart from image mapping, there is another category of spatial splitting methods utilising a lenselet array, namely multiple apertures. Again this idea has its roots in astronomy when Courtes suggests placing a lenselet array at the telescope's focal plane [35], essentially an integral field spectrometer labelled IFS-L in [68]. Accordingly such a lenselet array results in a corresponding array of pupil images on the detector array positioned at the conjugate plane. In other words, each pupil image is a mixture of light incident on the corresponding lenselet, which can be considered as a sub-sampling process. Thus a subsequent disperser, such as a grating, may follow to generate spectra of the pupil images. Modern IFS-L design is described in [36], and it has been employed in spectral imaging tasks other than astronomy [14].

Introduced as SHIFT in [68], this instrument is actually a multiple-image Fourier-transform spectrometer. To make it free of moving parts, thus insensitive to vibration, it replaces Michelson interferometers used by traditional Fourier transform spectrometers with a pair of Nomarski prisms covered by two linear polarisers [94]. Its birefringent nature results in a common-path interferometer sandwiched in between a lenselet array and a detector array [95]. Each lenselet pro-

jects a scene through the optical assembly and forms a sub-image on the detector array. A small angle formed between the detector array and the assembly makes the optical path difference vary from one sub-image to another. An extraction and concatenation of the sub-images would then give rise to a 3-D interferogram, to which Fourier transform can be applied so as to reconstruct the spectral image.

Computational sensing

With the advances in modern computers, snapshot spectral imaging methods relying on computationally intensive processing appeared. In [68] two of them are described: computed tomography based CTIS and compressive sensing based CASSI.

Unlike the tomographic approach described in [131] that depends on a rotatory prism, non-scanning tomographic techniques have been proposed through which all the slices of a 3-D image cube are imaged at the same time. The architecture of such an imaging apparatus is featured by a rectangle-shaped field stop and a 2-D disperser, but otherwise quite similar to that of a slit spectrometer. An objective lens images the scene onto the field stop and then collimated and projected through the 2-D disperser onto a detector array. The dispersed images of the field stop can be interpreted as multi-order 2-D projections of the 3-D data cube. Therefore reconstruction of the cube can be achieved with tomographic techniques. Examples of CTIS-type concepts or instruments differ in the implementation of the disperser and the reconstruction method [139, 21, 38]. Limiting factors of CTIS include computational complexity, calibration difficulty, and measurement artefacts [68].

Another computational approach to snapshot spectral imaging is compressive sensing. By definition, compressive sensing "compresses" a signal by sampling it with less samples then required by the Shannon-Nyquist theorem, and recovers it by finding solutions to such underdetermined linear systems making use of the sparsity of the signal [22, 39]. Similar to a coded aperture spectrometer that scans the image of the binary-coded aperture, a CASSI also employs a coded aperture. However, the binary code in the former case is an orthogonal matrix, whereas it is a random binary matrix in the latter case. The binary coded image of the scene is then collimated, dispersed and re-imaged onto a detector array. Clearly the sensed image is modulated by the mask and formed by overlapped measurements of the scene, which is equivalent to coded projections in the spectral domain, and hence can be treated with the compressive sensing frameworks [55]. Nevertheless it is essential to ensure compressibility of the scene, proper implementation of the mask, apart from the already computationally intensive reconstruction algorithm, all of

which limit the usefulness of CASSI [68].

Dispersive interferometer

From the very beginning of spectroscopy, interferometer has been one of the key components extensively used in spectral imaging devices. There are a variety of interferometers proposed, and some of them has been adapted to snapshot spectral imaging. Two examples are TEI and MSI in [68].

The idea of combing a Fabry-Pérot interferometer (étalon) and a disperser for the purpose of spectral imaging is realised by Le Coarer *et al.* [101]. Fabry-Pérot étalon acts as a narrow-band transmissive filter that positions the bands in accordance with corresponding orders resulting from resonances of the étalon. Peak transmittances of the pass-bands vary with the separation between the two reflective surfaces of the étalon. In order to further separate the ordered images spatially, a dispersive element, such as an échelle grating, may be placed. Baldry and Bland-Hawthorn describe a device, called Tunable Echelle Imager, consisting of a Fabry-Pérot étalon coupled with a cross-dispersed échelle grating [10]. Eventually what is incident on the detector array is a mosaic of band images, each of which represents a thin spectral slice of the data cube. Therefore this setup only provides images at discontinuous bands, the full spectrum may be estimated under the assumption that the original spectrum is sufficiently smooth. An disadvantage of the TEI is its relatively low transmission due to the optical inefficiency of the étalon and dispersers.

Kudenov *et al.* [96, 97] design an extension of dispersion compensated polarization Sagnac interferometer (PSI), by including two multi-order diffraction gratings in a standard PSI. In a Sagnac interferometer, an incoming beam is split into two counter propagating beams, both of which are dispersed and collimated by the gratings. When the two beams exit the interferometer and converge through a re-imaging objective, an interference pattern is generated which is a superposition of unique spectral pass-bands amplitude modulated onto coincident carrier frequencies. The spatial frequency is proportional to the diffraction order and thus related to the spectral characteristics of a given order. Later modulated multispectral images can be extracted in the Fourier domain. Similar to the TEI, MSI is also multispectral, capable of forming inherently registered spectral slices of the data cube simultaneously. The main disadvantage of this approach lies in the optical design that utilises only one dimension in the Fourier space and ties the spectral bands to the grating's orders.

Advanced detector array

The development of tunable or multi-layered sensors is desirable as it will eliminate the necessity of using external dispersive or wavelength selective elements, thus reducing the size and simplifying the complexity of a spectral imaging system.

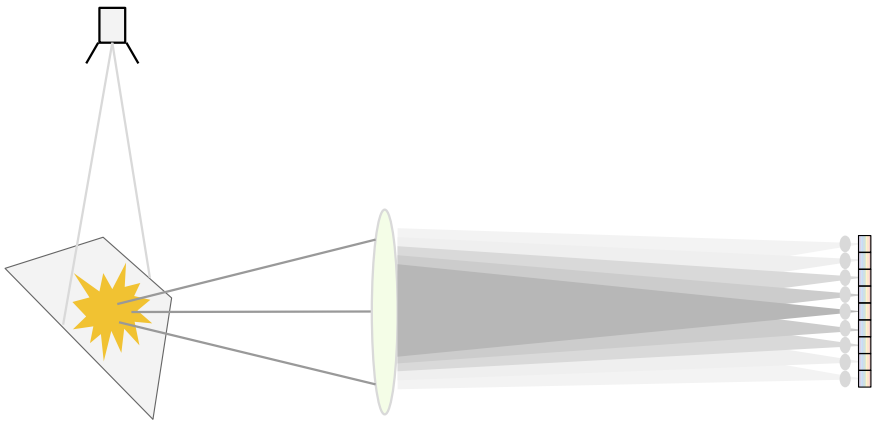

Figure 2.7: Illustration of multi-layered detector array. The multi-layered structure of the sensor acts as a stack of sensors, each sensing a spectral band. This renders optical dispersers unnecessary, nevertheless requires specific semiconductor design.

The transverse field detector (TFD) [98] is such a photosensitive device that exhibits different spectral responsivities at different depths by applying suitably biased voltage, as illustrated in Figure 2.7. An analysis of 6-band TFD for spectral imaging is carried out in [105], and one of the advantages of a TFD is the ability to tune the spectral responses on a pixel to pixel basis. Similarly quantum-well infrared photodetector (QWIP) is demonstrated for the purpose of multispectral infrared imaging application [93].

Although convenient, spectral characteristics of such detectors are bound to structure of semiconductor, and therefore not flexible to change. Moreover an increase in number of bands is also limited.

Image plane filtering - spectral filter array

The commercial success and wide application of colour imaging owe much to the advent of CFA by Bryce E. Bayer in 1976 [13]. Till now, it remains the most

widely used measure for colour imaging. The concept of CFA makes possible simultaneous colour separation and thus enabling electronic acquisition of trichromatic images at one exposure by a single sensor, which produces colour images in perfect registration, enables high-speed capture of fast moving objects or fast phenomena, and makes portable, solid and cost-effective colour imaging devices a reality. The advantages of CFA mentioned above are achieved at the cost of reduced spatial resolution, which is then overcome by demosaicking, a process where missing colour components are estimated, as introduced in Section 3.5.1. In recent years, the benefit of CFA has arouse academic and industrial interest in extending CFA for the purpose of spectral imaging by integrating more types of filter elements into the array, which results in SFA. That is, SFA sacrifices spatial resolution for spectral resolution. In essence, a SFA is an array of filter elements that spatio-spectrally sub-samples images formed on the focal plane, as demonstrated in Section 3.3 and 3.4. Designing a SFA, therefore, concerns spectral characteristics of filter elements, spatial arrangement of filter elements, and the associated demosaicking technique.

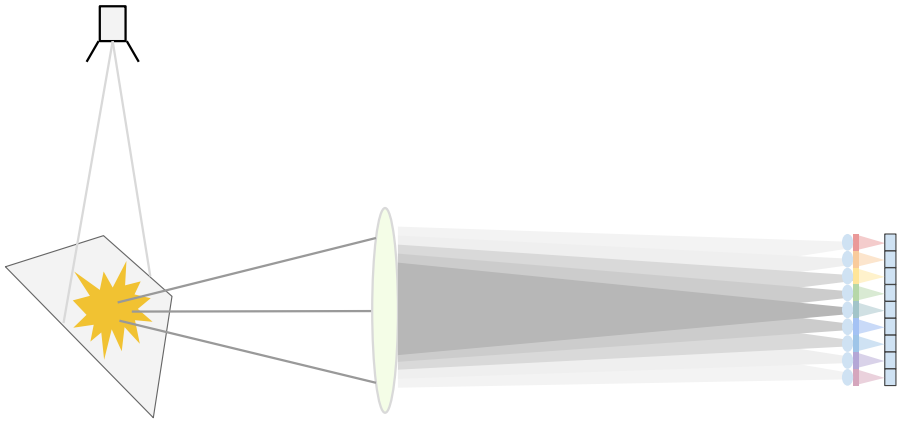

Figure 2.8: Illustration of the principle of spectral filter array. Sandwiched between the microlens array and the sensor, the spectral filter array filters the optical image on a pixel-by-pixel basis. Namely spatial resolution is sacrificed for spectral resolution in such a spectral imaging system.

Hybrid solutions

The aforementioned approaches to snapshot spectral imaging have their pros and cons, and a hybrid system may well overcome some drawbacks while still maintaining the advantages.

Murakami *et al.* [133] suggest a hybrid-resolution spectral imaging device by merging a four-channel beamsplitter with filtered and mosaicked sensors. Conceptually this is equivalent to three R/G/B images of high resolution coupled with a SFA mosaic image of low resolution. The image is then reconstructed on the basis of small regions by linearly combining the regions in the R/G/B band images with the weighting coefficients determined from SFA data.

Tamburrino *et al.* [162] integrate colour filter array and stacked photodiode structure of CMOS image sensor. The red and blue filter elements in the original Bayer pattern are replaced with green-absorptive magenta filters under which lies the two stacked and pinned diodes that mostly absorb blue and red light. Similarly Martínez *et al.* [115] combine colour filter array with TFD to narrow down the bandwidth of TFDs and improve the accuracy of spectral and colour reproduction. A similar idea is presented in [158] where a vertically staked multi-layer sensor, known as Foveon sensor [122], is covered by a 2-band filter array consisting of two types of triple bandpass filters, which forms a 6-band spectral imager.

As in a plenoptic camera, a lenselet array permits simultaneous observations of a point on the object by multiple photodetectors. Similarly, a filter array inserted in front of the lenselet array or image sensor enables observations of the spectra of the object when light passing through each lenselet is projected merely to the corresponding area on the sensor and the observation distance is set properly [154] (See Figure 2.9). Pixels in the captured image are geometrically rearranged onto a multi-channel virtual image plane in order to reconstruct the multispectral image. The resolution of the resultant images is slightly reduced in comparison with the captured sensor image. Although simple in concept, this approach requires fairly uniform irradiance in terms of angular distribution so that each filter and the corresponding lenselet capture similar power of the incident light. Another similar idea, light field microscopy, is put forward by Levoy *et al.* [103], which integrates adapts a light field camera with a pupil plane filter array. The latter is superior to the former in that it allows the use of a normal objective lens, however the latter is less compact than the former. Both of them are classified as MAFC in [68].

We have presented a variety of snapshot spectral imaging techniques that require

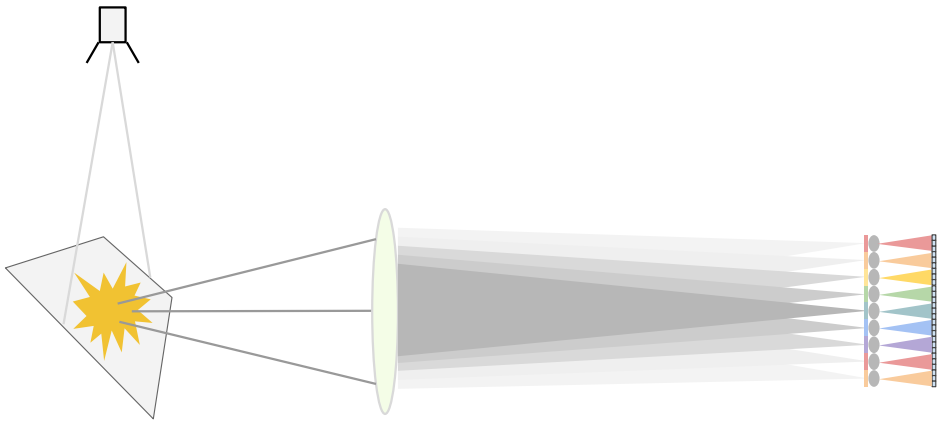

Figure 2.9: Illustration of filtered lenselet array [154]. This approach combines the principle of plenoptic camera, namely light-field camera, and spectral filter array. Its plenoptic nature ensures a fairly uniform distribution of power across the lenselets, whereas resolution of the resultant image is sacrificed.

a certain degree of multiplexation due to the dimensionality of image sensors. As a result, critical issues for imaging spectrometry include imaging foreoptics design, choice of spectral dispersing technique and spectrometer optical design, focal plane array detector technology as well as the complexity of subsequent data processing.

2.5 Motivation for SFA based spectral imaging

Seeing that most of the snapshot spectral imaging techniques introduced in this chapter require multiple specific optical elements or intensive data processing, we consider the SFA as a promising candidate for snapshot spectral imaging in terms of system simplicity, portability, cost effectiveness, robustness, ease of use and requirement for data processing. It also allows a flexible design that is adjustable between spatial and spectral resolution. These advantages are gained at the cost of relatively low light throughput, reduced spatial resolution and relatively high manufacture cost in case of small volume production.

The architecture of a SFA based imaging system bears a close similarity to that of a CFA system. And there may not exist superficial differences between SFA and

CFA systems. And a SFA based system is capable of reproducing trichromatic images. Some state-of-the-art SFA based systems and components will be examined in detail in Chapter 3.

Chapter 3

SFA based spectral imaging

3.1 Introduction

In comparison with other snapshot spectral imaging approaches, SFA permits a simple and compact system at a reasonable price in case of high-volume production. Although mass production of SFAs remains to be seen, the concept of SFA based imaging has aroused particular interest of the academia in extending the success of CFA to spectral domain. In recent years, sustained research effort has gone into the development of SFA-based spectral imaging. The core components of a SFA based spectral imaging system are filter array and associated demosaicking algorithms. Some focus on theoretical design of SFA, and others attempt at fabrication of SFA. Demosaicking techniques are also developed independently or as part of the systematic approach to functional SFA-based imaging systems. In this chapter, we first introduce the concept of moxel, and review theoretical SFA design and practical SFA development, before switching to SFA demosaicking. Lastly, the chapter concludes with a brief analysis.

3.2 From pixel to moxel

A SFA is usually composed of recurring patterns of filter elements. The smallest patterns are referred to as moxel (multispectral pixel) thereafter. A key distinction between CFA and SFA lies in the number of bands in a filter array, which largely determines the size of moxel.

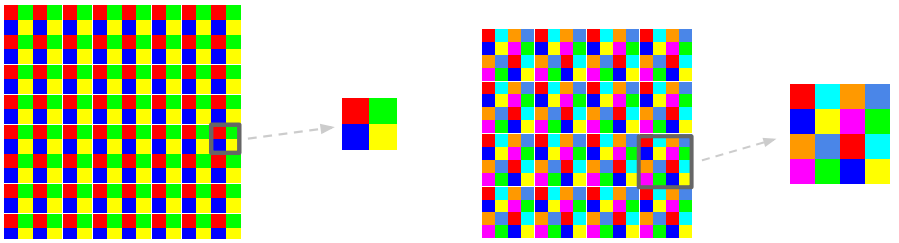

(a) Illustration of a moxel of 2×2 pixels. **(b)** Illustration of a moxel of 4×4 pixels.

Figure 3.1: Definition of moxel, the smallest recurring patterns that constitute a SFA. The SFA in (a) comprises 64 moxels of 2×2 pixels, whereas the one in (b) comprises 16 moxels of 4×4 pixels.

3.3 Theoretical SFA design

Unlike CFA mosaic design that mostly incorporates three types of primary colour filters, number of band in a SFA may vary a lot and the choice of filters can be rather specific to the application. In recent years, there have been quite a few proposals for SFA mosaic patterns as well as methodology of design.

To the best of our knowledge, Ramanath *et al.* first present a 4-band hexagonally arranged CFA for multispectral image acquisition [148] (see Figure 3.2j). Also proposed is another 7-band SFA where each pixel of a certain spectral band is surrounded by six pixels of distinct bands, depicted in Figure 3.2a. As a result, the demosaicking for each pixel may be performed with the nearest neighbourhood interpolation. This idea is further detailed in [149] along with the techniques in designing spectral sensitivities for the sake of recognition and reconstruction of certain objects.

To the best of our knowledge, the first systematic work in this regard is conducted by Miao *et al.*. Miao *et al.* put forward a generic method of SFA design where spectral bands' probability of appearance in the array can be represented in a binary tree [127, 123]. It starts from a checkerboard patten and further splits the pattern into children by the power of $1/2$ following the binary-tree. An accompanying generic demosaicking algorithm is also developed [124, 126]. These two proposals complement each other and are the very first systematic attempts on SFA based spectral imaging [125]. Also presented in [123] is a framework of evaluation of SFA design, and another similar quality metric is explained in [153].

In contrast to a complex pattern designed with e.g., the binary-tree approach,

Brauers and Aach [17] propose a 6-band SFA arranged in 3×2 moxels in a straightforward manner which is aimed at faster linear interpolation, shown in Figure 3.2b. Another simple SFA is from Aggarwal and Majumdar who arrange 4 filters in diagonal stripes [4], demonstrated in Figure 3.2c.

The spectral sensitivity of modern solid-state photodetectors range from ultraviolet through the visible region all the way to LWIR (long wavelength infrared). Thus Hershey and Zhang [72] design a camera integrating both visible light and non-visible light photodetectors in a single SFA. In fact, the mosaic is mostly the same as the Bayer pattern except one green in a 2×2 moxel is replaced with a non-visible filter element (see Figure 3.2k).

When consisting of sufficient types of narrowband filter elements, a SFA mounted sensor can be used as a spectrometer. Wang *et al.* design a 8×16 SFA that comprises 128 distinct narrow bandpass filters for capturing NIR (near-infrared) spectra [172], shown in Figure 3.2d.

In remote sensing applications, the band of LWIR plays an important role in material identification. In contrast to the conventional line-scan MSI sensor, Mercier *et al.* examine the usefulness of SFA snapshot LWIR imager [121]. Both the optimal number and width of the spectral channels are analysed with simulated typical background signals.

For the purpose of jointly capturing RGB and NIR images, Lu *et al.* formulate the design of SFA as an optimisation problem in spatial domain [109] and provide an iterative procedure to search for locally optimal solutions, considering that the spectral sensitivity of modern solid-state image sensors extends from visible range to IR region. The resulting mosaic pattern consists of 16 bandpass filters arranged in 4×4 moxels, 15 of which are visible and 1 IR, demonstrated in Figure 3.2e. An improved algorithm is later developed that takes into account the correlation between visible and NIR bands where the optimisation problem is addressed by means of regularisation [151], which results in SFA pattern drawn in Figure 3.2f.

Following the concept of a generalised assorted pixel (GAP) camera where post-capture adjustment is possible to find the best comprise among spatial resolution, spectral resolution and dynamic range, Yasuma *et al.* design a 7-band SFA composed of 3 primary-colour filters and 4 secondary-colour filters [184] (see Figure 3.2l).

Monno *et al.* propose a 5-band SFA [129] (see Figure 3.2m). In the moxel, the green-like channel is distributed in the form of quincunx, as in the Bayer CFA.

Other channels follow the binary-tree approach [127] so that the adaptive kernel can be estimated directly from the raw data for the purpose of subsequent demosaicking.

The spatial arrangement of the filter elements plays a more important role in SFA than in CFA, as reported by Shrestha and Hardeberg [155]. It has been found the influence of mosaic layout tends to be more prominent as the number of bands increases. Further, the authors design a particular SFA pattern comprising of two sets of trichromatic filters (see Figure 3.2n).

To integrate one more band, i.e., IR or UV, into a common CFA and maintain its compatibility with the CFA to the maximum, Kiku *et al.* propose a modified Bayer pattern where the additional band is sparsely sampled and the filter elements are arrayed on a slightly slanted square grid [89], presented in Figure 3.2g.

To verify the usefulness of compressive sensing in SFA demosaicking, Aggarwal and Majumdar present two 5-band SFAs [5]. One of them is a random pattern where each channel has equal probability of appearance (see Figure 3.2h), which is supposedly conducive for CS recovery since the measurements are incoherent. Another one is a uniform filter array similar to the one proposed in [4] (see Figure 3.2i). In theory, such uniform sampling patterns are not conducive to CS recovery, so it is experimented with for comparative purposes only. Both of the two SFAs are easily extendible to any number of channels.

3.4 Practical SFA realisation

SFA has not been as widely accepted by the industrial community as CFA. Among other difficulties, the production and fabrication of SFA present a major technical challenge. Sustained effort, therefore, went into realising the SFA.

In [20], a production process is presented where dichroic filter array can be produced on a wafer and later bonded to an image sensor for the purpose of spectroscopic imaging. Dichroic filters, also known as interference filters, enable custom filters with spectrally sharp transitions, thus better selectivity of colour. A compact imager with a lithographically patterned dichroic filter array is presented [44, 43, 42, 40] where at most 10 wavelength bands can be incorporated.

A 4-band SFA imager dedicated to medical application is described by Sprigle *et al.* [160]. The optical filter is fabricated with traditional multi-film vacuum deposition and modern micro-lithography technologies [186]. Further a means of evaluating the spectral interference between adjacent channels is also developed [188].

Further information and application is detailed later in a series of articles concerning the detection of erythema and bruising which are important to the prevention and diagnosis of pressure ulcers [91, 92, 185, 146, 187].

To fabricate the 128-band SFA [172], Wang *et al.* develop a technique named combinatorial deposition [171] that combines the techniques of deposition and etching in order to produce the spacer arrays with different thickness required by the corresponding Fabry-Pérot type filter element. Such a device makes possible *in situ* spectral measurement of NIR spectra ranging from 722 nm to 880 nm. Walls *et al.* design, fabricate and characterise a 23-band SFA of narrowband Fabry-Pérot filters with FWHM (full-width half-maximums) of 22-46nm covering the visible range (400-750nm) [169]. The fabrication is suitable for direct integration onto CMOS image sensors in industrial foundries, and the cost and complexity is reduced in comparison with other solutions that vary the physical cavity length only. Another Fabry-Pérot interferometer based snapshot multispectral imager is developed by Gupta *et al.* [67]. The imager employs a 16-band SFA arranged in 4×4 moxels that operate in the SWIR (short wavelength infrared) range from 1487 to 1769 nm with a spectral bandpass of about 10 nm. The SFA is installed in a commercial handheld InGaAs camera coupled with a customised micro-lens array with telecentric imaging performance in each of the 16 channels.

Geelen *et al.* introduce a SFA imager integrating tiled filters and optical duplication [53]. It is demonstrated that a prototype camera can acquire 32-band multispectral images of 256×256 pixels in the spectral range of 600-1000nm at a speed of about 30 cubes per second in daylight conditions and up to 340 cubes per second in typical machine vision applications of higher illumination levels. Later, Geelen *et al.* propose another SFA imager by depositing interference filters per pixel directly on a CMOS image sensor [54]. The monolithic deposition leads to a high degree of design flexibility, so that an application specific compromise between spatial and spectral resolution can be achieved.

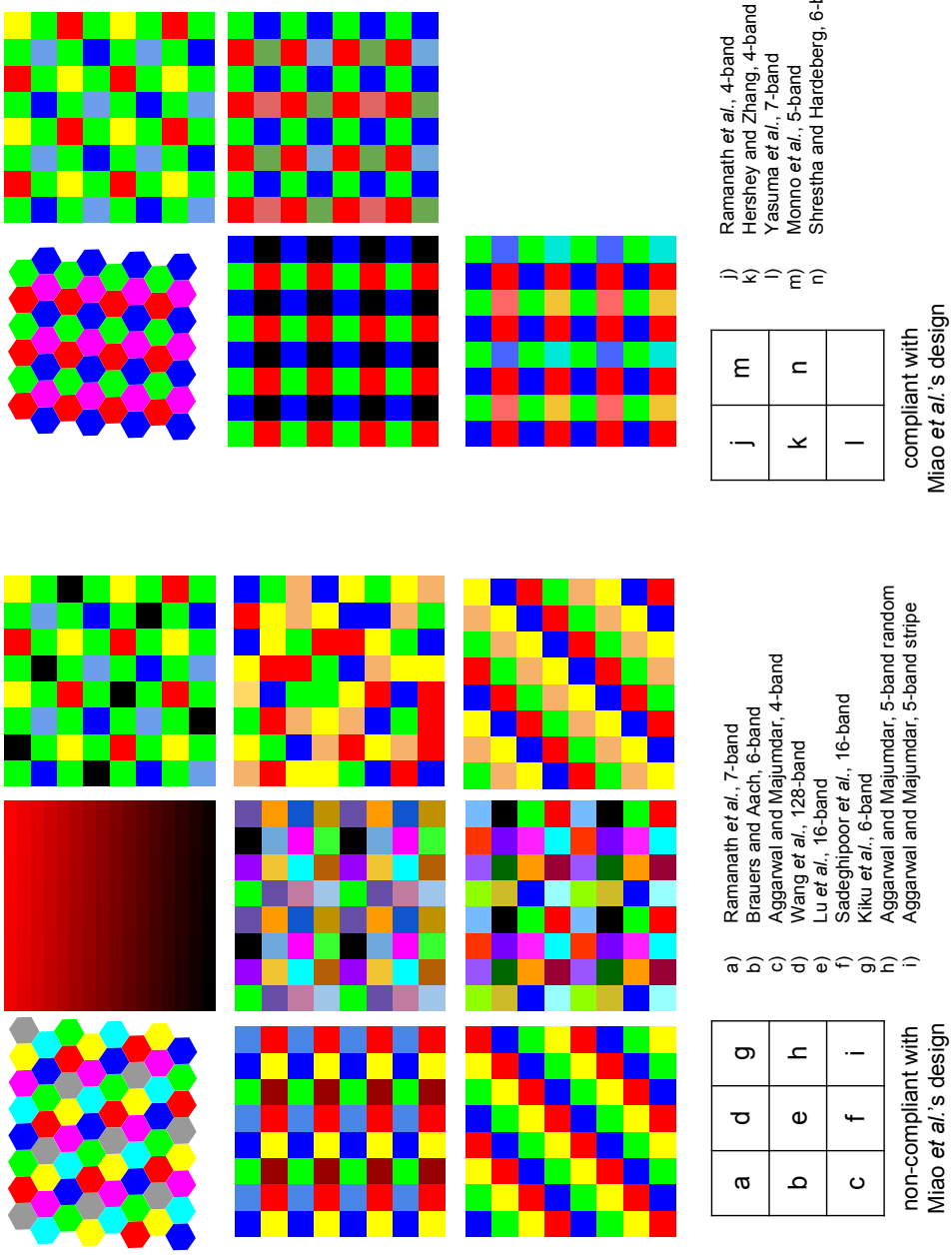

Figure 3.2: Illustration of spectral filter array design.

3.5 Development of SFA demosaicking

As CFA may be considered as an instance of SFA, SFA demosaicking is naturally an extension of CFA demosaicking. In this chapter, therefore, a brief description, and a means of classification, of CFA demosaicking methods are first presented in Section 3.5.1.

3.5.1 CFA demosaicking

Study of demosaicking arises from the advent of CFA in 1970s. Decades of research and development on CFA based colour imaging has resulted in a large number of evolving demosaicking algorithms. Many of them are present in research papers, and others have been filed as patents. Quite a few, embedded in commercial cameras, may never get published. Although it is rather difficult to obtain a complete list of demosaicking methods, they can be well classified into a few groups according to the techniques they are developed from, the assumptions on which they function, or the intrinsic properties of the images they take as input. The methods are classified differently in the literature [147, 65, 104, 108, 120]. Here we adopt the classification by Menon and Calvagno [120], and select a few representative techniques as candidates for SFA demosaicking, as shown in Figure 3.3.

The assumptions on which a variety of CFA demosaicking methods are based are very often not applicable to SFA demosaicking [126]. As an example, the luminance-chrominance colour space utilised by a number of CFA demosaicking techniques becomes ambiguous for SFA demosaicking, as a result of the difficulties in extracting luminance and chrominance information separately in spectral images.

The primary consideration in selecting the candidates is therefore the scalability of a CFA demosaicking algorithm. The naïve techniques, including bilinear interpolation and smooth hue transition interpolation, function on the basis of bands. In vector median filtering, each pixel in an image is treated as a vector regardless of its dimensionality. Wavelet based methods and reconstruction approaches are not limited to colour images as well. Obviously all of the candidates are scalable in terms of number of bands, which makes feasible the extension to spectral.

3.5.2 SFA demosaicking

Indicated by its name, bilinear interpolation is an extension of linear interpolation for interpolating functions of two variables (e.g., x and y) on a regular 2D grid. In

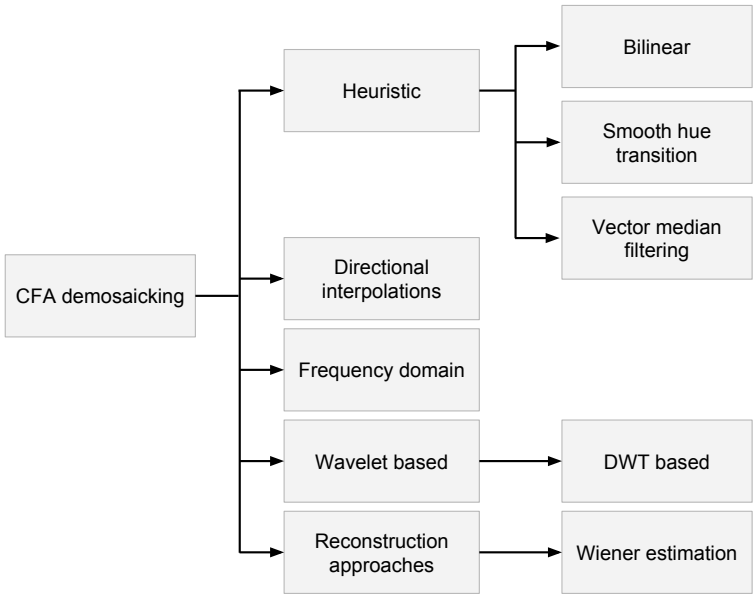

Figure 3.3: Classification of CFA demosaicking methods [120].

fact, bilinear interpolation estimates the unknown values by means of a distance weighted average of its neighbouring pixels. The presumption is that the image content in a vicinity of the pixel in question should vary smoothly thus sharing similar spatial features. It is applied to each spectral band individually. As a result, it is straightforward to apply this to SFA demosaicking. It should be sensitive to variation of spatial correlation, however insensitive to alteration of spectral correlation, thus producing unwanted colour fringes in areas of fine detail.

A series of methods take advantage of heuristics, to wit reasonable assumptions about colour images, and prove to provide higher performance. One common assumption in colour image processing is that hue, defined as the ratios or difference between the colour components, varies more subtly than colour components. In consequence, interpolation of hue, rather than colour planes themselves, is conducted. Although the assumption of smooth hue transition only holds within the boundary of the objects in the image, it has been extensively used for demosaicking [30]. Normally the most populated green channel is interpolated before other hue channels are evaluated. Unfortunately for spectral images, there might not be a "green"-like band and sufficient spectral overlap between bands , and the definition

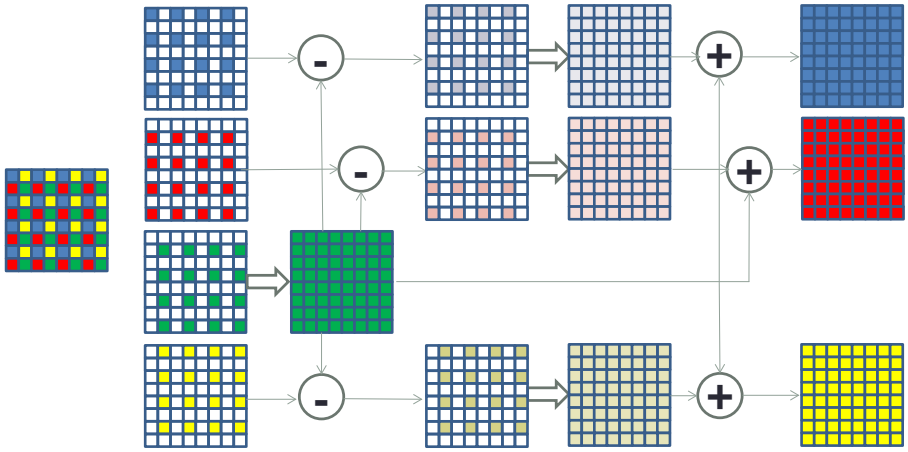

Figure 3.4: An illustration of smooth hue transition interpolation. In this approach, a channel is first interpolated separately prior to the interpolation of several hue channels, formed as the ratios or difference between each remaining band and the interpolated band. The subtracted part is then added back to complete the demosaicking.

of hue may also be equivocal. Be that as it may, it could still make sense to extend this technique to SFA interpolation considering that the objects taken might bear similarities between spectral regions which is in line with the assumption. Figure 3.4 demonstrates the algorithm.

Along with the SFA generation method, an accompanying generic demosaicking algorithm is also developed by Miao *et al.* [124, 126] which interpolates each band independently by tracing the same binary tree back. The interpolation is edge directed and performed level by level following the binary tree.

To interpolate the mosaic image associated with the SFA presented in [17], Brauers and Aach advance a demosaicking algorithm where channel difference is first smoothed before linearly interpolated.

Following the binary-tree approach [124, 126], Baone and Qi pose demosaicking as an image restoration problem and address it with the non-linear maximum a posteriori probability technique using the gradient descent optimization process, for images mosaicked by a 7-band SFA.

Lu *et al.* come up with the linear minimum mean square error (LMMSE) approach to the joint demosaicking of RGB and NIR images [109], formulating demosaicking as an image restoration problem. In this case, the objective of of SFA design is

meant to provide the minimum reconstruction error in terms of LMMSE.

To reconstruct multispectral images from GAP mosaicked sensor output, Yasuma *et al.* come up with a multimodal image reconstruction framework where primary and secondary colour images are reconstructed separately [184]. The former is demosaicked by means of low-pass filtering in the Fourier domain, since the sampling rate is relatively high. Therefore the demosaicking of the secondary colour bands, that are less sampled, exploit the inter-channel correlation between the most similar primary and secondary filter pair, in the principle of constant channel difference and residual interpolation.

Having designed the 5-band SFA keeping interpolation in mind, Monno *et al.* introduce adaptive kernel upsampling to SFA demosaicking [129]. The proposed adaptive Gaussian upsampling (A-GU) and joint bilateral upsampling (A-JBU) are extended from the corresponding non-adaptive methods respectively. The adaptive kernel is estimated directly from the mosaic image, which is first used by the A-GU to generate a guide image from the green-like band for the A-JBU. After that, A-JBU, with the same adaptive kernel, is applied to each of four other spectral bands. Later, Monno *et al.* replace the A-JBU with the guided filter [130], known as an edge-preserving filter that also requires and depend much on guide image. Recently Kiku *et al.* adapt this means to the demosaicking of the hybrid SFA pattern [89]. The sparsely sampled additional band is separately interpolated with a super-resolution technique with the sparse mixing estimators, whereas the R/G/B channel are interpolated following basically the framework described in [130] with a few improvements, including a newly proposed gradient based interpolation of the green channel as well as an iterative procedure that samples the reconstructed image as the input to the following iteration.

Aggarwal *et al.* put forward a series of SFA demosaicking methods. The first represents a pixel in question, also a central pixel in a given neighbourhood, as a linear combination of neighboring intensity values from same and other bands [7, 4]. In other words, the linear filtering is performed on the raw mosaic image with a given kernels whose parameters may be determined by means of training [6]. Recently, the authors attack SFA demosaicking with compressive sensing [5], where both group-sparse reconstruction and the Kronecker compressed sensing are explored. The results demonstrate that the latter method outperforms the former, and the random pattern always yields better results in both approaches, except that the uniform pattern does a better job in the Kronecker method for 3-band demosaicking.

Dealing with a SWIR sensor coupled with a 9-band SFA filled by 3×3 moxels,

Kanaev *et al.* are confronted with two difficulties in demosaicking: first, the inter-channel correlation in this case is not usable; second, the distribution of each band is equal to another, so there is no comparatively oversampled channel. To overcome these two drawbacks, the authors introduce two approaches to demosaicking. One makes use of the multi-band edge information, while the other applies multi-frame super-resolution to the enhancement of multi-spectral spatially multiplexed images [85].

As can be seen, there are already a number of attempts at SFA demosaicking, however little is known that focuses on adapting CFA demosaicking techniques based on vector median filtering, discrete wavelet transform and linear regularisation. These methods are intrinsically adaptive to SFA. As a result, we study three algorithms in detail in Part III.

Part II

Simulation framework

Chapter 4

Simulation framework

In general, filter arrays are made of layers of absorptive or interference filters, commonly sandwiched between microlenses and photosites of a solid-state image sensor. This implies that neither the spatial arrangement nor the spectral characteristics of the filter array may alter with ease as soon as the sensor is fabricated. And the cost of a single filter array will only be lowered to a reasonable range if produced in large quantities. The economic and physical constraints, therefore, motivated us to build the imaging pipeline numerically in order to vary the system design and study the role of each component in a SFA imaging system.

A typical imaging system consists of an image taking block and an image processing unit [107]. The former normally includes imaging optics and detectors, which could be modelled and simulated. The latter is very often a series of routines running on specialised or general-purpose processors, which can be simply simulated with standard software implementations. To that end, a simulation framework of high efficiency and sufficient flexibility is required, and a modular design is in line with the concept and meets our requirements for flexibility. In addition, such a framework would not be complete without appropriate inputs and means of evaluation. Figure 4.1 illustrates the SFA-based imaging pipeline, and Figure 4.4 presents the simulation workflow and the possible means of evaluation.

Radiometry is patently the key to a profound understanding of an optical imaging system. Thus each component of the framework is introduced in this chapter, coupled with radiometric analyses if necessary. Limitations of the framework are also discussed.

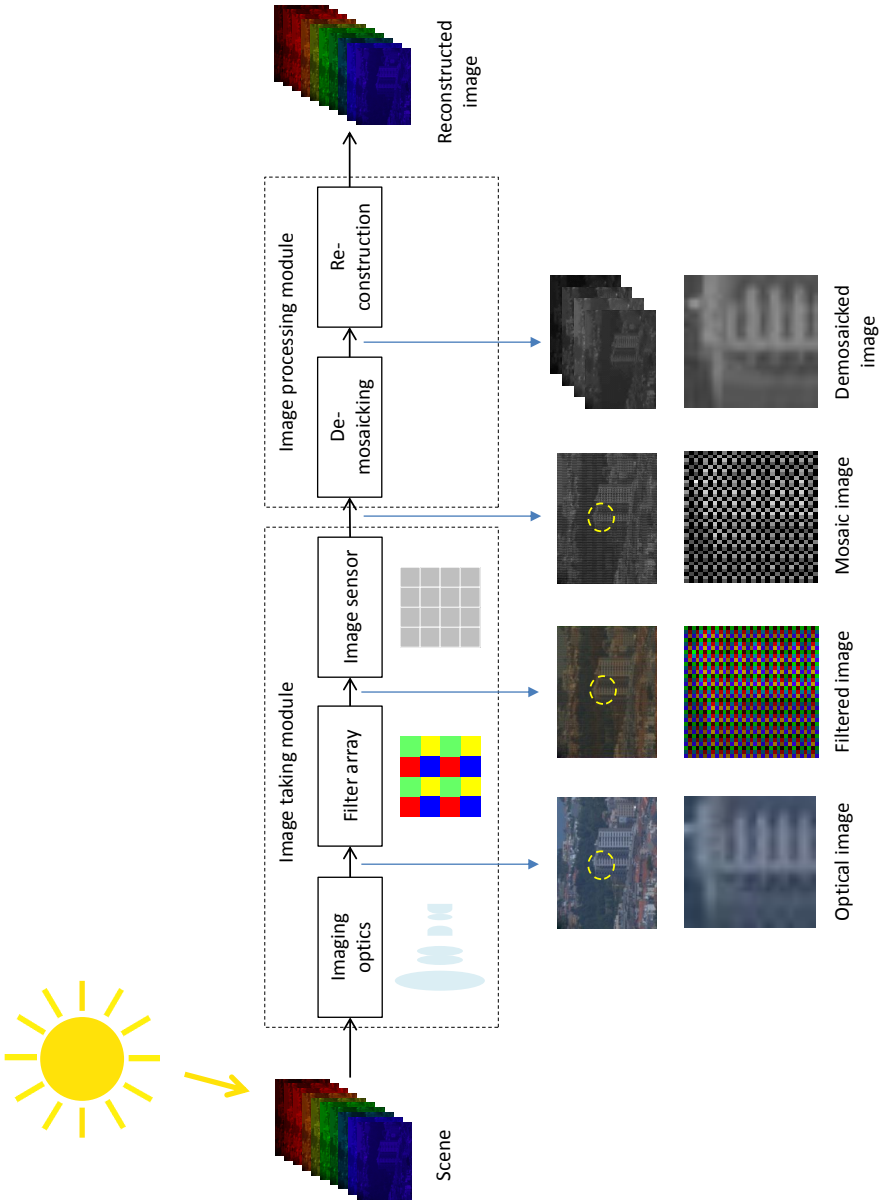

Figure 4.1: An illustration of the SFA-based imaging pipeline. As a signal source, scenes (Section 4.1) are projected through the imaging optics to form optical images (Section 4.2.1). Next, the optical images pass through the filter array (Section 4.2.2). The resultant mosaic images are integrated by the simulated sensor, which generates stacked sensor images (Section 4.2.3). Finally the sensor images are demosaicked (Section 4.3.1) and utilised to reconstruct spectral or colour images (Section 4.3.2).

4.1 Scene

The inputs to an optical imaging system are physical stimuli, i.e., the distribution of radiance over a scene in the radiometric sense. The relation between the illumination, the scene and the imaging system can be understood with a radiometric interpretation. In a typical and simplified scenario, a scene interacts with the incident radiation when illuminated by an illumination, as shown in Figure 4.1. A scene often reflects or transmits light in an omnidirectional manner. For an imaging system observing the scene at certain angle of view, therefore, radiance is an appropriate radiometric quantity that indicates the power of light received at the solid angle subtended by the entrance pupil of the optics. The influence of fluorescence, i.e., objects absorb incident radiation at certain wavelengths and emit light at some other wavelengths, is ignored.

For a simulated imaging system, the scene shall be numerical and representative of common objects. In comparison with the optics and the sensor, it is not straightforward to model a scene numerically. Common numerical scenes include synthetic scenes, e.g., the Macbeth ColorChecker and spatial frequency sweep patterns, and computer rendered imageries based on physical models, e.g., the Digital Imaging and Remote Sensing Image Generation (DIRSI) model developed by the Rochester Institute of Technology [75]. Another source of numerical scenes may be from the usage of appropriate spectral images of sufficient spatial and spectral resolution [47, p. 190]. In practice, the latter is easier to obtain and closer to reality.

In the simulations reported in this dissertation, both synthetic and spectral images, in the form of spectral reflectance, are employed. A synthetic image is designed manually and generated with a programme, and the spectral images are primarily obtained from the databases that cover both outdoor and indoor scenes [48, 183]. Foster's set consists of a mixture of rural scenes containing rocks, trees, leaves, grass, and earth and urban scenes [48], as shown in Figure 4.2. The spectral span ranges over 400-720 nm in 10 nm steps yielding 33 bands, while scene 5 has only 32 bands due to the noisy 720 nm band. Divided into 5 sections, CAVE images are of a wide variety of real-world materials and objects, covering various colourful stuffs, skin, hair, paints, food, drinks and fake objects mimicking the colour of real objects mentioned [183], as seen in Figure 4.3. The spectral span ranges over 400-700 nm in 10 nm steps yielding 31 bands. Table 4.1 shows the conditions in which the images were captured.

Figure 4.2: An overview of Foster's image database [48] consisting of a mixture of rural scenes containing rocks, trees, leaves, grass, and earth and urban scenes.

4.2 Image taking module

In practice, the image taking module consists primarily of imaging optics, image sensor coupled with filter array and readout circuits as well as additional optical components, e.g., neutral density filters, colour conversion filters, optical low-pass filters and infrared cut-off filters. Considering that the scenes have incorporated influence of certain optical elements in the course of acquisition, only the key modules of immediate relevance to our research are taken into consideration in order to avoid unnecessary complexity and unrealistic simulation. Therefore elements considered include the optics, the filter array and the sensor, as shown in Figure 4.1.

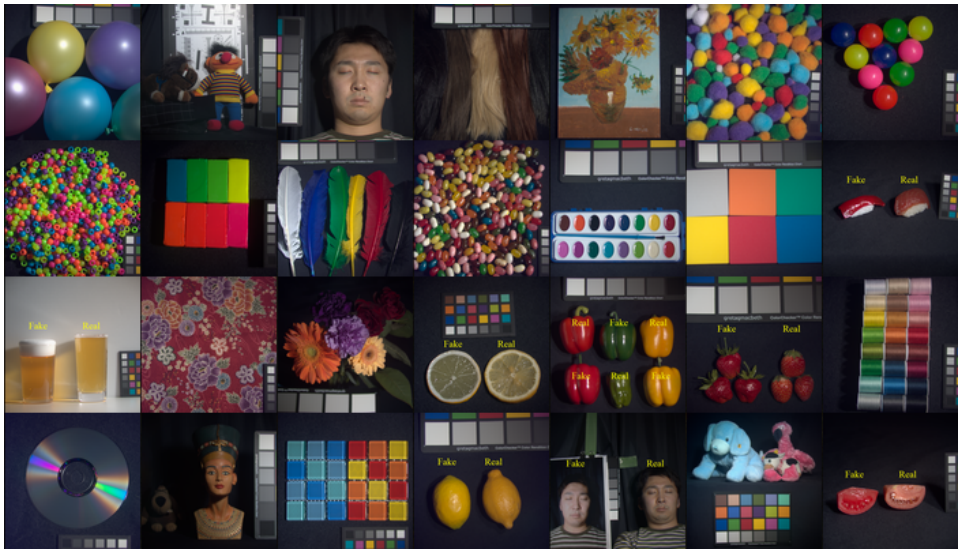

Figure 4.3: An overview of CAVE image database [183] made up of a wide variety of real-world materials and objects, covering various colourful stuffs, skin, hair, paints, food, drinks and fake stuffs mimicking the colour of real objects.

4.2.1 Imaging optics

As optics is in itself a standalone and well researched topic that is beyond the primary objective of this dissertation, it is considered mostly in this dissertation idealised thin lens which means aberration-free and transparent [118, p. 245]. The focal length and focal point of the lens is determined so that the scene is projected on the sensor and the size of the image is consistent with that of the image sensor located in the image plane.

In the case when optics matters, the imaging lens may be considered as diffraction-limited optics, that is, a linear shift-invariant system [46]. Therefore it may be represented by PSF (point spread function) that represents the spatial response of a shift-invariant system to an impulse, and the Fourier transform of PSF gives rise to OTF (optical transfer function) that reflects the system's frequency response. When necessary, shift-variant aberrations may be mimicked by applying shift-variant PSF or model-specific transformations to the images.

Diaphragm is an integral part of a lens whose shape and size influences the PSF/OTF. Circular apertures are quite common and assumed in the experiments. Not only does the size of an aperture have an impact on the PSF/OTF, but it also determines

Table 4.1: Information about Foster's [48] and the CAVE [183] databases where the scenes are extracted.

	CAVE	Foster's
Camera	CCD camera	CCD camera
Resolution	512×512	max. 820×820
Instrument	LCTF	LCTF
Illuminant	D65	Sunlight
Range	400-700 nm	410-710 nm
Interval	10 nm	10 nm
Num. of bands	31	31

the amount of light passing through the lens. An ideal lens of no diffraction limit should have an infinite aperture, therefore in most experiments the size of aperture is not considered.

The radiance of an image formed by a perfect lens equals the radiance of the object [118, p. 114]. Conceptually the action of an image receiving surface is to convert the spatial distribution of radiance incident on it into the irradiance of the image. This concept of radiance invariance simplifies the computation of the irradiance of the image [118, p. 252], as shown in Equation 4.1

$$E_i = \pi T L_o \left[\frac{1}{1 + (2\mathrm{F}_{\mathrm{number}})^2} \right] \tag{4.1}$$

where Ei and L_o denote the irradiance of the image and the radiance of the object respectively, T is the lens transmittance, here assumed to be the same for all rays, and $\mathrm{F}_{\mathrm{number}}$, the relative aperture of the lens in question. This formula applies to the on-axis pixels on the detector. The irradiance over the off-axis pixels ought to be reduced by $cos^2\theta'$ where θ' is the angle of a point in the image away from the optical axis. The falloff assumes lesser importance when θ' is not significant. As the majority of the scenes chosen have already suffered from this loss in the course of image acquisition, further application of the falloff will render the images unnaturally. Consequently the on-axis and off-axis pixels are dealt with equally.

As a result, it is theoretically sound to neglect the radiometric conversions in the simulation where the spatial distribution of light over the image is of higher priority. This lays a radiometric foundation for the simulation. In a real system, absolute radiometric quantities could be obtained by proper radiometric calibration.

A series of distortions of the optical image, known as optical aberration, is unavoidable in an optical imaging system. In this dissertation, we consider in particular the influence of chromatic aberration in Chapter 6.

4.2.2 Filter array - mosaicking

A spatio-spectral sampling apparatus, filter array is essentially an arrangement of optical filter elements tessellated in a generally repeated pattern corresponding to the array of pixels on the image sensor. Consequently the simulation of a filter array require both spectral complexion of filters and the way they are fitted geometrically.

Filters - spectral sampling

A large number of optical filters are band-pass or band-reject filters that can be well modelled by a Gaussian function with various bandwidth settings. Measured spectral transmittances is also of great importance and interest so that simulations may be more realistic. As a result, we make use of both in the experiments. Filter characteristics affect the performance of a SFA-based imaging system in terms of sensitivity and accuracy of spectral/colour reconstruction, therefore design of filters is often compromises between these two factors. We will look into this issue in Chapter 5.

Mosaic - spatial sampling

A filter array comprises a number of recurrent groups and each group is a particular tessellation of a few filter elements. The term “Moxel”, multispectral macro pixel, is used to refer to such groups in a SFA. Generally it is good practice to ensure an even distribution of various filter elements within a group. Nevertheless, a pseudo-random layout, in other words, non-uniform sampling pattern, may alleviate artefacts caused by uniform sampling. A fully randomised filter array is not impossible, however it requires a specifically developed demosaicking algorithm.

The module filters the irrandiance image formed before the filter array on a pixel-by-pixel basis. The optical image might need padding around the borders to ensure size of the padded image is a multiple of the size of the moxel, for the ease of mosaicking and demosaicking. All of the SFAs used in the experiments are designed to conform to the binary-tree approach [123].

4.2.3 Sensor

As the last part of the image taking module, a sensor in simulation integrates the radiant power at each pixel by weighting the pixel value in the incident image by the spectral responsivity over the spectrum.

Sensor parameters are simplified so as to keep the simulation simple yet reasonable. Pixel layout and pixel count are set to be identical to those in the scene and the filter array, to obviate the need for spatial translation, scaling and rotation. It is assumed that fill factor of the pixels is 100% such that no light falls on peripheral circuits that are insensitive to photons. Full-well capacity defines the total amount of charge an individual pixel can hold during integration, thus influencing the dynamic range of a sensor. In the simulation, the full-well capacity is considered together with the exposure time to match the intensity level to which a reference white sample would lead. Spectral responsivity, or quantum efficiency, of the sensor remains unity constantly over the useful wavelength range if not otherwise stated, for the sake of simplicity. In practice, nevertheless, the sensitivity is determined by the light sensitive material and the hardware design.

Noise

An intrinsic property of solid-state image sensors is noise. Palmer and Grant list 11 types of noise sources [141, p. 137], and Fiete [47, p. 84] summarises four major ones: photon noise, background noise, dark noise and quantisation noise. Background noise becomes significant when light from non-targeted objects interfere with that from the objects of interest, as are atmospheric effects in remote sensing. Quantisation noise refers to the discrepancy between the quantised signal of discrete amplitude and the original signal of continuous amplitude in analogue-to-digital conversion. Photon noise, often modelled by Poisson distribution, is due to the stochastic emission and propagation of photons. As the number of photons increases, photon noise closely follows a normal distribution in appearance. Photon noise is irrelevant to frequency, therefore it is white. Dark noise refers to electrons generated with no light incident onto the detector. It is primarily caused by read noise coming from readout electronics [47, p. 86]. And thermal noise may contribute largely to read noise and determines the noise floor of a sensor [134, p. 76], which arises from the random motion of carriers in any electrical conductor. Discovered by John B. Johnson [83] and explained by Harry Nyquist [138], thermal noise is also referred to as Johnson-Nyquist noise. Both the amplitude and frequency distribution of thermal noise are Gaussian. The sensor module is open for any type of noise, however certain types of noise are not considered in this disserta-

tion. For instance, as there is no scene visibly affected by stray light or atmospheric effects, background noise is neglected, and quantisation noise is skipped as well considering that no specific quantiser exists in the framework and the scenes are already quantised in the course of acquisition. Noise is artificially introduced in Chapter 5.

4.3 Image processing module

The image taking module produces raw digital images that resemble the readout from a staring array. In the subsequent image processing module, the digital image will pass through the image processing routines including demosaicking and spectral or colorimetric reconstruction. Other image processing tasks are not considered in the framework, and we do not handle compression and storage. As this is a computational module in practice, it is not different from that in a real SFA-based imaging system.

4.3.1 Demosaicking

The main input to a demosaicking algorithm is mosaic sensor images. It is also necessary to provide the algorithm with the exact layout of the entire filter array and the moxel. The essence of demosaicking lies in the estimation of the missing pixel values in the sensor output with the help of neighbouring pixels in the same or other bands, on the assumption that there exists spatial and spectral correlations between intra-band and/or inter-band pixels. Image borders padded previously in the mosaicking process for the case of demosaicking ought to be cut away after demosaicking. The methods of demosaicking implemented in this dissertation include BL (bilinear interpolation), SH (smooth hue transition based interpolation), BT (binary-tree based demosaicking), VM (vector median filtering, see Chapter 7), DWT (DWT based demosaicking, see Chapter 8) and LMMSE (LMMSE based demosaicking, see Chapter 9).

4.3.2 Spectral or colorimetric reconstruction

Demosaicked image is a multi-band image at full resolution. This is the output of a pipeline if these bands represent information of interest, e.g., band-specific features of the object. In most cases, however, this image does not furnish enough information meaningful and useful for visualisation or analytic purposes. Hence it is necessary to reconstruct the spectrum or colorimetric values represented by each pixel in the demosaicked image. Certainly it is an estimation process and requires some a-priori information through characterising the imaging system with some

targets of known characteristics. As a result, the input of this module include the sensor output as well as the characterisation results. Spectral reconstruction is considered in Chapter 7) and colorimetric reconstruction is investigated in Chapter 10.

4.4 Evaluation module

As the last module in the framework, quality evaluation is independent from the previous modules and the pipeline. However it is of great moment in the design of an imaging system. In this circumstance, evaluation may be carried out subjectively by performing psychophysical experiments or conducted objectively by computing scores of certain metrics. In this framework, merely objective evaluation is done by comparing signals before and after certain processing with appropriate quality metrics.

In the simulation workflow, evaluations may be performed in a flexible and suitable manner as shown in Figure 4.4. For instance, image quality assessment may be undertaken by comparing the full-resolution image prior to mosaicking and the demosaicked image. Similarly, metrics measuring spectra, colour and image quality can be utilised to evaluate the overall system performance by comparing the scene and the reconstructed scene. Although there are quality metrics customised for greyscale and colour images, there is no quality metrics widely accepted in the field of spectral imaging. Therefore we apply the well-known metrics to each band of the spectral images.

Common image quality metrics may be based on pure mathematical measures, like PSNR, or advanced models incorporating low- and high-level features of human vision, such as the SSIM. Apart from those, native and adapted colour difference formulae, such as CIE DE2000 and S-CIELAB, may also be used as metrics when the emphasis is placed on perceptual dissimilarity in colour.

4.5 Limitations

Now we have a brief overview of the imaging framework. In engineering a system, it is often the easiest to limit the model initially to the simplest case, which naturally leads to a departure from the truth, thus limiting to some extent the universality of the results and the conclusions.

Among other issues, probably the most crucial one arises from the input to the system, namely the scenes. The direct use of spectral images as scenes suffers from three major drawbacks.

Firstly, the limited availability and variety of spectral images present difficulties in generalising the conclusions. Results may be good for a certain type of scenes under certain system configurations, whilst not for other types of scenes. The scenes might lack certain characteristics of critical importance in evaluating the system or realising potential problems, such as high-frequency components in the database.

Secondly, it becomes difficult to interpret the results objectively with numerical scenes. Objects in a natural scene possess infinite spatial and spectral resolution, unlimited radiometric signal-to-noise ratios, and textures of varying degrees and styles, of which numerical scenes are short. It remains a question how well numerical scenes resemble real scenes.

Thirdly, it is often impossible to remove the optical aberrations and electronic aberrations from the already captured images, due to the uncertain and irreversible nature of image acquisition. Moreover, it is problematic to determine the amplitude of aberrations and noises artificially introduced to the numerical scenes that have already suffered from such optical and electronic distortions. Future verifications may be performed with the help of real sensor data [100].

That being said, we believe the simulation amply fulfils the major objective of the research reported in this dissertation.

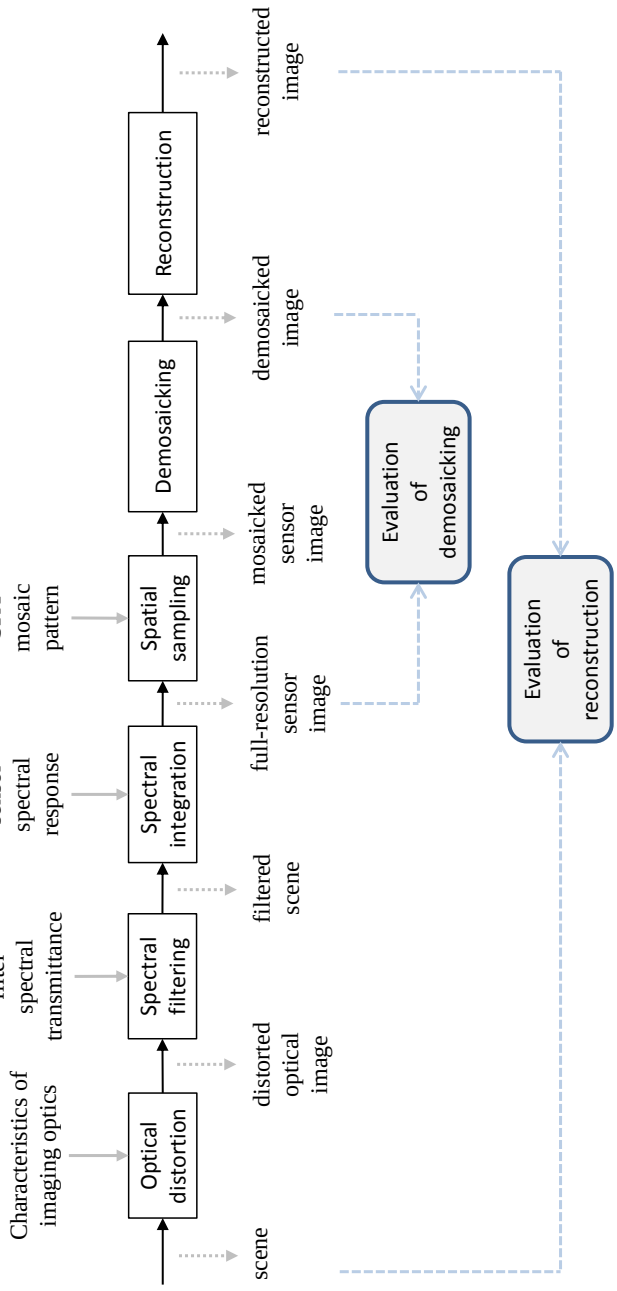

Figure 4.4: An illustration of the simulation workflow and the possible means of evaluation of SFA imaging pipeline. The workflow is slightly different from the physical pipeline due to the need of evaluation, e.g., spectral integration normally occurs after spatial sampling, is placed in front of it in the workflow to form full resolution images for the evaluation of demosaicking. The workflow is also flexible in that the modules may be connected as required by the simulation.

Chapter 5

Influence of filter bandwidth on spectral reconstruction

5.1 Introduction

In practice, a multiband image acquisition system often employs an objective lens, a set of optical filters and an area image sensor with the aim of recording the projected image of a scene captured by the system. Each filter corresponds to one band of the resulting multiband image, and a subsequent estimation step is commonly required in order to retrieve the CIE tristimulus values or spectral reflectance of the scene.

Filter design is the very first component of such a system. Spectral characteristics of filters therefore make a direct impact on the overall performance of the system. When simplified as a normal (Gaussian) distribution, a filter can be described primarily by two factors, i.e., central wavelength and bandwidth. The former specifies the dominating wavelength where the transmittance of a filter achieves the maximum, and the latter determines how the filter respond to the incident light distributed among the remaining part of the spectrum. The bandwidth of a filter is commonly measured by FWHM.

In a trichromatic system, three types of colour recording filters are often required. Primary colour filters whose peak transmittances are located in the blue, green and red region of the visible spectrum are commonplace in commercial colour cameras [13]. However, there exist colour cameras that possess complementary colour

filters in contrast to the primary colour filters commonly utilised. Complementary colour filters intrinsically bear wider pass-band than their primary counterparts, and it is demonstrated that the former gives rise to better colour reproduction and signal-to-noise ratio in sufficient lighting conditions, whereas the latter offers higher system responsivity and resolution [143, 142]. Similarly, the choice of filters remains a question in spectral capture. It is stated that narrowband filters should in theory outperform wideband ones with respect to the accuracy of spectral reconstruction [78, 79], whereas the wideband filters may produce superior results [78]. To the best of our knowledge, little research has been made so far to investigate the influence of various filter bandwidths on spectral acquisition.

In this chapter, we focus on the impact of filter bandwidth on the accuracy of spectral reflectance estimation in the context of a spectral image acquisition system, in a comprehensive and rigorous manner.

The following parts of this section are organised as follows. Section 5.2 describes three linear reflectance reconstruction methods that are widely adopted and used. The procedures of and conditions in which the experiments were conducted are introduced in Section 5.3 prior to a presentation of the results in Section 5.4. Section 5.5 draws some conclusions.[1]

5.2 Spectral reflectance estimation from spectral measurements

Spectral reflectance estimation is an inverse problem aimed at an estimation of the spectra of higher dimensions from the corresponding spectral measurements of lower dimensions. In concrete terms, a spectral capture process can be described in a linear form as

$$P = HSR \tag{5.1}$$

where P refers to the spectral responses represented by a $c \times q$ matrix, H corresponds to system responsivities represented by a $c \times l$ matrix, S is the spectral power distribution of the illumination represented by a $l \times l$ matrix, and R is the set of spectral reflectance represented by a $l \times q$ matrix. c is the number of spectral bands captured by the system, l is the number of spectral bands of incident spectra, and q is the number of reflectance spectra in the set. For spectral image capture $c > 3$, whereas trichromatic acquisition can be considered as a special case where

[1] Content of this chapter is adapted from a published paper [178].

$c = 3$. In comparison, the visible spectral range between 400 nm and 700 nm with an interval of 10 nm would yield $l = 31$. As a result, $c < l$ is common for multispectral imaging.

Spectral reflectance estimation aims at an estimation of R from P. Equation 5.1 is solvable if HS is known and invertible, so that we have $R' = WP$ where $W = (HS)^{-1}$. However it is not true in the case of reflectance reconstruction. Nevertheless W can be estimated by means of training where a collection of training spectra R_t and corresponding responses P_t are utilised to derive an approximation of W. Three representative methods based on different principles were experimented with to this end. The method of linear least squares attempts to solve Equation 5.1 by means of least-squares which leads to Equation 5.2,

$$W = r_t p_t^+ \tag{5.2}$$

where P_t^+ is a right pseudoinverse of P_t : $P_t^+ = P_t^T(P_t P_t^T)^{-1}$.

Imai and Berns [77] proposed to employ PCA (principal component analysis) to analyse the training spectra, which gives rise to Equation 5.3

$$W = U_t P_t^+ \tag{5.3}$$

where U_t is a matrix consisting of the i most significant eigenvectors of the training spectra by means of PCA. The parameter i is determined so that the RMSE (root mean square error) between R_t and the estimated R_t' is minimised.

Wiener estimation [152] is yet another method taking noise into consideration in the following manner,

$$W = R_t R_t^T (HS)^T ((HS) R_t R_t^T (HS)^T + N)^{-1} \tag{5.4}$$

where N is a term reflecting additive noise intrinsic to the system in form of $\sigma^2 I$, σ^2 being the variance of estimated noise and I being an identity matrix. σ^2 is estimated using the method proposed by Hironaga and Shimano [73].

5.3 Experiment

The experiments were conducted on a simplified simulation framework, as shown in Figure 5.1.

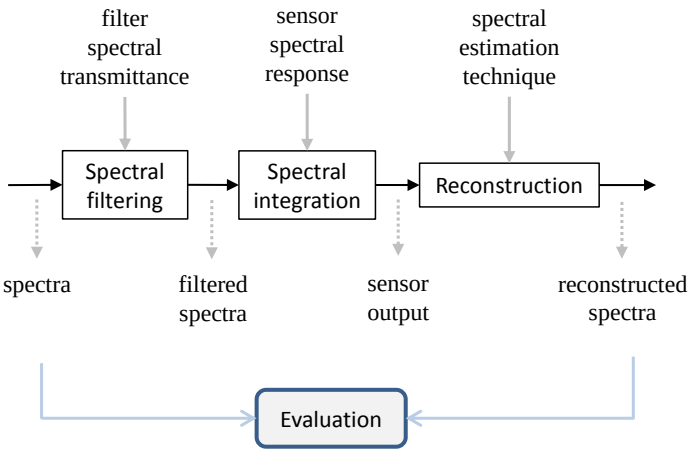

Figure 5.1: Simulation framework. The pipeline that appears in Figure 4.4 was modified to meet the requirements of the experiment in this chapter.

In total, 48 hyperspectral images were used in this study. 16 of them from Foster's database [48] and another 32 from the CAVE project [183]. Spectral reflectance images were derived respectively and re-lit by the illuminant of CIE D65. A selection of pixel was selected from each image by means of horizontal and vertical down-sampling at the ratio of 1:5 without low-pass filtering, in order to reduce the computational intensity.

For the ease of processing and comparison, all images were linearly interpolated in the spectral dimension, and filters were designed accordingly, to cover the range between 400 nm and 700 nm with an interval of 1 nm.

Six types of filter sets in three pairs were chosen. A 4-band filter set used in this research are depicted in Figure 5.2. We were interested in narrowband and wideband band-pass filters as well as corresponding inverted ones as band-stop filters. The FWHM of pass-band and stop-band was set to 10/40/160 nm respectively. In practice, a pass-band of 10 nm simulates very narrow band-pass filters like LCTF, a stop-band of 10 nm mimics notch filters relying on destructive interference. Similarly, a pass-band and a stop-band of 40/160 nm resemble the spectral transmittances of thin-film absorptive filters. The peak wavelengths were determined so that the intersection between both ends of the spectrum and the 40 nm band-pass filters correspond to the 3σ location, namely the filters cover the short end and long

end of the spectrum with rather low transmittances. The number of filters studied ranged from 3 to 20.

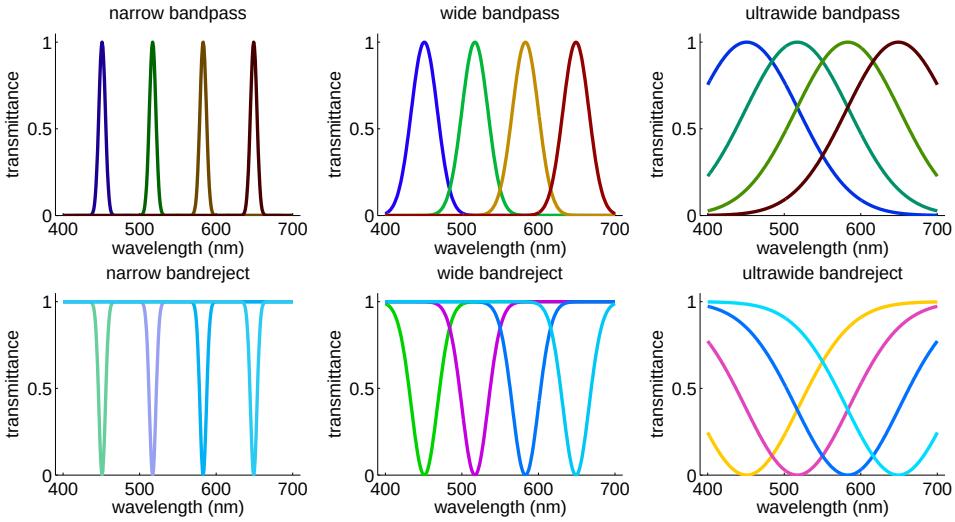

Figure 5.2: An illustration of a 4-band filter set. Copyright ©International Colour Association

In Figure 5.2, the three graphs in the upper row show narrow, wide and ultra-wide band-pass filters' spectral transmittances with FWHM of 10, 40 and 160 nm respectively. The three drawings in the lower row present spectral transmittances of the corresponding band-reject filter sets.

To make the results more robust and realistic, we also introduced a certain level of normally distributed noise to the simulated sensor responses. The ratio between the maximum signal level to the mean noise level is set to 50 dB with the standard deviation at 10% of the noise level.

To simplify the simulation, we also made an approximation that the sensor possesses constant quantum efficiency over the spectrum. The influence of the above filters in terms of the spectrum estimation accuracy was evaluated by means of RMSE (Root Mean Square Error) and GFC (Goodness of Fit Coefficient) (GFC) [150] averaged among the 48 virtual scenes, as indicated underneath by Equation 5.5 and 5.6.

Table 5.1: Parameters and setup of the experiments.

Spectral range	400 nm – 700 nm
Spectral interval	1 nm
Illuminant	CIE D65
Type of spectra	subsampled reflectance images
Number of images	48
Number of bands	3-20
Type of filters	6 sets of bandpass and bandreject filters
Reconstruction methods	least-squares, Imai and Berns, Wiener
Quality metrics	RMSE, GFC

$$RMSE = \sqrt{\frac{\sum_{j=1}^{301}[|r(\lambda_j) - r'(\lambda_j)|^2])}{301}} \tag{5.5}$$

$$GFC = \frac{|\sum_{j=1}^{301} r(\lambda_j) r'(\lambda_j)|}{|\sum_{j=1}^{301} [r(\lambda_j)]^2|^{1/2} |\sum_{j=1}^{301} [r'(\lambda_j)]^2|^{1/2}} \tag{5.6}$$

where r and r' represent the original and estimated spectral reflectance at any pixel in an image. It is worth noting that lower RMSE scores mean higher performance and an RMSE of zero means a perfect estimation, whereas, GFC values range from 0 to 1 and an exact reconstruction would yield 1.

5.4 Results

As depicted by Figure 5.3 and 5.4, in general, the wide band-pass filter set consistently outperforms others, followed by its band-reject version. On the other hand, the pair of ultra-wideband filter sets results in similar and comparatively lower accuracy of reflectance estimation. Clearly the narrowband filters are not simply the best on all occasions as opposed to what Imai *et al.* concluded [78].

Surprisingly, the performance of the narrow band-pass filter sets varies significantly and decreases dramatically from 13-band onward suggested by both of the two metrics. Otherwise results of other filter sets shift rather smoothly.

Results obtained with the first and second methods illustrate very similar tendencies, whereas the Wiener estimation yields somewhat different results potentially due to the involvement of noise in the computation. As the number of bands increases, Wiener estimation tends to provide more stable results, whereas the performance of the other two methods reduces gradually, except the narrow band-pass

set.

The optimal number of filters largely depends on the methods used, and the two metrics do not seem to make a difference, however the metrics do change the order of performance. For instance, the narrow band-reject filter set is the worst method in terms of GFC, while it is not the case of RMSE.

5.5 Conclusion

We evaluated the performance of 6 types of filters of varying bandwidths in terms of the accuracy of spectral reflectance estimation with three linear estimation methods in the context of spectral image acquisition, with the help of a simulated imaging framework.

The results are not fully consistent with the conclusions drawn by previous work that narrow band-pass filters always yield higher spectral reproduction accuracy. Nevertheless, we found that band-pass and band-reject filters of reasonably wide band commonly seen in practice benefit spectral acquisition. Further, band-pass or band-reject filters of extremely narrow or broad bandwidths perform unsatisfactorily or unsteadily.

The experiments were conducted in simulated lighting condition that is sufficient in terms of intensity. In insufficient lighting conditions, we assume that the advantages of wider bandwidths would be more significant in the system sensitivity as well as the signal-to-noise ratio.

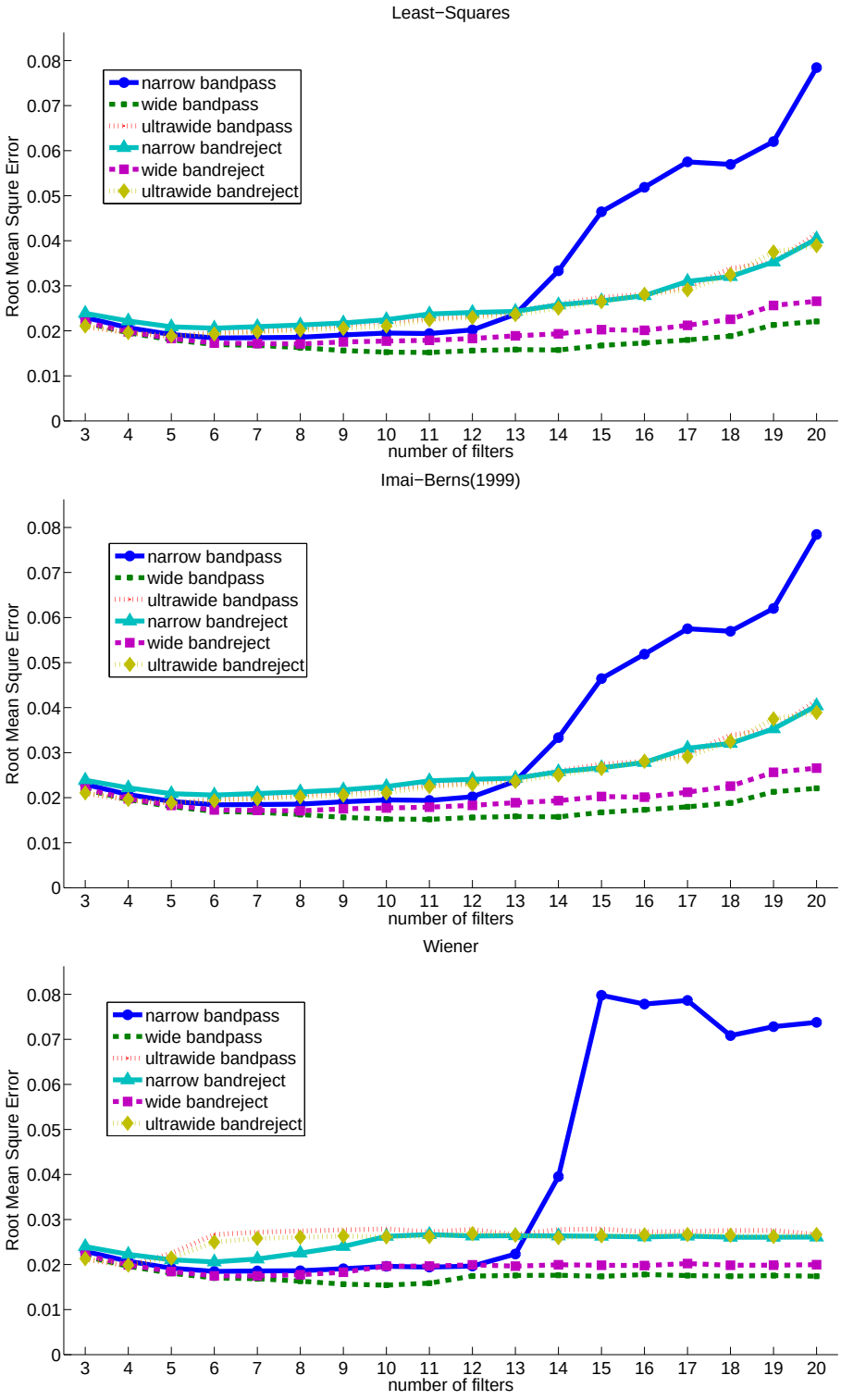

Figure 5.3: Accuracy of spectra reconstruction evaluated by RMSE. Copyright ©International Colour Association

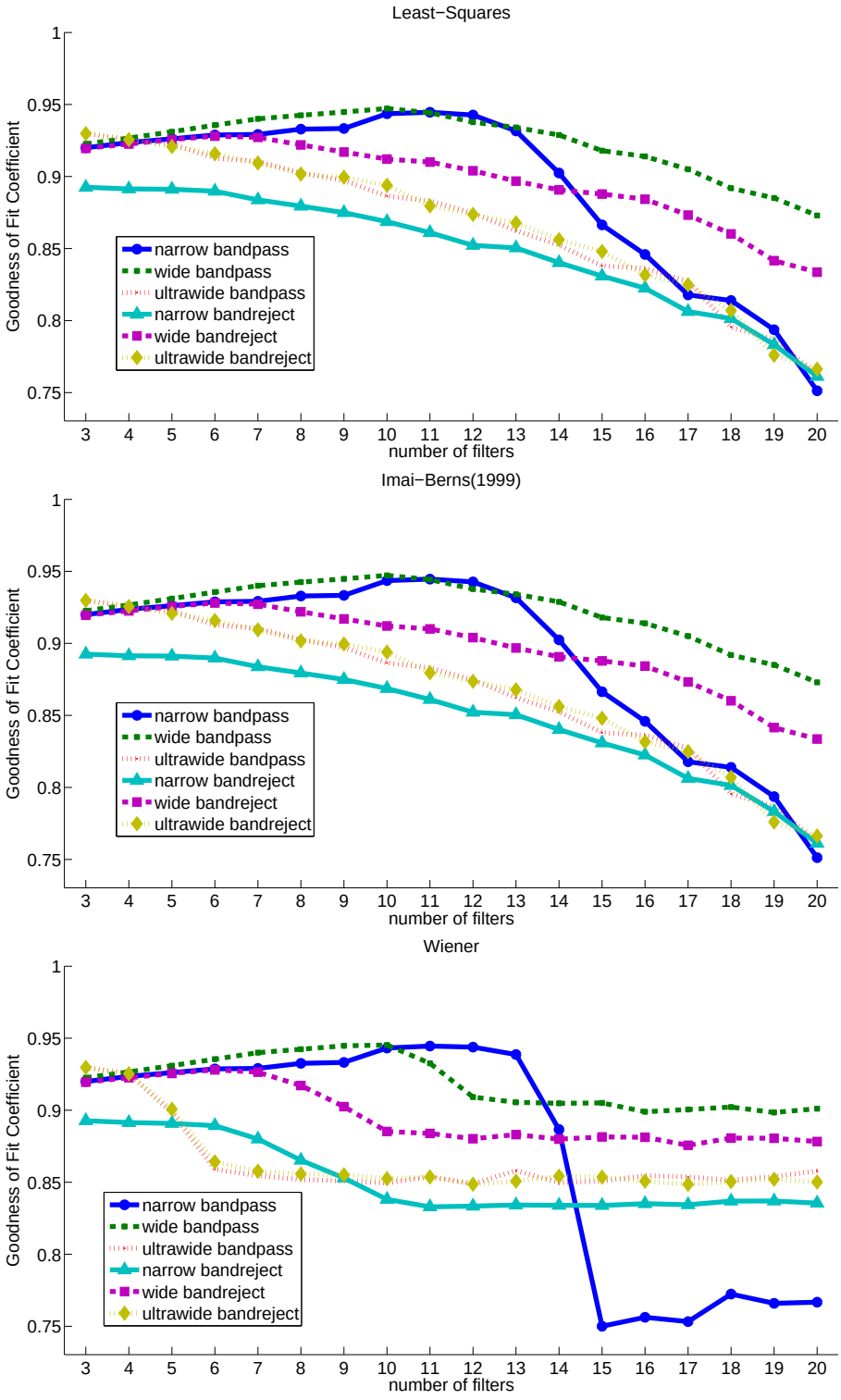

Figure 5.4: Accuracy of spectra reconstruction evaluated by GFC. Copyright ©International Colour Association

Chapter 6

Influence of chromatic aberration on CFA demosaicking

6.1 Introduction

Optical images are commonly distorted by optical elements in form of various types of optical aberrations, and one of them resulting in colour artefacts is denoted chromatic aberration (CA) [102, p. 257]. It occurs because lenses, typically made of glass or plastic, bear different refractive indices for different wavelengths of light, that is, the dispersion of a lens. The refractive index decreases with increasing wavelength. The main consequence of CA in imaging is that rays at different wavelengths are focused at different image distances (axial/longitudinal CA) and at different locations in the image (transverse/lateral CA). In theory and reality only rays at a certain wavelength are focused accurately on the image plane, all other rays are focused before or behind the image plane, which leads to blur when observed from the image plane. Similarly, magnification of a lens varies from wavelength to wavelength as well. On the optical axis, there appears as axial CA, since magnification is zero. In a plane perpendicular to the optical axis, the difference of magnification rate turns more prominent as the distance from the optical axis increases, which produces transverse CA. The problem of CA may be corrected optically to some extent by using superior glass substrate whose refraction index varies to a lower degree and combining positive and negative lenses, nevertheless it is not avoidable in practice where cost, compactness, and weight matter.

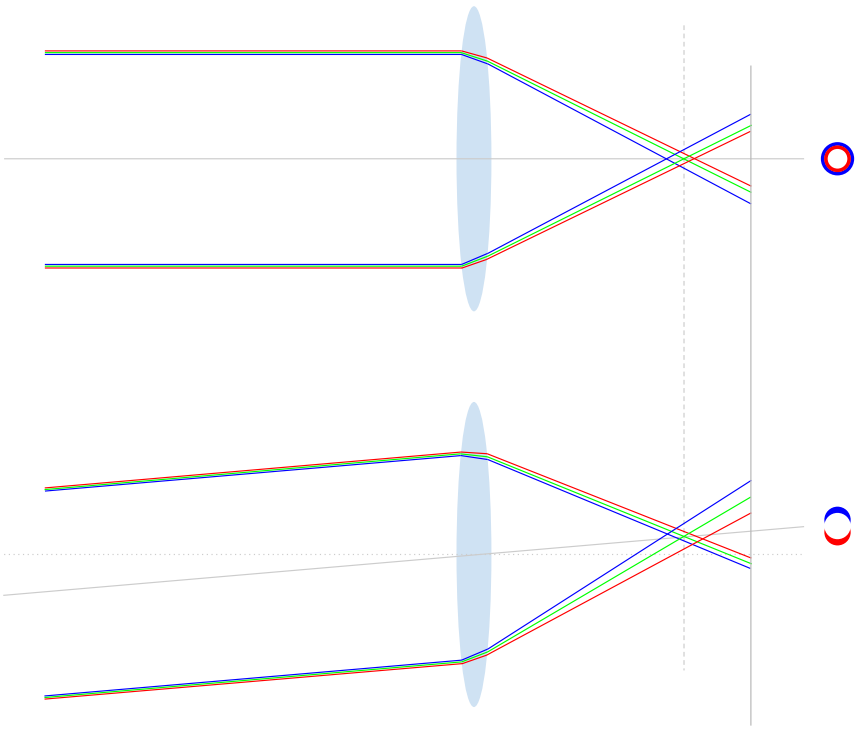

Figure 6.1: Formation of chromatic aberrations.

CA influences the spatial and spectral correlations of images through the artefacts, such as blur and mis-registration, which also affect demosaicking. To the best of our knowledge, an evaluation of the influence of CA on demosaicking has not been performed. Therefore we will address this issue in this chapter.

The rest of the chapter begins with a description of the simulation of CA in Section 6.2. Section 6.3 details the experimental setup. Results are demonstrated in Section 6.4 and discussed in Section 6.5.[1]

6.2 Simulation of chromatic aberration

CA occurs in the formation of an optical image, therefore the best way of observing and studying CA is through various optical design. However, this is not flexible and convenient. In consequence, we opt to simulate CA with spectral images as an

[1]Content of this chapter is adapted from a published paper [174]. Copyright ©IEEE.

alternative solution. The two types of aberrations are simulated individually and jointly. The simulation of axial and transverse CAs are demonstrated in Fig. 6.2 and Fig. 6.4.

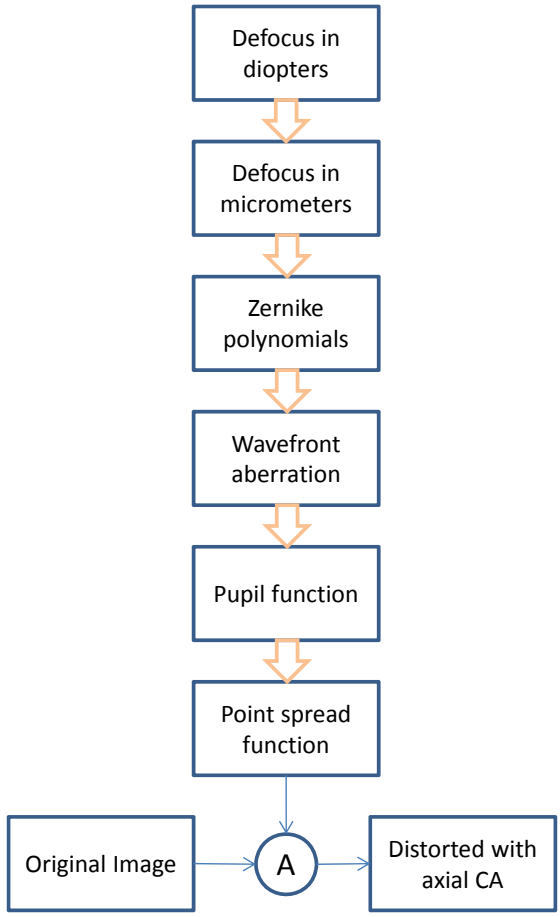

Figure 6.2: Workflow for the simulation of axial CA. Copyright ©IEEE.

Keeping in mind the reason for axial CA, we suppose the rays at 550 nm are focused on the sensor, such that green channel at about 550 nm remains in focus and thus little changed, which is consistent with the peak in the CIE luminosity function. Then the rays at other wavelengths will be focused at a range of planes before and behind the intended image plane. This is seen as a blur. CA is an optical aberration closely bound to the optical design of a lens, and the degree of blur depends primarily on the position of the image plane for a given lens at given

aperture size. It is often analysed in optical design and fabrication by means of ray tracing. However it varies from one optical design to another, and there is not a parametric model of such aberration to the best of our knowledge. To that end, we rely on the ISETBIO toolbox [1] that makes use of an ocular CA model [164, 165]. With this reduced eye model, the chromatic refractive error, that is the dioptric difference of refraction, can be derived by Eq. 6.1,

$$\Delta R_E(\lambda) = \frac{n(\lambda_1) - n(\lambda_2)}{r_c n_D} \tag{6.1}$$

where λ_1 and λ_2 refer to the wavelengths in question, and $n(\lambda_1)$ and $n(\lambda_2)$, the refractive indices at these two wavelengths. n_D is the refractive index for the sodium D-line (589 nm), which is wavelength for which the model eye is emmetropic. r_c is the corneal radius of curvature, set to 5.5 mm. The refractive index is obtained by Eq. 6.2,

$$n(\lambda) = a + \frac{b}{\lambda - c} \tag{6.2}$$

where $a = 1.320535, b = 0.004685, c = 0.214102$.

Now the defocus obtained is expressed in diopters. To make it suitable for the next step, which is the calculation of the pupil function, it is necessary to convert the defocus expressed in diopters to that expressed in micrometres by Eq. 6.3.

$$D_m = \frac{r_c^2 D_d}{16\sqrt{3}} \tag{6.3}$$

where D_m and D_d denote defocus in micrometres and diopters respectively. The pupil function, or sometimes referred to as aperture function, is a complex function of the position in the pupil or aperture (an iris in this case) that represents the amplitude and phase of the wavefront across the pupil, also known as wavefront aberrations. It is an important tool to study optical imaging systems and their performance.

Optical system aberrations have historically been described, characterized, and catalogued by power series expansions, where the wave aberration is expressed as a weighted sum of power series terms that are functions of the pupil coordinates. Each term is associated with a particular aberration or mode, such as spherical

aberration, coma, astigmatism, field curvature, distortion, and other higher order modes. Zernike polynomials form a complete set of functions or modes that are orthogonal over a circle of unit radius and are convenient for serving as a set of basis functions. Pupil functions are calculated here with the use of Zernike polynomials [112] and pupil function at a given wavelength is demonstrated in Eq. 6.4.

$$PF(\lambda) = Ae^{-i2\pi\frac{Z}{\lambda}} \tag{6.4}$$

where A represents the amplitude, calculated entirely based on the assumed properties of the Stiles-Crawford effect, and the exponential function is actually the phase of the aberration. The Zernike polynomials, denoted by Z, may consist of a series of modes, however, as the only aberration we are interested in this context is defocus (4^{th} mode), we simply neglect others.

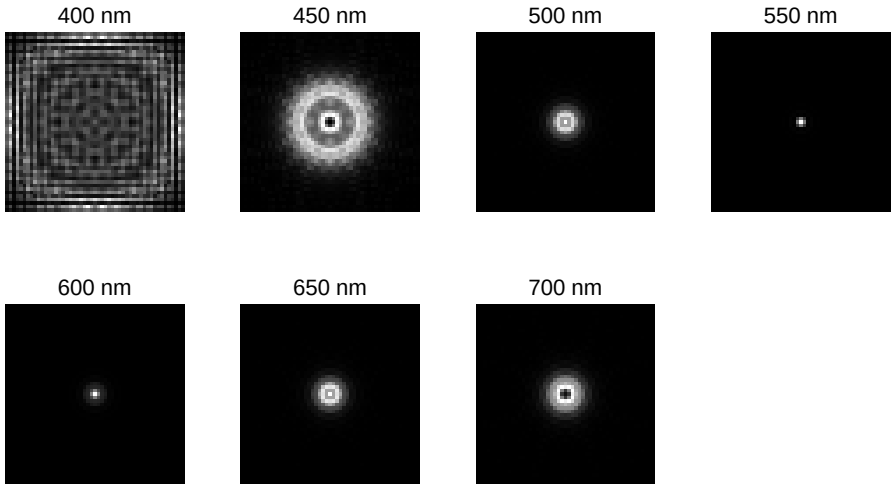

Figure 6.3: A series of PSFs at visible wavelengths. Copyright ©IEEE.

The pupil function is related to the point spread function (PSF) by the Fourier transform [61, p. 131]. The reduced eye model simplifies the aberration and assumes the axial CA is shift-invariant, the generated PSF is static for each wavelength. An example of PSFs at a few wavelengths over the visible spectrum is demonstrated in Fig. 6.3. It is clear that the support of the PSFs vary in size as the wavelength increases, and achieves the minimum at 550 nm. A PSF is in fact the impulse response of an imaging system in spatial domain, and the Fourier transform of a PSF leads to the optical transfer function that integrates the modulation

transfer function (MTF) and the phase transfer function (PhTF). A convolution of a PSF and an image will produce the simulated image distorted by axial CA.

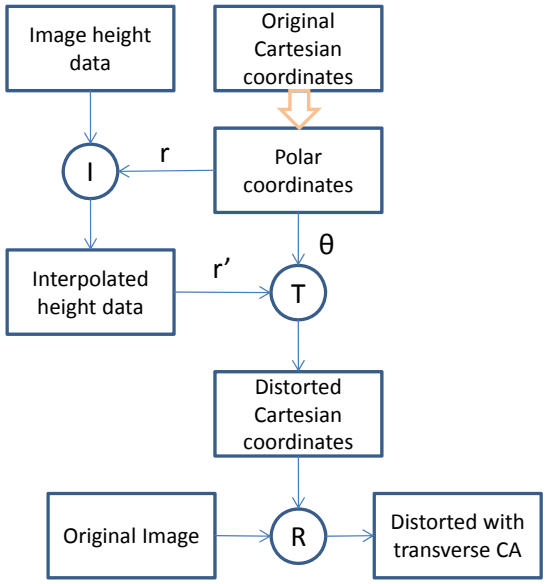

Figure 6.4: Workflow for the simulation of transverse CA. Copyright ©IEEE.

The mechanism of transverse CA lies in a varying rate of geometric distortion, that is in fact a radial operation depending on wavelengths. Therefore we first represent the images of each band in polar coordinates. Subsequently the radius can be manipulated in such a manner that the magnification varies in radial direction, following the ray tracing analysis of a real lens design. In practice, the measurement of transverse CA is often provided in form of a series of samples by the ray tracing software, which reflects the wavelength dependent radial distortion, as shown in Table 6.1. Accordingly, interpolation becomes essential to map and resample the original band images in order to simulate transverse CA.

As mentioned above, the reduced eye model simulates merely axial CA, and transverse CA depends on the results of ray tracing analysis. When combined, the two types of CA may be simulated sequentially as implemented by ISET [45]. Namely, transverse CA is applied prior to axial CA.

Table 6.1: Positions of radial samples before and after transverse CA.

Radial samples	Distorted radial samples				
	400 nm	475 nm	550 nm	625 nm	700 nm
0.0518	0.0507	0.0510	0.0511	0.0512	0.0513
0.1037	0.1014	0.1019	0.1022	0.1024	0.1025
0.1555	0.1519	0.1527	0.1531	0.1534	0.1537
0.2073	0.2023	0.2033	0.2039	0.2044	0.2047
0.2591	0.2525	0.2538	0.2545	0.2551	0.2554
0.3110	0.3025	0.3040	0.3049	0.3055	0.3060
0.3628	0.3521	0.3539	0.3549	0.3557	0.3562
0.4146	0.4014	0.4034	0.4046	0.4054	0.4061
0.4664	0.4503	0.4525	0.4539	0.4548	0.4555
0.5183	0.4987	0.5012	0.5028	0.5038	0.5046
0.5701	0.5467	0.5495	0.5511	0.5523	0.5531
0.6219	0.5942	0.5972	0.5990	0.6003	0.6012
0.6737	0.6411	0.6443	0.6463	0.6477	0.6487
0.7256	0.6874	0.6909	0.6930	0.6945	0.6956
0.7774	0.7330	0.7368	0.7391	0.7407	0.7418
0.8292	0.7780	0.7821	0.7846	0.7862	0.7875
0.8810	0.8224	0.8267	0.8293	0.8311	0.8324
0.9329	0.8660	0.8705	0.8734	0.8753	0.8767
0.9847	0.9089	0.9137	0.9167	0.9187	0.9202
1.0365	0.9511	0.9561	0.9593	0.9614	0.9629

6.3 Experiment

We implemented and experimented with two representative methods, namely bilinear interpolation and gradient-corrected linear interpolation. The former relies on merely spatial correlation, whereas the latter also makes use of, and thus sensitive to, spectral correlation.

Gradient based demosaicking solutions are aimed at reduced artefacts by avoiding interpolating across the edges. Malvar *et al.* [113] advance a gradient-corrected bilinear interpolated approach, with a gain parameter to control how much correction is applied. In other words, the results of bilinear interpolation is corrected by a measure of the gradient for the known colour at the pixel location. To determine appropriate values for the gain parameters, a Wiener approach is employed which computes the values leading to minimum mean-square errors, given second order statistics computed from the Kodak data set [2].

Evaluation of the demosaicking algorithms can be seen in general as an image quality evaluation task.

In the last decade when demosaicking gains much attention, the evaluation of demosaicking also attracts the interest of the academic community. Longère *et al.* conduct perceptual quality evaluation on a few demosaicking approaches, and state that perceptual results cannot be easily predicted using an image metric [106]. Even so, there are several attempts for objective quality evaluation. Lu and Tan propose two types of quality measures specifically for demosaicking, one computes the PSNR (peak signal-to-noise ratio) and CIE ΔE^*_{ab} for edge and smooth regions respectively, whereas the other one deals in particular with the zipper artefact [110]. Yang *et al.* show that low-level features (colours or edges) extracted from demosaicked images are affected by resolution, whatever the demosaicing method used, and therefore propose new criteria designed for low-level image analysis [182].

The most widely used criteria for the evaluation of demosaicing quality are MSE (mean squared error) and PSNR, primarily because they are simple thus easy to implement. However, the PSNR criterion provides a general estimation of the demosaicking quality, but does not really reflect the human judgement. Alternatives such as CIE ΔE^*_{ab} and S-CIELAB [189] are also widely used, however they require a-priori information like the reference white or illuminant [108].

In this section, we concern mostly the signal fidelity of each colour channel. Therefore we base our judgement on PSNR. In comparison with PSNR, the SSIM (Structural SIMilarity) index [179] provides more structural information and tends to be more consistent with subjective image quality assessment, which matches CA that blurs and shifts structures. Therefore we also adopted the SSIM as a method for measuring the similarity between the images before and after demosaicking.

In contrast to straightforward assessment of demosaicking methods or image quality, an evaluation of the influence of CA on demosaicking seems a bit more complicated, as there are two types of source images, i.e., with and without CAs. In consequence, with the two full reference quality metrics, we not only computed the image quality between the source and demosaicked images with and without distortions, but also cross compared the non-distorted source images and distorted demosaicked images.

The experiment was conducted in the following manner. First, simulated CA was applied to spectral bands separately. Then, a mosaic image is formed by filtering the distorted spectral image with a Bayer CFA [13] and converting it to sRGB colour space. Next, the mosaic image was interpolated with one of the demosaicking methods. Finally, the demosaicked images were fed into a quality metric channel

by channel.

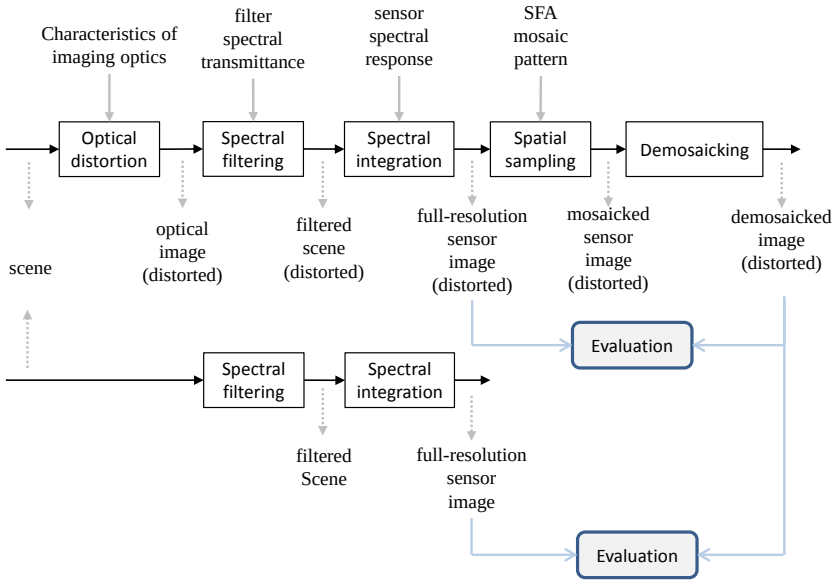

Figure 6.5: Simulation framework.

Conditions and parameters in relation to the experiment are presented as follows. and the images were cropped into square matrices by the shorter dimension. Spectral range was set to 400 nm to 700 nm, with an interval of 10 nm. The CFA conforms to the common design of Bayer. Transverse CA was simulated according to real lens data provided by the ISET [45]. The SSIM index was computed with the empirical formula specified on the official webpage to determine the scale for images viewed from a typical distance [3].

6.4 Results

Experimental results are depicted below. Lines and markers in red, green and blue represent the results for the corresponding channels, and those in black indicate the average values. Due to the space limitation, some similar results are not shown here. Concerning the performance with and without CAs, Fig. 6.7-6.8 show the results in terms of PSNR, while Fig. 6.9-6.10 display the results in terms of SSIM index. Similarly, Fig. 6.11-6.12 demonstrate the results in terms of PSNR and SSIM respectively for the cross comparison between non-distorted sources and

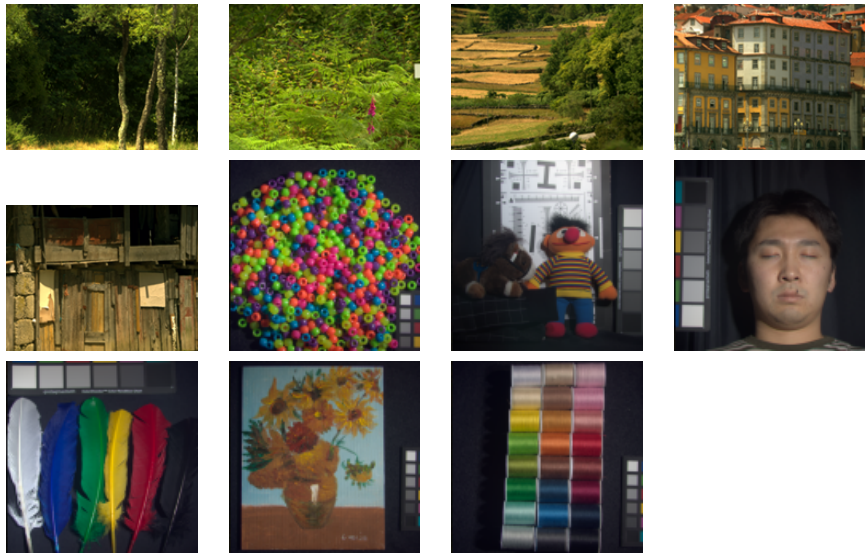

1	2	3	4
5	6	7	8
9	10	11	

Figure 6.6: Thumbnails of the images used. Scene 1-5 were selected from the Foster set [48] and scene 6-11 from the CAVE set [183].

distorted demosaicked images.

It can be seen from Fig. 6.7-6.8 that combined and axial CA yield higher performance, regardless of the demosaicking methods used. This is true for all red, green and blue channels. However, in Fig. 6.7 the best result was achieved by the blue channel under axial and combined aberrations, whereas in Fig. 6.8 for the green channel under the same aberrations. Such findings are consistent with Fig. 6.9-6.10. This indicates that CA surprisingly benefit demosaicking. In particular, blur benefit both demosaicking methods by higher spatial correlation. In theory, transverse CA in form of mis-registration should reduce correlation, thus decreasing the performance. On the contrary, the figures show opposite results. Perhaps the resampling involved blurs the images to some extent as well. In comparison with intra-channel methods, inter-channel interpolation is more sensitive to the content of the green channel. The drop of Image 10 in Fig. 6.9-6.10 may be because of the specific characters of the image, i.e., oil painting as the foreground on top of black background. Furthermore, the two distinct models of CA simulation may

Table 6.2: Parameters and setup of the experiments.

Spectral range	400 nm – 700 nm
Spectral interval	10 nm
Illuminant	CIE D65
Type of images	Reflectance image
Number of images	11
Type of chromatic aberration	transversal, lateral and combined
Type of filters	CIE 1931 $\tilde{x}(\lambda)\tilde{y}(\lambda)\tilde{z}(\lambda)$
Type of mosaics	Bayer CFA
Demosaicking	bilinear, constant-hue, gradient-corrected
Quality metrics	PSNR, SSIM

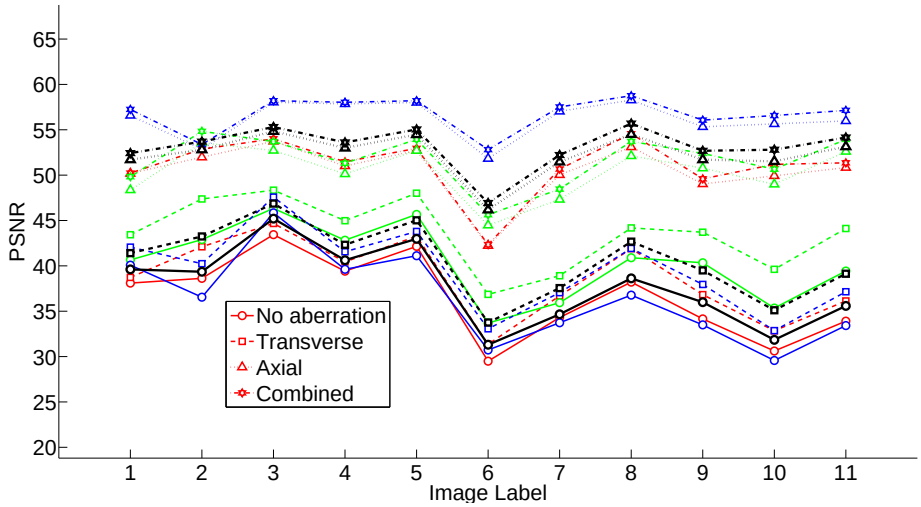

Figure 6.7: PSNR computed from straight comparisons between distorted source images and distorted demosaicked images for R/G/B channels and the average with bilinear interpolation.

also affect the results.

Suggested by Fig. 6.11 and Fig. 6.12, axial CA results in higher performance in terms of cross comparison, indicating that blur influences less the signal fidelity and similarity. In comparison, both of the other two types of CA involve transversal CA and lead to significantly worse results. Obviously CA lowers the overall image quality by any means.

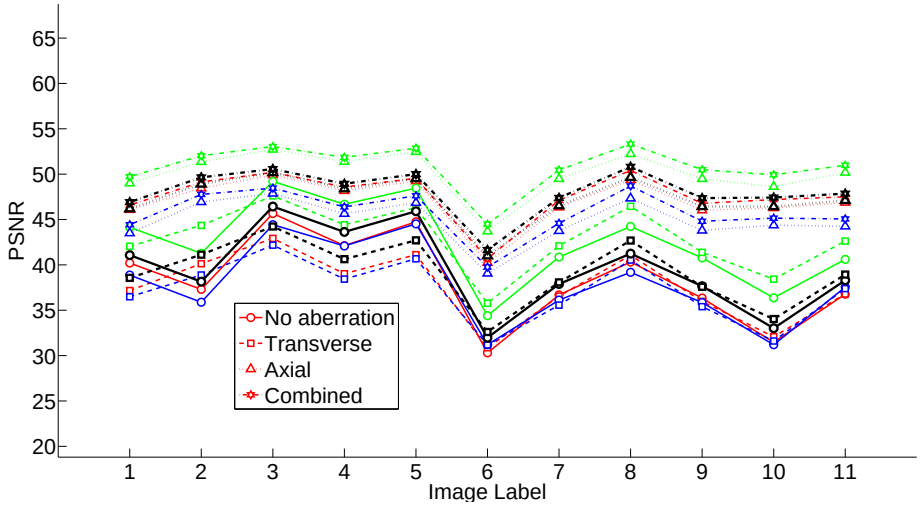

Figure 6.8: PSNR computed from straight comparisons between distorted source images and distorted demosaicked images for R/G/B channels and the average with gradient corrected linear interpolation. Copyright ©IEEE.

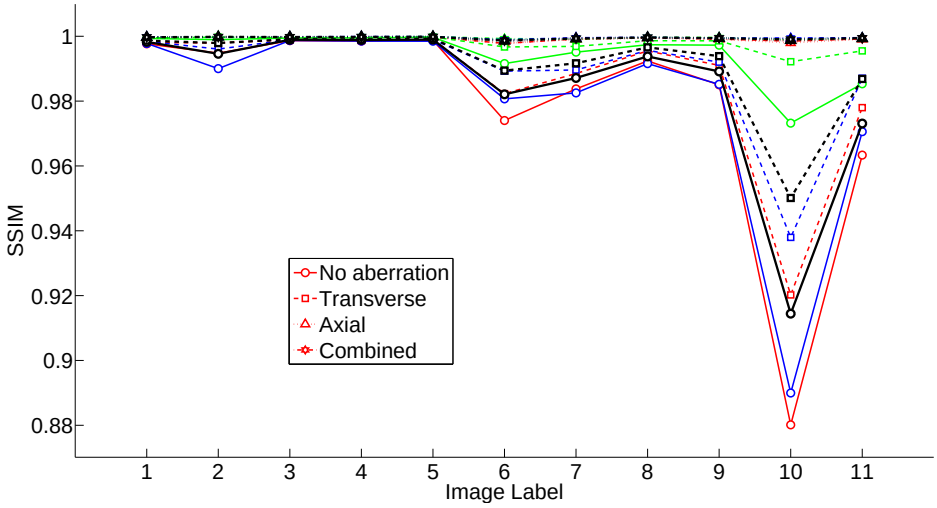

Figure 6.9: SSIM indices computed from straight comparisons between distorted source images and distorted demosaicked images for R/G/B channels and the average with bilinear interpolation. Copyright ©IEEE.

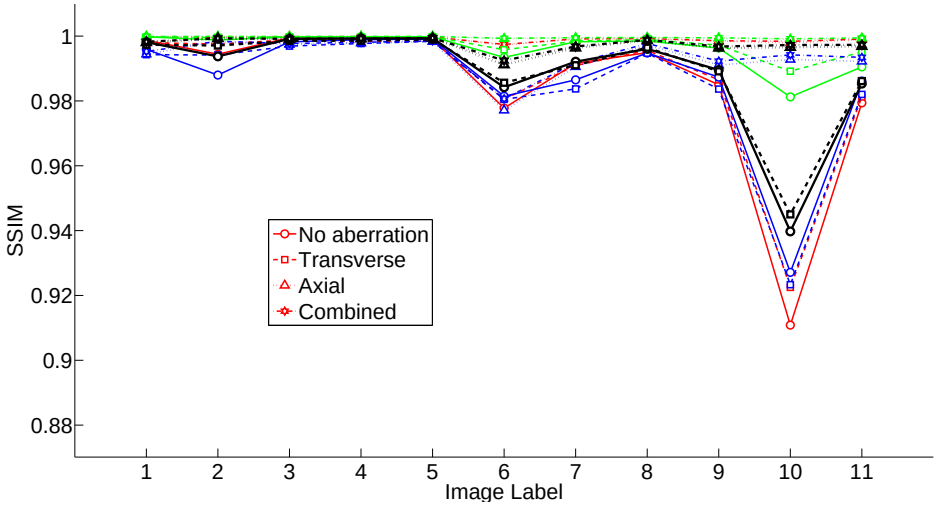

Figure 6.10: SSIM indices computed from straight comparisons between distorted source images and distorted demosaicked images for R/G/B channels and the average with gradient corrected linear interpolation. Copyright ©IEEE.

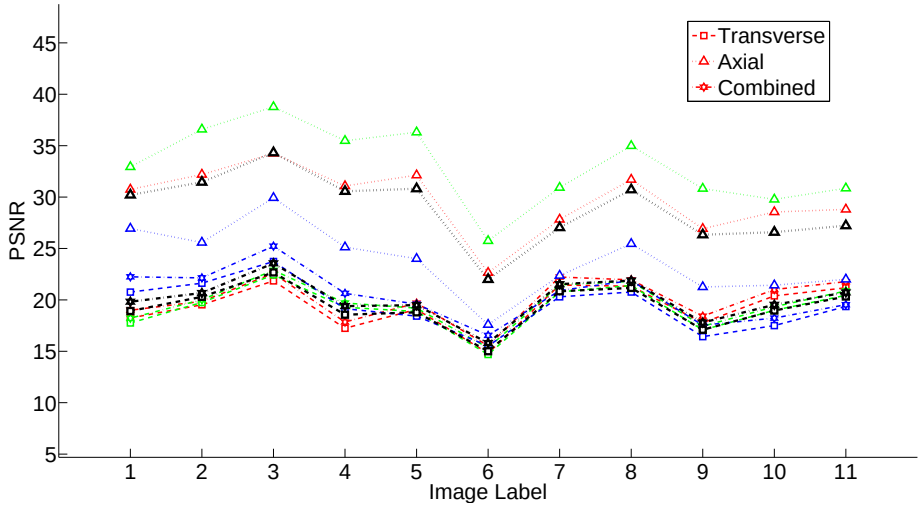

Figure 6.11: PSNR computed from cross comparisons between non-distorted source images and distorted demosaicked images for R/G/B channels and the average with gradient corrected linear interpolation. Copyright ©IEEE.

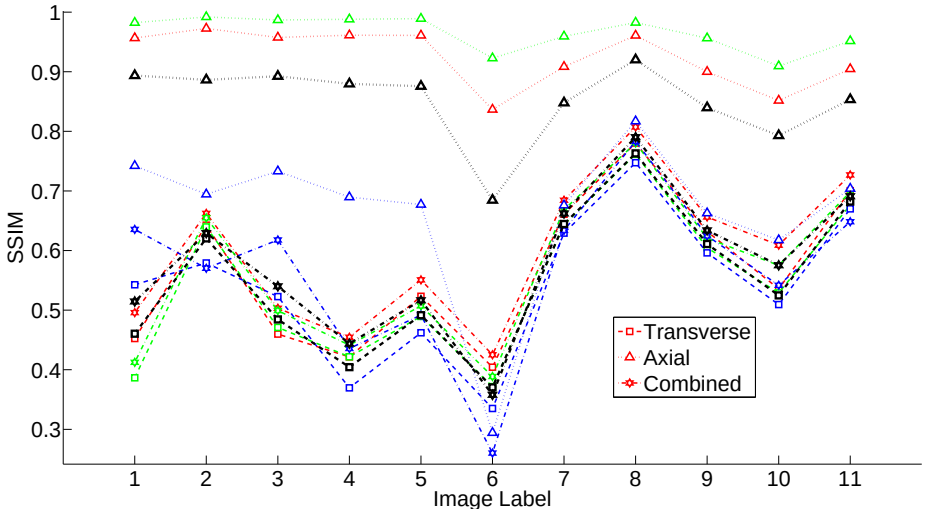

Figure 6.12: PSNR computed from cross comparisons between non-distorted source image and distorted demosaicked image for R/G/B channels and the average with gradient corrected linear interpolation. Copyright ©IEEE.

6.5 Conclusion

In this chapter we propose a framework to investigate the influence of chromatic aberration (CA) on demosaicking. Experimental results show that CA benefits demosaicking to some extent, however any type of CA decreases image quality by means of blur and mis-registration.

There is also a philosophical question, that is, which pair of images should be compared. An image quality evaluation performed between the original image and demosaicked image with and without CA does not reveal all mysteries. However it is also somewhat unfair to compare an original image without CA and a demosaicked image with CA.

Certainly more demosaicking algorithms and sample images would be helpful. And experiments in subjective assessment of image quality are desirable, which may reveal better how human observers perceive the issue. Further, the degree of CA may be varied to obtain more data, and ray tracing analysis of real lenses is expected to make the simulation more realistic.

Part III

Proposed methods for SFA demosaicking

Chapter 7

SFA demosaicking based on vector median filtering

7.1 Introduction

Among a wide spectrum of algorithms proposed for CFA demosaicking in the last decades, some of them might be able to be adapted to SFA demosaicking due to the intrinsic properties that CFA and SFA share. When each pixel in an image is considered as a vector, a normal trichromatic image constitutes a three-dimensional vector space. Clearly this concept is compatible with multispectral images, and so are the demosaicking methods based on that. For instance, a CFA demosaicking method that applies *vector median filters* to the pseudo-pixels formed in a given neighbourhood, is devised by Gupta and Chen[66]. To reduce the artefacts introduced by demosaicking, such as false colours and degraded edges, Keren and Osadchy[87] present a post-processing step that transforms each colour vector in a demosaicked image into an n-sphere and applies median filtering to the spherical coordinates, for the sake of the preservation of luminance discontinuities and the reduction of irregular chromatic variation among neighbouring pixels. As shown in respective literature, both methods give rise to satisfactory results despite their simplicity. As a consequence, we determined to extend and experiment with these two approaches.

Chapter 7 is organised as follows. The two aforementioned methods are described in Section 7.2 and 7.3, followed by the procedures and conditions of the experiments presented in Section 7.4. The primary results are demonstrated and dis-

cussed in Section 7.5 and 7.6 respectively.[1]

7.2 Vector median filtering for SFA demosaicking

In itself, vector median operation originally advanced by Astola *et al.* [9] is at the core of the idea detailed in Gupta and Chen [66]. Different from median filters, vector median is specifically designed for vector-valued signals, for instance, multispectral and colour images. It reduces to the scalar median when the inputs are one-dimensional vectors, and possesses similar properties to scalar median filters, such as the capability of smoothing noisy data while retaining sharp edges. Another basic property of the vector median, inherited from the median filter, is that it does not introduce any new values that do not exist in the input. Therefore the output of the vector median filter must be one of the input vectors.

According to *Definition 1* provided by Astola *et al.* [9], the vector median $\mathrm{VM}_{\mathrm{L2}}$ of $\underline{\mathrm{x}}_1, \ldots, \underline{\mathrm{x}}_\mathrm{N}$ is $\underline{\mathrm{x}}_\mathrm{VM}$ such that

$$\underline{x}_{\mathrm{VM}} \in \{\underline{x}_i | i = 1, \ldots, N\}, \tag{7.1}$$

and for all $j = 1, \ldots, N$

$$\sum_{i=1}^{N} \|\underline{x}_{\mathrm{VM}} - \underline{x}_i\|_2 \leq \sum_{i=1}^{N} \|\underline{x}_j - \underline{x}_i\|_2, \tag{7.2}$$

where $\|\|_2$ denotes the L^2-norm[2].

To take advantage of vector median filtering for demosaicking, multiple input vectors are necessary. Gupta and Chen [66] propose a concept of pseudo-pixel by grouping neighbouring red, green and blue pixels within a given neighbourhood. This leads to quite a few vectors representing all possible pseudo-pixels, each of which consists of three types of pixels connected horizontally or vertically in a mosaicked image.

Taking multispectral image into consideration, we extend this idea from two aspects. Firstly, our implementation associates the size of neighbourhood where the pseudo-pixels are formed with the dimension of a moxel, a mosaic element corresponding to an elementary filter mosaic repeated across an SFA. Figure 7.1(a) shows an example of a moxel when the filter array is composed of four types of

[1] Content of this chapter is adapted from a published paper [176]. Copyright ©SPIE.

[2] For a real number $p \geq 1$, the $\boldsymbol{L^p}$-norm of x is defined by $\|x\|_p = (|x_1|^p + |x_2|^p + \cdots + |x_n|^p)^{\frac{1}{p}}$.

filters labelled by the numbers. Figure 7.1(b) demonstrates the neighbourhood of $(2(n-1)+1) \times (2(m-1)+1)$ pixels and Figure 7.1(c) of $(2n+1) \times (2m+1)$ pixels, where n and m denote the number of rows and columns of the moxel. As can be seen, in the larger neighbourhood, there is a rectangular occurrence of 8 neighbouring pixels bearing the same label as the pixel in question situated in the centre. Secondly, in the original work [66], only horizontally and vertically connected pixels may be grouped as pseudo-pixels, whereas in this work diagonally connected pixels were also considered. Figure 7.2(a) illustrates a case where four pixels connected horizontally and vertically are grouped into one pseudo-pixel, while Figure 7.2(b) displays a pseudo-pixel formed by pixels connected both horizontally and diagonally.

Astola *et al.* [9] refers to a straightforward algorithm to find the vector median of $\underline{x}_1, \ldots, \underline{x}_N$ as follows, which was adopted in this work.

a) For each vector $\underline{x}_i$, compute the distances to all the other vectors using either the L^1-norm or the L^2-norm and add them together, resulting in

$$S_i = \sum_{j=1}^{N} \|\underline{x}_i - \underline{x}_j\|, \quad i = 1, \ldots, N. \tag{7.3}$$

b) Find min such that S_{min} is the minimum of S_i.

c) The vector median is $\underline{x}_{min}$.

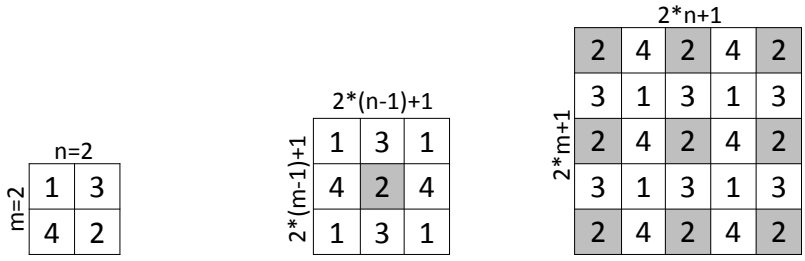

(a) A moxel **(b)** Small neighbourhood **(c)** Large neighbourhood

Figure 7.1: Moxel and modes of neighbourhood. Copyright ©SPIE

(a) A pseudo-pixel formed by rectangularly connected pixels

(b) A pseudo-pixel formed by diagonally connected pixels

Figure 7.2: Formation of pseudo-pixels. Copyright ©SPIE

7.3 Median filtering in n-sphere as a refinement step

As demosaicking is an operation of estimation, most methods fail in some situations of one kind or another which often results in false colour artefacts such as blurs and zips. As known, median filtering is effective at correcting such defects. As described in the original paper [87], median filtering in spherical space may be used as a post processing step subsequent to demosaicking. However, the median operation should be applied to angular components of the vectors, whilst the luminance related radius should be kept unmodified, so as to keep the luminance to some extent. We followed the principle and carried out the procedure by extending spherical space and three-dimensional Euclidean space to n-sphere and n-dimensional Euclidean space respectively.

To be specific, four steps were conducted in succession as follows.

a) Each pixel is represented by a vector $\underline{x} = \{\underline{x}_1, \ldots, \underline{x}_n\}$ in an n-dimensional Euclidean space, where n denotes the number of spectral bands of the demosaicked multispectral image.

b) Each vector $\underline{x}$ is transformed to $\underline{y} = \{r, \phi_1, \ldots, \phi_{n-1}\}$ in the n-sphere according to Equation 7.4.

c) Two-dimensional median filtering is applied one by one among the $n-1$ angular planes $\{\phi_1, \ldots, \phi_{n-1}\}$, whilst the radial plane r remains unchanged.

d) Each vector is transformed back to $\underline{\hat{x}} = \{\underline{\hat{x}}_1, \ldots, \underline{\hat{x}}_n\}$ in the n-dimensional Euclidean space according to Equation 7.5.

$$
\begin{aligned}
r &= \sqrt{\underline{x}_n^2 + \underline{x}_{n-1}^2 + \cdots + \underline{x}_2^2 + \underline{x}_1^2}, \\
\phi_1 &= \operatorname{arccot} \frac{\underline{x}_1}{\sqrt{\underline{x}_n^2 + \underline{x}_{n-1}^2 + \cdots + \underline{x}_2^2}}, \\
\phi_2 &= \operatorname{arccot} \frac{\underline{x}_2}{\sqrt{\underline{x}_n^2 + \underline{x}_{n-1}^2 + \cdots + \underline{x}_3^2}}, \\
&\vdots \\
\phi_{n-2} &= \operatorname{arccot} \frac{\underline{x}_{n-2}}{\sqrt{\underline{x}_n^2 + \underline{x}_{n-1}^2}}, \\
\phi_{n-1} &= 2\operatorname{arccot} \frac{\sqrt{\underline{x}_n^2 + \underline{x}_{n-1}^2} + \underline{x}_{n-1}}{\underline{x}_n}.
\end{aligned}
\tag{7.4}
$$

$$
\begin{aligned}
\hat{\underline{x}}_1 &= r\cos(\phi_1), \\
\hat{\underline{x}}_2 &= r\sin(\phi_1)\cos(\phi_2), \\
\hat{\underline{x}}_3 &= r\sin(\phi_1)\sin(\phi_2)\cos(\phi_3), \\
&\vdots \\
\hat{\underline{x}}_{n-1} &= r\sin(\phi_1)\cdots\sin(\phi_{n-2})\cos(\phi_{n-1}), \\
\hat{\underline{x}}_n &= r\sin(\phi_1)\cdots\sin(\phi_{n-2})\sin(\phi_{n-1}).
\end{aligned}
\tag{7.5}
$$

7.4 Experiment

8 hyperspectral reflectance images from the Foster database [48] were selected as scenes. As little information is contained in the band of 720 nm, it was removed from all images yielding 8 hyperspectral images of 32 bands. In order to reduce the computational cost, a region of $200px \times 200px$ is extracted from each image. In addition, one artificial spectral image that comprises one circle and one line and resembles the first publicly broadcast test card, was also created. It measures $200px \times 200px$ and contains 32 bands with each band being a binary image. Figure 7.4 provides an overview on the 9 images. Images were rendered with the illuminant of CIE D65.

Table 7.1: Parameters and setup of the experiments.

Spectral range	400 nm – 710 nm
Spectral interval	10 nm
Illuminant	CIE D65
Spectral responsivity	$S(\lambda) = 1$
Type of images	Reflectance image
Number of images	9
Type of filters	Gaussian bandpass
Type of mosaics	Bayer CFA, 4-/8-band SFAs
Demosaicking	bilinear, binary-tree, the proposed
Quality metrics	PSNR

A set of algorithms and parameters on which the experiments were conducted are described below.

In each case, spectral transmittances of the filters were determined so that each of them had a regular Gaussian shape and the centres of them were evenly distributed over the pertinent spectrum with the overlapping point located at one sigma, as shown in Figure 7.5.

Three filter array patterns were chosen, Bayer type 3-band setup, 4-band setup in form of 2×2 moxel and 8-band in form of 4×4 moxel, the moxels were repeated across the whole image. The filter arrays were executed in accordance with the binary tree approach proposed by Miao *et al.* [123], a perfect binary tree to be exact, with two levels and three levels corresponding to 4-band and 8-band arrangements respectively, as indicated in Figure 7.6.

Two demosaicking algorithms, bilinear interpolation and Miao *et al.*'s binary tree based progressive demosaicking [126], were implemented and compared with vector median technique. For the 3-band setup, vector median was conducted in accordance with the parameter specified by Gupta and Chen [66], whilst in case of 4-band and 8-band setup, two types of neighbourhood (small and large) and two ways of connectivities for forming pseudo-pixels were combined, giving rise to 6 groups of parameters. Median filtering in n-sphere was used as a refinement step in combination with all three demosaicking algorithms, and the size of the window was fixed.

To visualise the images, the original hyperspectral images were transformed into sRGB colour space, and the demosaicked multispectral images were first restored to hyperspectral images with a spectral reconstruction method exploiting a priori

knowledge of the imaged objects [69] and then rendered to sRGB.

In addition to subjective observations, evaluation of the performance was carried out by means of PSNR computed between the original and reproduced multispectral images, so as to avoid the error introduced by the spectrum reconstruction.

The way pseudo-pixels are formed resulted in a considerable amount of pseudo-pixels, 4600 at most in the experiment, which makes vector median filtering process computationally expensive. However it is highly parallelisable, as the neighbourhood of any pixel does not depend on another, and 4 cores in the processor were utilised to run 4 demosaicking threads in parallel.

The simulation framework is plotted in Figure 7.3 and the parameters are also shown in Table 7.1.

7.5 Results

Table 7.2 compares the performance of the three demosaicking algorithms in various conditions by means of PSNR. The best results for each type of the filter array are in bold, while results in italic font correspond to the worst ones. The global best results are emphasised in grey.

As seen in the tables, in general, the PSNRs decrease with the increase of number of filters. Among the three demosaicking algorithms, the binary tree approach, in most cases, gives rise to better results than the bilinear interpolation does. The PSNRs yielded by vector median are generally much lower than those of the other two methods, except for Image 9. In extreme conditions, such as binary images akin to Image 9, vector median yields both the best and worst results, since it may either select a vector that represents an original pixel value in the image or pick a bizarrely formed vector. The former results in the best results, whereas the latter leads to the worst ones.

The large neighbourhood is not beneficial to the vector median in general, nevertheless, it improves the performance significantly when pseudo-pixels do not have to pass through the centre pixel in question in case of the 4-band set-up. The utilisation of diagonally connected pixels is favourable to the vector median for large neighbourhoods. The freedom from the necessity of forming pseudo-pixels passing through the centre in the vicinity improves the performance of the vector median in particular for large neighbourhood.

Furthermore, PSNRs shown in Table 7.3 are mostly slightly higher in comparison

Table 7.2: The performance of the demosaicking algorithms in terms of the PSNR. sNB/lNB denote small/large neighbourhood, PC/nPC indicates whether the pseudo-pixels have to pass the central pixel, HV/DIAG signifies whether the pseudo-pixels are formed by horizontally and vertically connected pixels only or diagonally connected pixels are considered as well. The best results for each type of the filter array are in bold, while results in italic font correspond to the worst ones. The global best results are emphasised in grey.

SFA	Methods	Image								
		1	2	3	4	5	6	7	8	9
3-band	Bilinear	46.06	45.97	33.01	48.80	51.85	51.56	36.16	44.86	*23.87*
	Binary Tree	**46.75**	**48.38**	**33.37**	**50.98**	**52.16**	**55.12**	**37.88**	**46.24**	24.66
	VM	40.64	*41.67*	*28.37*	*44.20*	*46.89*	*45.42*	*31.81*	*40.51*	**32.57**
4-band	Bilinear	**44.48**	45.87	**32.82**	47.51	**50.99**	51.35	35.97	44.50	23.62
	Binary Tree	44.21	**46.03**	32.25	**48.57**	50.47	**53.14**	**36.04**	**44.78**	23.32
	VM(sNB/PC/HV)	38.64	39.52	27.77	40.67	45.41	42.53	28.78	37.72	21.93
	VM(sNB/PC/DIAG)	38.87	39.43	27.78	40.62	45.53	42.62	28.93	37.86	20.93
	VM(lNB/PC/HV)	*37.02*	*37.58*	*25.46*	*39.55*	*43.16*	*41.56*	*28.34*	*36.64*	*20.24*
	VM(lNB/nPC/HV)	39.62	40.79	28.41	42.96	46.63	44.54	31.24	39.96	**39.55**
	VM(lNB/PC/DIAG)	37.27	38.01	25.85	40.14	43.53	41.99	28.50	37.04	20.41
8-band	Bilinear	**40.58**	39.90	27.73	42.81	45.91	44.90	30.12	40.10	21.34
	Binary Tree	40.07	**41.03**	**28.26**	**44.40**	**47.10**	**48.66**	**34.69**	**42.15**	22.21
	VM(sNB/PC/HV)	38.34	38.85	26.96	40.85	45.37	43.29	30.21	38.86	**22.29**
	VM(sNB/nPC/HV)	37.22	37.90	25.98	40.64	43.98	42.46	28.80	37.96	21.57
	VM(sNB/PC/DIAG)	38.09	38.62	26.71	40.86	44.84	42.71	29.01	38.17	21.37
	VM(lNB/PC/HV)	35.38	*35.58*	*24.03*	*37.99*	*41.92*	*40.07*	*26.57*	*35.45*	18.57
	VM(lNB/nPC/HV)	*35.29*	36.36	24.53	39.62	42.59	40.89	27.22	36.83	*16.72*
	VM(lNB/PC/DIAG)	35.93	36.23	24.59	38.91	42.52	40.76	27.26	36.28	18.57

with those in Table 7.2. This indicates the refinement is beneficial to some extent.

Selected pictorial results are demonstrated in Figure 7.7-7.10 for visual assessment. Demonstrated results of vector median was computed within large neighbourhood where passing centre pixel is not a necessity and diagonally connected pixels are not considered for the formation of pseudo-pixels. The images basically correspond to the numerical results shown before, although the influence of the refinement is not visible enough.

7.6 Conclusion

In this chapter, we applied vector median filtering to SFA demosaicking and made use of median filtering in n-sphere for refinement.

As can be seen from the results, vector median filters perform reasonably in ex-

Table 7.3: The performance of the demosaicking algorithms after refinement in terms of the PSNR. sNB/lNB denote small/large neighbourhood, PC/nPC indicates whether the pseudo-pixels have to pass the central pixel, HV/DIAG signifies whether the pseudo-pixels are formed by horizontally and vertically connected pixels only or diagonally connected pixels are considered as well. The best results for each type of the filter array are in bold, while results in italic font correspond to the worst ones. The global best results are emphasised in grey.

SFA	Methods	Image								
		1	2	3	4	5	6	7	8	9
3-band	Bilinear	46.50	45.86	32.13	48.41	**52.65**	52.24	37.64	46.48	*25.23*
	Binary Tree	**46.70**	**47.36**	**32.18**	**49.74**	52.60	**54.45**	**39.37**	**47.49**	25.69
	VM	*41.49*	*41.24*	*28.18*	*41.41*	*45.98*	*44.64*	*31.89*	*41.99*	**28.54**
4-band	Bilinear	**45.00**	**45.75**	**32.28**	47.12	**51.87**	51.81	**37.41**	**45.88**	24.90
	Binary Tree	44.41	45.59	31.62	**47.70**	50.98	**52.82**	37.22	45.68	23.93
	VM(sNB/PC/HV)	40.25	41.22	28.73	42.30	47.34	44.75	30.93	39.97	23.90
	VM(sNB/PC/DIAG)	41.67	41.99	29.18	43.22	48.60	46.61	32.43	41.61	23.01
	VM(lNB/PC/HV)	*37.93*	*38.38*	*25.87*	*40.52*	*44.03*	*43.17*	*30.05*	*38.05*	*21.27*
	VM(lNB/nPC/HV)	40.39	41.43	28.46	43.92	47.49	46.05	32.62	41.47	**39.55**
	VM(lNB/PC/DIAG)	38.09	38.73	26.19	41.13	44.35	43.53	30.18	38.39	21.71
8-band	Bilinear	**41.54**	40.82	**28.58**	43.35	47.18	46.07	31.67	41.53	22.13
	Binary Tree	40.44	**41.30**	28.47	**44.34**	**47.53**	**48.80**	**35.30**	**42.72**	22.58
	VM(sNB/PC/HV)	39.86	40.37	28.17	42.32	47.02	45.11	32.35	40.81	**22.93**
	VM(sNB/nPC/HV)	37.94	38.75	26.52	41.83	44.76	43.72	30.04	39.15	21.61
	VM(sNB/PC/DIAG)	39.35	39.87	27.50	42.45	46.13	45.18	30.96	40.39	21.87
	VM(lNB/PC/HV)	36.13	*36.28*	*24.69*	*38.82*	*42.60*	*41.01*	*27.46*	*36.31*	19.59
	VM(lNB/nPC/HV)	*35.59*	36.75	24.75	40.23	42.93	41.52	27.70	37.43	*16.72*
	VM(lNB/PC/DIAG)	36.66	36.85	25.07	39.70	43.14	41.79	28.16	37.20	19.02

treme conditions as is the case of binary images. Otherwise it does not behave as well as bilinear and binary tree approaches, contrary to expectations. It is somewhat surprising that we failed to reproduce similar results to those shown by the original work [66]. The results also indicate that it is necessary to bear more than one pixel of a certain spectral band occur in the vicinity where pseudo-pixels are formed.

It is of importance that in most cases median filtering in n-sphere reduces to some extent the disparity between original and demosaicked images in terms of the PSNR, and the improvement coincides with visual judgements in that less aliasing appears in refined images. This proves that the advantages of median filtering in angular space still holds in multispectral domain. However, the impact of variable filter window size, remains to be seen.

Another point of particular interest is that none of the demosaicking methods takes advantage of inter-channel correlation directly, whereas this is one of the basic premises of most CFA demosaicking techniques. The correlation should be utilised more efficiently in the demosaicking process, therefore some measures are expected later to be introduced in this regard.

It is clear that the increased number of spectral bands significantly reduces the spatial resolution of the image and the reproduced image quality suffers in consequence, which deserves further consideration. Also the results show that median filtering in n-sphere (n-dimensional spherical space) reduces aliasing numerically for most test images, thus improving resulting image quality. Also the results initially demonstrate the validity of our assumption that certain demosaicking algorithms developed for trichromatic images may be useful for SFA demosaicking purpose. In addition, some image quality metrics specific to SFA demosaicking is reasonably expected.

In conclusion, median filtering itself for demosaicking may not be the best solution, especially when it comes to its computational cost. However a refinement in n-sphere reduces consistently artefacts independently of the demosaicking methods tested.

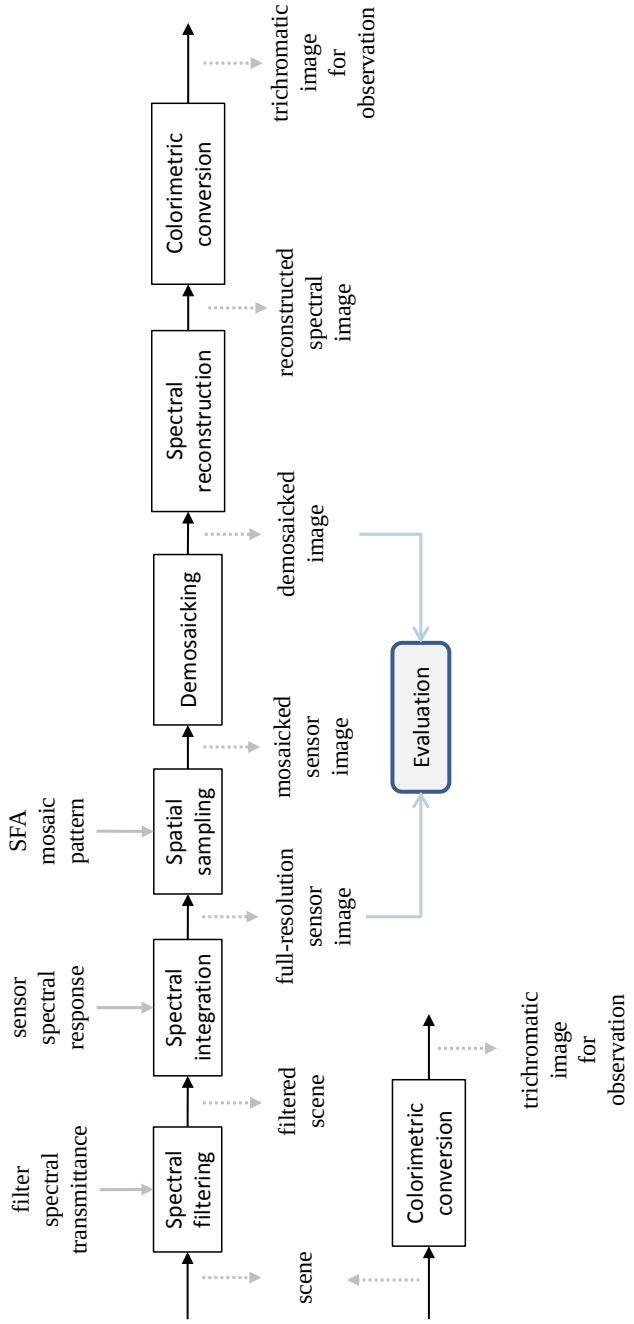

Figure 7.3: Design of the experimental framework.

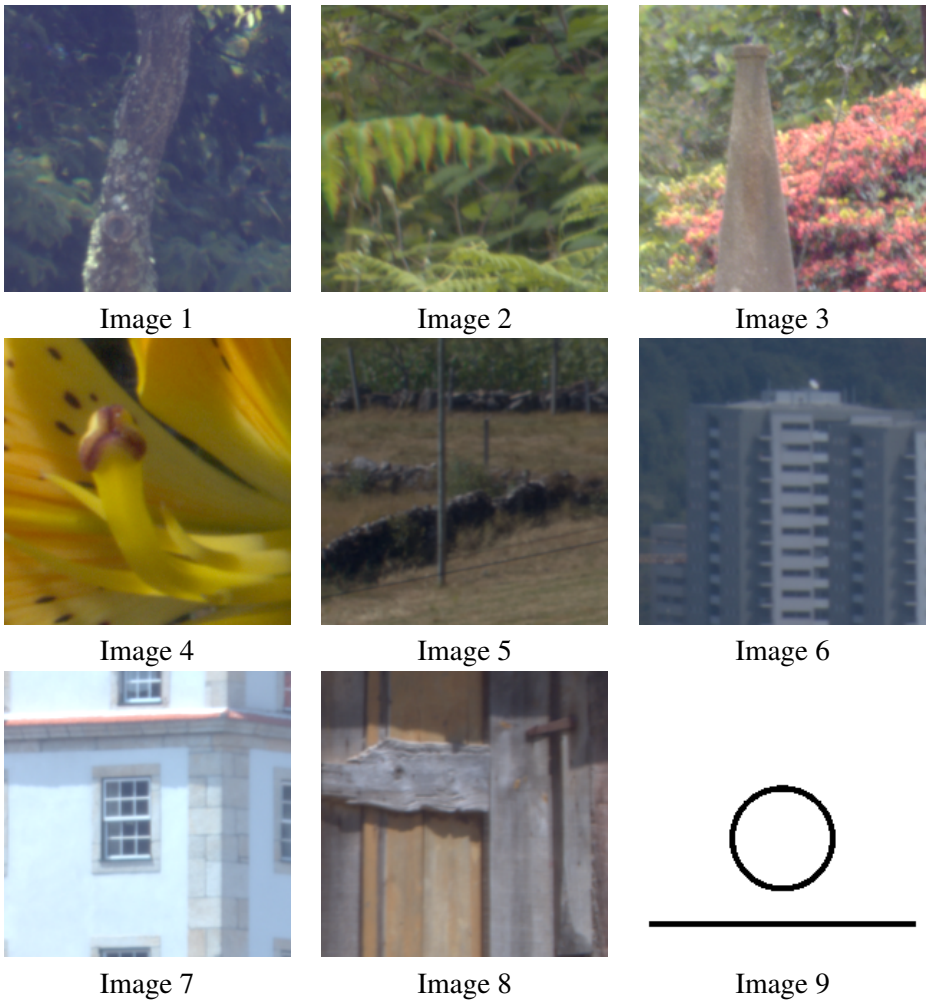

Figure 7.4: Scenes used in the experiments. Copyright ©SPIE

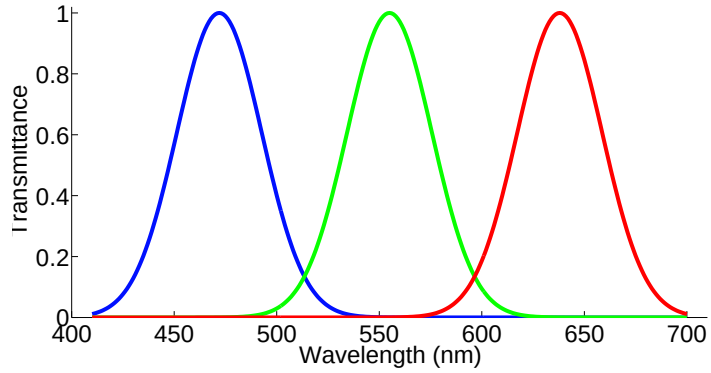

(a) 3-band filter set.

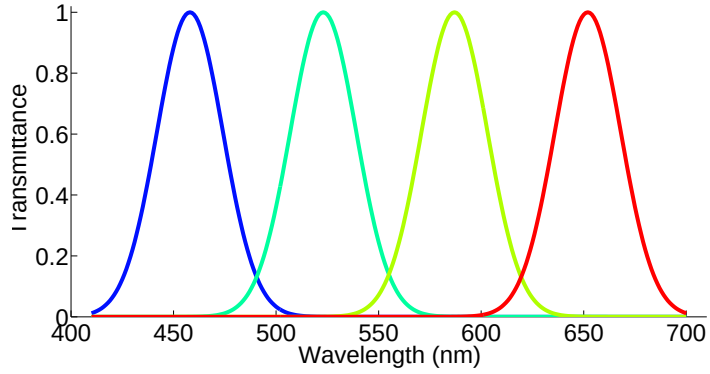

(b) 4-band filter set.

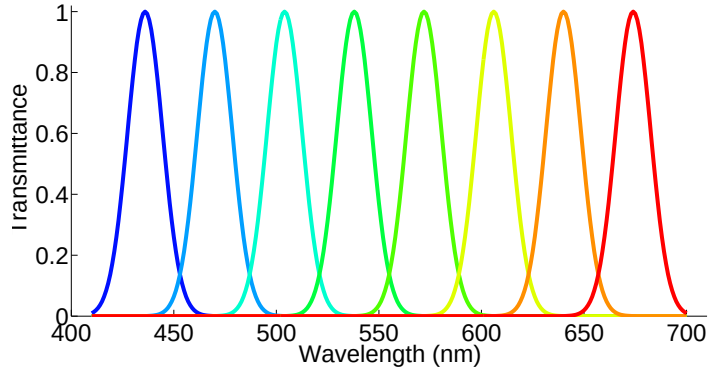

(c) 8-band filter set.

Figure 7.5: Filter design for 3-band, 4-band and 8-band set-up. Copyright ©SPIE

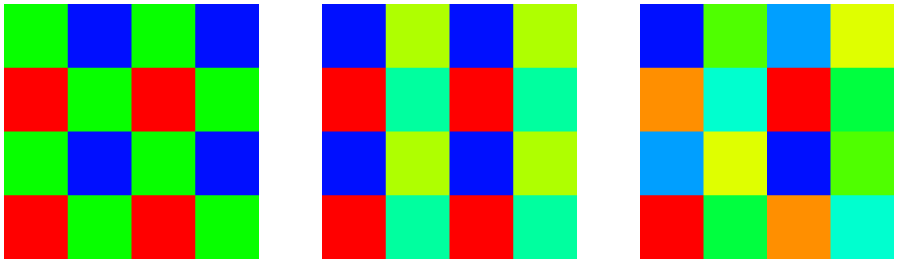

2	1	2	1
3	2	3	2
2	1	2	1
3	2	3	2

1	3	1	3
4	2	4	2
1	3	1	3
4	2	4	2

1	5	2	6
7	3	8	4
2	6	1	5
8	4	7	3

Figure 7.6: SFA design for 3-band, 4-band and 8-band set-up. Copyright ©SPIE

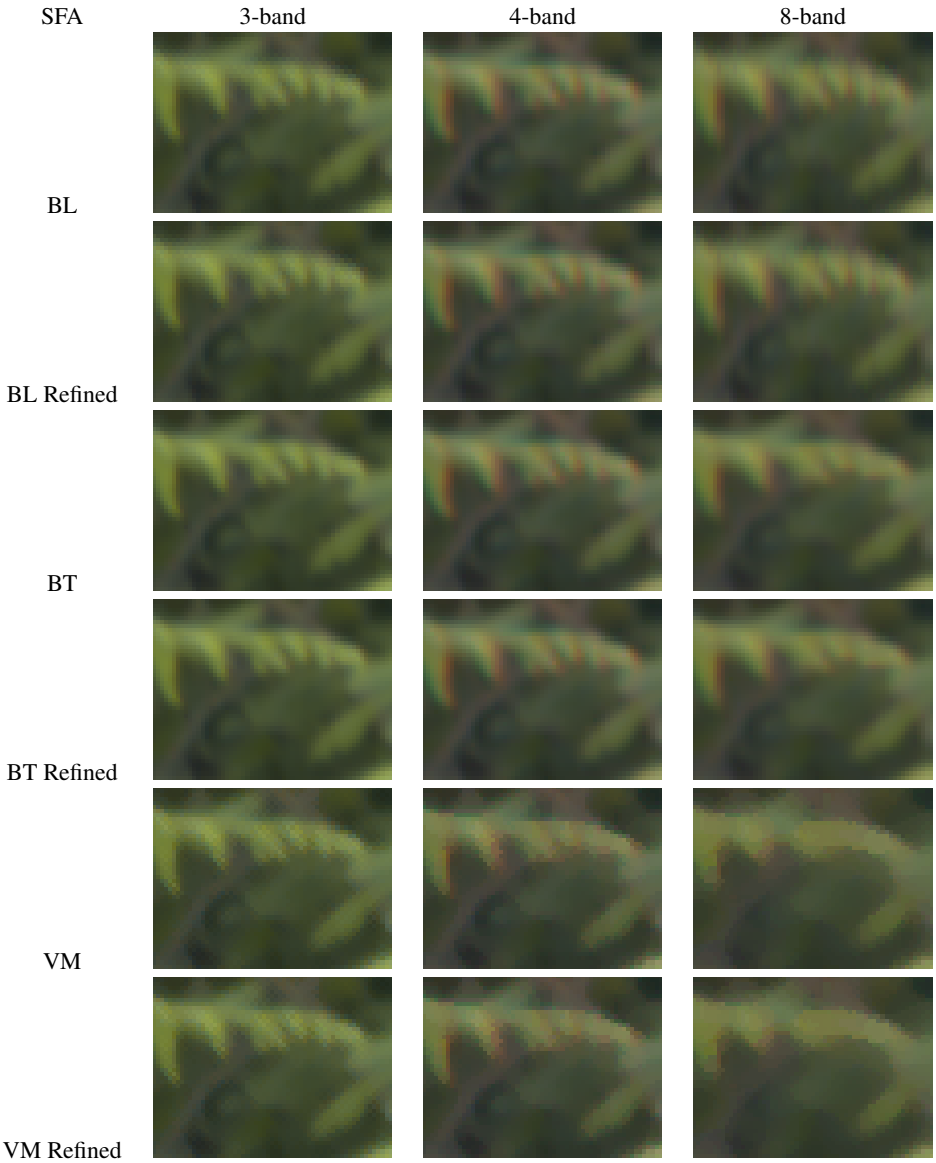

Figure 7.7: An illustration of Scene 2, processed with 3, 4 and 8-band SFAs and multiple demosaicking methods, with and without refinement. Copyright ©SPIE

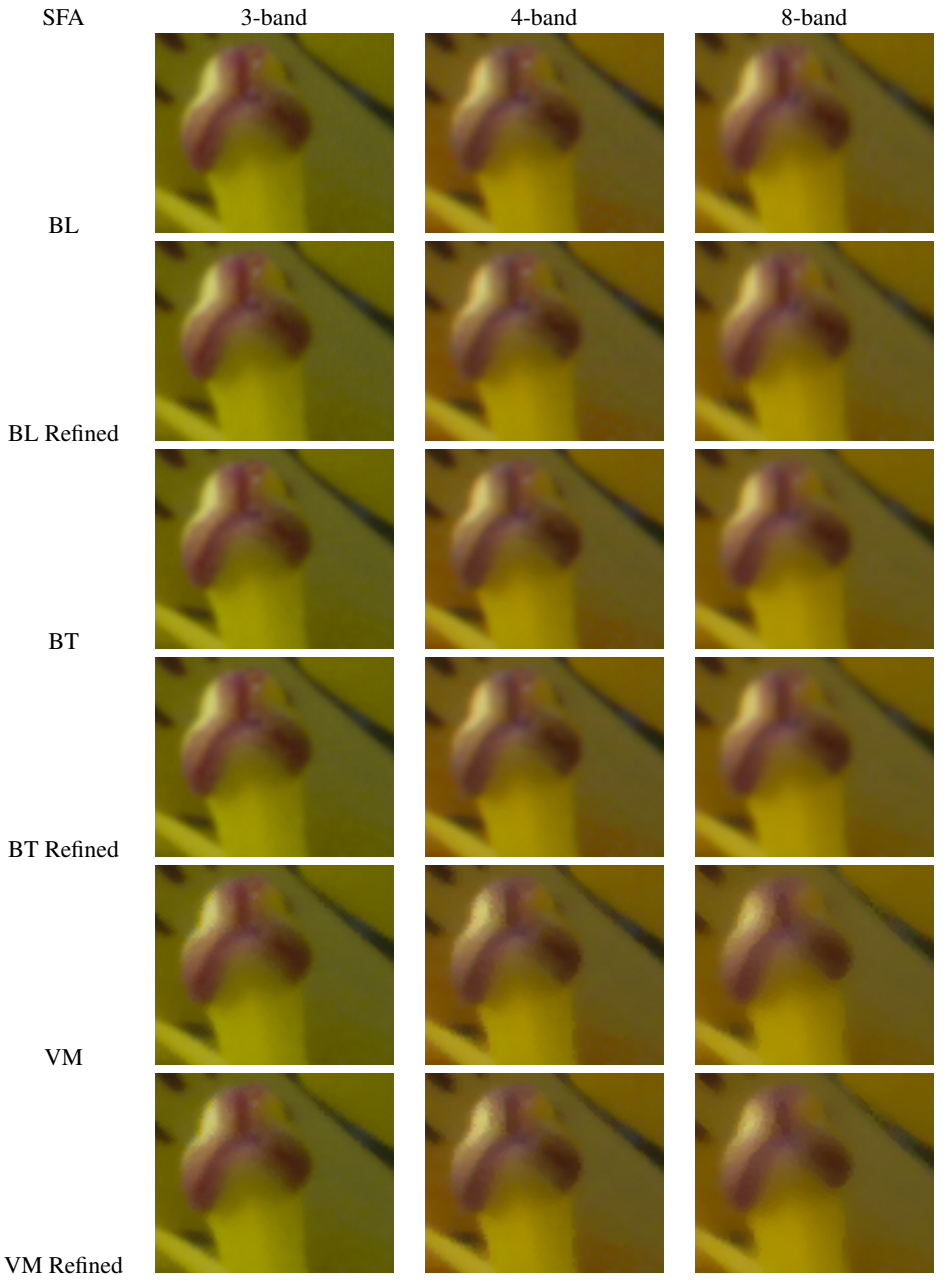

Figure 7.8: An illustration of Scene 4, processed with 3, 4 and 8-band SFAs and multiple demosaicking methods, with and without refinement. Copyright ©SPIE

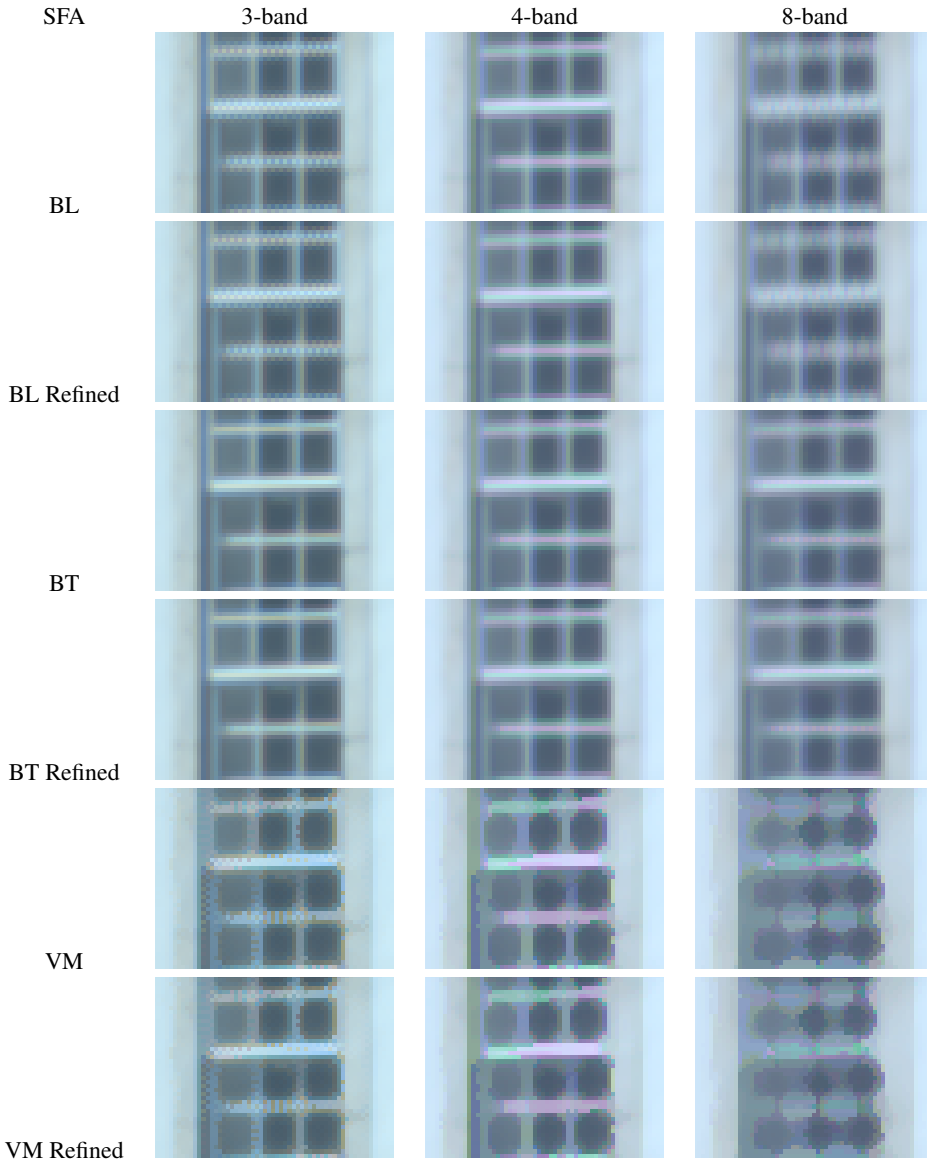

Figure 7.9: An illustration of Scene 7, processed with 3, 4 and 8-band SFAs and multiple demosaicking methods, with and without refinement. Copyright ©SPIE

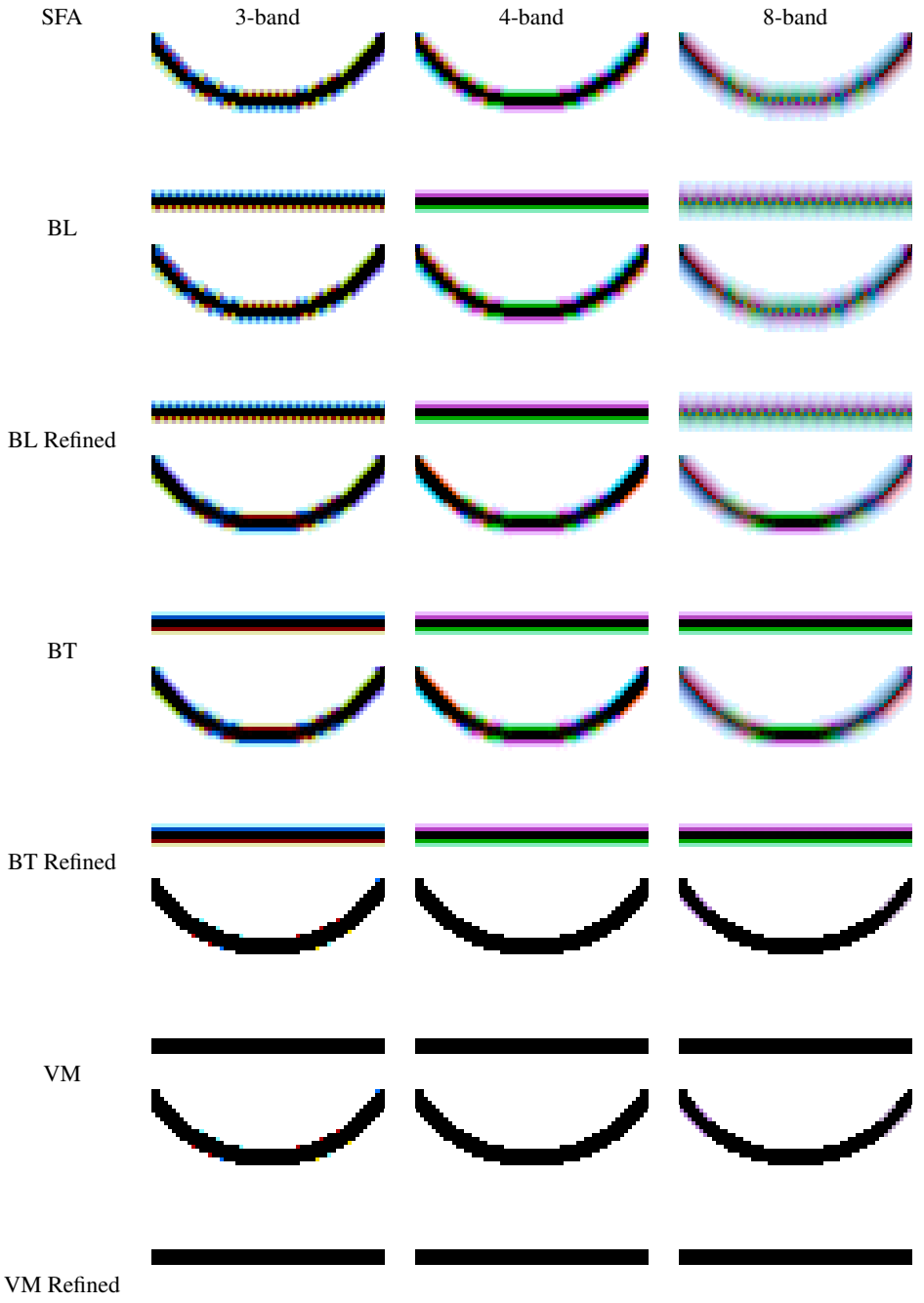

Figure 7.10: An illustration of Scene 9, processed with 3, 4 and 8-band SFAs and multiple demosaicking methods, with and without refinement. Copyright ©SPIE

Chapter 8

SFA demosaicking based on discrete wavelet transform

8.1 Introduction

DWT (Discrete wavelet transform) transforms an image into various frequency bands, and natural images often possess rather similar high-frequency information among these bands. Therefore DWT provides yet another solution to CFA demosaicking. The intrinsic similarity between colour and multispectral images in terms of inter-band correlation makes the utilisation of DWT potentially beneficial to SFA demosaicking.

In this chapter, we present a demosaicking algorithm making use of DWT. It begins by a review of related work in Section 8.2. A description of the proposed method is explained in Section 8.3. An introduction of the experiments is shown in Section 8.4. However, we observe unexpected results in Section 8.5 and subsequently perform brief analyses on the results in Section 8.6.[1]

8.2 CFA demosaicking based on DWT

In recent years, DWT is referred to and taken advantage of by a succession of research work on CFA demosaicking. As known, DWT makes use of subband coding in which an image is decomposed into a set of bandlimited components. A commonly seen four-band decomposition splits an image into four quadrants con-

[1] Content of this chapter is adapted from a published paper [175]. Copyright ©IEEE.

taining an approximation subband, a horizontal detail subband, a diagonal detail subband, and a vertical detail subband, respectively. All subbands, except of the approximation subband, represent high frequency information at a certain scale. It is the subband coding that builds a viable foundations for DWT based demosaicking by taking into account the inter-channel correlation most images bear.

To the best of our knowledge, Gunturk *et al.* [64] first bring the DWT in CFA demosaicking. The algorithm begins by an initial estimation of all channels by means of intra-channel interpolation. It then decomposes the channels with a filter bank into four sub-bands and the high-frequency sub-bands of the red and blue channels are updated according to some criteria. Next, the ground truth red/blue samples are inserted back to the reconstructed channels. The last two steps are repeated until a stopping criterion is satisfied. The initial estimates of the green samples follow the same procedure as red/blue samples do.

Driesen and Scheunders [41] propose a similar approach. However the initial interpolation is performed on the luminance image derived from the original RGB channels, as the interpolated luminance image possess higher spatial resolution than interpolated red, green and blue channels. Then both the luminance image and the original RGB channels are discrete wavelet transformed resulting in wavelet coefficients. Two merging rules are applied singly in order to benefit from the inter-channel correlation. One of them, named “replace” rule, simply replaces at each scale the coefficients of each band of red, green and blue band images with the corresponding coefficients in the luminance image, whereas the other, labelled “max” rule, compares the coefficients of each band with those of the luminance image, and assigns the larger one to each band. The demosaicking is accomplished when the updated wavelet coefficients are inversely transformed.

Chen *et al.* [24] introduce the concept of downsampled (DS) images. First, this method is initiated by an estimation of missing green pixels with edge-directed interpolation and missing red/blue pixels with bilinear interpolation, from which the DS images are then derived and wavelet transformed. Next, the “replace” rule is applied to the high-frequency sub-bands. The last step aims to reduce colour artefacts by median filtering the low-frequency wavelet sub-bands and updating high-frequency sub-bands of Red/Blue images with those of the Green images. A simplified version of such an idea was implemented by Courroux *et al.* [34].

Jeong *et al.* [82] also use the polyphase-like downsampling prior to DWT. The wavelet coefficients of the low frequency sub-bands are then estimated by means of an edge adaptive interpolation method using high frequency wavelet coefficients

as the edge indicators. An estimation of the coefficients of the high frequency sub-bands is performed in accordance with the "replace" rule.

Slightly different from the above approaches, Kim *et al.* [90] perform DWT on observed DS images to obtain the missing high-frequency sub-bands by linear estimation, and estimate the low-frequency sub-bands by wavelet transforming the DS images that have been interpolated beforehand.

Indicated by the aforementioned literature, DWT based demosaicking methods outperform the conventional counterparts relying merely on intra-channel correlation.

8.3 SFA demosaicking based on DWT

As mentioned above, DWT decompose images into a series of sub-bands with different frequency components. The spectral correlation, namely the inter-plane similarities, then comes into play. In theory, the idea is also applicable to multispectral images. Inspired by this, we extend the application of DWT into SFA demosaicking.

The essence of the proposed method may be encapsulated by the concept of DS images, the Haar wavelet (D2), the "replace" rule for the estimation of high-frequency sub-bands and bilinear interpolation for the estimation of low-frequency sub-bands. The workflow is summarised as follows.

1. Estimate high-frequency coefficients.
   (a) Construct DS image using polyphase transform.
   (b) Apply discrete wavelet transform.
   (c) Estimate the coefficients of the missing DS images at high-frequency sub-bands according to the "replace" rule, shown in Figure 8.1.
2. Estimate the low-frequency coefficients.
   (a) Apply bilinear interpolation to the mosaicked image plane by plane.
   (b) Construct DS image using polyphase transform.
   (c) Apply discrete wavelet transform.
   (d) Replace the coefficients of the missing DS images at low-frequency sub-bands with those of the interpolated DS images, shown in Figure 8.2.

3. Recombine the low-frequency and high-frequency components, and apply inverse DWT.

4. Reconstruct the demosaicked image with the DS images.

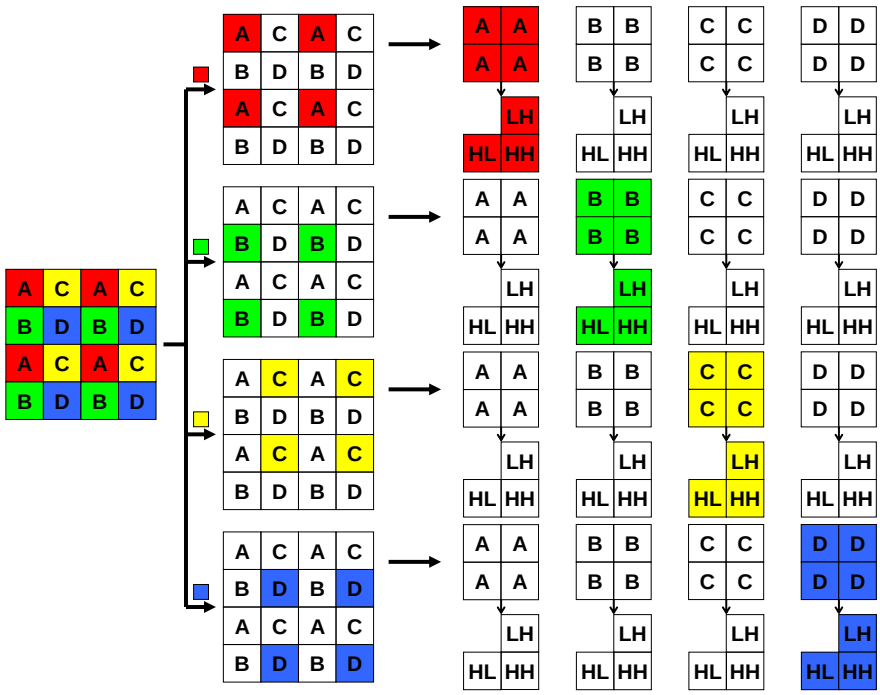

Figure 8.1: Treatment of high-frequency sub-bands. Unknown high-frequency sub-bands (LH/HL/HH) are replaced with those of the known ones for a specific set of pixels corresponding to a type of filter elements.

This method is compatible with any SFAs with regular mosaic patterns regardless of number of channels. For the purpose of evaluation and comparison, we apply this method to a set of RGB images in addition to multispectral images.

8.4 Experiment

In the experiment, we selected 13 images from Foster's database *et al.* [48], and another 32 hyperspectral images from the CAVE project [183]. For the ease of processing and comparison, the spectral range between 410 nm and 700 nm is used

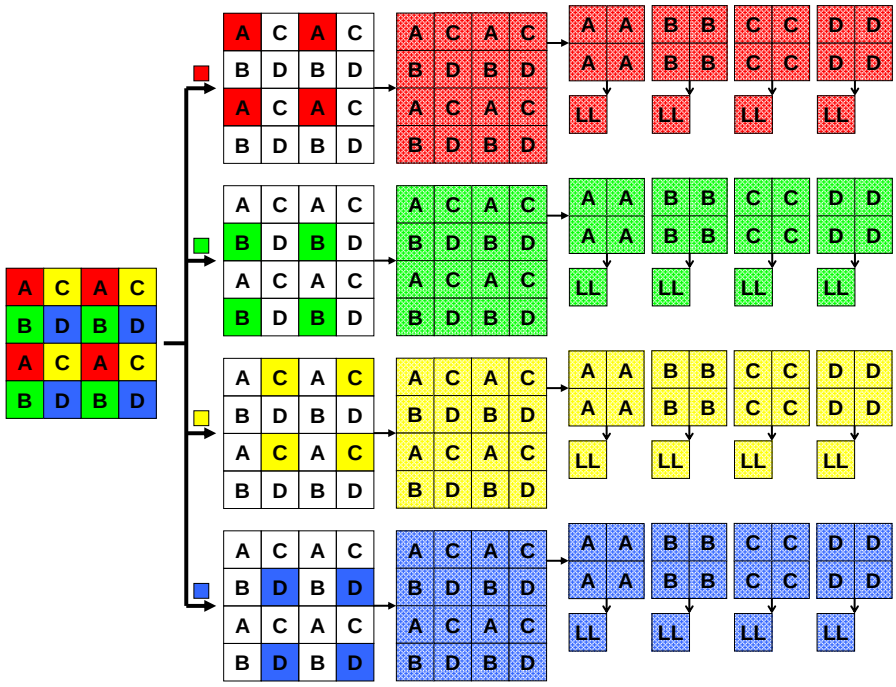

Figure 8.2: Treatment of low-frequency sub-bands. Each band is interpolated individually to obtain the low-frequency sub-bands (LL).

in this study resulting in 45 hyperspectral images of 30 bands. The framework is illustrated in Figure 7.3.

Also employed are 24 Kodak RGB test images [2] for the sake of evaluation of the proposed methods. These images are widely used in the realm of image related research, and are utilised to evaluate the performance of algorithms in the majority of aforementioned papers about DWT based CFA demosaicking.

Hyperspectral scene images were rendered with the illuminant of CIE D65. In each case, spectral transmittances were determined so that each of them had a regular Gaussian shape and the centres of them were evenly distributed over the pertinent spectrum with the distance of $2 \times \sigma$, as shown in Figure 7.5. Three filter array patterns were chosen, Bayer type 3-band setup, 4-band setup in form of 2×2 moxel and 8-band in form of 4×4 moxel, the moxels were repeated across the whole image, as depicted in Figure 7.6. The filter arrays were designed in accordance

Table 8.1: Parameters and setup of the experiments.

Spectral range	410 nm – 700 nm
Spectral interval	10 nm
Illuminant	CIE D65
Spectral responsivity	$S(\lambda) = 1$
Type of images	Reflectance image
Number of images	45 spectral and 24 colour
Type of filters	Gaussian bandpass
Type of mosaics	Bayer CFA, 4-/8-band SFAs
Demosaicking	bilinear, binary-tree, the proposed
Quality metrics	PSNR

with the binary tree approach proposed by Miao *et al.* [123], a perfect binary tree to be exact, with two levels and three levels corresponding to 4-band and 8-band arrangements respectively, as indicated in Figure 7.6. To visualise the images, the original hyperspectral scene images were rendered in the sRGB colour space, and the demosaicked multispectral images were first restored to hyperspectral images with a spectrum reconstruction method exploiting a priori knowledge of the imaged objects [69] and then rendered to sRGB. In contrast, colour images from the Kodak set are coupled only with the 3-band CFA.

Two additional demosaicking algorithms, bilinear interpolation and Miao *et al.*'s binary tree based progressive demosaicking [126], were implemented as reference for the purpose of comparison. Evaluation of the performance was carried out by means of the PSNR computed between the original and reproduced multispectral images, so as to avoid errors introduced by the spectral reconstruction.

8.5 Results

Results for Kodak and hyperspectral images are shown in Figure 8.3 – Figure8.6 respectively. As can be seen, the proposed method outperforms two other algorithms for most Kodak RGB images. Surprisingly and interestingly, the order of performance is almost inverted in case of hyperspectral images regardless of the number of channels.

8.6 Conclusion

Indicated by the results is a seemingly obscure issue. Nevertheless, further analyses of the cross-correlation between high frequency sub-bands of the DS images partly uncover the mystery. As shown by Figure 8.7, Kodak images represented

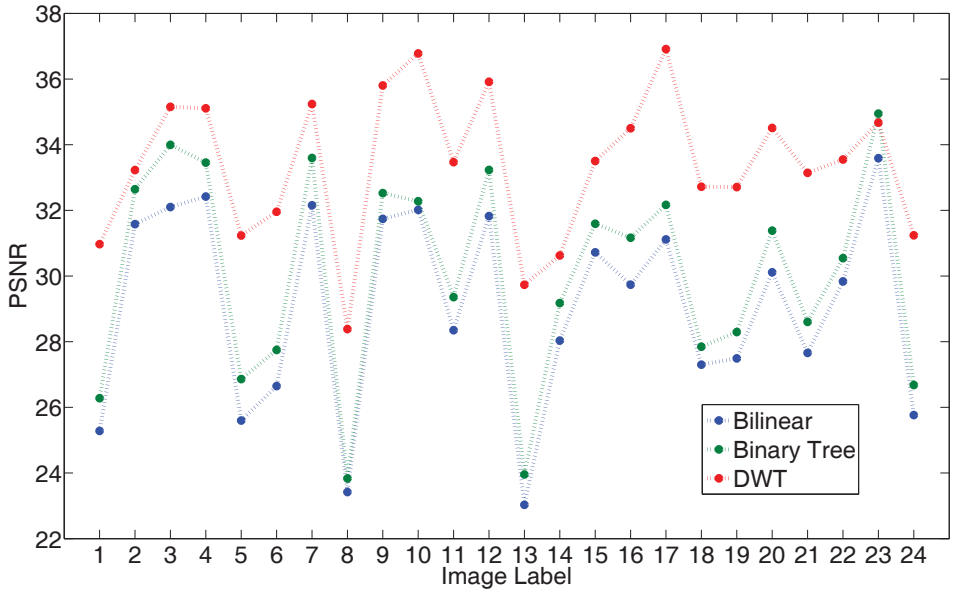

Figure 8.3: Comparison of performance on Kodak images. Copyright ©IEEE.

in yellow circles possess relatively higher correlation than the multispectral images plotted in red/green/blue. Further, PSNR difference between the proposed method and bilinear interpolation bears a somewhat linear relationship with the cross-correlation between the DS images. That is to say, the higher the correlation of the images is, the more we may gain from the proposed DWT demosaicking approach. It is consistent with the basic assumption and principles of the method.

Obviously the spectral correlation of a multispectral image depends not only on the original scene and the illumination, but also on the design of filters present on the CFA/SFA. Tests performed have shown that the correlation increases when degree of overlap between adjacent filters increases. In addition, Kodak images were originally acquired by film cameras and scanned, whereas the hyperspectral images employed in our study were captured by digital cameras and filtered with idealised Gaussian-shaped filters. The discrepancy between the two systems might influence the correlation in a way.

Also notable is the fact that most of the images from the Foster set appear blurred to some extent in comparison with the CAVE set and Kodak images. This might be pertinent to chromatic aberration or vibration in the course of acquisition, and this also influences the spectral correlation. To verify the hypothesis, we blurred Kodak

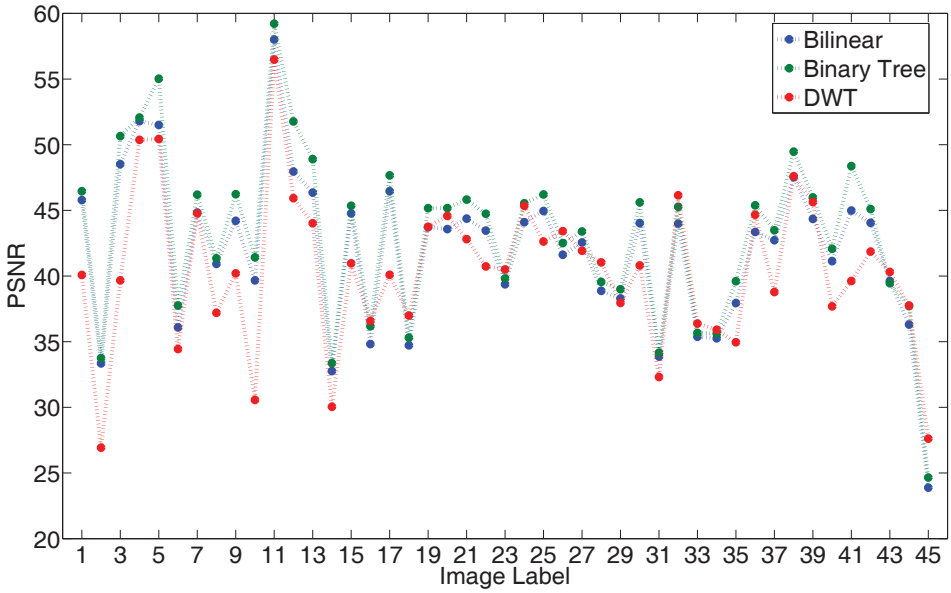

Figure 8.4: Comparison of performance on 3-band multispectral images. Copyright ©IEEE.

images by means of the convolution of each plane of an image and a Gaussian kernel and applied the same algorithms as in the previous experiment. Figure 8.8 illustrates the case when the kernel measures 5×5 pixels with σ of 3. Clearly the DWT based algorithm turns the worst in contrast to the other two, contrary to the situation shown in Figure 8.3, which again illustrates the dependence of DWT demosaicking on the intrinsic properties of images.

Experiments and analyses indicate that the spectral cross-correlation plays an important role in determining the performance of the proposed algorithm. In other words, the "replace" rule depends largely on the assumption that the images are highly correlated, which explains the unexpected results.

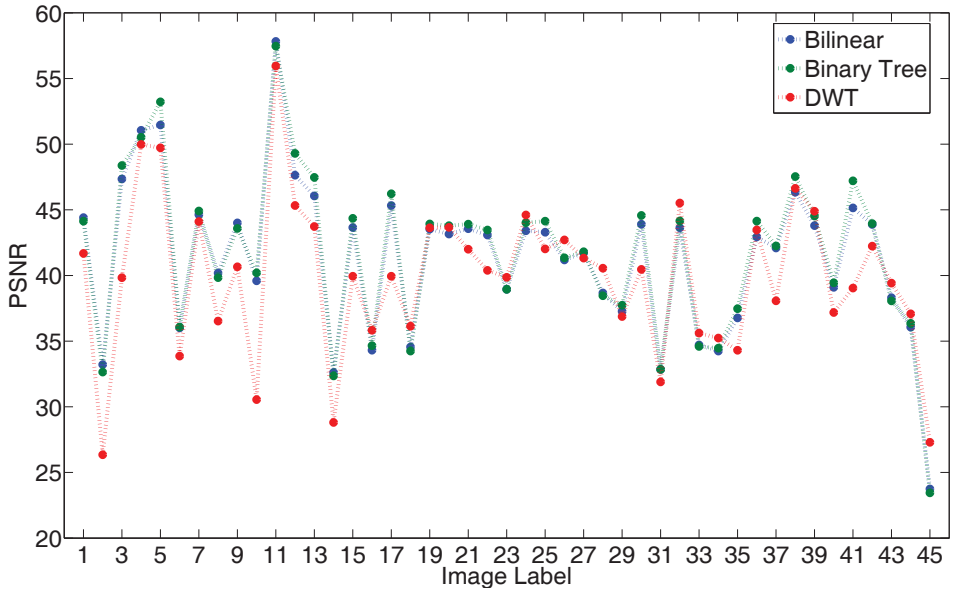

Figure 8.5: Comparison of performance on 4-band multispectral images. Copyright ©IEEE.

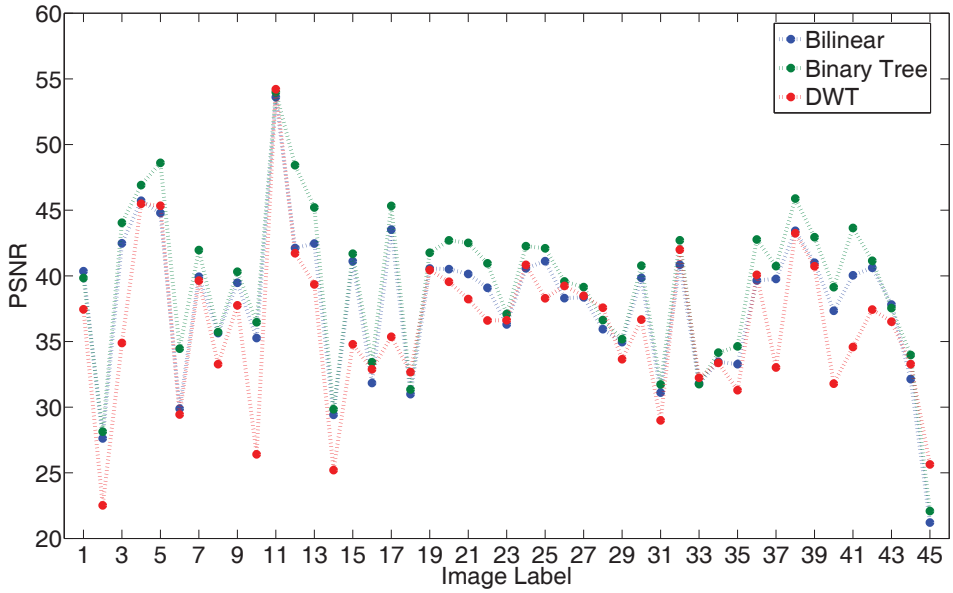

Figure 8.6: Comparison of performance on 8-band multispectral images. Copyright ©IEEE.

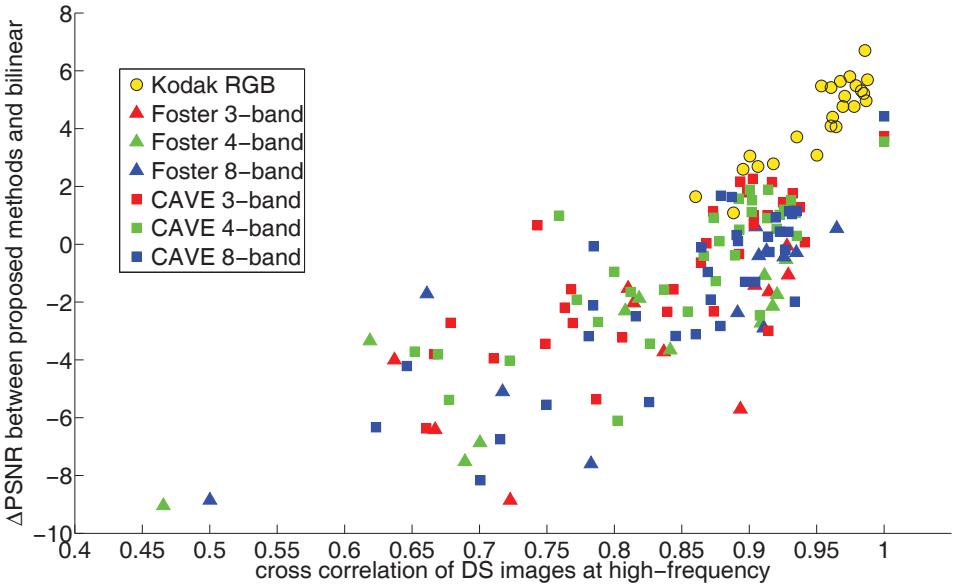

Figure 8.7: Difference of PSNR between proposed method and bilinear interpolation versus cross correlation of high-frequency sub-bands of the DS images. Copyright ©IEEE.

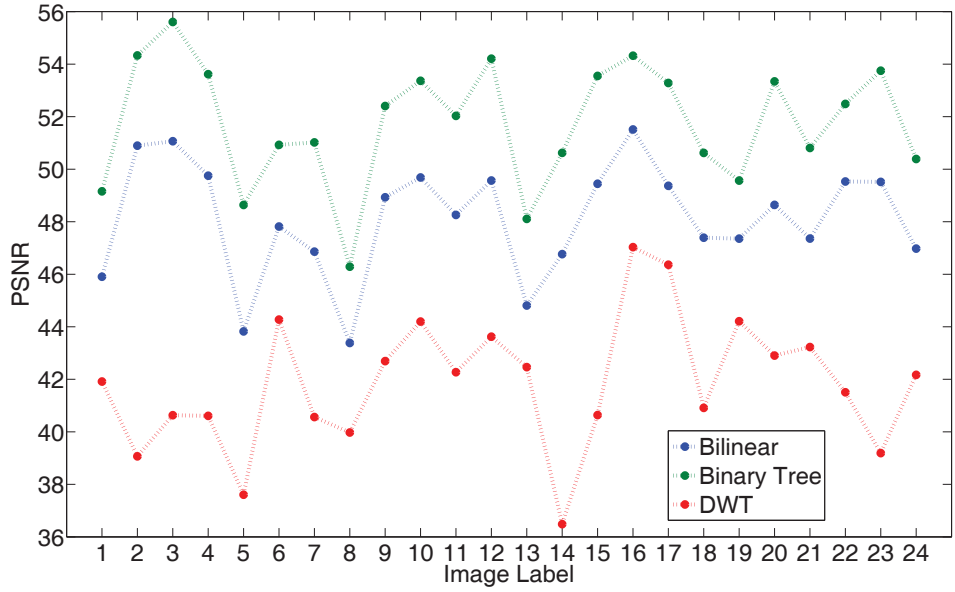

Figure 8.8: Comparison of performance on blurred Kodak images. Copyright ©IEEE.

Chapter 9

SFA demosaicking based on linear minimum mean square error estimation

9.1 Introduction

When considered as an inverse problem in the mathematical point of view, demosaicking could be solved by statistical approaches with the help of a-priori information. Among others, the Wiener estimation is a linear method that minimises the mean square error, resulting in minimum mean square error. Therefore it is known as an LMMSE (linear minimum mean square error) estimator widely used for addressing image reconstruction problems. The linear nature of the Wiener estimation makes it computationally efficient and easy to implement. In the literature, it has been considered as a suitable solution to CFA demosaicking [163, 166, 23]. Moreover, it is flexible and adaptive to filter arrays with varying classes of filters and varied arrangements, thus being naturally a candidate for SFA demosaicking.

As a result, in this chapter, we introduce the Wiener estimation to SFA demosaicking. Section 9.2 presents the method in detail. Experimental setup and results are shown in Section 9.3 and Section 9.4 respectively. Section 9.5 compares the results yielded by the extended method with other algorithms.[1]

[1] Content of this chapter is adapted from a published paper [170]. Copyright ©Springer.

9.2 SFA demosaicking based on LMMSE estimation

Trussell and Hartwig [166] and Taubman [163] develop stacked notation that permits the use of matrix manipulation in formulating the mosaicking and demosaicking models. Chaix de Lavarène *et al.* simplify and further refine the model to ease the computation [23], which we adopt in this chapter for SFA demosaicking.

$$X = P_r Y \tag{9.1}$$

In Equation 9.1, Y is a spectral image representing a scene to capture, X is the mosaic image, and P_r denotes a projection matrix that transforms the scene into the mosaic image. As can be seen, this model corresponds to the mosaicking process. A stacked version of Equation 9.1 for a 4-band SFA is illustrated in Figure 9.1 where X and Y are organised on the basis of windows (Moxels here).

$$\tilde{Y} = QX \tag{9.2}$$

Accordingly the reconstruction process can be expressed in Equation 9.2. The aim of demosaicking is to evaluate $\tilde{Y}$, an estimation of Y, which requires Q. Figure 9.1 indicates, however, that Q cannot simply be the inverse of P_r, as P_r is not invertible.

$$e = E[\|Y - \tilde{Y}\|^2] \tag{9.3}$$

The Wiener estimation is a common solution to Equation 9.3, which functions to find Q that minimises the mean square error between $\tilde{Y}$ and Y:

$$Q = (E[YX^T])(E[XX^T])^{-}1 \tag{9.4}$$

Therefore, a priori information is required for the evaluation of Q. In practice, this is carried out by means of training. A full resolution image and the corresponding mosaic image, when expressed in stack form, may be used as Y and X respectively. The resultant Q can then be used for the reconstruction from other mosaic images.

$$\begin{bmatrix} A_1 \\ \vdots \\ A_4 \\ B_1 \\ \vdots \\ B_4 \\ C_1 \\ \vdots \\ C_4 \\ D_1 \\ \vdots \\ D_4 \end{bmatrix} = \begin{bmatrix} Q^1_{A_1} & \cdots & Q^4_{A_1} \\ \vdots & \ddots & \vdots \\ Q^1_{A_4} & \cdots & Q^4_{A_4} \\ Q^1_{B_1} & \cdots & Q^4_{B_1} \\ \vdots & \ddots & \vdots \\ Q^1_{B_4} & \cdots & Q^4_{B_4} \\ Q^1_{C_1} & \cdots & Q^4_{C_1} \\ \vdots & \ddots & \vdots \\ Q^1_{C_4} & \cdots & Q^4_{C_4} \\ Q^1_{D_1} & \cdots & Q^4_{D_1} \\ \vdots & \ddots & \vdots \\ Q^1_{D_4} & \cdots & Q^4_{D_4} \end{bmatrix} \begin{bmatrix} A_1 \\ B_2 \\ C_3 \\ D_4 \end{bmatrix} \tag{9.5}$$

In the image formation model illustrated in Figure 9.1, Y is a 4-band spectral image and X is its corresponding mosaic image resulting from a 4-band SFA. Similarly Equation 9.5 demonstrates a stacked version of Equation 9.2. The horizontal dimension of Q is equivalent to the vertical dimension of X. That is, each column of X corresponds to a window (or a superpixel) in the mosaic image, and each element in the column contributes to demosaicking through the corresponding weights stored in the rows of Q. In the aforementioned example, the size of the window is chosen to be the same as that of the Moxel. However, a larger window might provide more useful information for demosaicking at the cost of higher computational cost. Q depends not only on the arrangement of filter arrays, but also on the a priori information, i.e., sample images for training.

9.3 Experiment

With the help of the simulation framework, the experiment was designed with most parameters remaining the same with Chapter 7 and 8. 8 reflectance images, grouped by genre into four types, were selected from the Foster and CAVE image database, and each group consists of 2 images. All of the images are lit by the CIE D65 illuminant to obtain the radiance. Three filter arrays of 3, 4 and 8 bands and the corresponding band-pass filters used in Chapter 7 are reused in this experiment, as illustrated in Figure 7.6 and 7.5. To simplify the computation, responsivity of the sensor is assumed to be 1 over the spectrum. Parameters are also listed in Table 9.2 in detail.

Table 9.1: Images used in the experiments.

Label	Genre	Dataset and designation
Image 1	Landscape	Scene 5 from the Foster 2004 set
Image 2		Scene 4 from the Foster 2002 set
Image 3	Buildings	Scene 6 from the Foster 2004 set
Image 4		Scene 8 from the Foster 2002 set
Image 5	Objects	"Beads" from the CAVE set
Image 6		"Pompom" from the CAVE set
Image 7	Paintings	"Oil painting" from the CAVE set
Image 8		"Water colors" from the CAVE set

Table 9.2: Parameters and setup of the experiments.

Spectral range	410 nm – 700 nm
Spectral interval	10 nm
Illuminant	CIE D65
Spectral responsivity	$S(\lambda) = 1$
Type of images	Reflectance image
Number of images	8
Type of filters	Gaussian bandpass
Type of mosaics	3-/4-/8-band SFAs
Demosaicking	bilinear, binary-tree, LMMSE
Quality metrics	PSNR, SSIM

Considering the requirement for training, we opted to follow the "leave-one-out" method. Every mosaic image is demosaicked with the aid of Q trained with the remaining spectral images. Apart from the LMMSE approach, bilinear interpolation and binary tree based demosaicking [126] were also experimented with for the purpose of comparison. Performance of the demosaicking methods were evaluated with two metrics, PSNR and SSIM index. The former measures physical distortion of the signal, whereas the latter reflects perceptual similarity between the original and reconstructed images. Both of them were evaluated on a band-by-band basis, and the averages were then computed.

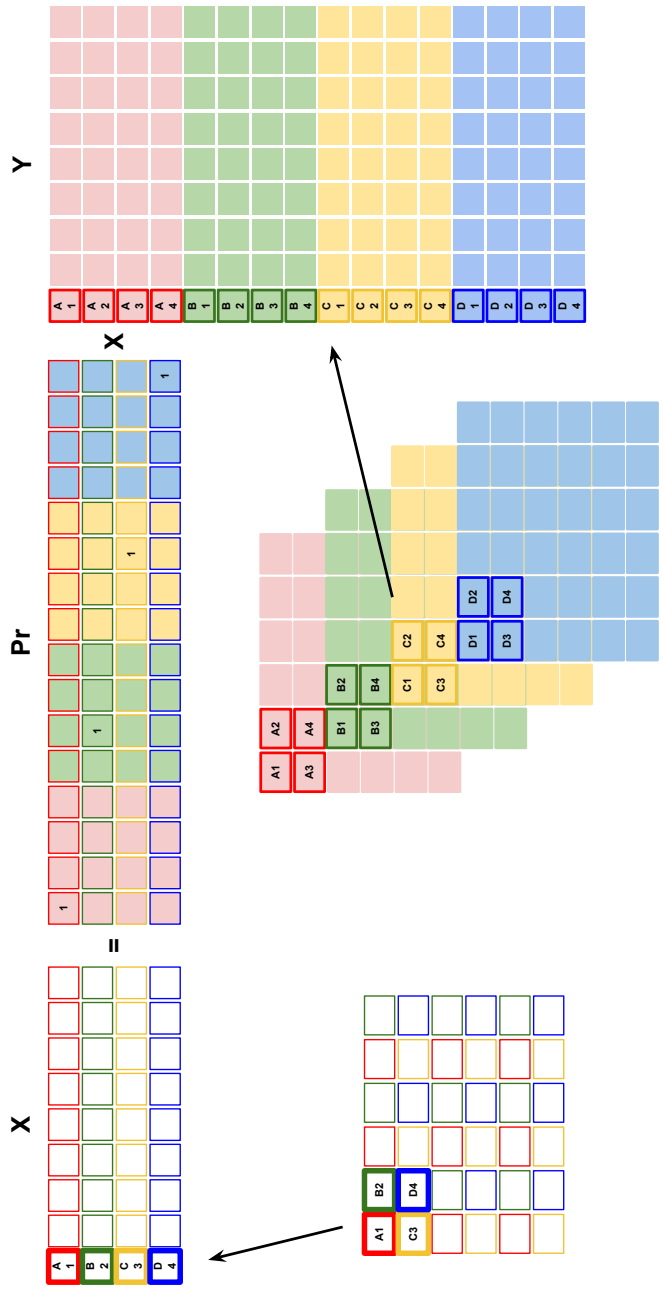

Figure 9.1: 4-band image formation model. Both of the spectral image and mosaic image are divided into windows that are stacked to form Y and X.

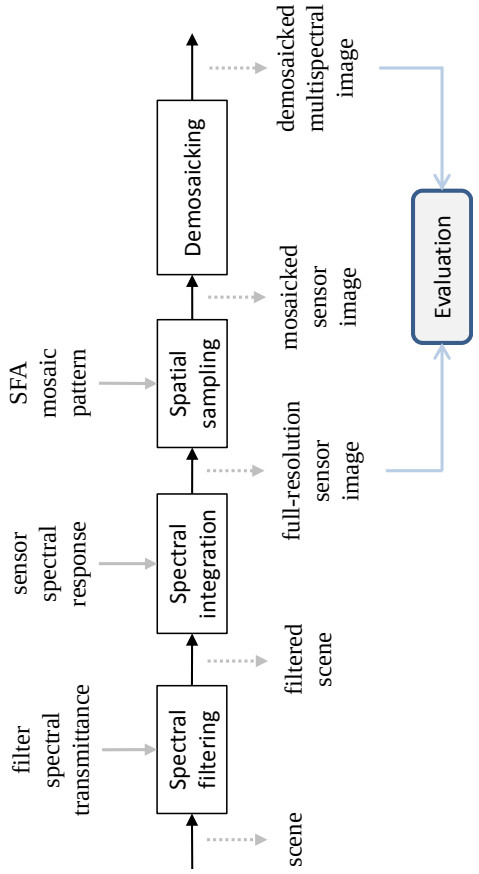

Figure 9.2: Design of the evaluation framework.

9.4 Results

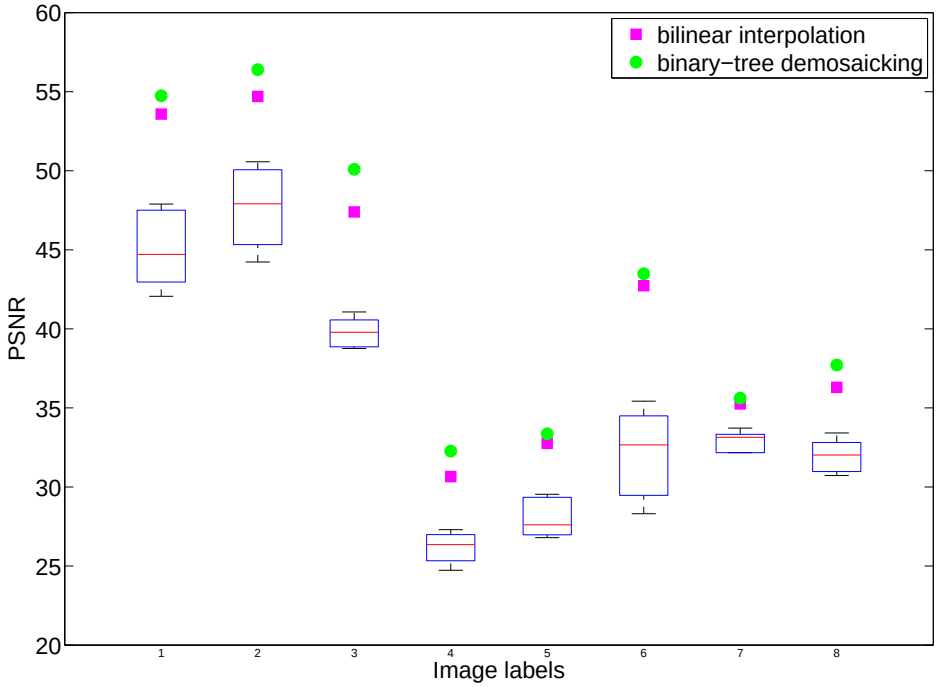

Figure 9.3: PSNR for the 3-band filter array.

Since the "leave-one-out" method yields multiple results for each image demosaicked with the LMMSE estimation, they are depicted graphically in the form of box plot. On each box, the central line in red is median, and the upper and lower edges of the box represent the first and the third quartiles. The whiskers extended from the edges indicate the extreme values not considered as outliers. In comparison, results for the other two demosaicking methods are plotted in magenta squares and green circles respectively.

Figure 9.3-9.5 show the results in terms of PSNR. It can be seen from Figure 9.3-9.4 that the LMMSE estimation results in lower PSNRs than bilinear interpolation and the binary-tree demosaicking method for the 3-band and 4-band filter arrays. In Figure 9.8, however, the LMMSE estimation achieves higher median while the performance of the other two approaches decrease. Moreover, for most images, markers indicating the results of the other two methods fall in the box or between the whiskers, which means the LMMSE estimation may outperform the others two

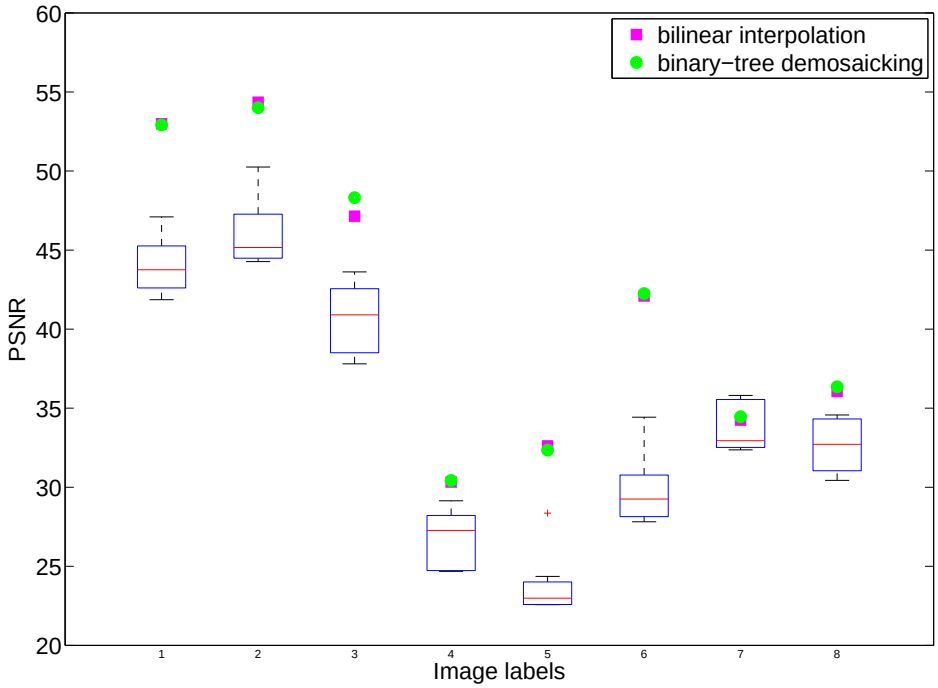

Figure 9.4: PSNR for the 4-band filter array.

for the 8-band SFA given proper a priori information. Figure 9.6-9.8 demonstrate the SSIM indices. Similarly the LMMSE estimation results in comparative or even higher median than the other two for most images in the 8-band configuration, whereas the situation reverses for the 3-band and 4-band setup.

In general, higher number of bands in a filter array lowers spatial resolution and intra-channel correlation, however it improves the spectral resolution and inter-channel correlation. Therefore the performance of bilinear interpolation and the binary-tree demosaicking which utilise the intra-channel correlation deceases with an increasing number of bands. In comparison, the LMMSE estimation involves all pixels in a neighbourhood, thus making use of both spatial and spectral correlation. This is consistent with what is shown in the figures, and it also reveals the advantages of larger neighbourhood for the LMMSE estimation.

In addition, it is interesting that there exist significant variations in the results for each image and among the images. For bilinear interpolation and the binary-tree demosaicking, the variations depend merely on the content of images. For in-

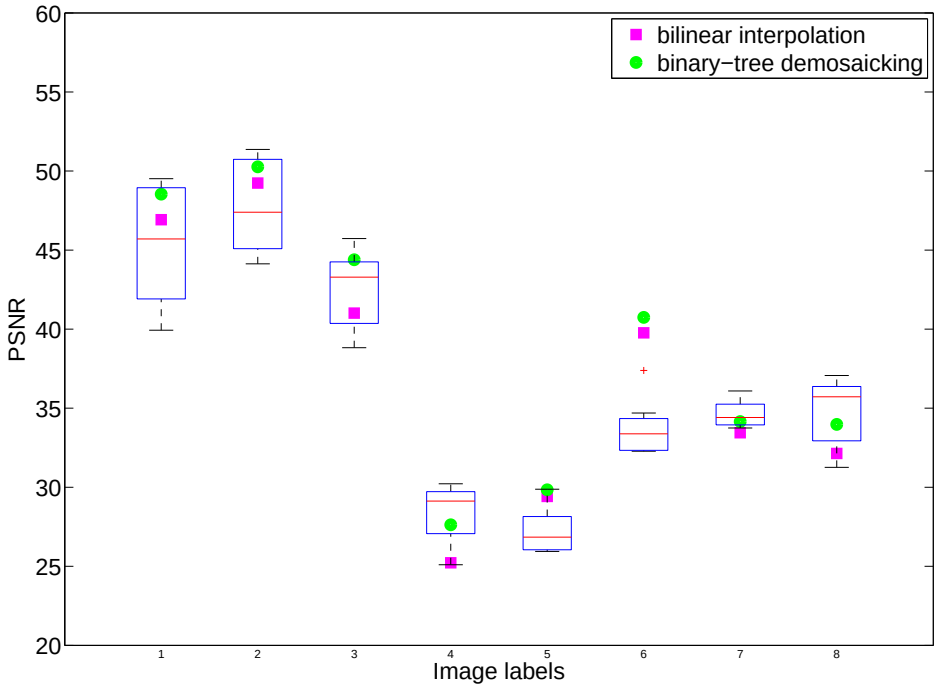

Figure 9.5: PSNR for the 8-band filter array.

stance, Image 4 and 5 lead to low PSNRs in Figure 9.3-9.5, as they contain rich details of wide diversity that are difficult to interpolate and such images are prone to aliasing introduced by demosaicking. For the LMMSE estimation, the variations are also connected with the a priori information, namely, the choice of training images.

Table 9.3: The influence of training images on LMMSE demosaicking for 8-band SFA in terms of PSNR.

Image Label	Training Image							
	1	2	3	4	5	6	7	8
1 (Landscape 1)	N/A	**49.5183**	49.0595	45.9704	*39.9311*	48.8319	43.8885	45.4407
2 (Landscape 2)	**51.3684**	N/A	50.6855	47.5380	*44.1280*	50.7898	46.0461	47.2577
3 (Building 1)	44.0602	42.5580	N/A	44.0200	*38.8260*	**45.7301**	41.9009	44.4460
4 (Building 2)	29.0364	29.4063	**30.2170**	N/A	*25.0997*	29.0961	29.1599	30.0424
5 (Sphere 1)	27.1688	26.5177	29.0460	26.1538	N/A	**29.8779**	*25.9420*	27.2510
6 (Sphere 2)	34.6974	33.9937	**37.3883**	32.3890	32.8568	N/A	*32.2820*	33.9077
7 (Painting 1)	34.3033	34.1420	35.2789	35.2349	*33.7477*	34.5180	N/A	**36.0892**
8 (Painting 2)	35.4156	34.6189	**37.0699**	36.4686	*31.2568*	36.2725	36.0317	N/A

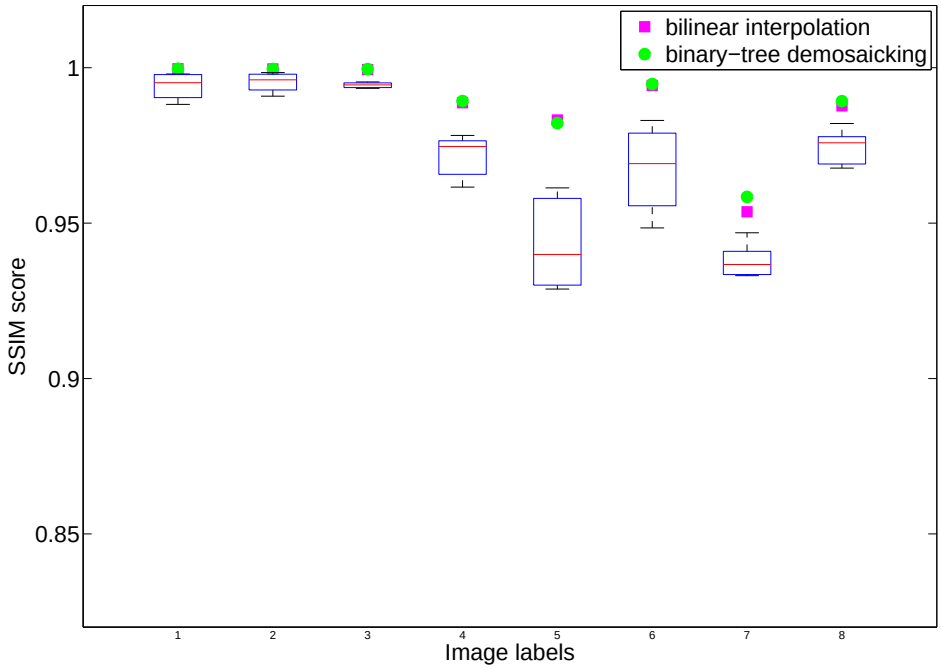

Figure 9.6: SSIM scores for the 3-band filter array.

Table 9.4: The influence of training images on LMMSE demosaicking for 8-band SFA in terms of SSIM index.

Image Label	Training Image							
	1	2	3	4	5	6	7	8
1 (Landscape 1)	N/A	**0.9986**	0.9984	0.9958	*0.9885*	0.9985	0.9945	0.9958
2 (Landscape 2)	**0.9986**	N/A	0.9983	0.9963	*0.9926*	0.9983	0.9948	0.9963
3 (Building 1)	0.9983	0.9978	N/A	0.9982	*0.9958*	**0.9987**	0.9969	0.9982
4 (Building 2)	0.9711	0.9744	0.9748	N/A	*0.9578*	0.9692	0.9723	**0.9752**
5 (Sphere 1)	0.8981	*0.8902*	0.9298	0.8992	N/A	**0.9427**	0.9063	0.9110
6 (Sphere 2)	0.9367	0.9322	**0.9658**	0.9375	*0.9317*	N/A	0.9551	0.9516
7 (Painting 1)	*0.9379*	0.9420	0.9507	0.9569	0.9394	0.9394	N/A	**0.9617**
8 (Painting 2)	0.9812	0.9774	0.9853	**0.9866**	*0.9669*	0.9829	0.9846	N/A

Table 9.3 and 9.4 reveals the influence of training images on LMMSE estimation based demosaicking performance. Each row in the tables represents the results for one image to demosaick, and each column corresponds to one training image. The best and worst results in each row are emphasised in bold and italic fonts respectively. In Table 9.3, 5 out of 8 images are demosaicked the best with the training

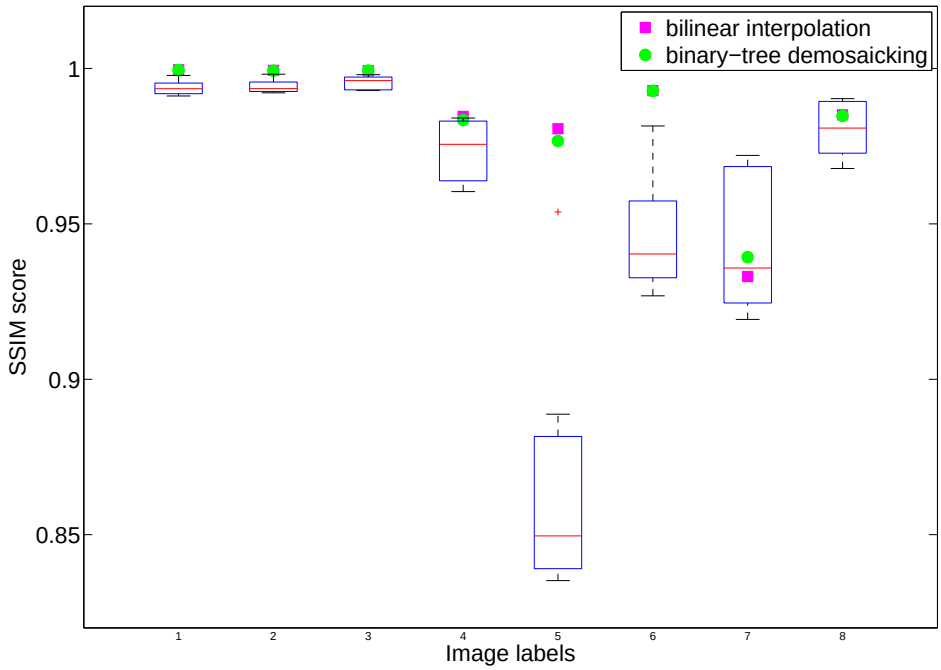

Figure 9.7: SSIM scores for the 4-band filter array.

image of the same genre. In Table 9.4, training images in the same group generally tend to give rise to high SSIM scores. There are some exceptions, though. For instance, the highest SSIM score for Image 8 (painting 2) is achieved with Image 4 (building 2) and vice versa. Similarly, the combination of Image 6 (sphere 2) and Image 3 (building 1) achieve the highest SSIM scores and vice versa. A closer look into the images reveals that these image pairs share similar structural or colour information although they might not belong to the same group.

9.5 Conclusion

In this chapter, we extend the use of the Wiener estimation, yet another adaptive demosaicking method, into the realm of filter array based spectral imaging. Experiments were designed in a similar way to those in the previous chapters in order to ensure the consistency.

The results disclose the benefit to make use of this approach with higher number of bands. In certain cases, this method outperforms bilinear interpolation and the binary-tree based demosaicking. Its performance is largely influenced by the size

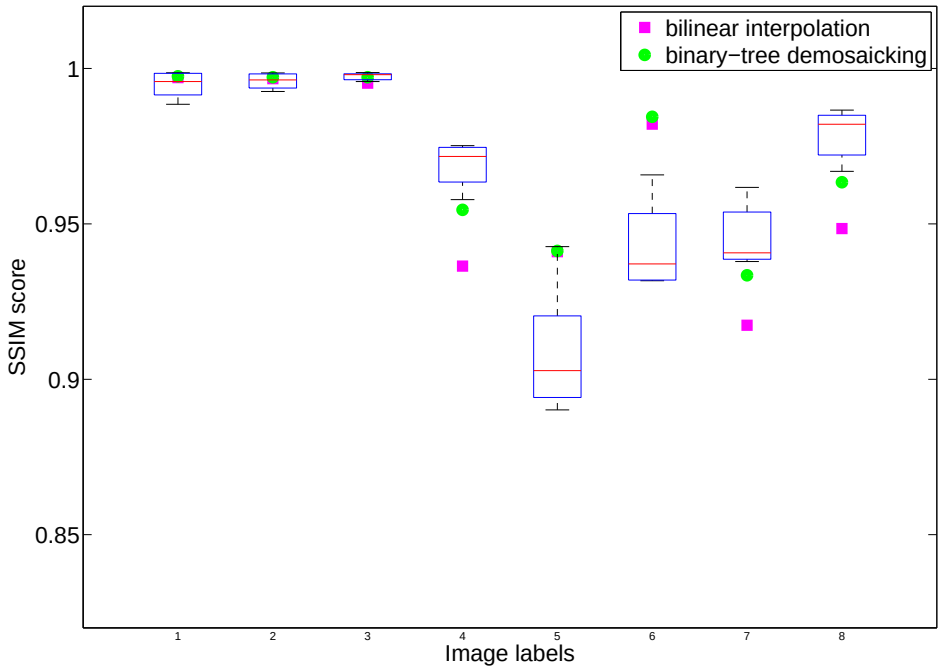

Figure 9.8: SSIM scores for the 8-band filter array.

of the window (neighbourhood) and the similarity shared between the images to demosaick and the training images. The need for a prior information is considered by some as one major drawback, however, it reduces the complexity of demosaicking and is compatible with any mosaic pattern given proper training beforehand.

When it comes to the computational efficiency, the LMMSE estimation is based purely on linear computation. In the experiments, it costs merely a fraction of time spent by other two methods.

In conclusion, we believe the LMMSE estimation is a good candidate for SFA demosaicking in particular for application-specific imaging tasks. The choice of training images and window size merit further development to make better use of this technique.

Part IV

Evaluation of SFA-based imaging

Chapter 10

Colorimetric performance of SFA imaging system

10.1 Introduction

In comparison with CFAs, SFAs often populate higher number of channels, thus reducing the number of pixels assigned to a certain channel for a given sensor. Obviously this lowers spatial resolution, however SFA may offer higher spectral resolution. While the former effect generally lowers the colorimetric performance of the system, the latter should improve the accuracy of colour reproduction. It is therefore of particular interest to evaluate the colorimetric performance of such SFA imaging systems and investigate the trade-off between spatial resolution and spectral resolution by comparing CFA and SFA systems utilising various filter characteristics and demosaicking methods.

The following parts of the chapter are organised as follows. Section 10.2 introduces the experimental platform and the parameters. Section 10.3 show the results, which leads to the conclusions drawn in Section 10.4.[1]

10.2 Experiment

Figure 10.1 depicts the imaging pipeline. In contrast to the experimental setup in previous chapters, colorimetry features in this framework and evaluation is carried out on colour images. Components in the pipeline are detailed in this section.

[1]Content of this chapter is adapted from a published paper [173]. Copyright ©Springer.

Among the derivatives of Bayer mosaic, some possess complementary colour filters in comparison to the primary colour filters utilised in the original patent [13]. Literature presents distinct results. It is obvious that complementary colour filters intrinsically bear wider pass-band than their primary counterparts, and it is widely accepted that the former gives rise to better colour reproduction and signal-to-noise ratio in sufficient lighting conditions, whereas the latter offers higher sensitivity as well as resolution [143, 142]. In Chapter 5, nevertheless, we show that appropriate pass-bands outperform some narrower ones. In addition, Section 8 on SFA demosaicking poses the question of filter design in relation to the inter-band correlation.

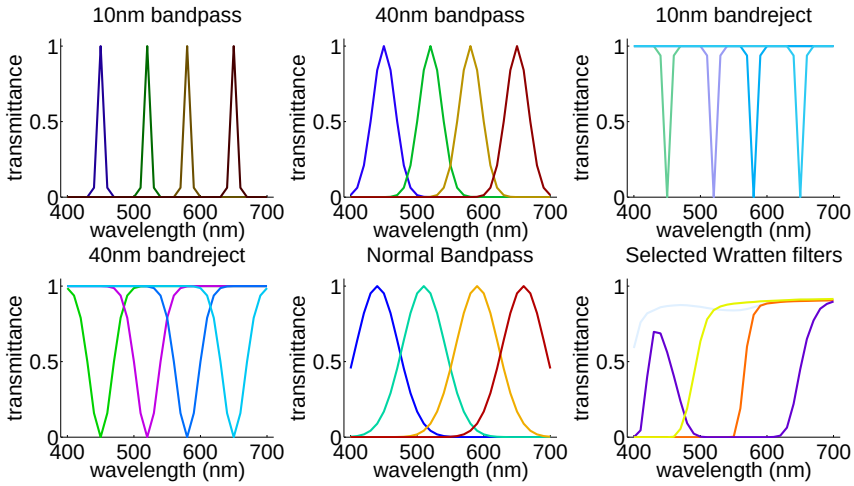

Figure 10.2: Spectral characteristics of a 4-band filter set. Copyright ©Springer.

An instance of 4-band filter set used in this research is depicted in Figure 10.2. Following the aforementioned findings, we are interested in narrowband and broadband bandpass filters as well as corresponding inverted ones such as bandstop filters. The FWHM (Full Width at Half Maximum) of passband and stopband have been set to 10 nm and 40 nm respectively. In practice, a passband of 10 nm simulates very narrow bandpass filters like LCTF (Liquid Crystal Tunable Filter), a stopband of 10 nm mimics notch filters relying on destructive interference. Similarly, a passband and a stopband of 40 nm resemble the spectral transmittances of thin-film filters.

In addition to the filters mentioned above, we introduced two more types. One is based on the principle that the transmittances of filters should sample the spectrum

evenly with their FWHM. The other is produced by a filter selection method [69] that chooses a given number of optimal (or suboptimal) filters from a set of physically practicable candidates, on the assumption that high spectral performance is yielded by the "brightest" filter that transmits the most light combined with other filters which are orthogonal to each other in a vector space. Here we employed a set of transmittance data measured from Wratten filters produced by Kodak, as shown in Figure 10.3.

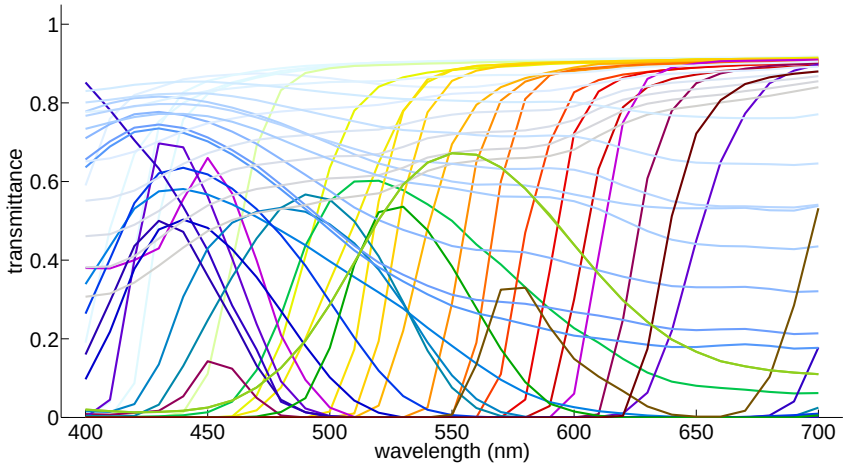

Figure 10.3: Transmittances of a set of Wratten filters. Copyright ©Springer.

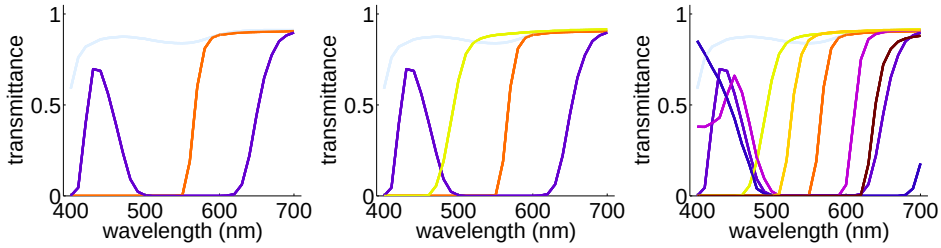

Figure 10.4: Transmittances of three sets of Wratten filters chosen for the 3-band, 4-band and 8-band SFAs by the filter selection algorithm [69].

Filter arrays experimented with in this project were designed with the help of a generic binary tree based generation method of SFA spatial arrangement starting

from a chequerboard pattern introduced by Miao *et al.* [123]. By manipulating the pattern through a combination of decomposition and subsampling steps, the method presented may generate SFAs that satisfy varied design requirements proposed by the authors including probability of appearance, spectral consistency and uniform distribution. It is shown, through case studies, that most of the CFAs currently used by the industry can be derived as special cases.

Three demosaicking algorithm were employed in the experiment, i.e., intra-channel bilinear interpolation, smooth-hue transition interpolation (see Section 3.5.2) and discrete wavelet transform (DWT) based demosaicking (see Section 8.3).

Similar to spectra reconstruction, colour reconstruction is an inverse problem aimed at an estimation of the tristimulus values of the stimuli from the corresponding measurements obtained from sensors. In this experiment, we employed the method of linear least squares explained in Section 5.2.

Colorimetric performance of CFA and SFA based imaging systems can be evaluated by means of colour difference formula. CIEDE2000 is the latest colour difference formula developed and recommended by the CIE [28]. It further improves perceptual uniformity in comparison with the CIE94 formula by introducing a few revised compensation terms for lightness, chroma and hue respectively. In addition, there are three corresponding parameters that are usually set to 1:1:1 and can be adjusted according to specific applications, as shown in Equation 10.1. For instance, CIE recommended 2:1:1 for textile industry. In this work, we used 2:2:1 to evaluate image colour difference.

$$\Delta E^*_{00} = \sqrt{(\frac{\Delta L'}{k_L S_L})^2 + (\frac{\Delta C'}{k_C S_C})^2 + (\frac{\Delta H'}{k_H S_H})^2 + R_T \frac{\Delta C'}{k_C S_C} \frac{\Delta H'}{k_H S_H}} \qquad (10.1)$$

In addition, considering that the targets are digital images rather than uniform colour patches, a metric incorporating some low-level HVS features, such as S-CIELAB, might be suitable as well and may provide more information. The S-CIELAB metric extends the CIELAB Delta E metric to colour images by adding a spatial pre-processing step to the standard CIE $\Delta E_{a^*b^*}$ metric to account for the spatial-colour sensitivity of the human eye [189]. It measures how accurate the reproduction of a colour is to the original when viewed by a human observer. In the preprocessing, the image data is transformed into an opponent-colour space. Each opponent-colour image is convolved with a kernel whose shape is determined by the visual spatial sensitivity to that colour dimension. Then the filtered

representation is transformed to a CIE XYZ representation, and this representation is transformed using the CIE $L^*a^*b^*$ formulae. The resulting S-CIELAB representation includes both the spatial filtering and the CIELAB processing. Parameters in the S-CIELAB formula were set to reflect the experimental conditions, e.g., the viewing distance was set to 60 cm and the resolution was set to 95.78 dpi, so as to mimic a 23-inch LCD monitor of 1920×1080 pixels and an aspect ratio of 16:9.

The experiments were conducted in such conditions as follows. Spectral range covers the spectrum between 400 nm and 700 nm with 10 nm interval. CIE D65 was used as the illuminant. Among the 48 hyperspectral images used as virtual scenes, 16 are from Foster database [48] and 32 are from CAVE database [183]. Three types of SFA were considered, namely 3-band CFA, 4-band and 8-band, as seen in Figure 7.6. For the least-square regression, 170 spectral reflectances of natural objects [168] and the corresponding CIE XYZ tristimulus values were utilised as the training targets. Tristimulus values were calculated with colour-matching functions for the CIE 1931 standard colorimetric observer [27].

Table 10.1: Parameters and setup of the experiments.

Spectral range	400 nm – 700 nm
Spectral interval	10 nm
Illuminant	CIE D65
Type of images	Reflectance image
Number of images	48
Type of filters	Gaussian bandpass/bandreject & Wratten
Type of mosaics	Bayer CFA, 4-/8-band SFAs
Demosaicking	bilinear, smooth hue, DWT
Colour reconstruction	least squared
Quality metrics	CIEDE2000, S-CIELAB

10.3 Results

Results are presented in Figure 10.5 and 10.6. The highest and lowest results for each combination of number of band and demosaicking technique are emphasised in **bold** and *italic* fonts respectively. It is of great moment to realise that the colour difference shown here reflect the overall performance of the system consisting of filter characteristics, spatial arrangements, demosaicking methods as well as colour estimation techniques. However, a comparative analysis of the results reveal some clues.

From the results we can observe that increased number of bands in general offer lower or comparable colour difference especially when paired with 10 nm and 40

Table 10.2: Experimental results in terms of CIE DE2000 and S-CIELAB colour difference formulae. The highest and lowest results for each combination of number of band and demosaicking technique are emphasised in **bold** and *italic* fonts respectively.

		CIEDE2000 colour difference			S-CIEL*a*b* colour difference		
Demosaicking	Filter Type	3-band	4-band	8-band	3-band	4-band	8-band
Intra-band bilinear interpolation	10 nm bandpass	3.1144	2.4467	2.2065	4.1305	3.0673	2.1484
	40 nm bandpass	**2.7186**	**2.0183**	**1.9569**	**3.3927**	**1.9547**	**1.4420**
	10 nm bandreject	*13.2315*	*12.9965*	*14.0255*	*10.5164*	*14.8141*	*19.2470*
	40 nm bandreject	6.0888	5.9170	7.0161	5.0866	4.6263	6.9980
	normal bandpass	3.1257	4.5054	1.9785	4.6252	7.2437	1.6989
	selected wratten	5.4936	4.9674	5.0412	8.0401	5.4206	3.1208
Inter-band difference bilinear interpolation	10 nm bandpass	3.2230	2.5239	2.2574	4.1694	3.0725	2.1086
	40 nm bandpass	**2.8079**	**2.0541**	**1.9849**	**3.4259**	**1.9565**	**1.3500**
	10 nm bandreject	*12.6060*	*12.9006*	*13.1182*	*11.8015*	*17.6517*	*21.7559*
	40 nm bandreject	5.8238	5.9354	6.4077	5.1469	5.2912	7.5383
	normal bandpass	3.0884	4.4671	1.9890	4.5747	7.2073	1.5749
	selected wratten	7.1457	5.9275	5.7762	9.1898	6.3239	4.5734
Wavelet demosaicking	10 nm bandpass	3.3142	2.6207	2.8593	4.2254	3.1866	2.8348
	40 nm bandpass	**2.9421**	**2.2110**	**2.6320**	**3.5001**	**2.0812**	**2.2040**
	10 nm bandreject	*9.6220*	*9.4756*	*10.7873*	*9.0688*	*11.4131*	*12.5745*
	40 nm bandreject	4.5303	4.2931	5.3824	4.9461	4.3156	5.3712
	normal bandpass	3.3172	4.6585	2.6515	4.6595	7.2143	2.4322
	selected wratten	7.1310	4.2547	5.1924	9.0337	5.9222	4.9088

nm bandpass filters and a selected range of Wratten filters. In particular, the 40 nm bandpass filters result in the lowest colour difference among all of the methods and configurations, whereas the 10 nm bandstop filters yield larger errors.

In general, the DWT based demosaicking outperforms the other two where the widths of passband are significantly broader, whereas bilinear interpolation carried out on smooth-hue transition interpolation does not perform satisfactorily. This is also related to insufficient high-frequency components in the image databases mentioned in Chapter 8, as inter-channel demosaicking should benefit from inter-channel correlation at high frequencies and broader passband may boost this correlation.

In most cases S-CIELAB results coincide with CIE DE2000 ones, although the former tends to exaggerate the discrepancy of the results between the CFA and the SFAs.

10.4 Conclusion

In this chapter, the colorimetric performance of a SFA imaging system was evaluated, in terms of the CIEDE2000 and S-CIELAB colour difference. Results of both metrics coincide in most cases. In general, the 4-band SFA provides better or comparable performance in comparison with the 3-band setup except the case of 10 nm bandreject and normal bandpass filters. Similarly the 8-band SFA delivers higher colour accuracy expect the case of 10 nm and 40 nm bandreject filters. Therefore SFA is generaly helpful for an application where colorimetric reproduction is required.

Moreover, it is obvious to see that spectral characteristics of a filter set not only make a direct impact on the colour reconstruction, but also influence the spectral correlation of the observed image on which some demosaicking methods depend.

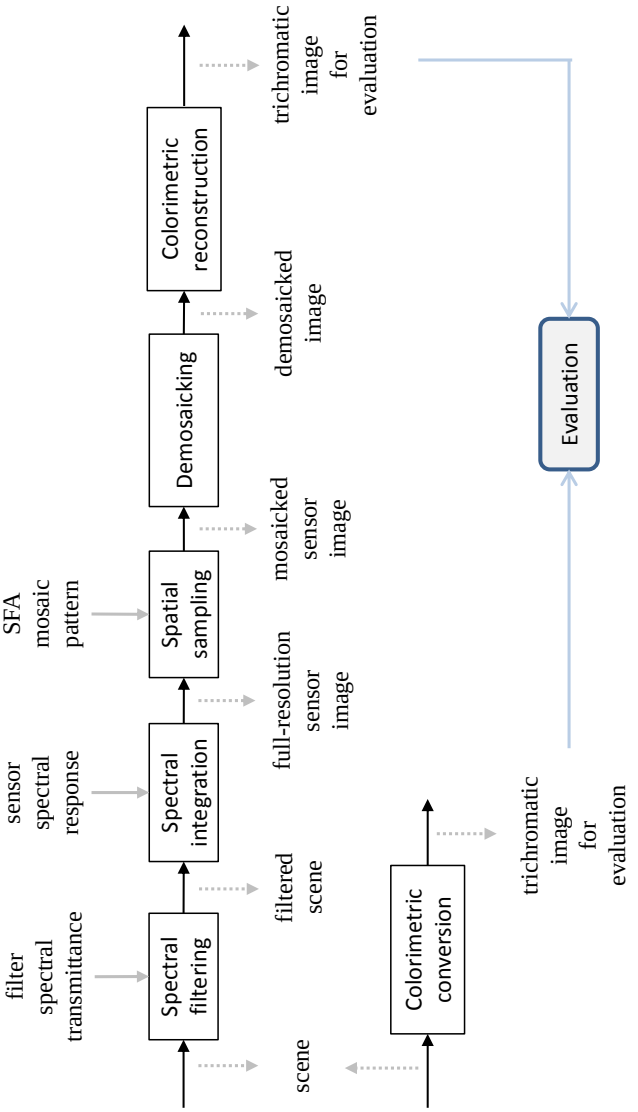

Figure 10.1: The imaging pipeline for the evaluation of colorimetric performance of SFA imaging system.

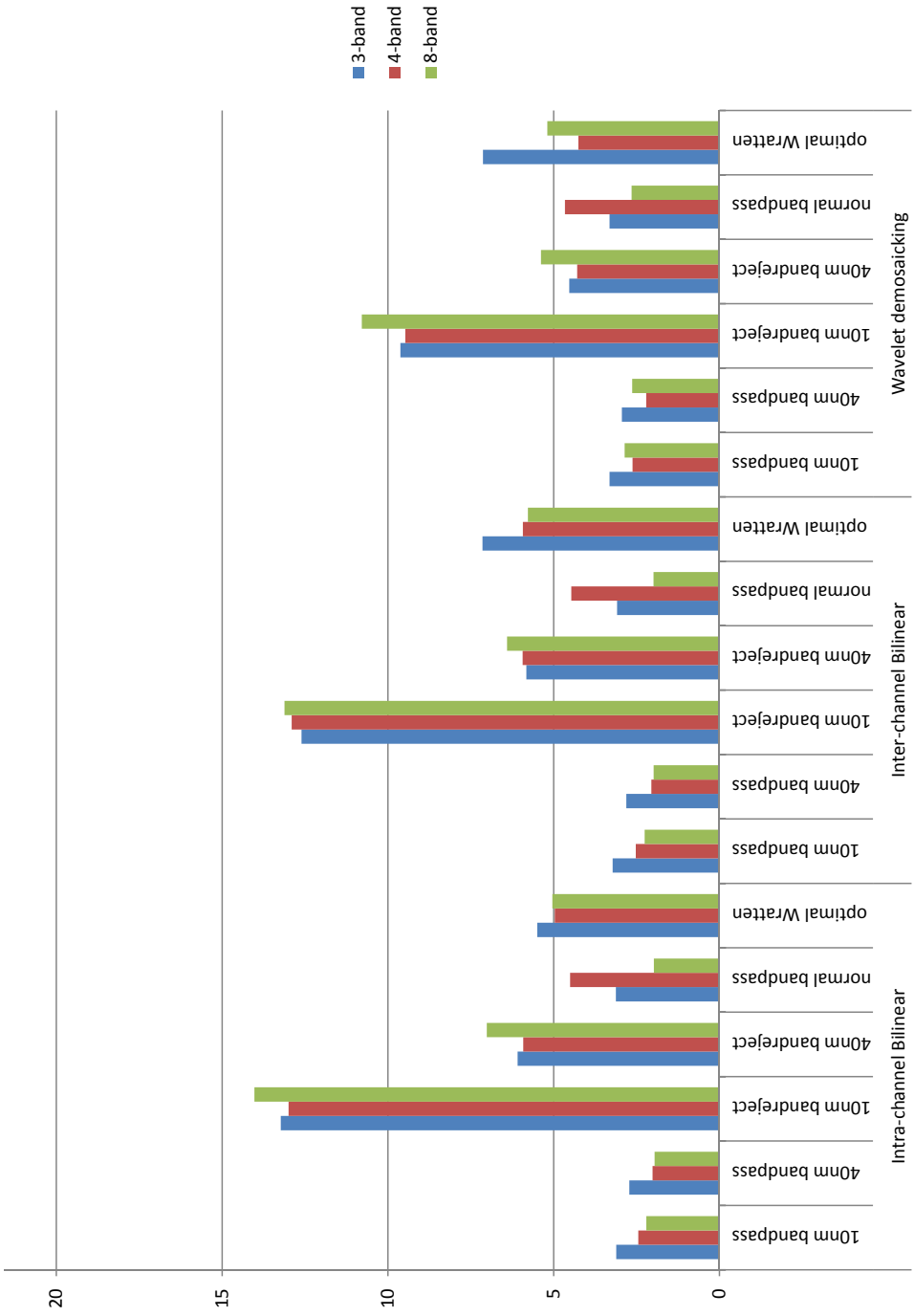

Figure 10.5: Average CIEDE2000 colour difference among test images. Copyright ©Springer.

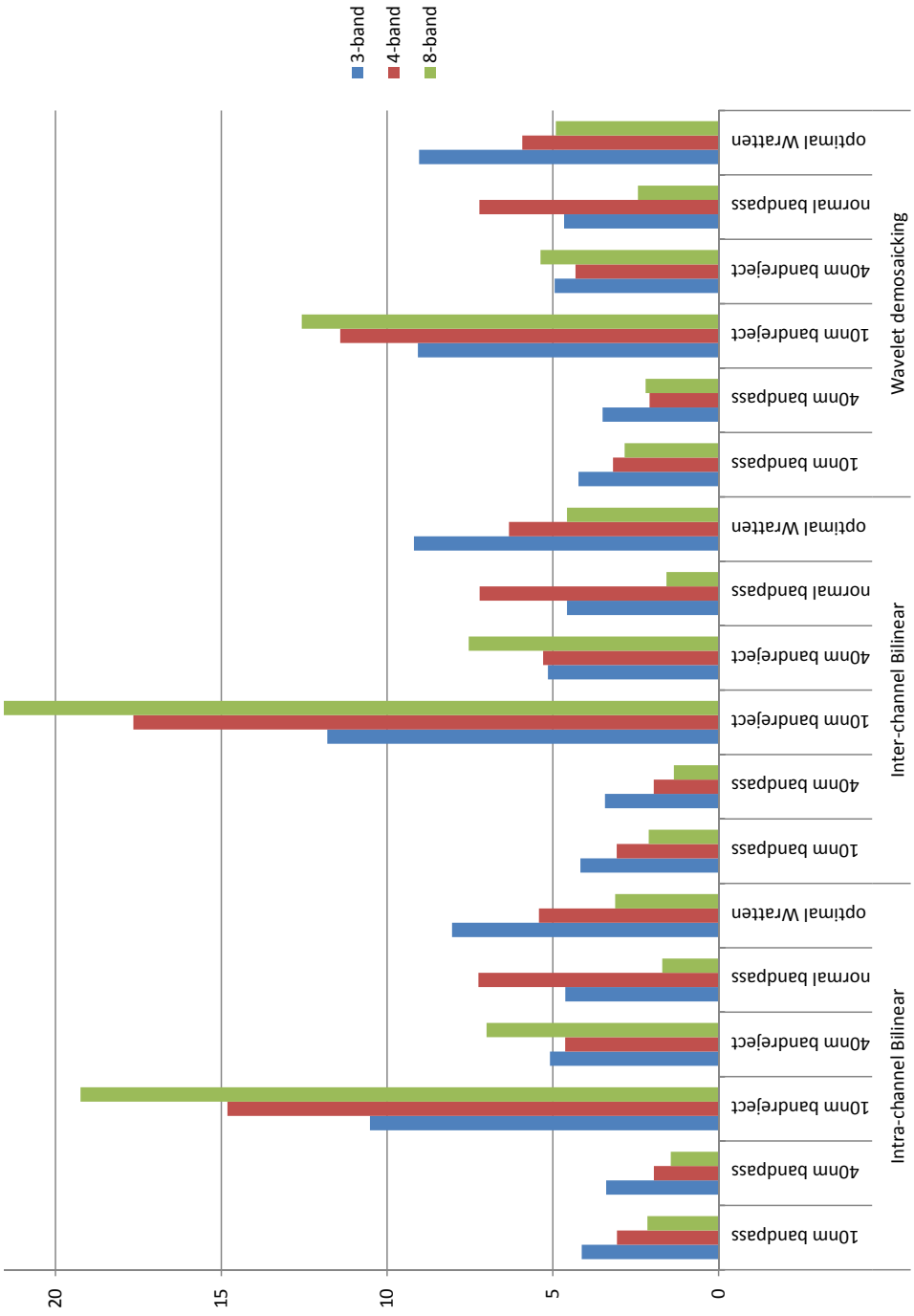

Figure 10.6: Average S-CIELAB colour difference among test images. Copyright ©Springer.

Chapter 11

Comparative study of SFA demosaicking algorithms

11.1 Introduction

In Part III, we proposed three SFA demosaicking methods. The experimental results have demonstrated the potential and usefulness of the proposed methods as well as the merits and drawbacks. In this chapter, we perform comparative analyses and evaluations of the proposed and basic SFA demosaicking techniques given characteristics of 2 practical SFA-based imagers [100] and 8 scenes covering both visible and IR bands. The performance are evaluated by means of the PSNR and the SSIM index. Such an analysis will provide us with more comprehensive information valuable for developing SFA-based spectral imaging devices.

The chapter is organised as follows. Section 11.2 introduces the setup and procedures for conducting the experiment. The results are presented in Section 11.3 which leads to conclusions drawn in Section 11.4.

11.2 Experiment

11.2.1 Overview of the experimental framework

The pipeline illustrated in Figure 4.4 is utilised for the purpose of this experiment. In addition, the experiment covers a portion of the NIR region to which modern solid-state image sensors are sensitive.

Demosaicking methods are normally evaluated by means of image quality assessment. In the pipeline illustrated in Figure 11.1, full reference quality metrics are applied to the full resolution multispectral image prior to spatial sampling and the demosaicked image. This is in line with practical single-sensor imaging systems and serves the comparative purpose of this experiment.

Table 11.1: Parameters of the experiment.

Spectral range	420 nm – 950 nm
Spectral interval	10 nm
Illuminant	indoor, outdoor illumination depending on the scenes
Number of images	8
Type of images	Radiance, reflectance images
Type of filters	8 band-pass transmissive filters
Type of mosaics	2 SFAs of symmetric and asymmetric arrangement
Spectral responsivity	measured from e2v sensor
Normalisation	intra-channel normalisation to the maximum possible code value
Noise	noise-free mode, noise-present mode (photon shot noise and read noise)
Demosaicking	bilinear, smooth hue, binary-tree, vector median filtering, DWT, LMMSE
Quality metrics	PSNR, SSIM

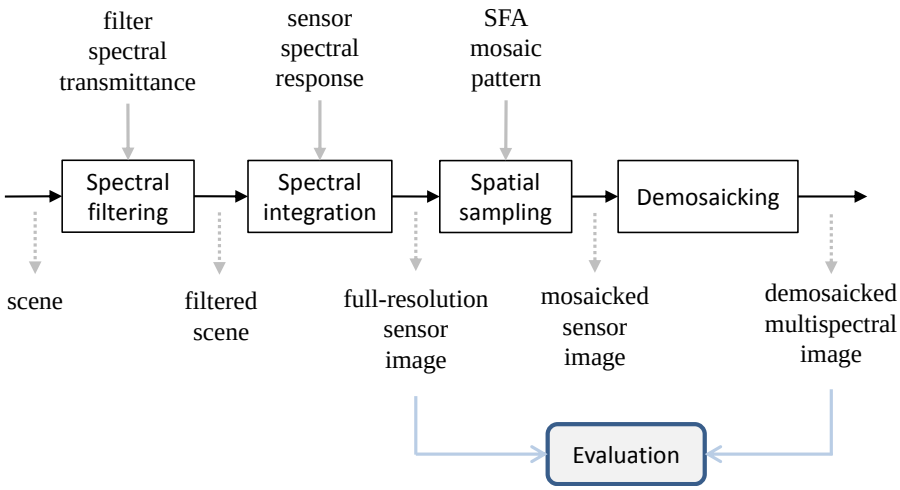

Figure 11.1: Design of the experimental framework.

11.2.2 Scene

In order for a close simulation, the scenes should represent what real-life spectral imaging systems capture. By this criterion, four categories of scenes, i.e., hu-

man faces (1&2), landscape (3&4), manuscripts (5&6) and paintings (7&8), were finally selected. Each consists of two spectral images. Scenes of the first two categories were reproduced from the Hyperspectral Image Data set provided by the Stanford Center for Image Systems Engineering (SCIEN) [156], and the last two categories were captured by researchers in the Norwegian Colour and Visual Computing Laboratory [57, 56, 29].

1	2	3	4
5	6	7	8

Figure 11.2: Preview of the cropped scenes used in the experiment that cover various objects including human faces (1&2), landscape (3&4), manuscripts (5&6) and paintings (7&8).

The scene images of the last two categories bear a pixel count of 500×500. To make the evaluation easier, the images of the first two categories are spatially manipulated to bear the same dimension as those of the last two. To that end, the original images are cropped to form square regions which are then resized by means of bicubic resampling. The x,y coordinates of the vertex pixels in the original images and the cropped size are listed in Table 11.2 for reference.

The 8 scene images are expressed in the form of reflectance and radiance respectively, each stored with the spectral power distribution of the illumination. As can be seen in Figure 11.3, there are two types of lighting conditions. Scene 3-4 are lit by skylight-like outdoor illumination, and the curves fluctuate considerably and peak in the VIS range. The other scenes, however, are lit by tungsten-like indoor illumination, and the curves feature smooth and nearly monotonic shape with peaks

Table 11.2: The x,y coordinates of the cropped regions.

Scene	x_1	x_2	y_1	y_2	cropped size
Face 1 (HiResFemale12)	255	936	449	1130	682×682
Face 2 (HiResMale11)	154	935	479	1260	782×782
Landscape 1 (SanFrancisco)	150	851	1	702	702×702
Landscape 2 (StanfordTower)	101	901	1	801	801×801

in the NIR region.

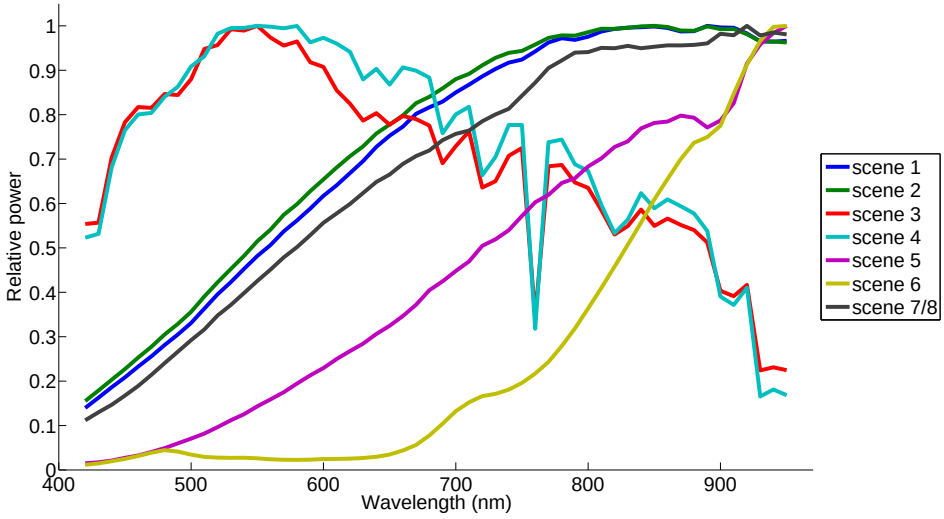

Figure 11.3: Spectral radiance of the illuminants that light the scenes.

Scene 1-4 cover the spectral range between approximately $415nm$ and $950nm$, and scene 5-8 extend the higher end to about 993 nm. All scenes share the same interval of about 3.64 nm. This results in 148 bands and 160 bands respectively.

11.2.3 Spectral filtering

As depicted in Figure 11.4, the filter set used in the experiment is reproduced from the previous work [100]. Although the distinctions between the theoretical design and the practical implementation are recognisable, we consider it appropriate to use the theoretical design here in this simulation-based experiment. The set includes 8 band-pass filters, 7 of which have the peak transmittance in the VIS range, leaving 1 that peaks in the NIR region. In particular, filter 8's wide pass-

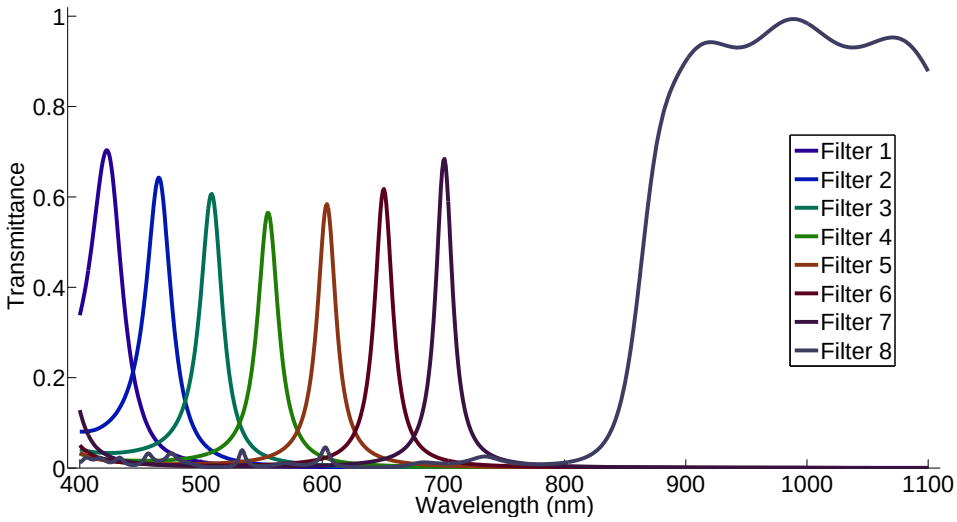

Figure 11.4: Theoretical spectral transmittances of the experimental filter set.

band of high transmittance is rather noticeable. The transmittance data covers the spectral range between 400 nm and 1100 nm with an interval of 1 nm.

11.2.4 Spatial sampling

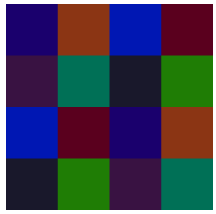

1	5	2	6
7	3	8	4
2	6	1	5
8	4	7	3

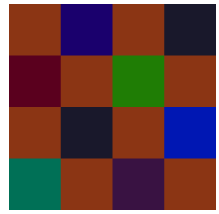

5	1	5	8
6	5	4	5
5	8	5	2
3	5	7	5

Figure 11.5: Illustration of the SFA I (left) and SFA II (right). The design of both conforms to the designing philosophy of the binary-tree approach [123]. The left one consists of 8 equally distributed channels, whereas the right one resembles the Bayer CFA arrangement with 1 densely sampled channel and 7 sparsely sampled channels.

As shown in Figure 11.5, both of the SFA arrangements proposed in the previous work [100] can be considered as instances of the binary-tree SFA design principle [123]. SFA I consists of 8 filter elements of equal probability of appearance, that is, each appears twice in the mosaic pattern. SFA II comprises of 1 filter of 1/2 probability of appearance, 1 filter element of 1/8 as well as 6 filter elements of 1/16 each. Generally speaking, SFA I is a balanced design for the majority of scenes, whereas the oversampled channel of SFA II, i.e. the channel labelled 5 in the mosaic pattern, should yield resultant images of higher spatial resolution in particular for scenes rich in detail around 500 nm.

11.2.5 Spectral integration

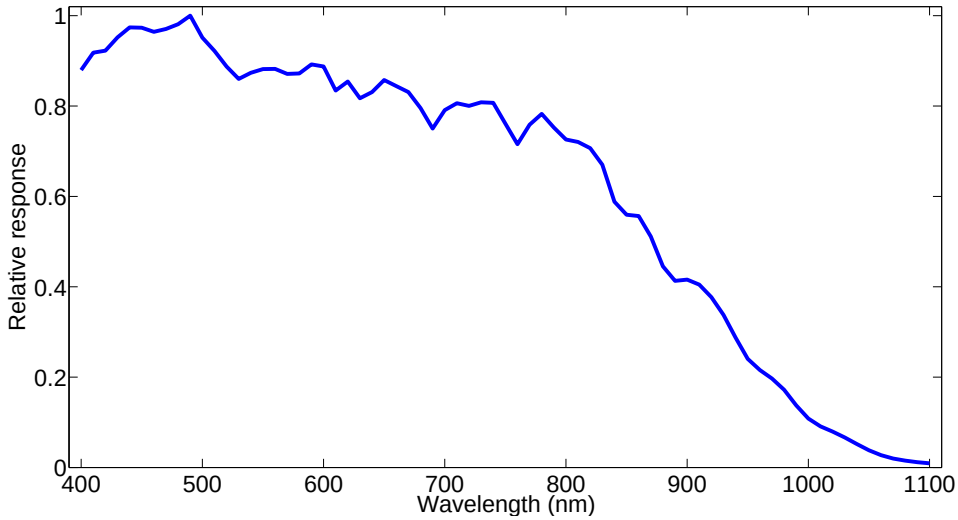

Figure 11.6: Relative response of the sensor.

In our practical implementation [100], the CMOS image sensor from e2v, model EV76C661, is incorporated into the prototype of an SFA-based imaging system. The relative response of the sensor averages approximately 0.888 over the visible spectrum (400 nm to 700 nm) and peaks at 490 nm. The high sensitivity extends into the NIR region and the response halves at about 870 nm. Such characteristics meet our requirements for, and are therefore employed in, this experiment. The response data covers the spectral range between 400 nm and 1100 nm with an interval of 1 nm.

For the purpose of spectral integration, it is necessary to unify the spectral characteristics of each module, i.e. range and interval. To that end, in this experiment

we decide to use the widest common range, to wit the region between $420nm$ and $950nm$, that makes efficient use of the data, and an interval of $10nm$ to reach a compromise between spectral accuracy and computational complexity. This configuration yields 54-band spectral images as scenes and the spectral filtering reduces the number of band to 8. After the spatial sampling and spectral integration, stacked multispectral images, namely mosaic images, are formed.

Nevertheless, the integration of the scenes (illumination), the filters and the sensors causes an imbalance in power between certain channels [144], in particular between the VIS channels and the NIR channel. Figure 11.7(a) demonstrates the substantial discrepancy between channels after normalisation, especially for Scene 6. The glaring inconsistency will add difficulties in interpreting the results and comparing the performance of the methods in question. Therefore we normalise each band individually according to the maximum possible value occurring when perfect diffuse white is present under the same illumination as the scenes, which mimics the white balancing operation seen in colour cameras. The effect can be seen clearly in Figure 11.7(b) and in Table 11.3 that the inter-band variance decreases when normalised per band.

Table 11.3: The inter-band variance resulting from the two normalisation techniques.

Normalisation	Scene 1	Scene 2	Scene 3	Scene 4	Scene 5	Scene 6	Scene 7	Scene 8
per image	0.0025	0.0028	0.0022	0.0023	0.0795	0.0694	0.0415	0.0348
per band	0.0027	0.0021	0.0014	0.0021	0.0066	0.0178	0.0145	0.0068

11.2.6 Demosaicking

In order for a comprehensive comparison, six demosaicking methods are incorporated in the experiment. Apart from the three methods proposed in Part III, three fundamental techniques that may provide a benchmark, i.e. bilinear interpolation, the smooth-hue transition based interpolation and the binary-tree based demosaicking are also included. Although the methods have already been implemented in the previous experiment, there are still a few minor yet important changes.

For the smooth-hue transition based interpolation, unlike the previous experiments, hue is defined now as the ratio between one selected band (band 5 in the experiment) and each of the remaining bands. This should reflect better the original proposal by Cok [30], since intensity of the sensor image can be considered as linearly proportional to radiance of the scene. To avoid division-by-zero, a small constant is added to the dominator and subtracted subsequently from the resultant images.

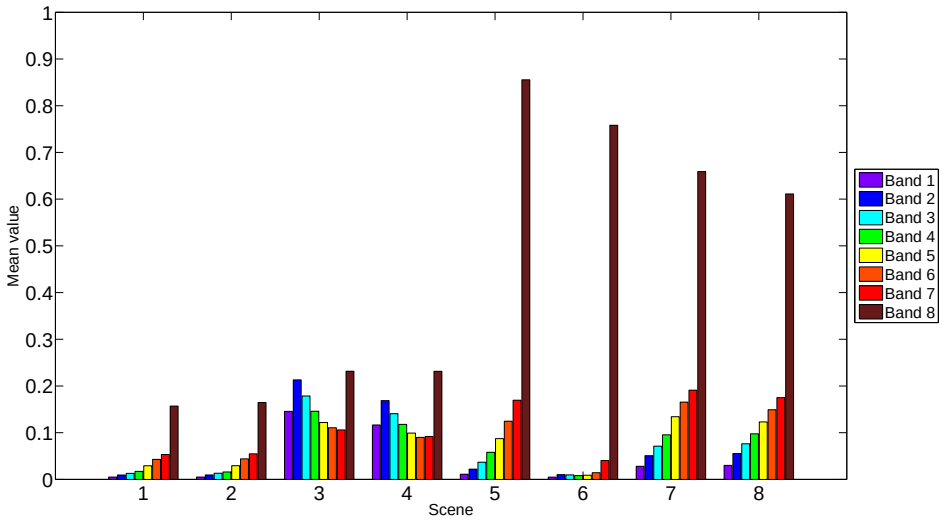

(a) Mean of the images normalised with the peak value of the whole image.

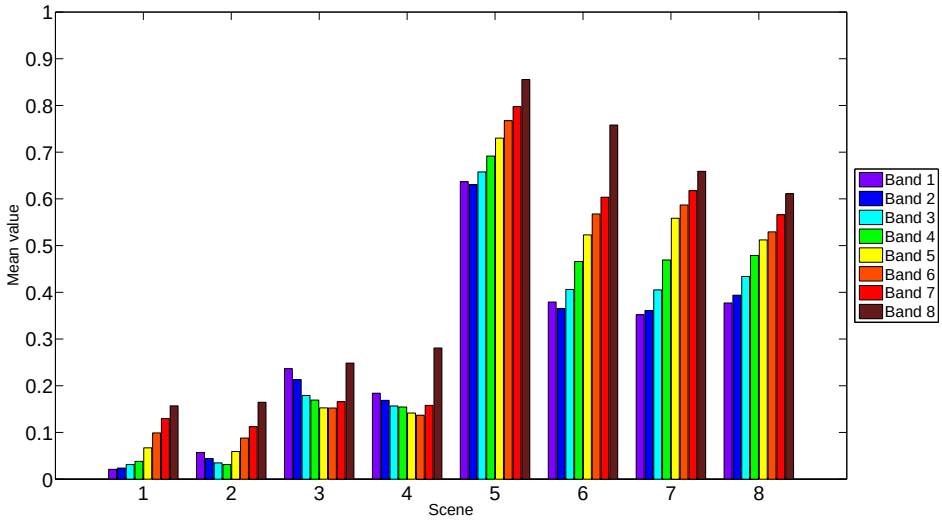

(b) Mean of the images normalised with the peak value of each band.

Figure 11.7: Balance of scale over the bands with two normalisation techniques.

As the tessellation of SFA II is asymmetric, for the vector median filtering based demosaicking, it is impossible to make use of a single set of pseudopixel indices as in the previous experiments. In other words, each location in the moxel requires

a unique set of pseudopixel indices. Based on the findings presented in Chapter 7, the indices are generated by constructing pesudopixels in any direction and selecting those passing through the central pixel only, to strike a reasonable compromise between the computational cost and the demosaicking performance.

For the LMMSE based demosaicking, selection of the a priori information plays a key role, as shown in Chapter 9. Considering the scenes chosen for this experiment, we use the one image as the a priori information to demosaic the other image of the same genre. Such pairs of images bear stronger similarity than other images, and may therefore achieve better results.

11.3 Results

The combination of the parameters shown in Table 11.1 lead to copious results that form a penteract, namely a five-dimensional hypercube with parameters including the scenes, SFAs, demosaicking methods, bands and quality metrics. To ease the observation and analysis of the results, we will have to reduce the dimensionality of the hypercube by slicing the cube or averaging it along a certain dimension.

Table 11.4 and 11.5 present an in-depth overview of the results averaged over 8 bands. For each scene image, the results yielded by the 6 demosaicking methods are compared, given one specific SFA arrangement. For each scene mosaicked with each SFA, the highest and lowest values in the results are emphasized in bold and italic fonts respectively. For each scene, the overall highest value is highlighted in grey. For the ease of observation and analysis, Figure 11.8 and 11.9 show the same results with bar graphs.

Table 11.4: Performance of the demosaicking algorithms under evaluation in terms of the PSNR including BL (bilinear interpolation), SH (smooth hue transition based interpolation), BT (binary-tree based demosaicking), VM (vector median filtering), DWT (DWT based demosaicking), LMMSE (LMMSE based demosaicking). For one specific SFA arrangement, the maximum and the minimum results are emphasized in bold and italic fonts respectively. For each scene, the best result is highlighted in grey.

SFA	Methods	PSNR (dB)							
		Image 1	Image 2	Image 3	Image 4	Image 5	Image 6	Image 7	Image 8
I	BL	45.0580	45.7414	36.6529	33.0698	37.6219	34.7061	33.4195	32.6282
	SH	45.3837	46.2587	37.0653	33.4767	**38.0652**	**36.4897**	33.9099	33.2751
	BT	46.1270	46.8100	38.0614	34.4459	37.9707	34.7827	35.0126	34.0840
	VM	45.6386	46.1935	37.4070	33.8147	36.1826	*31.7167*	33.2588	*32.4840*
	DWT	**46.3541**	**48.0611**	*35.6784*	*32.4894*	33.1971	32.0512	*32.0318*	33.3440
	LMMSE	*42.7437*	*37.7278*	**41.0607**	**39.4191**	*31.5179*	35.6382	**38.5306**	**38.8083**
II	BL	44.6326	45.2818	36.0911	32.3174	35.9082	31.6342	32.7044	31.7318
	SH	46.1109	47.0840	38.2031	34.4288	**39.4826**	**39.1369**	34.9696	34.7383
	BT	45.5420	46.3655	36.9111	33.2192	36.6984	33.0979	33.4905	32.6152
	VM	*44.2582*	45.0464	*35.4666*	*31.7596*	34.6446	*29.9734*	*31.2031*	*30.5146*
	DWT	**46.5521**	**48.0552**	35.6046	32.2862	33.4475	31.3541	32.3851	33.2627
	LMMSE	44.7859	*41.2290*	**40.8216**	**39.1891**	*32.9932*	35.1414	**39.3266**	**39.3107**

Table 11.5: Performance of the demosaicking algorithms under evaluation in terms of the SSIM index including BL (bilinear interpolation), SH (smooth hue based interpolation), BT (Binary-tree based demosaicking), VM (vector median filtering), DWT (DWT based demosaicking), LMMSE (LMMSE based demosaicking). For one specific SFA arrangement, the maximum and the minimum results are emphasized in bold and italic fonts respectively. For each scene, the best result is highlighted in grey.

SFA	Methods	SSIM index							
		Image 1	Image 2	Image 3	Image 4	Image 5	Image 6	Image 7	Image 8
I	BL	0.9954	0.9960	0.9610	0.9449	0.9672	0.9822	0.9572	*0.9543*
	SH	0.9961	**0.9967**	0.9668	0.9528	0.9695	0.9881	0.9630	0.9631
	BT	**0.9962**	0.9966	0.9696	0.9556	**0.9700**	0.9813	0.9676	0.9649
	VM	0.9960	0.9965	0.9705	0.9570	0.9693	0.9807	0.9667	0.9653
	DWT	0.9938	0.9954	*0.9454*	*0.9205*	*0.9352*	*0.9733*	*0.9467*	0.9638
	LMMSE	*0.9887*	*0.9692*	**0.9855**	**0.9809**	0.9375	**0.9905**	**0.9866**	**0.9893**
II	BL	0.9940	0.9943	0.9489	0.9258	0.9417	*0.9466*	0.9378	*0.9307*
	SH	**0.9969**	**0.9976**	0.9762	0.9648	**0.9697**	**0.9911**	0.9668	0.9728
	BT	0.9944	0.9946	0.9502	0.9281	0.9446	0.9577	0.9380	0.9315
	VM	0.9941	0.9946	0.9508	0.9289	0.9494	0.9642	0.9405	0.9378
	DWT	0.9929	0.9948	*0.9410*	*0.9128*	*0.9302*	0.9632	*0.9357*	0.9556
	LMMSE	*0.9805*	*0.9683*	**0.9801**	**0.9745**	0.9469	0.9874	**0.9801**	**0.9853**

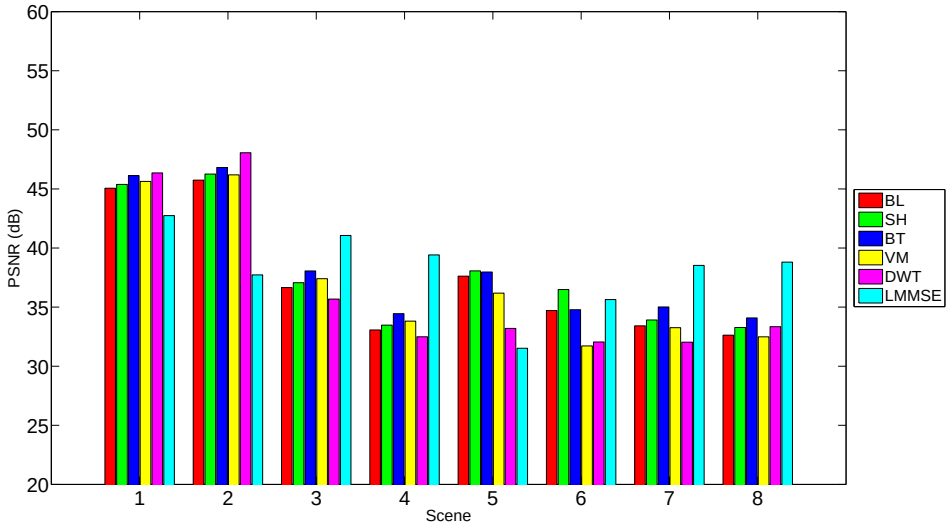

(a) PSNR for each scene mosaicked with SFA I.

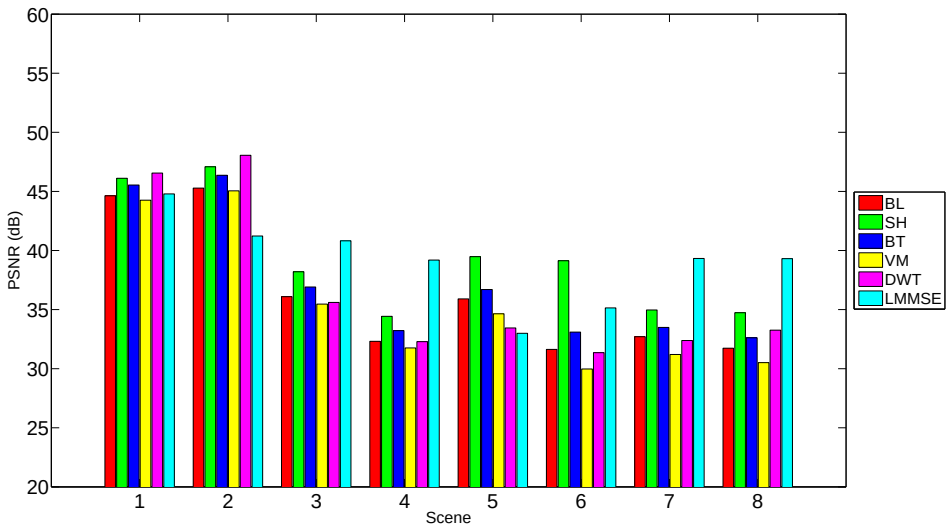

(b) PSNR for each scene mosaicked with SFA II.

Figure 11.8: Experimental results (PSNRs) for each scene. The horizontal axis represents the 8 scenes, and the vertical axis represents the results in terms of the PSNR. For each scene, results produced by all of the demosaicking methods are grouped together. Results connected with SFA I and SFA II are plotted separately.

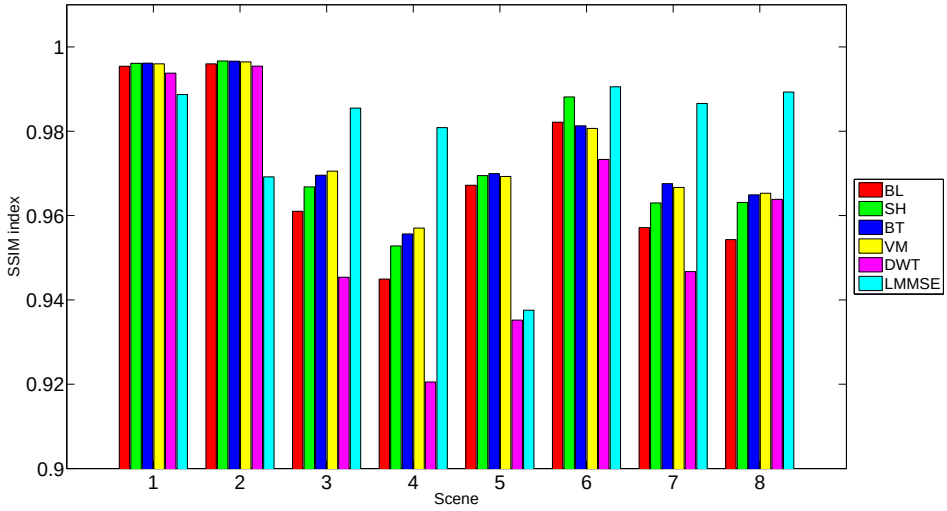

(a) SSIM indices for each scene mosaicked with SFA I.

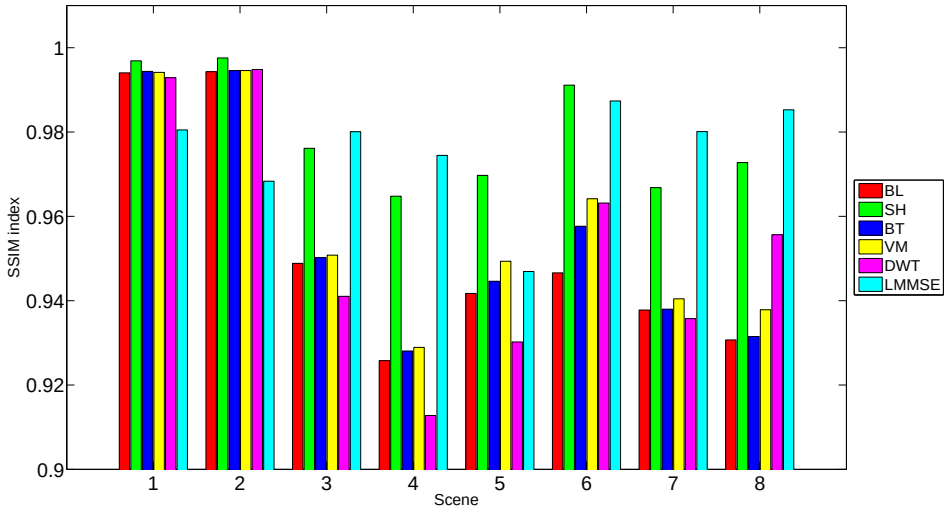

(b) SSIM indices for each scene mosaicked with SFA II.

Figure 11.9: Experimental results (SSIM indices) for each scene. The horizontal axis represents the 8 scenes, and the vertical axis represents the results in terms of the SSIM index. For each scene, results produced by all of the demosaicking methods are grouped together. Results connected with SFA I and SFA II are plotted separately.

In Table 11.4 and 11.5, the maximum and the minimum PSNRs are respectively produced by DWT for Scene 2 and by VM for Scene 6, whereas the maximum and the minimum SSIM indices are respectively produced by SH for Scene 2 and by DWT for Scene 4. The discrepancies are due partly to the differences in principle between the two quality metrics. Regardless of the SFA arrangement, LMMSE notably outperforms the other methods constantly for Scene 3/4/7/8, but delivers lower performance than others for Scene 1/2. The polarity indicates the dependence of LMMSE on the selection of the training data. In 11.8(a) and Figure 11.8(b), DWT shows the greatest variance over the 8 scenes, and LMMSE the slightest. In Figure 11.9(a) and Figure 11.9(b), DWT shows the greatest variance, whereas VM and LMMSE lead to the slightest variance for SFA I and SFA II respectively.

When it comes to the impact of mosaic arrangement, the results show definite distinctions. As expected, SFA II results in an overall increase in the performance of SH among all 8 scenes, accordingly the bars in relation to SH is visibly higher than others in Figure 11.8(b) and 11.9(b) in comparison with Figure 11.8(a) and 11.9(a). The rank order of the methods according to the PSNR is:
BT>LMMSE>SH>BL>VM>DWT for SFA I, and SH>LMMSE>BT>DWT>BL>VM for SFA II. The order according to the SSIM index is:
LMMSE>VM>BT>SH>BL>DWT for SFA I, and SH>LMMSE>VM>BT>DWT>BL for SFA II. The alteration of the orders show the positive advantage of SFA II to SH, as the Bayer-like arrangement of SFA II sacrifices the spatial sampling rate of 7 channels for 1 relatively higher resolution channel. In general, however, SFA II reduces the overall results by about 0.3 dB in terms of the PSNR, and by 0.01 in terms of the SSIM index.

Table 11.4 and 11.5 show considerable variations among the scenes. Category 1 comfortably exceeds other categories by an average of about 10.4 dB in terms of the PSNR and 0.033 in terms of the SSIM index. This is demonstrated more clearly with bar graphs in Figure 11.8 and 11.9, where the discrepancies between the bars for each scene and between the scenes are glaring, especially in Figure 11.8.

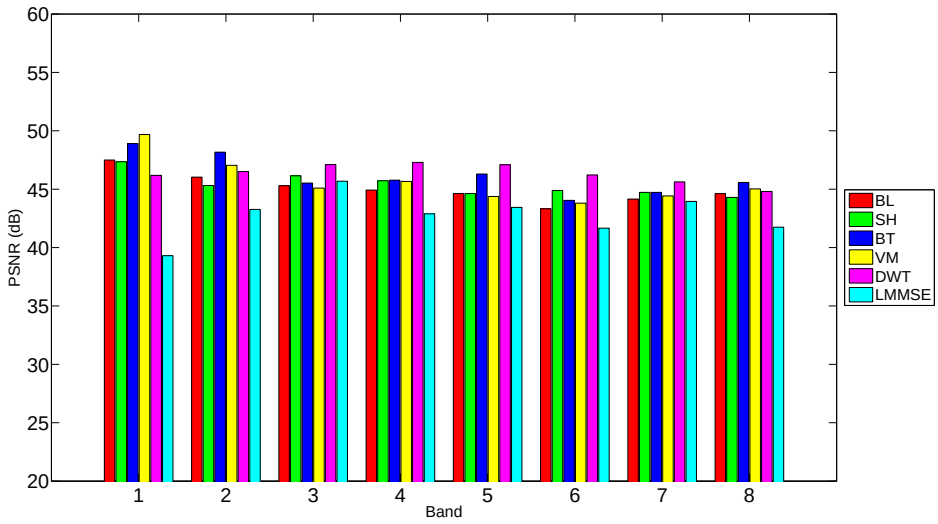

(a) PSNR for each band of Scene 1 mosaicked with SFA I.

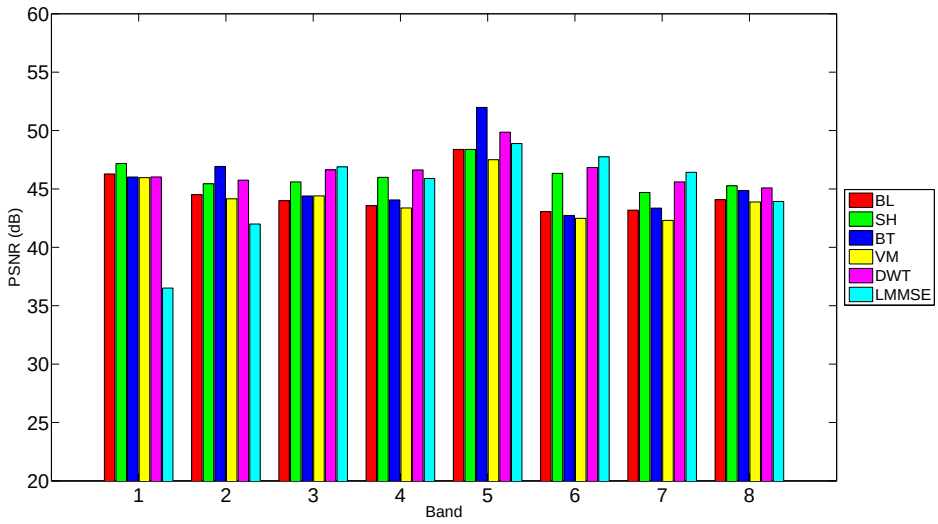

(b) PSNR for each band of Scene 1 mosaicked with SFA II.

Figure 11.10: Experimental results (PSNRs) for each band of Scene 1. The horizontal axis represents the 8 bands, and the vertical axis represents the results in terms of the PSNR. For each band, results produced by all of the demosaicking methods are grouped together. Results connected with SFA I and SFA II are plotted separately.

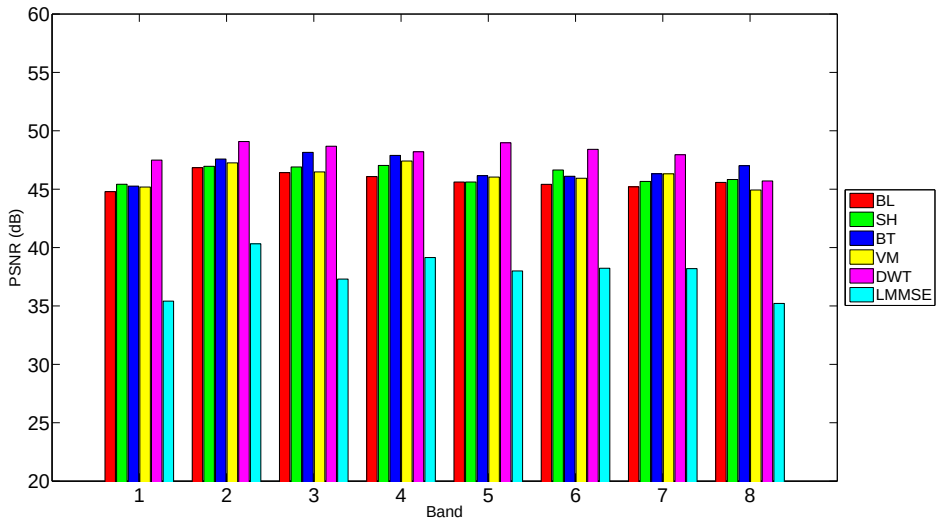

(a) PSNR for each band of Scene 2 mosaicked with SFA I.

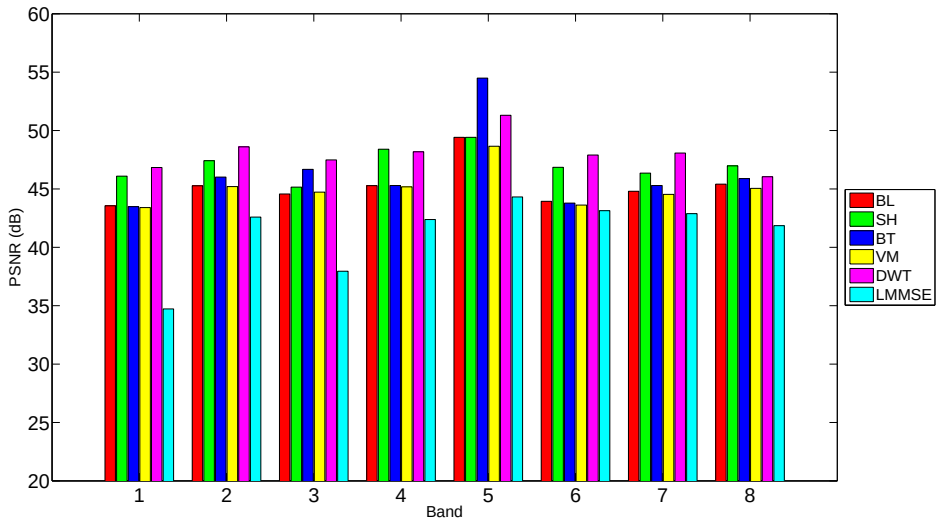

(b) PSNR for each band of Scene 2 mosaicked with SFA II.

Figure 11.11: Experimental results (PSNRs) for each band of Scene 2. The horizontal axis represents the 8 bands, and the vertical axis represents the results in terms of the PSNR. For each band, results produced by all of the demosaicking methods are grouped together. Results connected with SFA I and SFA II are plotted separately.

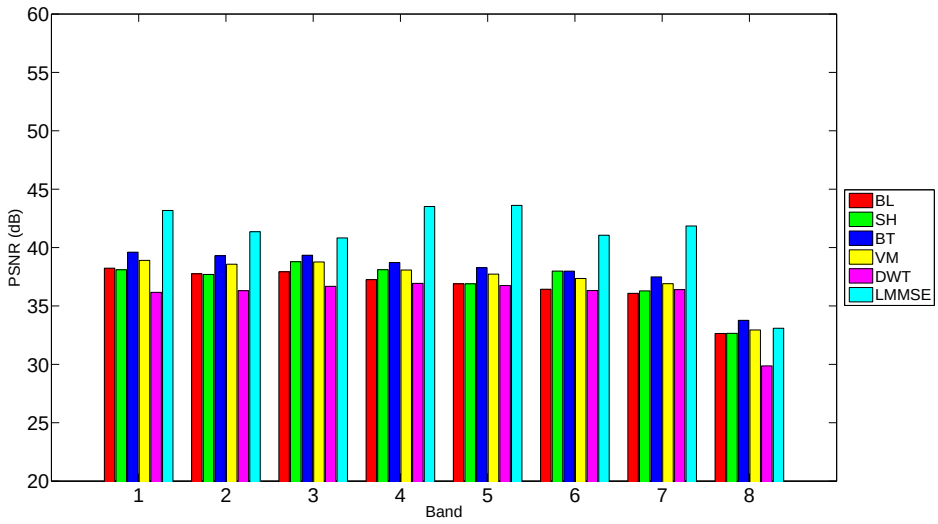

(a) PSNR for each band of Scene 3 mosaicked with SFA I.

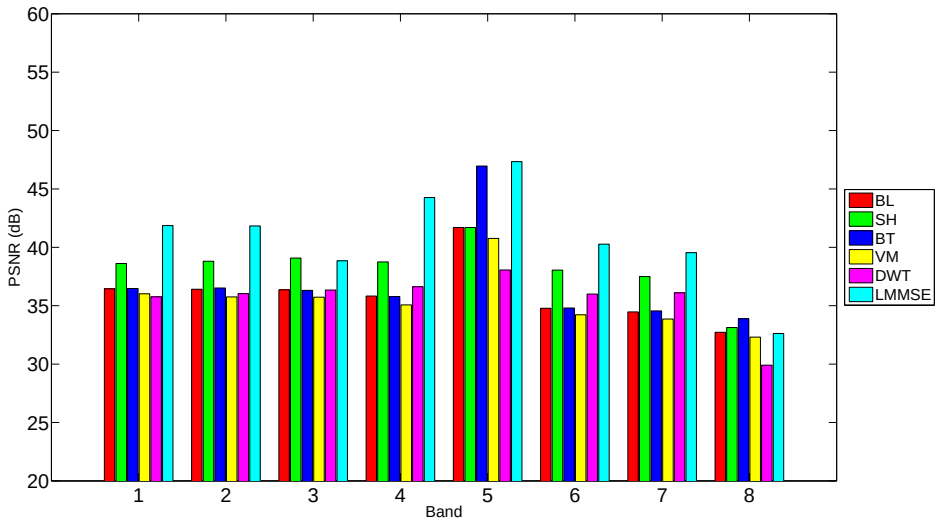

(b) PSNR for each band of Scene 3 mosaicked with SFA II.

Figure 11.12: Experimental results (PSNRs) for each band of Scene 3. The horizontal axis represents the 8 bands, and the vertical axis represents the results in terms of the PSNR. For each band, results produced by all of the demosaicking methods are grouped together. Results connected with SFA I and SFA II are plotted separately.

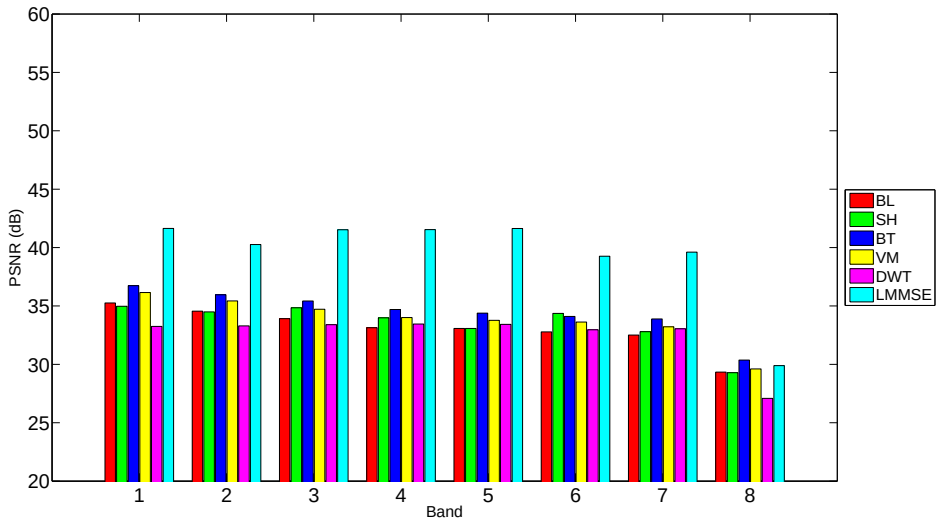

(a) PSNR for each band of Scene 4 mosaicked with SFA I.

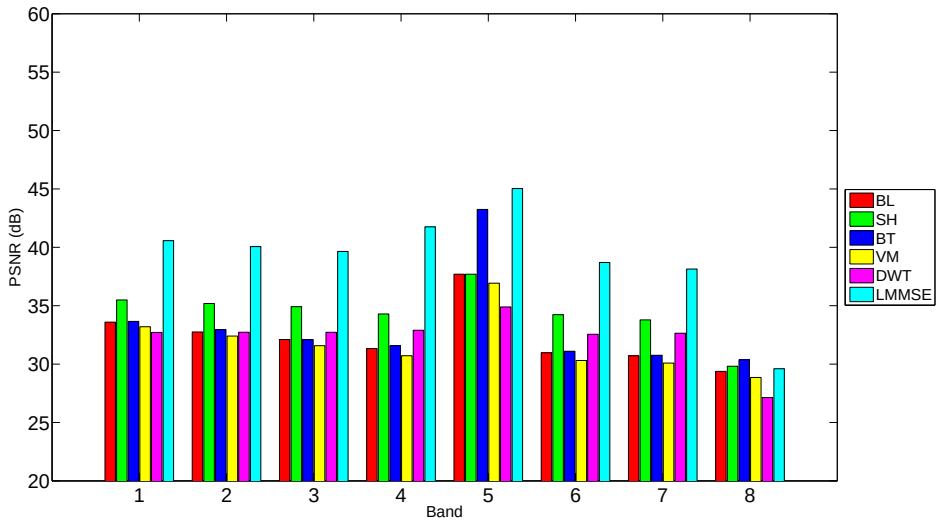

(b) PSNR for each band of Scene 4 mosaicked with SFA II.

Figure 11.13: Experimental results (PSNRs) for each band of Scene 4. The horizontal axis represents the 8 bands, and the vertical axis represents the results in terms of the PSNR. For each band, results produced by all of the demosaicking methods are grouped together. Results connected with SFA I and SFA II are plotted separately.

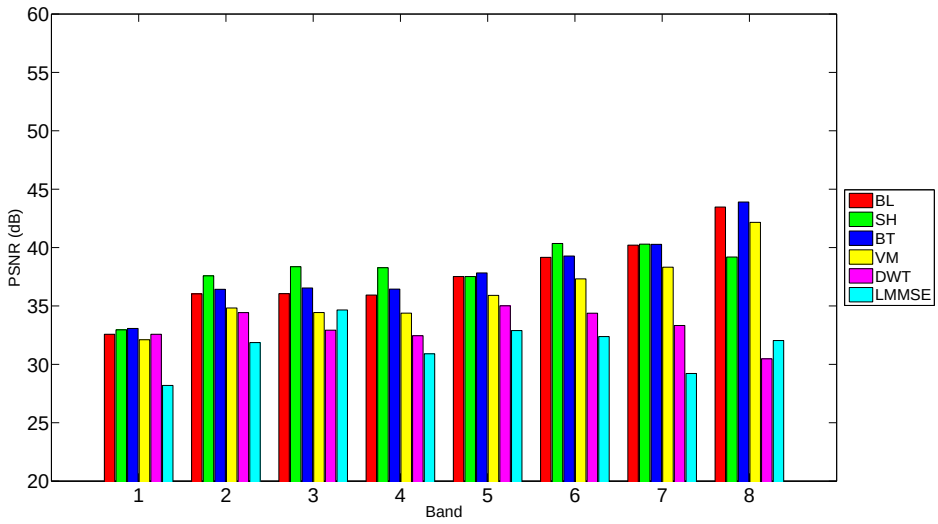

(a) PSNR for each band of Scene 5 mosaicked with SFA I.

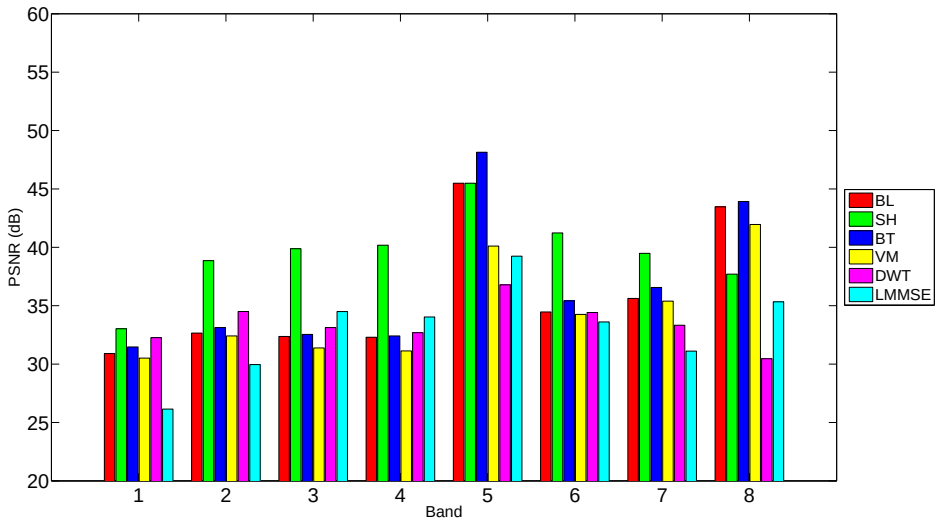

(b) PSNR for each band of Scene 5 mosaicked with SFA II.

Figure 11.14: Experimental results (PSNRs) for each band of Scene 5. The horizontal axis represents the 8 bands, and the vertical axis represents the results in terms of the PSNR. For each band, results produced by all of the demosaicking methods are grouped together. Results connected with SFA I and SFA II are plotted separately.

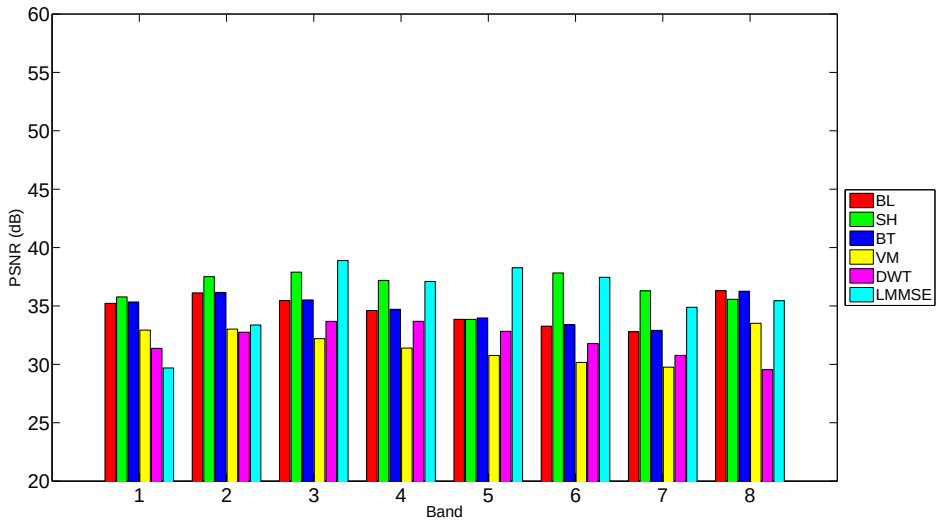

(a) PSNR for each band of Scene 6 mosaicked with SFA I.

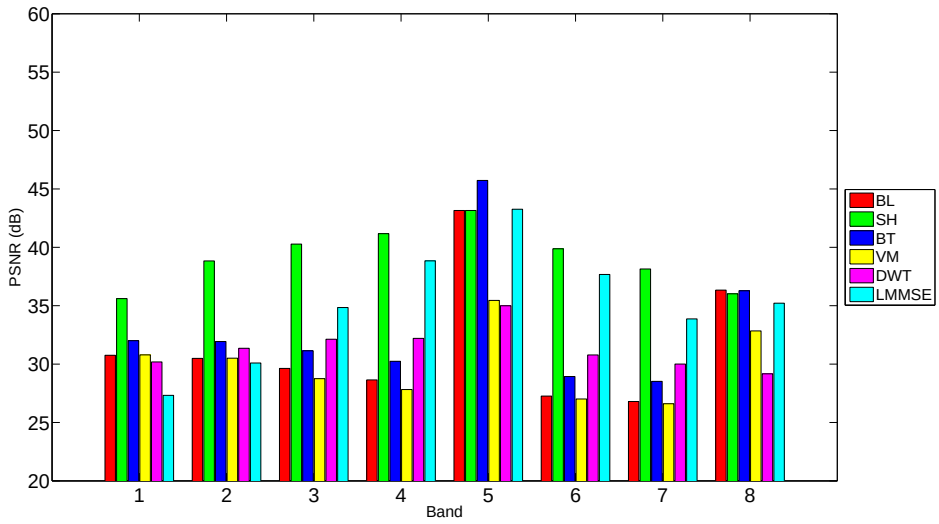

(b) PSNR for each band of Scene 6 mosaicked with SFA II.

Figure 11.15: Experimental results (PSNRs) for each band of Scene 6. The horizontal axis represents the 8 bands, and the vertical axis represents the results in terms of the PSNR. For each band, results produced by all of the demosaicking methods are grouped together. Results connected with SFA I and SFA II are plotted separately.

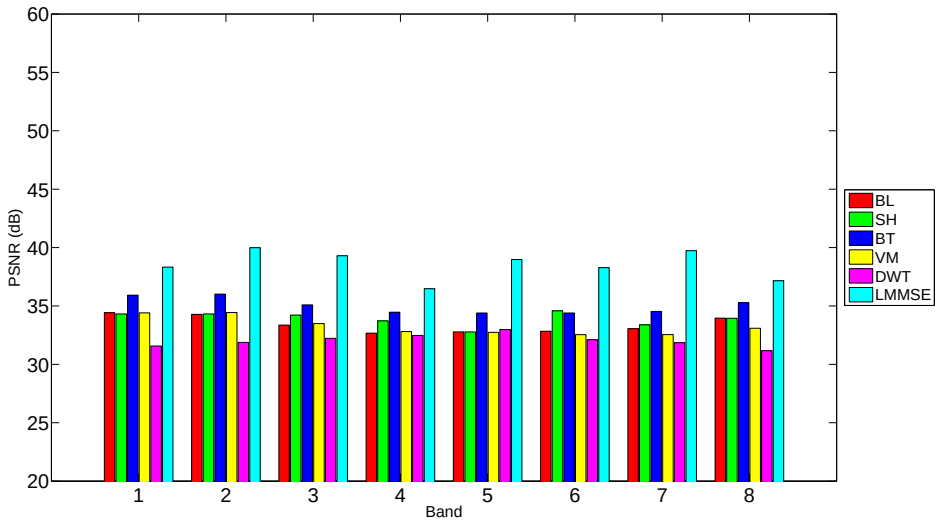

(a) PSNR for each band of Scene 7 mosaicked with SFA I.

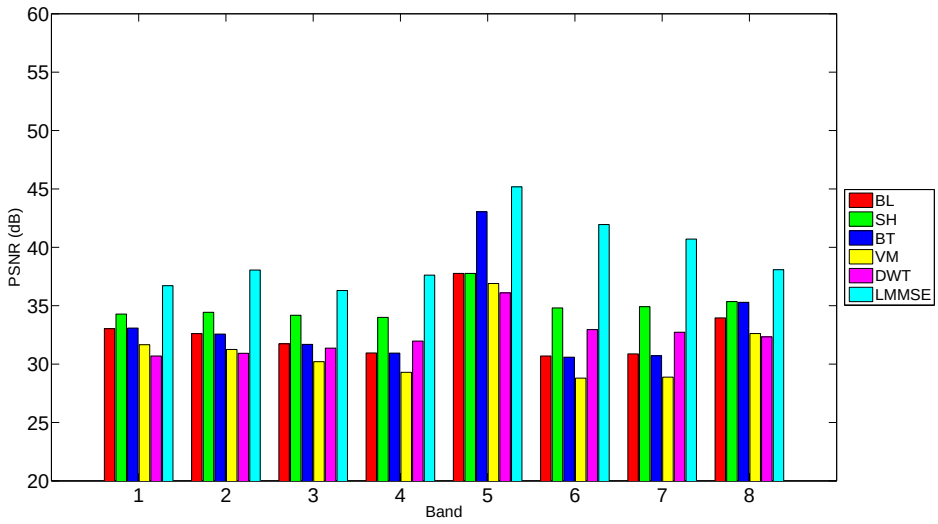

(b) PSNR for each band of Scene 7 mosaicked with SFA II.

Figure 11.16: Experimental results (PSNRs) for each band of Scene 7. The horizontal axis represents the 8 bands, and the vertical axis represents the results in terms of the PSNR. For each band, results produced by all of the demosaicking methods are grouped together. Results connected with SFA I and SFA II are plotted separately.

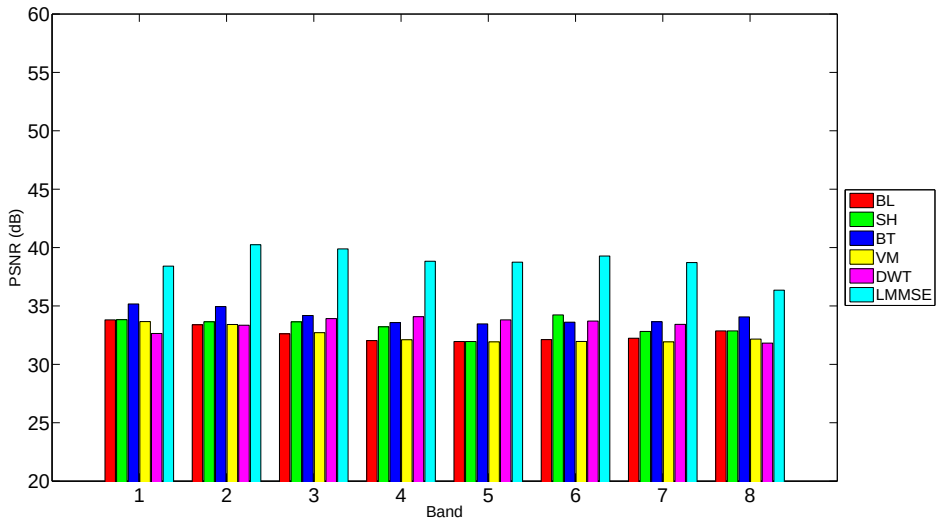

(a) PSNR for each band of Scene 8 mosaicked with SFA I.

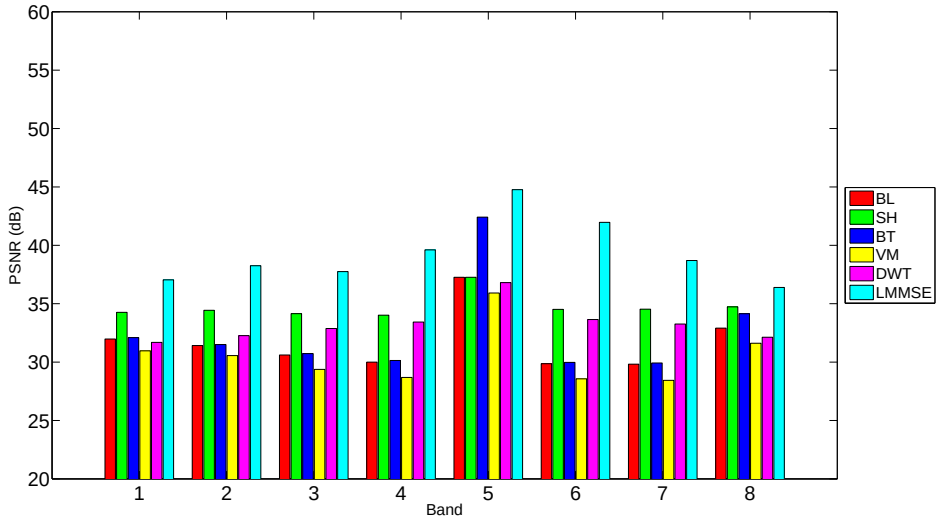

(b) PSNR for each band of Scene 8 mosaicked with SFA II.

Figure 11.17: Experimental results (PSNRs) for each band of Scene 8. The horizontal axis represents the 8 bands, and the vertical axis represents the results in terms of the PSNR. For each band, results produced by all of the demosaicking methods are grouped together. Results connected with SFA I and SFA II are plotted separately.

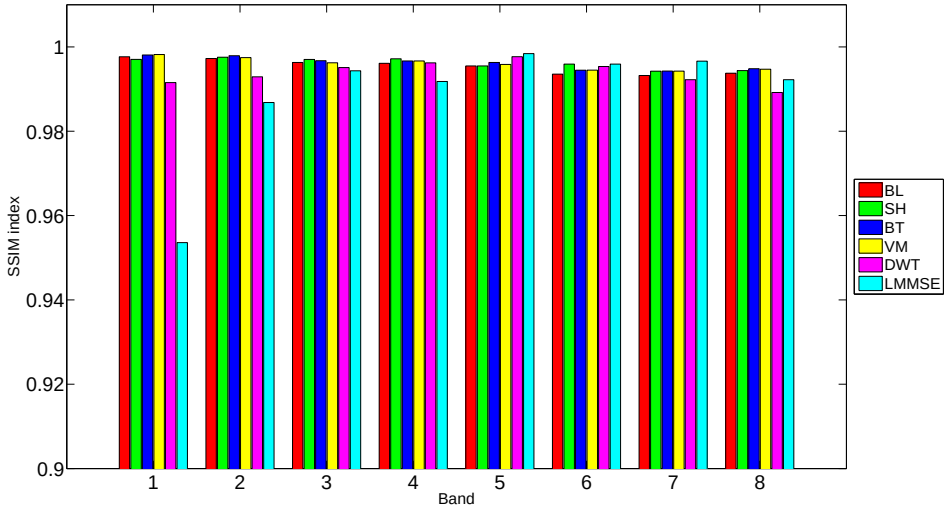

(a) SSIM indices for each band of Scene 1 mosaicked with SFA I.

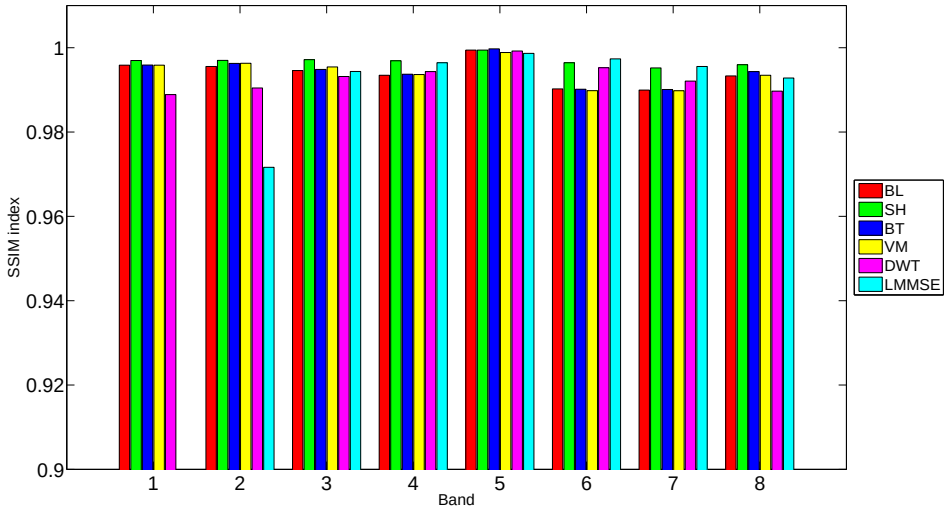

(b) SSIM indices for each band of Scene 1 mosaicked with SFA II.

Figure 11.18: Experimental results (SSIM indices) for each band of Scene 1. The horizontal axis represents the 8 bands, and the vertical axis represents the results in terms of the SSIM index. For each band, results produced by all of the demosaicking methods are grouped together. Results connected with SFA I and SFA II are plotted separately.

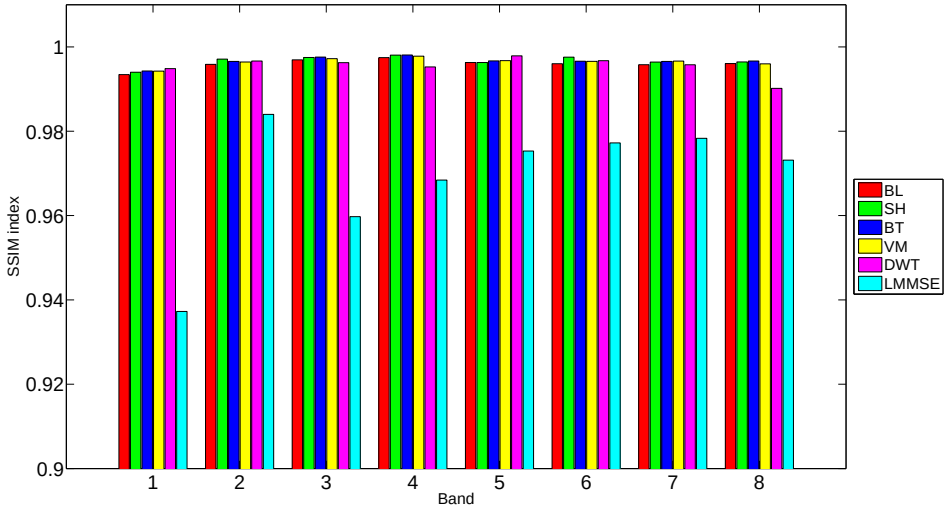

(a) SSIM indices for each band of Scene 2 mosaicked with SFA I.

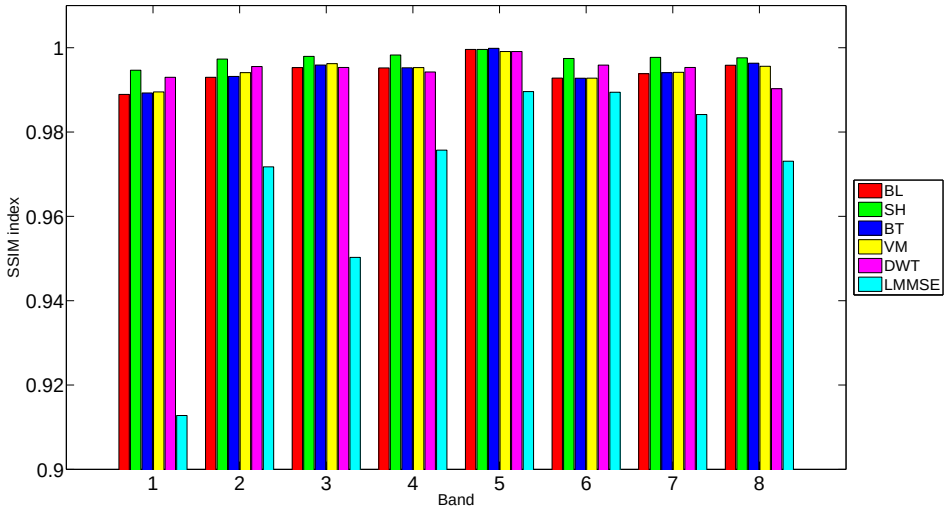

(b) SSIM indices for each band of Scene 2 mosaicked with SFA II.

Figure 11.19: Experimental results (SSIM indices) for each band of Scene 2. The horizontal axis represents the 8 bands, and the vertical axis represents the results in terms of the SSIM index. For each band, results produced by all of the demosaicking methods are grouped together. Results connected with SFA I and SFA II are plotted separately.

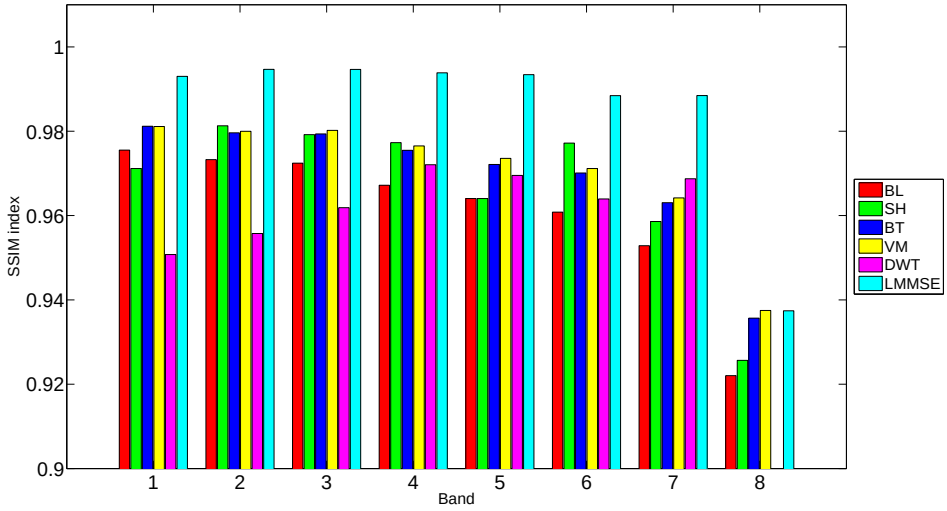

(a) SSIM indices for each band of Scene 3 mosaicked with SFA I.

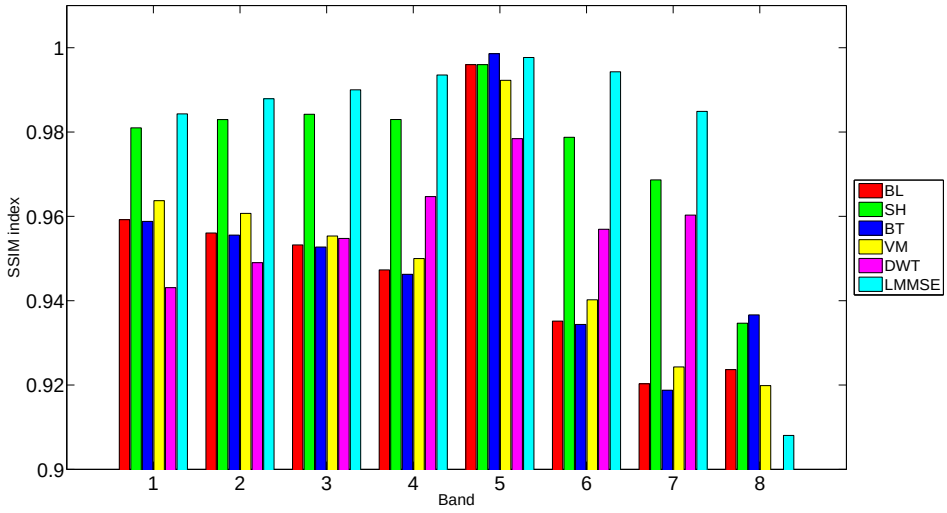

(b) SSIM indices for each band of Scene 3 mosaicked with SFA II.

Figure 11.20: Experimental results (SSIM indices) for each band of Scene 3. The horizontal axis represents the 8 bands, and the vertical axis represents the results in terms of the SSIM index. For each band, results produced by all of the demosaicking methods are grouped together. Results connected with SFA I and SFA II are plotted separately.

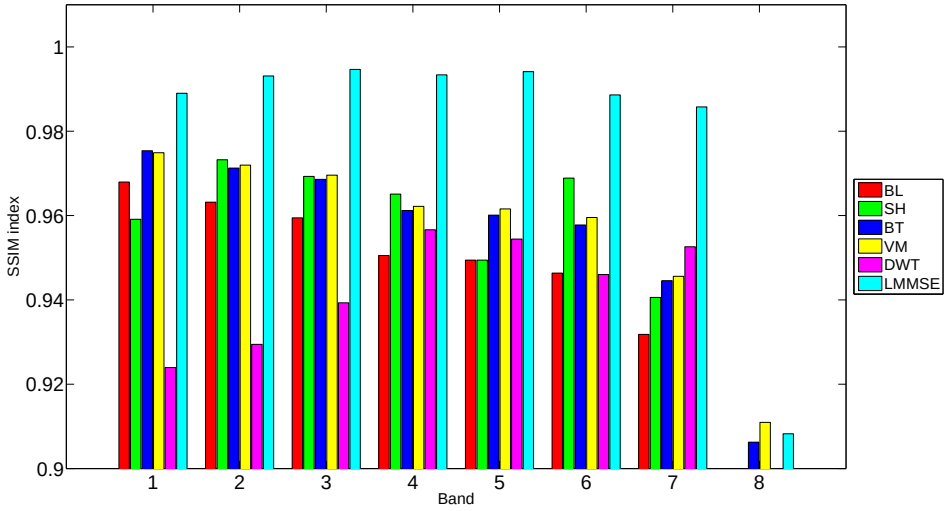

(a) SSIM indices for each band of Scene 4 mosaicked with SFA I.

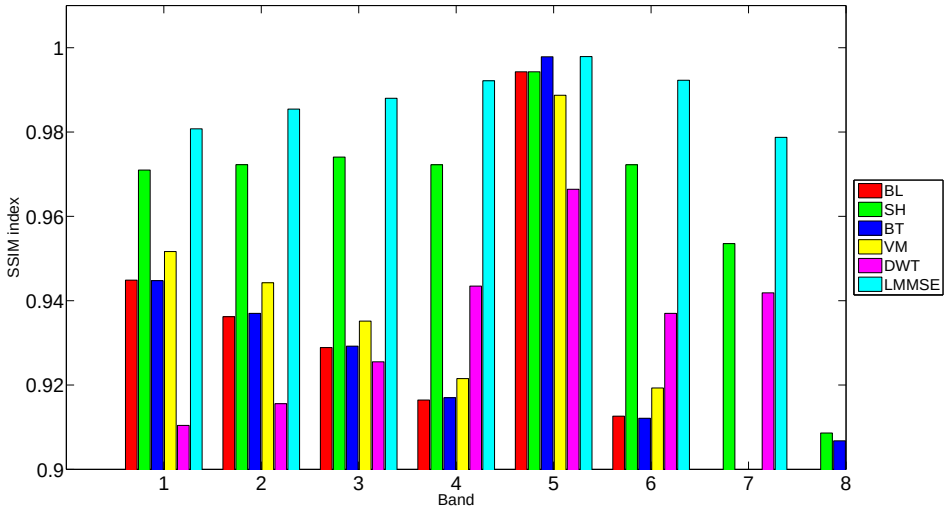

(b) SSIM indices for each band of Scene 4 mosaicked with SFA II.

Figure 11.21: Experimental results (SSIM indices) for each band of Scene 4. The horizontal axis represents the 8 bands, and the vertical axis represents the results in terms of the SSIM index. For each band, results produced by all of the demosaicking methods are grouped together. Results connected with SFA I and SFA II are plotted separately.

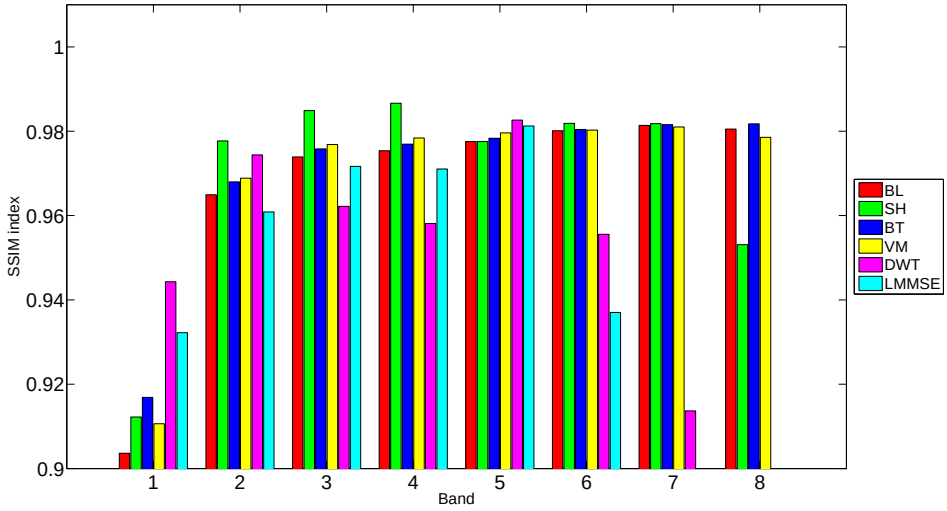

(a) SSIM indices for each band of Scene 5 mosaicked with SFA I.

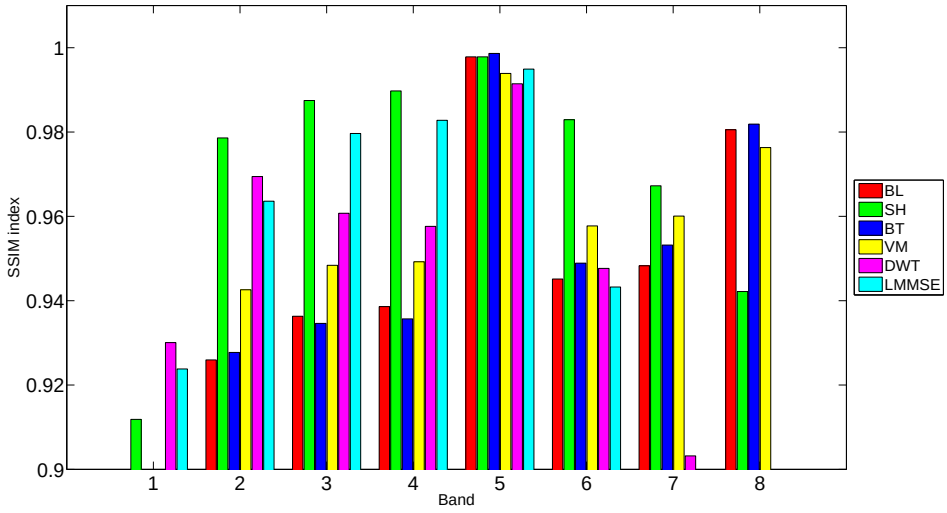

(b) SSIM indices for each band of Scene 5 mosaicked with SFA II.

Figure 11.22: Experimental results (SSIM indices) for each band of Scene 5. The horizontal axis represents the 8 bands, and the vertical axis represents the results in terms of the SSIM index. For each band, results produced by all of the demosaicking methods are grouped together. Results connected with SFA I and SFA II are plotted separately.

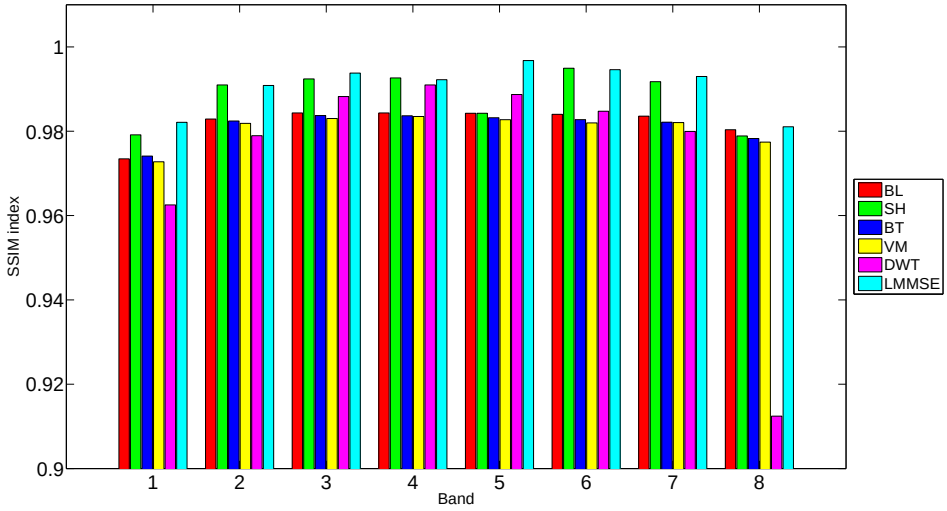

(a) SSIM indices for each band of Scene 6 mosaicked with SFA I.

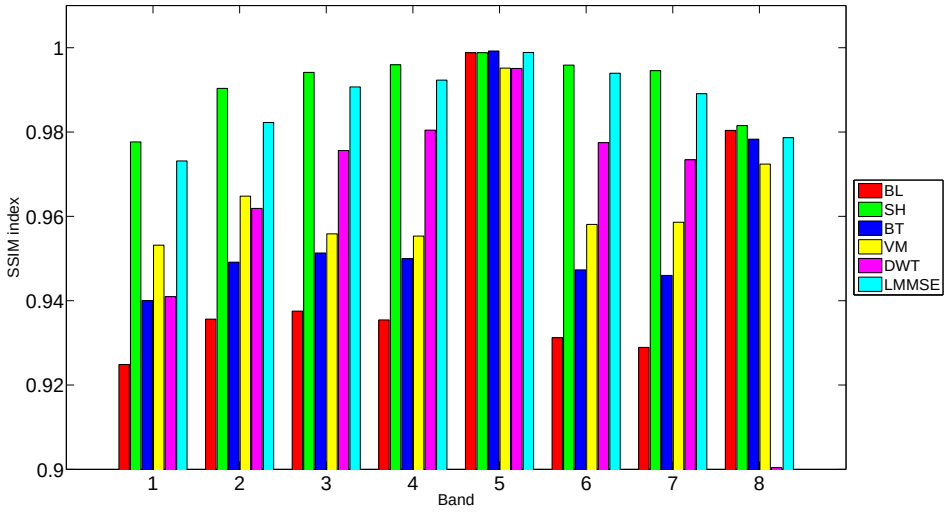

(b) SSIM indices for each band of Scene 6 mosaicked with SFA II.

Figure 11.23: Experimental results (SSIM indices) for each band of Scene 6. The horizontal axis represents the 8 bands, and the vertical axis represents the results in terms of the SSIM index. For each band, results produced by all of the demosaicking methods are grouped together. Results connected with SFA I and SFA II are plotted separately.

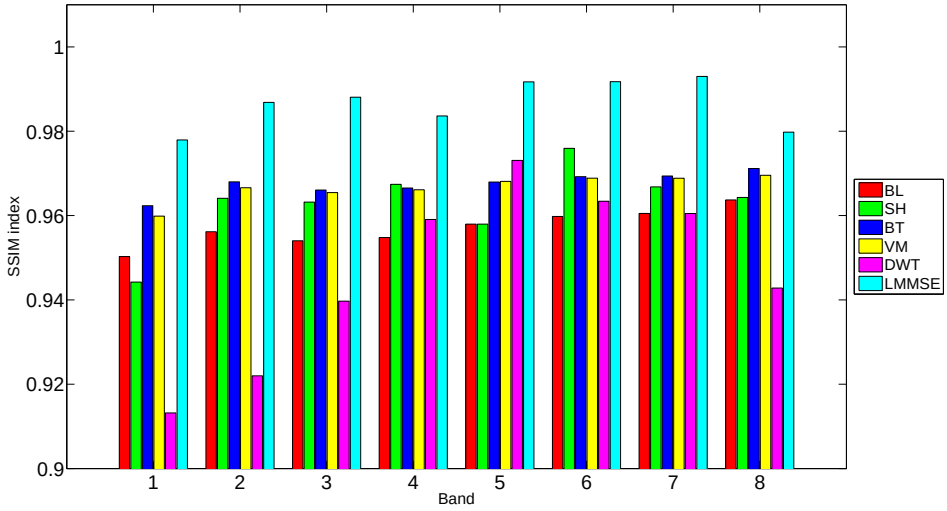

(a) SSIM indices for each band of Scene 7 mosaicked with SFA I.

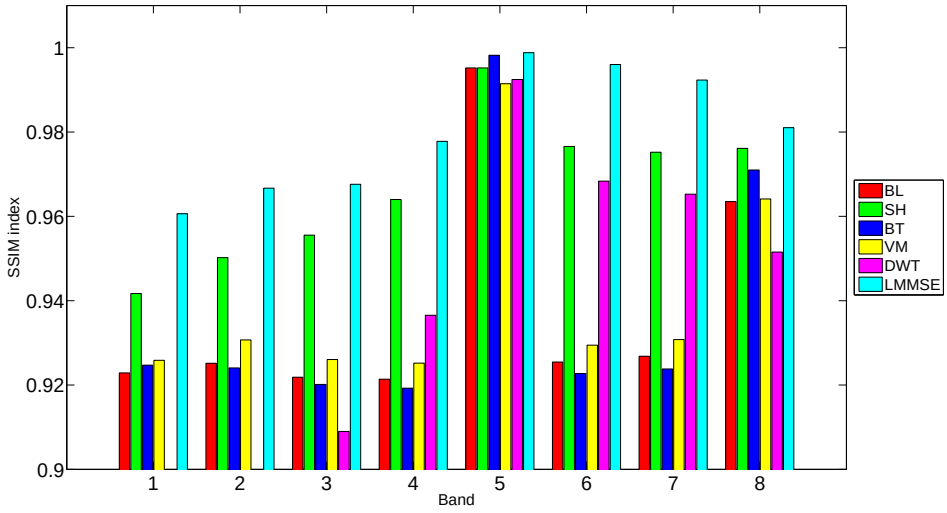

(b) SSIM indices for each band of Scene 7 mosaicked with SFA II.

Figure 11.24: Experimental results (SSIM indices) for each band of Scene 7. The horizontal axis represents the 8 bands, and the vertical axis represents the results in terms of the SSIM index. For each band, results produced by all of the demosaicking methods are grouped together. Results connected with SFA I and SFA II are plotted separately.

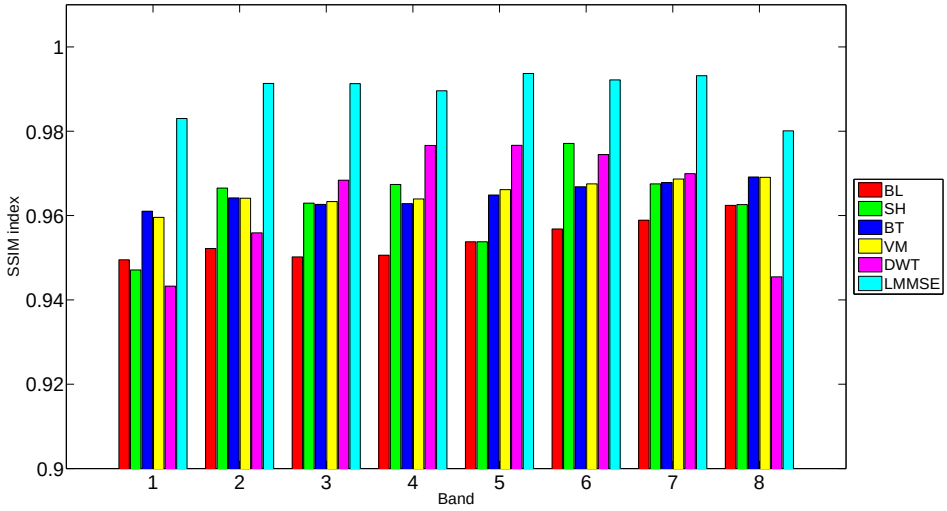

(a) SSIM indices for each band of Scene 8 mosaicked with SFA I.

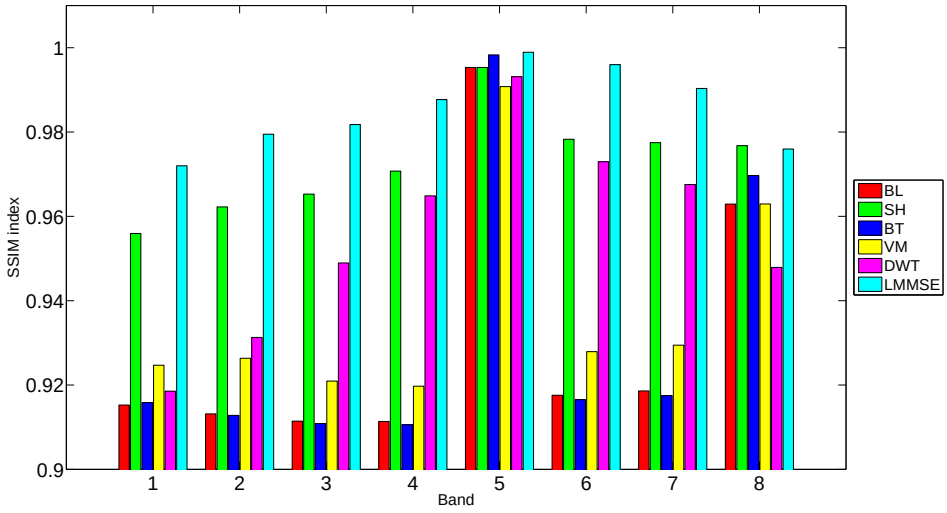

(b) SSIM indices for each band of Scene 8 mosaicked with SFA II.

Figure 11.25: Experimental results (SSIM indices) for each band of Scene 8. The horizontal axis represents the 8 bands, and the vertical axis represents the results in terms of the SSIM index. For each band, results produced by all of the demosaicking methods are grouped together. Results connected with SFA I and SFA II are plotted separately.

By far the analyses have been carried out on the basis of the results averaged among the bands. What makes a distinction between CFA and SFA imaging systems is largely, if not entirely, the number of bands. As a result, it is of particular interest to look into the results for each band of the images which may reveal more valuable information.

Figure 11.10-11.17 show the results for all scenes in terms of the PSNR. As illustrated by the graphs, there exists varying inter-band variance that peaks at 37.02 for scene 5 mosaicked with SFA II and demosaicked with BT and reaches the lowest value at 0.31 for scene 7 mosaicked with SFA I and demosaicked with DWT. The inter-band variance is significantly wider for SFA II in comparison with SFA I, 5.86 times, to be precise. The sharp contrast is mainly attributed to the increase in performance for the more densely sampled band 5 in SFA II. However, the rank order according to the inter-band variance is not affected much by the SFAs, i.e., DWT<SH<VM<BL<BT<LMMSE for SFA I, and DWT<SH<VM<BL<LMMSE<BT for SFA II. With SFA I, the performance of the methods are well-matched except LMMSE which leads to visibly lower PSNRs than others for scene 1/2/5 yet results in higher PSNRs for scene 3/4/6/7. With SFA II, the advantage of SH over other methods is ubiquitous among all bands, and interestingly, DWT mostly outperforms other methods for Band 5, as depicted by Figure 11.10-11.17. All methods achieve better results for Band 5 with SFA II compared with the results with SFA I, whereas the results of most results for the other bands decrease with varying degrees.

The results in terms of the SSIM indices are generally consistent with those in terms of the PSNRs, as demonstrated in Figure 11.18-11.25.

a	b	c	d
e	f	g	h
	i	j	k
l	m	n	o

Figure 11.26: An extraction from band 1 of Scene 1 in the absence of noise. (a) full-resolution image, (b) SFA I mosaicked image, (c) SFA I demosaicked image with BL, (d) SFA I demosaicked image with SH, (e) SFA I demosaicked image with BT, (f) SFA I demosaicked image with VM, (g) SFA I demosaicked image with DWT, (h) SFA I demosaicked image with LMMSE, (i) SFA II mosaicked image, (j) SFA II demosaicked image with BL, (k) SFA II demosaicked image with SH, (l) SFA II demosaicked image with BT, (m) SFA II demosaicked image with VM, (n) SFA II demosaicked image with DWT, (o) SFA II demosaicked image with LMMSE

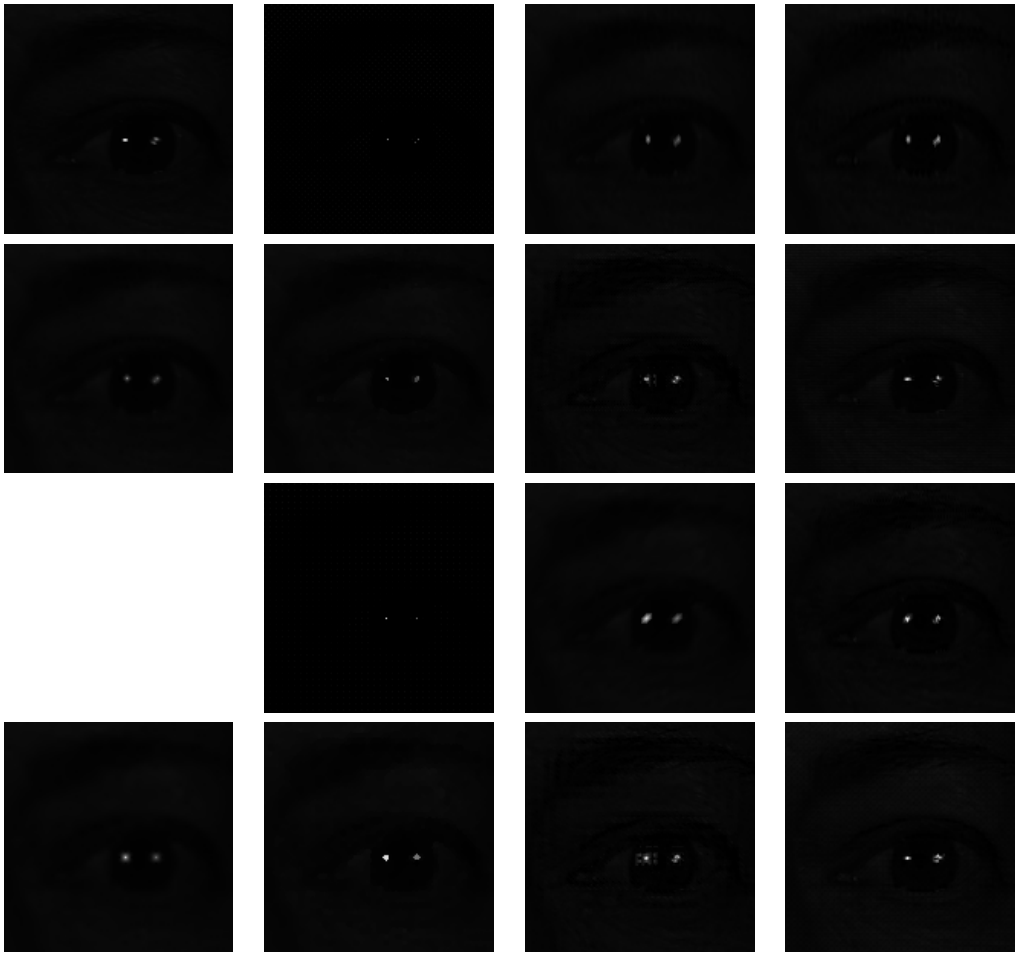

a	b	c	d
e	f	g	h
	i	j	k
l	m	n	o

Figure 11.27: An extraction from band 2 of Scene 1 in the absence of noise. (a) full-resolution image, (b) SFA I mosaicked image, (c) SFA I demosaicked image with BL, (d) SFA I demosaicked image with SH, (e) SFA I demosaicked image with BT, (f) SFA I demosaicked image with VM, (g) SFA I demosaicked image with DWT, (h) SFA I demosaicked image with LMMSE, (i) SFA II mosaicked image, (j) SFA II demosaicked image with BL, (k) SFA II demosaicked image with SH, (l) SFA II demosaicked image with BT, (m) SFA II demosaicked image with VM, (n) SFA II demosaicked image with DWT, (o) SFA II demosaicked image with LMMSE

a	b	c	d
e	f	g	h
	i	j	k
l	m	n	o

Figure 11.28: An extraction from band 3 of Scene 1 in the absence of noise. (a) full-resolution image, (b) SFA I mosaicked image, (c) SFA I demosaicked image with BL, (d) SFA I demosaicked image with SH, (e) SFA I demosaicked image with BT, (f) SFA I demosaicked image with VM, (g) SFA I demosaicked image with DWT, (h) SFA I demosaicked image with LMMSE, (i) SFA II mosaicked image, (j) SFA II demosaicked image with BL, (k) SFA II demosaicked image with SH, (l) SFA II demosaicked image with BT, (m) SFA II demosaicked image with VM, (n) SFA II demosaicked image with DWT, (o) SFA II demosaicked image with LMMSE

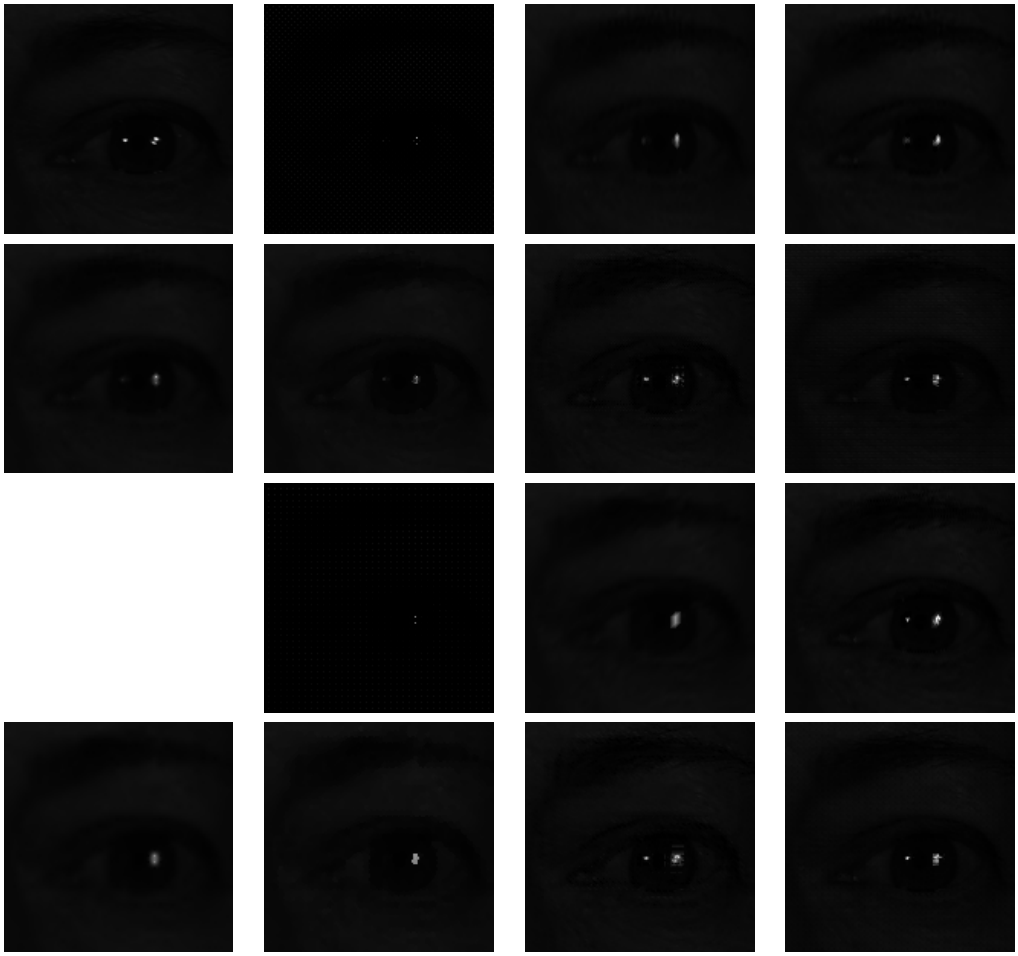

a	b	c	d
e	f	g	h
	i	j	k
l	m	n	o

Figure 11.29: An extraction from band 4 of Scene 1 in the absence of noise. (a) full-resolution image, (b) SFA I mosaicked image, (c) SFA I demosaicked image with BL, (d) SFA I demosaicked image with SH, (e) SFA I demosaicked image with BT, (f) SFA I demosaicked image with VM, (g) SFA I demosaicked image with DWT, (h) SFA I demosaicked image with LMMSE, (i) SFA II mosaicked image, (j) SFA II demosaicked image with BL, (k) SFA II demosaicked image with SH, (l) SFA II demosaicked image with BT, (m) SFA II demosaicked image with VM, (n) SFA II demosaicked image with DWT, (o) SFA II demosaicked image with LMMSE

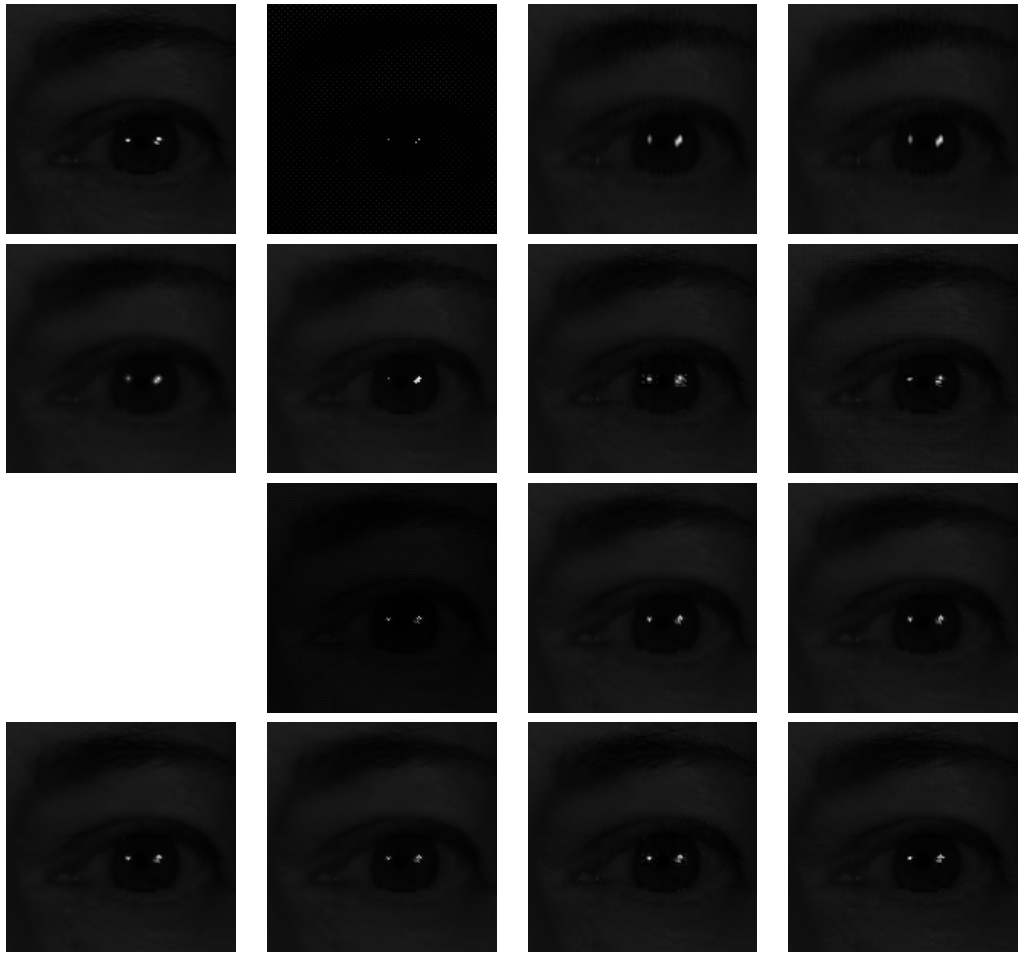

a	b	c	d
e	f	g	h
	i	j	k
l	m	n	o

Figure 11.30: An extraction from band 5 of Scene 1 in the absence of noise. (a) full-resolution image, (b) SFA I mosaicked image, (c) SFA I demosaicked image with BL, (d) SFA I demosaicked image with SH, (e) SFA I demosaicked image with BT, (f) SFA I demosaicked image with VM, (g) SFA I demosaicked image with DWT, (h) SFA I demosaicked image with LMMSE, (i) SFA II mosaicked image, (j) SFA II demosaicked image with BL, (k) SFA II demosaicked image with SH, (l) SFA II demosaicked image with BT, (m) SFA II demosaicked image with VM, (n) SFA II demosaicked image with DWT, (o) SFA II demosaicked image with LMMSE

a	b	c	d
e	f	g	h
	i	j	k
l	m	n	o

Figure 11.31: An extraction from band 6 of Scene 1 in the absence of noise. (a) full-resolution image, (b) SFA I mosaicked image, (c) SFA I demosaicked image with BL, (d) SFA I demosaicked image with SH, (e) SFA I demosaicked image with BT, (f) SFA I demosaicked image with VM, (g) SFA I demosaicked image with DWT, (h) SFA I demosaicked image with LMMSE, (i) SFA II mosaicked image, (j) SFA II demosaicked image with BL, (k) SFA II demosaicked image with SH, (l) SFA II demosaicked image with BT, (m) SFA II demosaicked image with VM, (n) SFA II demosaicked image with DWT, (o) SFA II demosaicked image with LMMSE

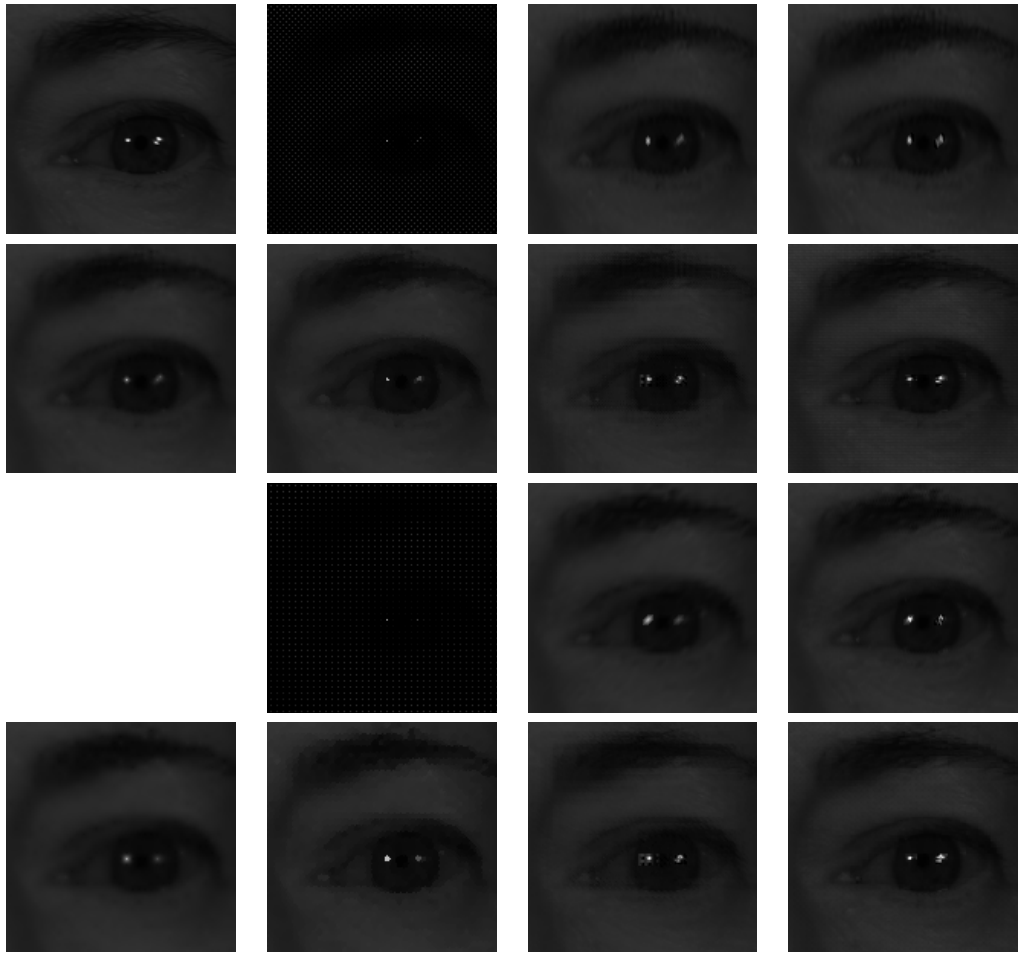

a	b	c	d
e	f	g	h
	i	j	k
l	m	n	o

Figure 11.32: An extraction from band 7 of Scene 1 in the absence of noise. (a) full-resolution image, (b) SFA I mosaicked image, (c) SFA I demosaicked image with BL, (d) SFA I demosaicked image with SH, (e) SFA I demosaicked image with BT, (f) SFA I demosaicked image with VM, (g) SFA I demosaicked image with DWT, (h) SFA I demosaicked image with LMMSE, (i) SFA II mosaicked image, (j) SFA II demosaicked image with BL, (k) SFA II demosaicked image with SH, (l) SFA II demosaicked image with BT, (m) SFA II demosaicked image with VM, (n) SFA II demosaicked image with DWT, (o) SFA II demosaicked image with LMMSE

a	b	c	d
e	f	g	h
	i	j	k
l	m	n	o

Figure 11.33: An extraction from band 8 of Scene 1 in the absence of noise. (a) full-resolution image, (b) SFA I mosaicked image, (c) SFA I demosaicked image with BL, (d) SFA I demosaicked image with SH, (e) SFA I demosaicked image with BT, (f) SFA I demosaicked image with VM, (g) SFA I demosaicked image with DWT, (h) SFA I demosaicked image with LMMSE, (i) SFA II mosaicked image, (j) SFA II demosaicked image with BL, (k) SFA II demosaicked image with SH, (l) SFA II demosaicked image with BT, (m) SFA II demosaicked image with VM, (n) SFA II demosaicked image with DWT, (o) SFA II demosaicked image with LMMSE

a	b	c	d
e	f	g	h
	i	j	k
l	m	n	o

Figure 11.34: An extraction from band 1 of Scene 2 in the absence of noise. (a) full-resolution image, (b) SFA I mosaicked image, (c) SFA I demosaicked image with BL, (d) SFA I demosaicked image with SH, (e) SFA I demosaicked image with BT, (f) SFA I demosaicked image with VM, (g) SFA I demosaicked image with DWT, (h) SFA I demosaicked image with LMMSE, (i) SFA II mosaicked image, (j) SFA II demosaicked image with BL, (k) SFA II demosaicked image with SH, (l) SFA II demosaicked image with BT, (m) SFA II demosaicked image with VM, (n) SFA II demosaicked image with DWT, (o) SFA II demosaicked image with LMMSE

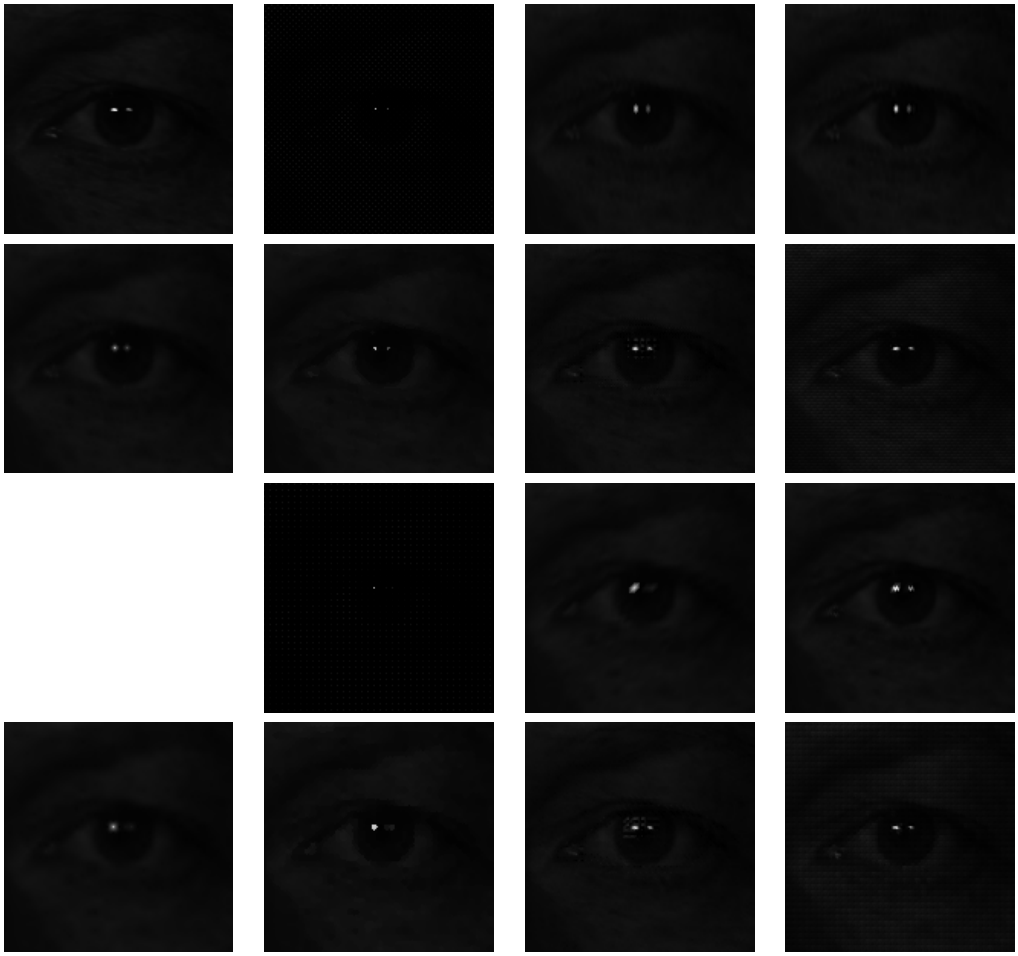

a	b	c	d
e	f	g	h
	i	j	k
l	m	n	o

Figure 11.35: An extraction from band 2 of Scene 2 in the absence of noise. (a) full-resolution image, (b) SFA I mosaicked image, (c) SFA I demosaicked image with BL, (d) SFA I demosaicked image with SH, (e) SFA I demosaicked image with BT, (f) SFA I demosaicked image with VM, (g) SFA I demosaicked image with DWT, (h) SFA I demosaicked image with LMMSE, (i) SFA II mosaicked image, (j) SFA II demosaicked image with BL, (k) SFA II demosaicked image with SH, (l) SFA II demosaicked image with BT, (m) SFA II demosaicked image with VM, (n) SFA II demosaicked image with DWT, (o) SFA II demosaicked image with LMMSE

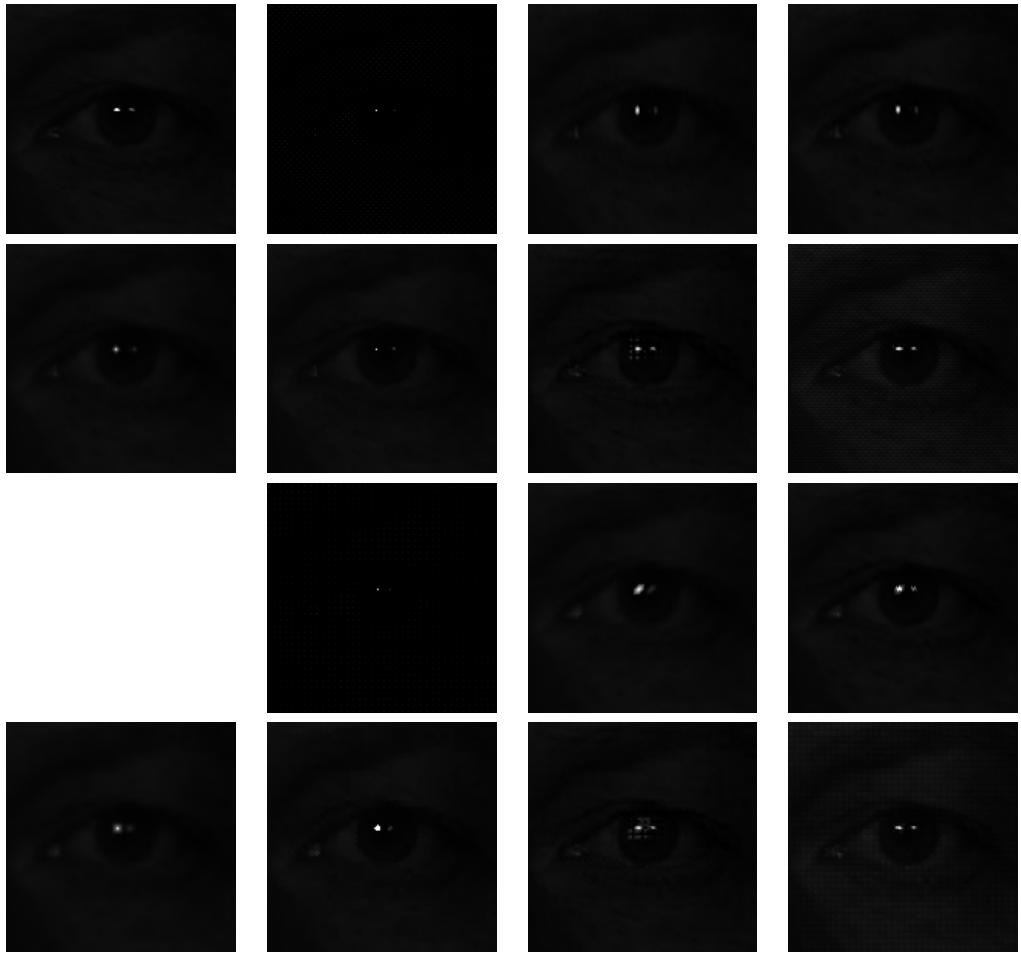

a	b	c	d
e	f	g	h
	i	j	k
l	m	n	o

Figure 11.36: An extraction from band 3 of Scene 2 in the absence of noise. (a) full-resolution image, (b) SFA I mosaicked image, (c) SFA I demosaicked image with BL, (d) SFA I demosaicked image with SH, (e) SFA I demosaicked image with BT, (f) SFA I demosaicked image with VM, (g) SFA I demosaicked image with DWT, (h) SFA I demosaicked image with LMMSE, (i) SFA II mosaicked image, (j) SFA II demosaicked image with BL, (k) SFA II demosaicked image with SH, (l) SFA II demosaicked image with BT, (m) SFA II demosaicked image with VM, (n) SFA II demosaicked image with DWT, (o) SFA II demosaicked image with LMMSE

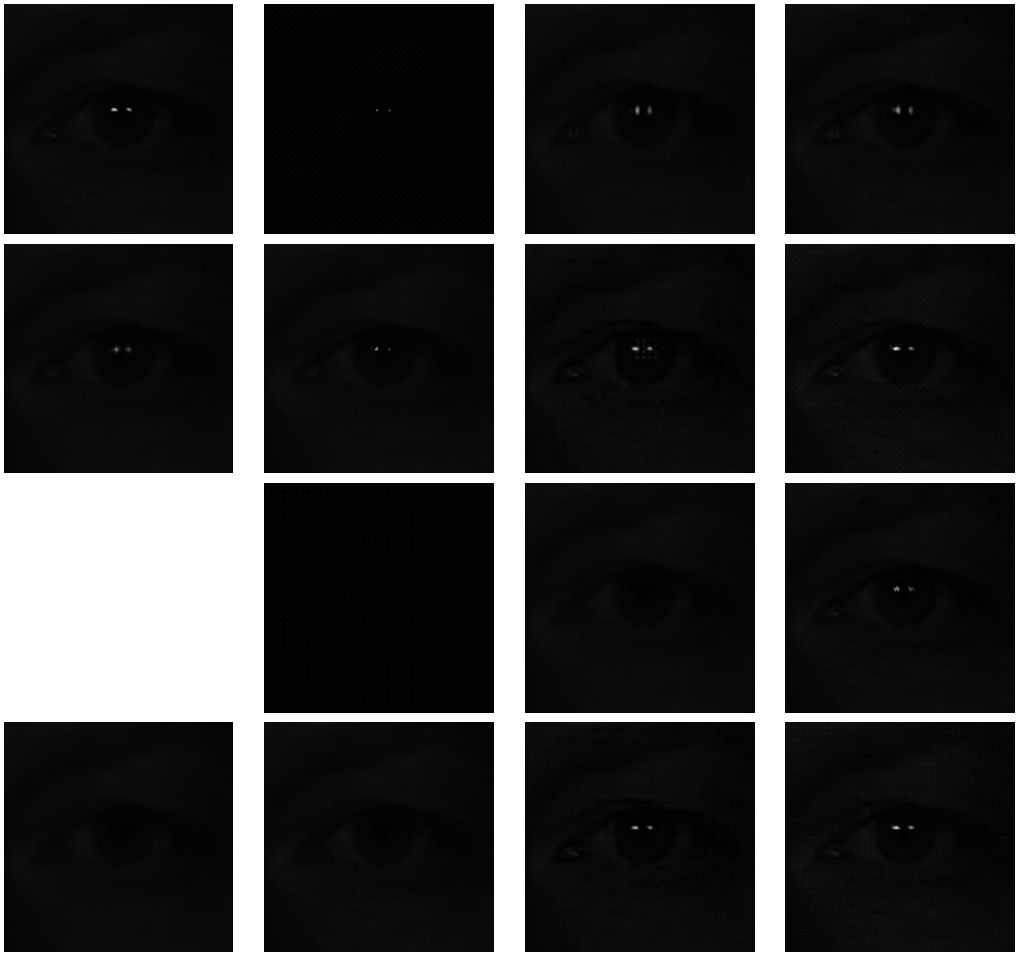

a	b	c	d
e	f	g	h
	i	j	k
l	m	n	o

Figure 11.37: An extraction from band 4 of Scene 2 in the absence of noise. (a) full-resolution image, (b) SFA I mosaicked image, (c) SFA I demosaicked image with BL, (d) SFA I demosaicked image with SH, (e) SFA I demosaicked image with BT, (f) SFA I demosaicked image with VM, (g) SFA I demosaicked image with DWT, (h) SFA I demosaicked image with LMMSE, (i) SFA II mosaicked image, (j) SFA II demosaicked image with BL, (k) SFA II demosaicked image with SH, (l) SFA II demosaicked image with BT, (m) SFA II demosaicked image with VM, (n) SFA II demosaicked image with DWT, (o) SFA II demosaicked image with LMMSE

a	b	c	d
e	f	g	h
	i	j	k
l	m	n	o

Figure 11.38: An extraction from band 5 of Scene 2 in the absence of noise. (a) full-resolution image, (b) SFA I mosaicked image, (c) SFA I demosaicked image with BL, (d) SFA I demosaicked image with SH, (e) SFA I demosaicked image with BT, (f) SFA I demosaicked image with VM, (g) SFA I demosaicked image with DWT, (h) SFA I demosaicked image with LMMSE, (i) SFA II mosaicked image, (j) SFA II demosaicked image with BL, (k) SFA II demosaicked image with SH, (l) SFA II demosaicked image with BT, (m) SFA II demosaicked image with VM, (n) SFA II demosaicked image with DWT, (o) SFA II demosaicked image with LMMSE

a	b	c	d
e	f	g	h
	i	j	k
l	m	n	o

Figure 11.39: An extraction from band 6 of Scene 2 in the absence of noise. (a) full-resolution image, (b) SFA I mosaicked image, (c) SFA I demosaicked image with BL, (d) SFA I demosaicked image with SH, (e) SFA I demosaicked image with BT, (f) SFA I demosaicked image with VM, (g) SFA I demosaicked image with DWT, (h) SFA I demosaicked image with LMMSE, (i) SFA II mosaicked image, (j) SFA II demosaicked image with BL, (k) SFA II demosaicked image with SH, (l) SFA II demosaicked image with BT, (m) SFA II demosaicked image with VM, (n) SFA II demosaicked image with DWT, (o) SFA II demosaicked image with LMMSE

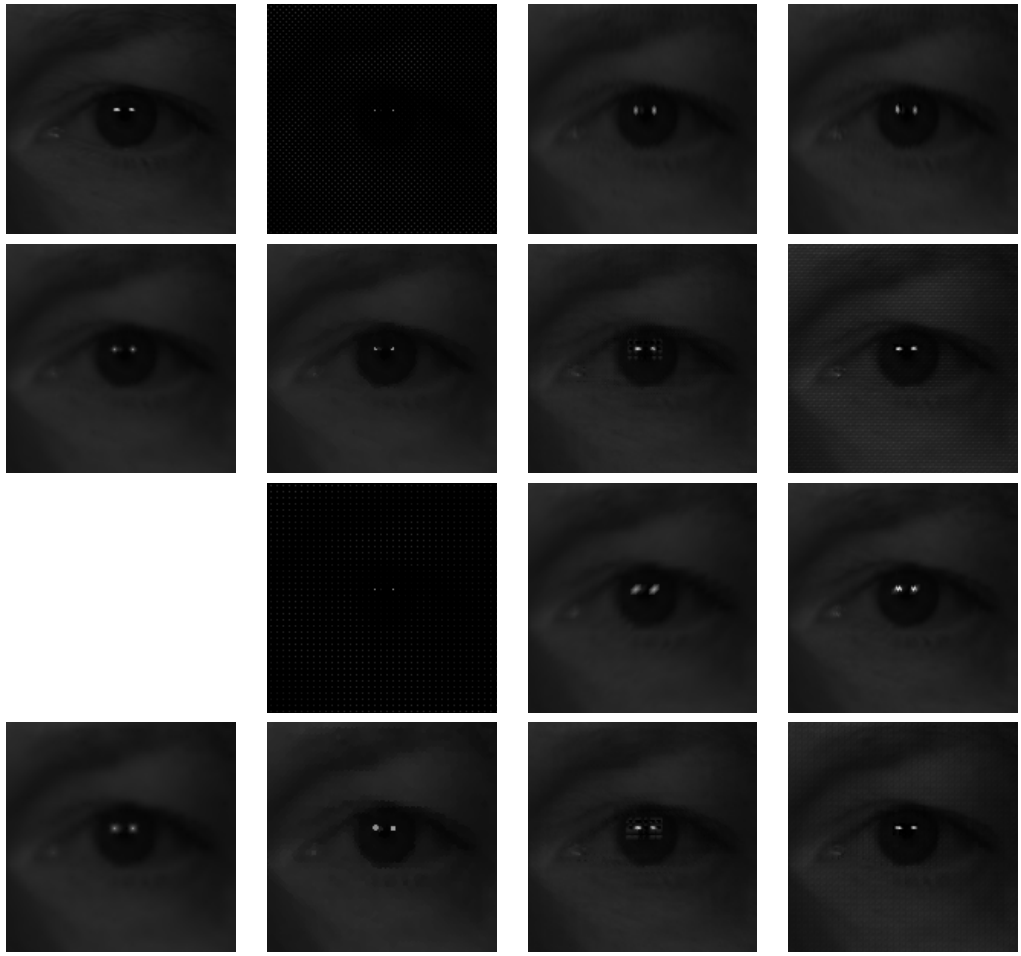

a	b	c	d
e	f	g	h
	i	j	k
l	m	n	o

Figure 11.40: An extraction from band 7 of Scene 2 in the absence of noise. (a) full-resolution image, (b) SFA I mosaicked image, (c) SFA I demosaicked image with BL, (d) SFA I demosaicked image with SH, (e) SFA I demosaicked image with BT, (f) SFA I demosaicked image with VM, (g) SFA I demosaicked image with DWT, (h) SFA I demosaicked image with LMMSE, (i) SFA II mosaicked image, (j) SFA II demosaicked image with BL, (k) SFA II demosaicked image with SH, (l) SFA II demosaicked image with BT, (m) SFA II demosaicked image with VM, (n) SFA II demosaicked image with DWT, (o) SFA II demosaicked image with LMMSE

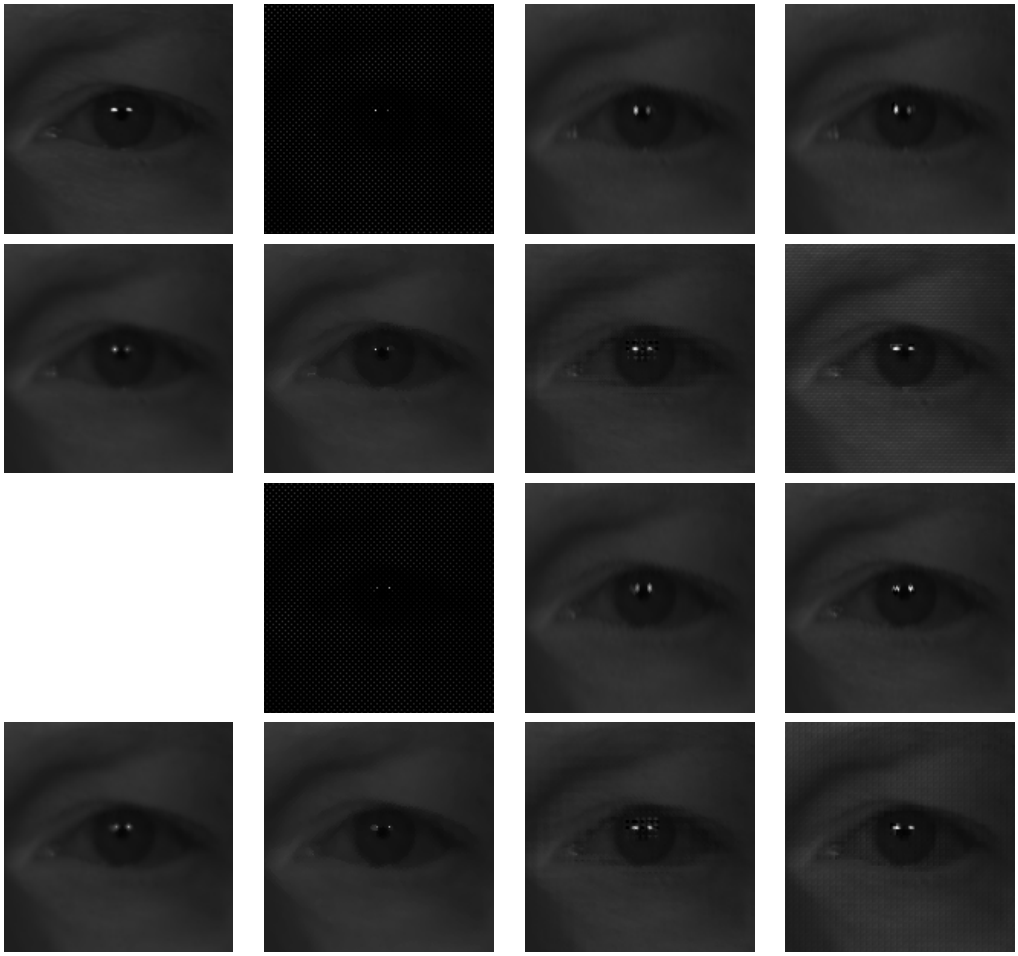

a	b	c	d
e	f	g	h
	i	j	k
l	m	n	o

Figure 11.41: An extraction from band 8 of Scene 2 in the absence of noise. (a) full-resolution image, (b) SFA I mosaicked image, (c) SFA I demosaicked image with BL, (d) SFA I demosaicked image with SH, (e) SFA I demosaicked image with BT, (f) SFA I demosaicked image with VM, (g) SFA I demosaicked image with DWT, (h) SFA I demosaicked image with LMMSE, (i) SFA II mosaicked image, (j) SFA II demosaicked image with BL, (k) SFA II demosaicked image with SH, (l) SFA II demosaicked image with BT, (m) SFA II demosaicked image with VM, (n) SFA II demosaicked image with DWT, (o) SFA II demosaicked image with LMMSE

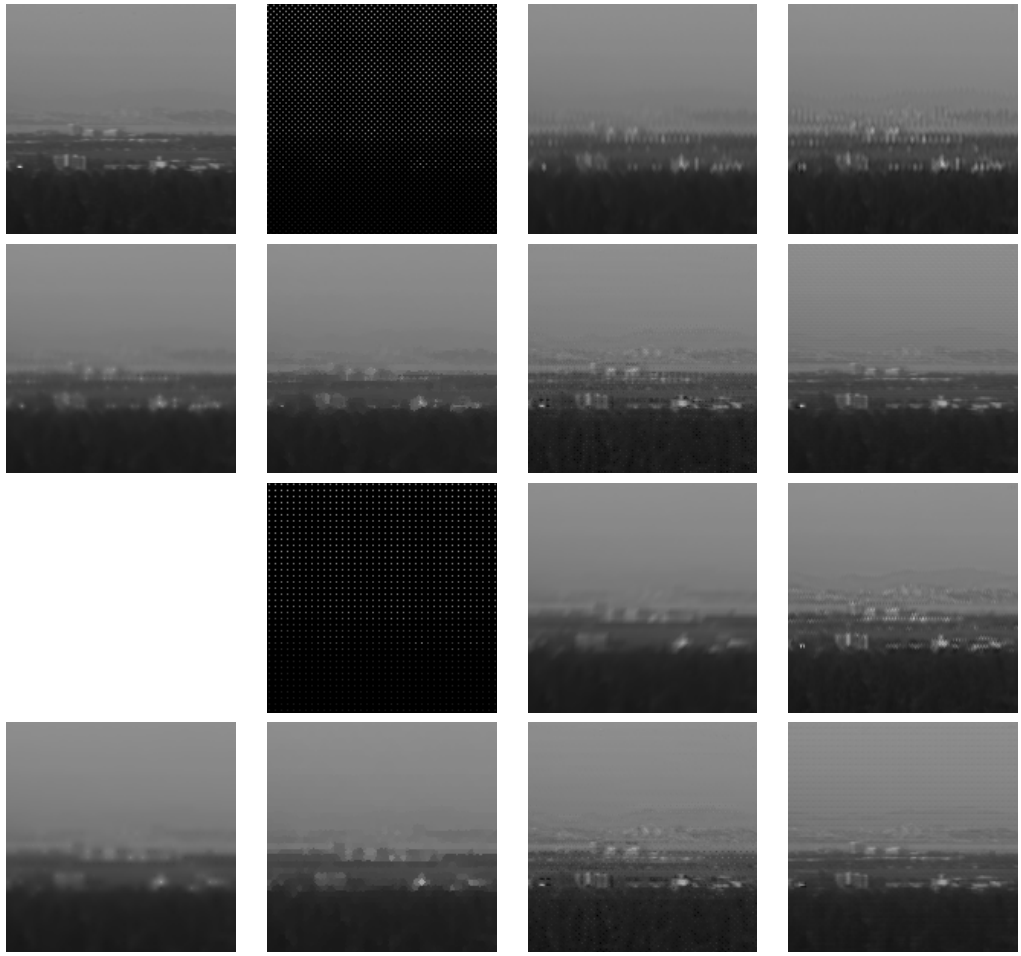

a	b	c	d
e	f	g	h
	i	j	k
l	m	n	o

Figure 11.42: An extraction from band 1 of Scene 3 in the absence of noise. (a) full-resolution image, (b) SFA I mosaicked image, (c) SFA I demosaicked image with BL, (d) SFA I demosaicked image with SH, (e) SFA I demosaicked image with BT, (f) SFA I demosaicked image with VM, (g) SFA I demosaicked image with DWT, (h) SFA I demosaicked image with LMMSE, (i) SFA II mosaicked image, (j) SFA II demosaicked image with BL, (k) SFA II demosaicked image with SH, (l) SFA II demosaicked image with BT, (m) SFA II demosaicked image with VM, (n) SFA II demosaicked image with DWT, (o) SFA II demosaicked image with LMMSE

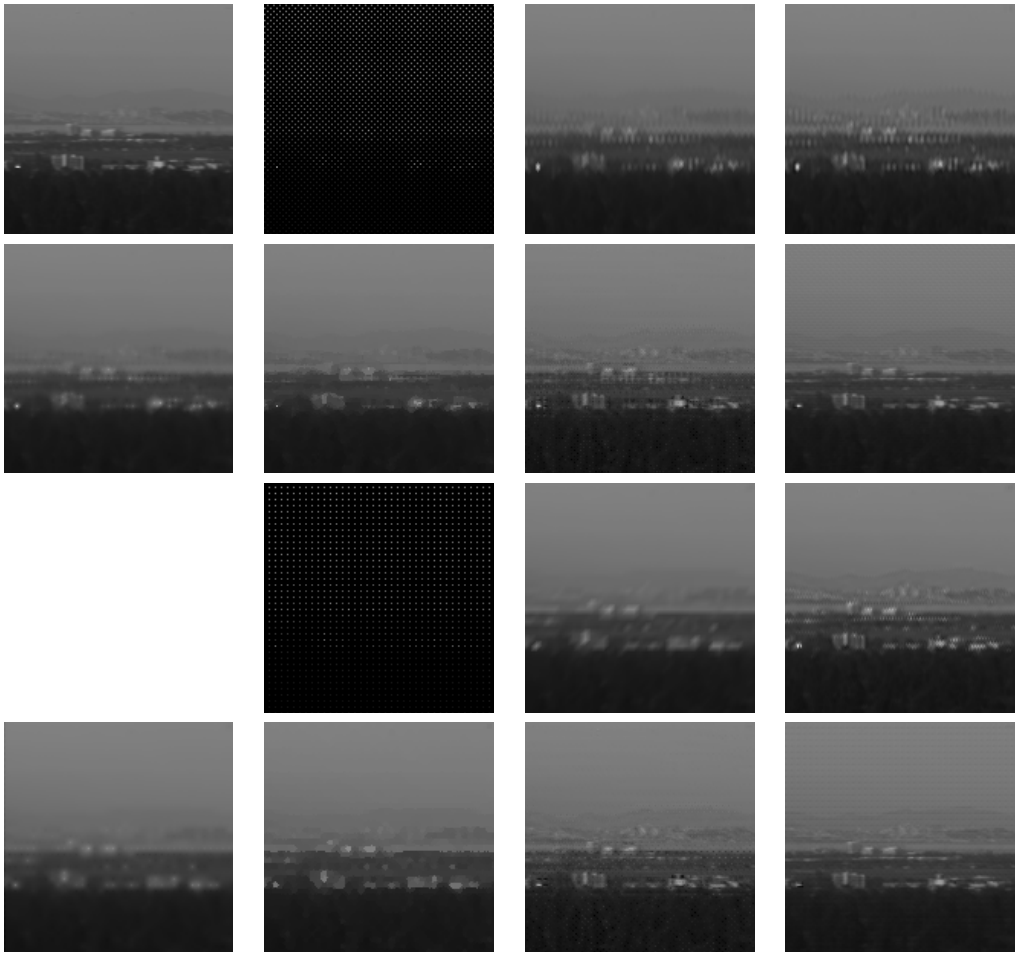

a	b	c	d
e	f	g	h
	i	j	k
l	m	n	o

Figure 11.43: An extraction from band 2 of Scene 3 in the absence of noise. (a) full-resolution image, (b) SFA I mosaicked image, (c) SFA I demosaicked image with BL, (d) SFA I demosaicked image with SH, (e) SFA I demosaicked image with BT, (f) SFA I demosaicked image with VM, (g) SFA I demosaicked image with DWT, (h) SFA I demosaicked image with LMMSE, (i) SFA II mosaicked image, (j) SFA II demosaicked image with BL, (k) SFA II demosaicked image with SH, (l) SFA II demosaicked image with BT, (m) SFA II demosaicked image with VM, (n) SFA II demosaicked image with DWT, (o) SFA II demosaicked image with LMMSE

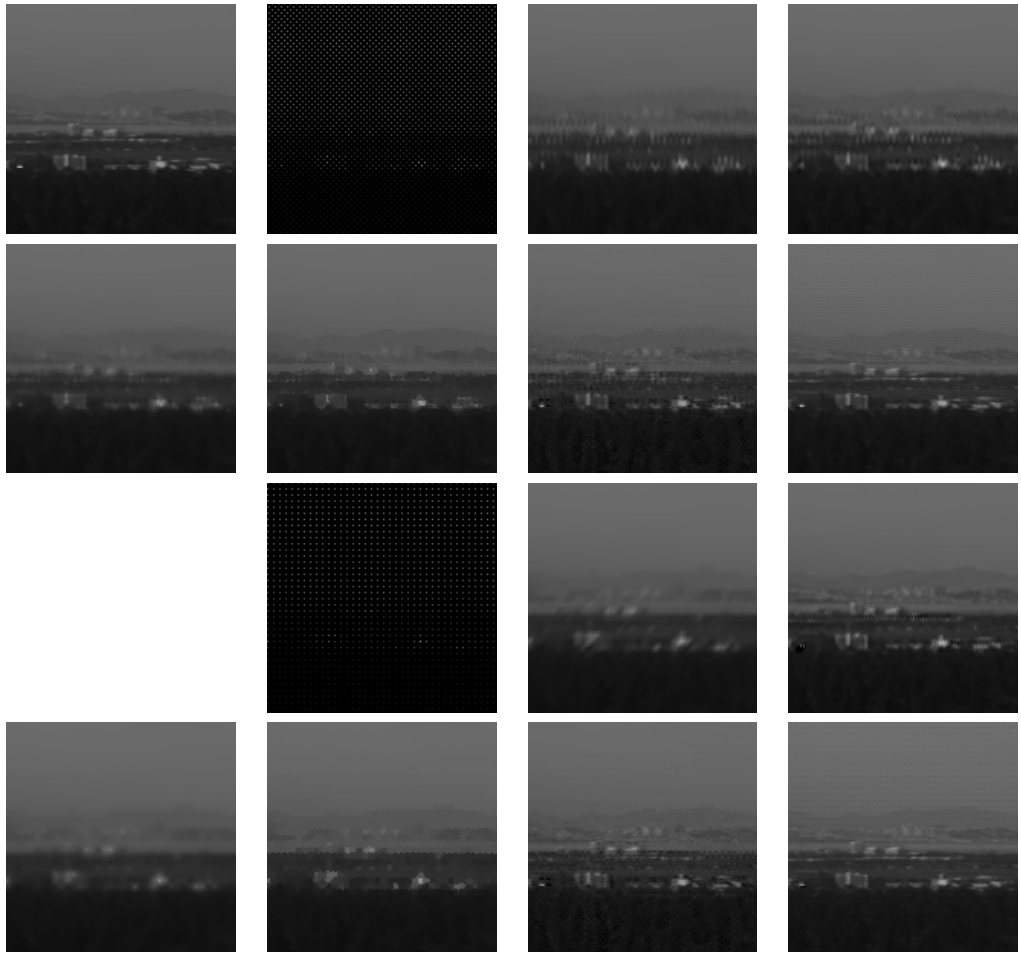

a	b	c	d
e	f	g	h
	i	j	k
l	m	n	o

Figure 11.44: An extraction from band 3 of Scene 3 in the absence of noise. (a) full-resolution image, (b) SFA I mosaicked image, (c) SFA I demosaicked image with BL, (d) SFA I demosaicked image with SH, (e) SFA I demosaicked image with BT, (f) SFA I demosaicked image with VM, (g) SFA I demosaicked image with DWT, (h) SFA I demosaicked image with LMMSE, (i) SFA II mosaicked image, (j) SFA II demosaicked image with BL, (k) SFA II demosaicked image with SH, (l) SFA II demosaicked image with BT, (m) SFA II demosaicked image with VM, (n) SFA II demosaicked image with DWT, (o) SFA II demosaicked image with LMMSE

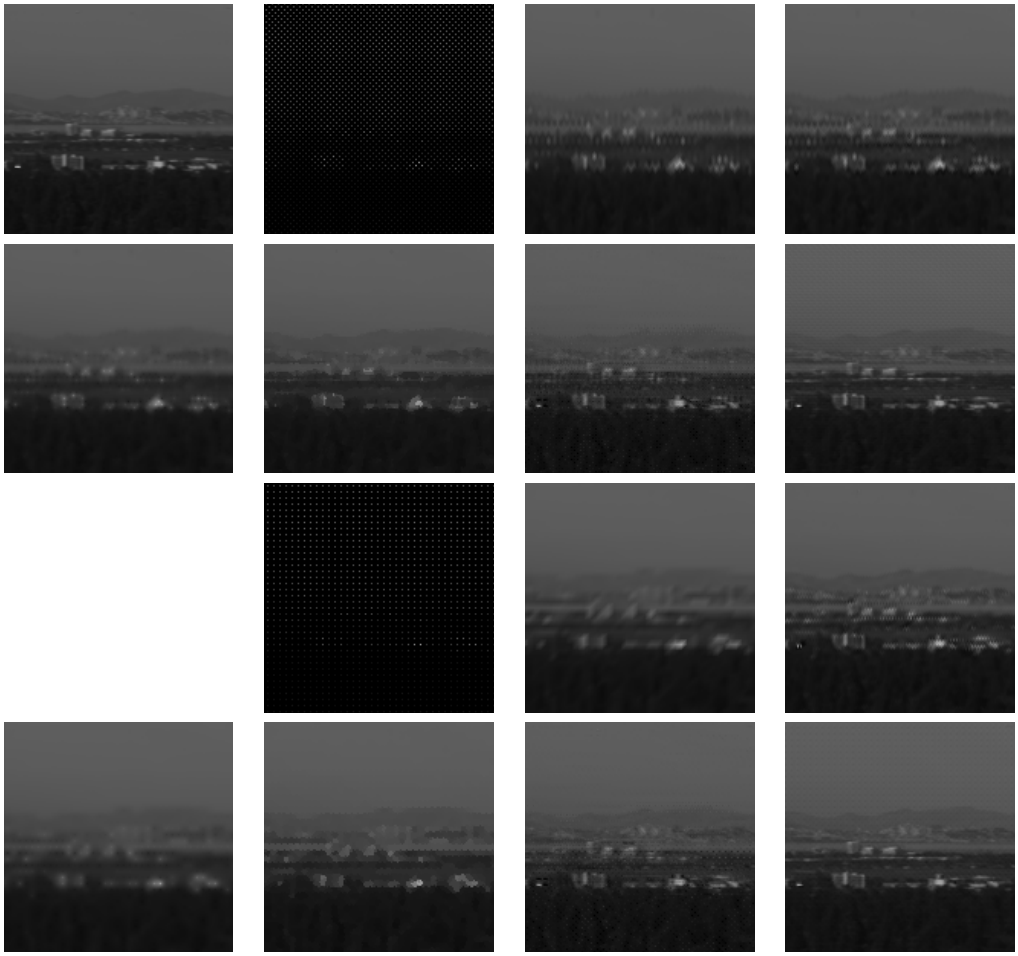

a	b	c	d
e	f	g	h
	i	j	k
l	m	n	o

Figure 11.45: An extraction from band 4 of Scene 3 in the absence of noise. (a) full-resolution image, (b) SFA I mosaicked image, (c) SFA I demosaicked image with BL, (d) SFA I demosaicked image with SH, (e) SFA I demosaicked image with BT, (f) SFA I demosaicked image with VM, (g) SFA I demosaicked image with DWT, (h) SFA I demosaicked image with LMMSE, (i) SFA II mosaicked image, (j) SFA II demosaicked image with BL, (k) SFA II demosaicked image with SH, (l) SFA II demosaicked image with BT, (m) SFA II demosaicked image with VM, (n) SFA II demosaicked image with DWT, (o) SFA II demosaicked image with LMMSE

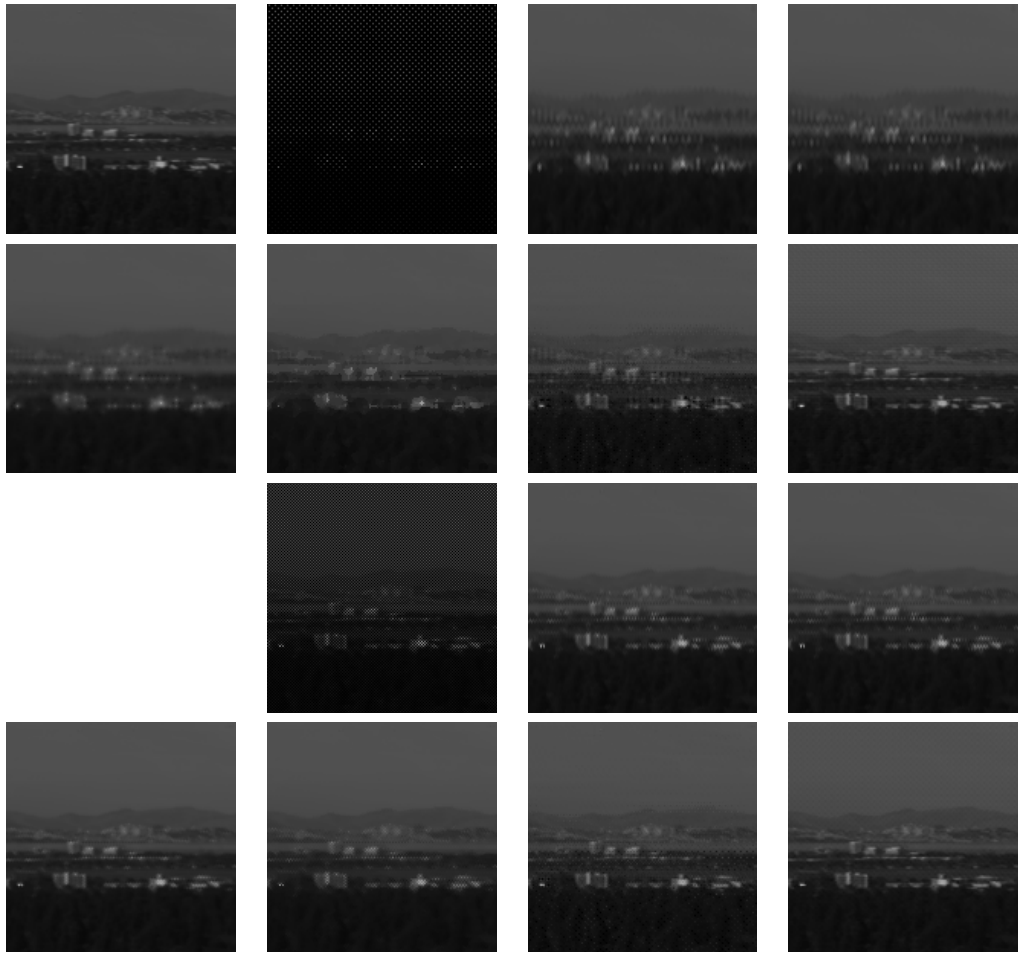

a	b	c	d
e	f	g	h
	i	j	k
l	m	n	o

Figure 11.46: An extraction from band 5 of Scene 3 in the absence of noise. (a) full-resolution image, (b) SFA I mosaicked image, (c) SFA I demosaicked image with BL, (d) SFA I demosaicked image with SH, (e) SFA I demosaicked image with BT, (f) SFA I demosaicked image with VM, (g) SFA I demosaicked image with DWT, (h) SFA I demosaicked image with LMMSE, (i) SFA II mosaicked image, (j) SFA II demosaicked image with BL, (k) SFA II demosaicked image with SH, (l) SFA II demosaicked image with BT, (m) SFA II demosaicked image with VM, (n) SFA II demosaicked image with DWT, (o) SFA II demosaicked image with LMMSE

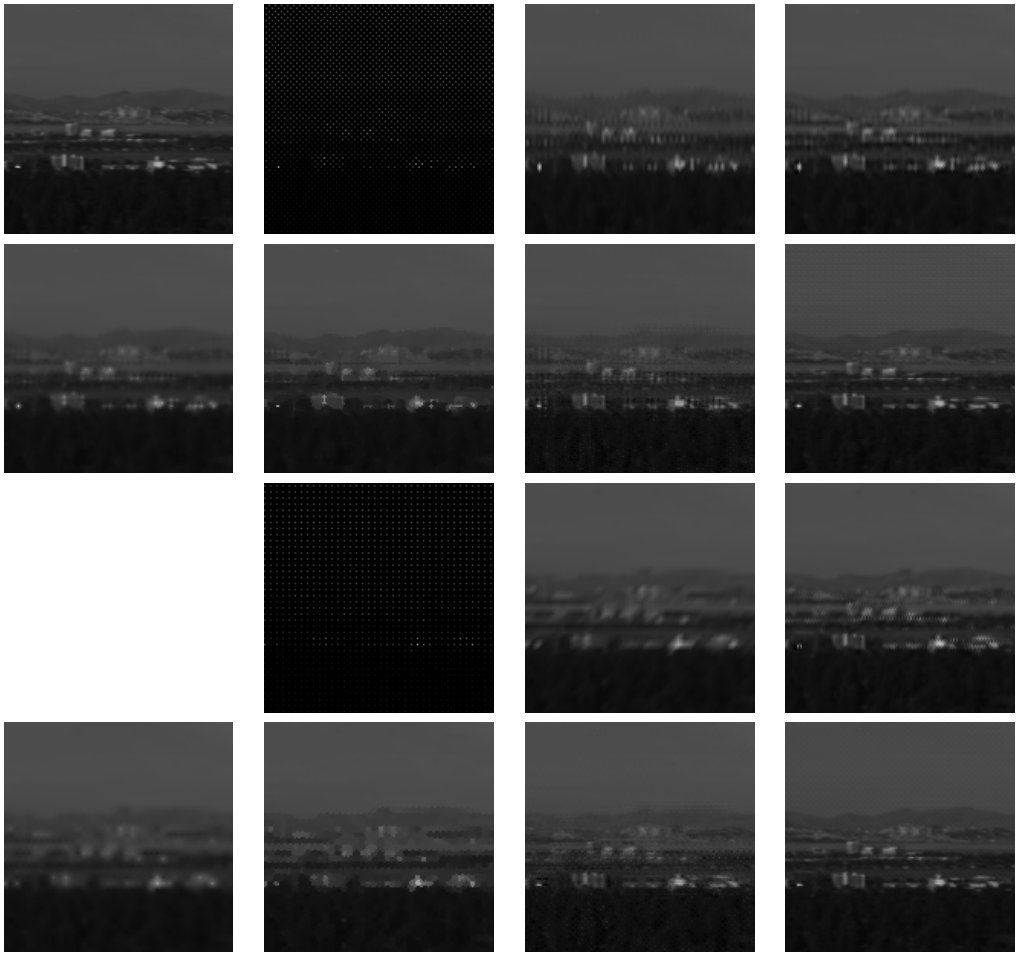

a	b	c	d
e	f	g	h
	i	j	k
l	m	n	o

Figure 11.47: An extraction from band 6 of Scene 3 in the absence of noise. (a) full-resolution image, (b) SFA I mosaicked image, (c) SFA I demosaicked image with BL, (d) SFA I demosaicked image with SH, (e) SFA I demosaicked image with BT, (f) SFA I demosaicked image with VM, (g) SFA I demosaicked image with DWT, (h) SFA I demosaicked image with LMMSE, (i) SFA II mosaicked image, (j) SFA II demosaicked image with BL, (k) SFA II demosaicked image with SH, (l) SFA II demosaicked image with BT, (m) SFA II demosaicked image with VM, (n) SFA II demosaicked image with DWT, (o) SFA II demosaicked image with LMMSE

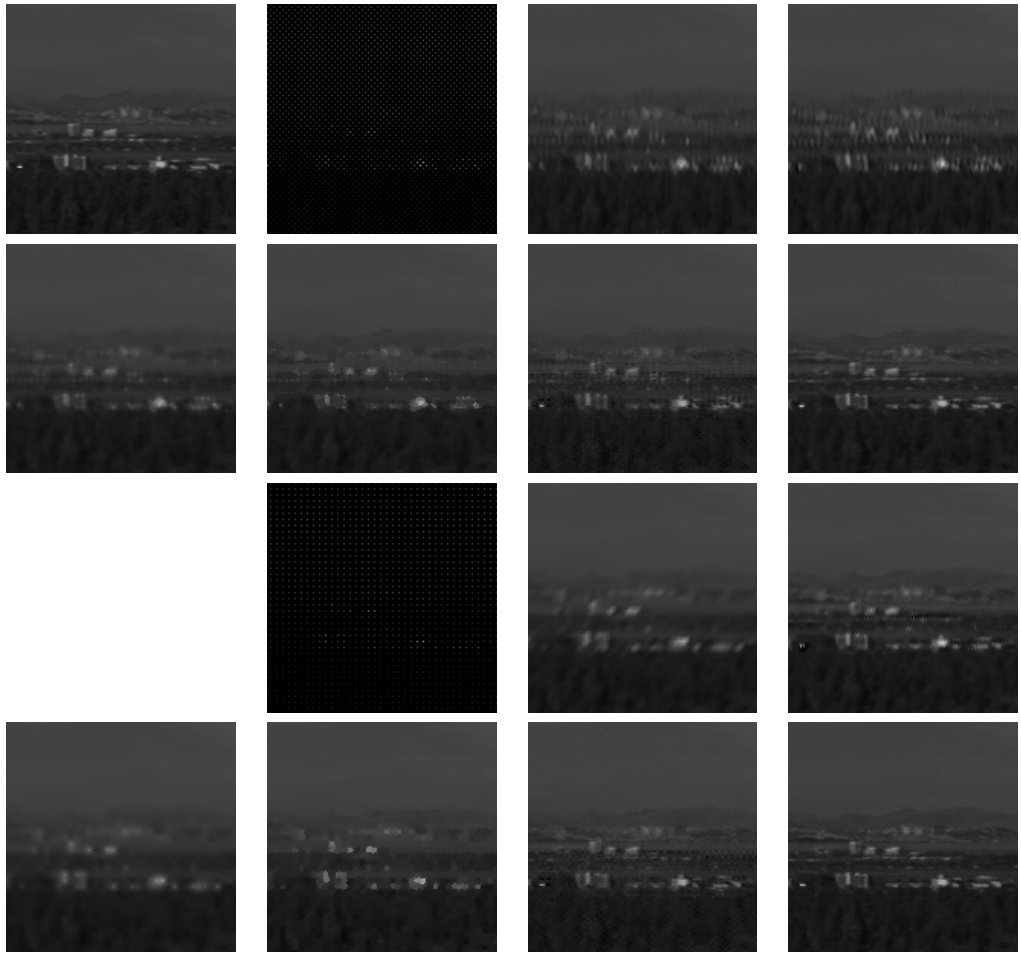

a	b	c	d
e	f	g	h
	i	j	k
l	m	n	o

Figure 11.48: An extraction from band 7 of Scene 3 in the absence of noise. (a) full-resolution image, (b) SFA I mosaicked image, (c) SFA I demosaicked image with BL, (d) SFA I demosaicked image with SH, (e) SFA I demosaicked image with BT, (f) SFA I demosaicked image with VM, (g) SFA I demosaicked image with DWT, (h) SFA I demosaicked image with LMMSE, (i) SFA II mosaicked image, (j) SFA II demosaicked image with BL, (k) SFA II demosaicked image with SH, (l) SFA II demosaicked image with BT, (m) SFA II demosaicked image with VM, (n) SFA II demosaicked image with DWT, (o) SFA II demosaicked image with LMMSE

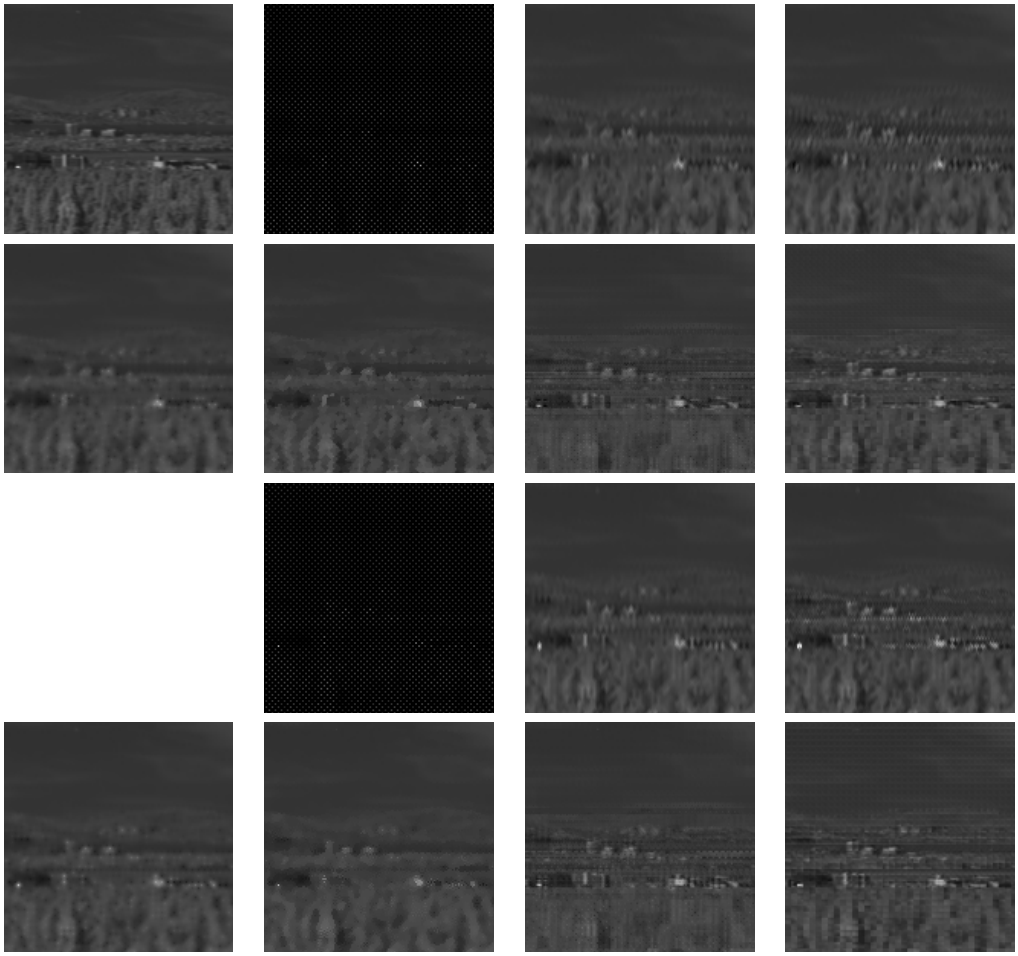

a	b	c	d
e	f	g	h
	i	j	k
l	m	n	o

Figure 11.49: An extraction from band 8 of Scene 3 in the absence of noise. (a) full-resolution image, (b) SFA I mosaicked image, (c) SFA I demosaicked image with BL, (d) SFA I demosaicked image with SH, (e) SFA I demosaicked image with BT, (f) SFA I demosaicked image with VM, (g) SFA I demosaicked image with DWT, (h) SFA I demosaicked image with LMMSE, (i) SFA II mosaicked image, (j) SFA II demosaicked image with BL, (k) SFA II demosaicked image with SH, (l) SFA II demosaicked image with BT, (m) SFA II demosaicked image with VM, (n) SFA II demosaicked image with DWT, (o) SFA II demosaicked image with LMMSE

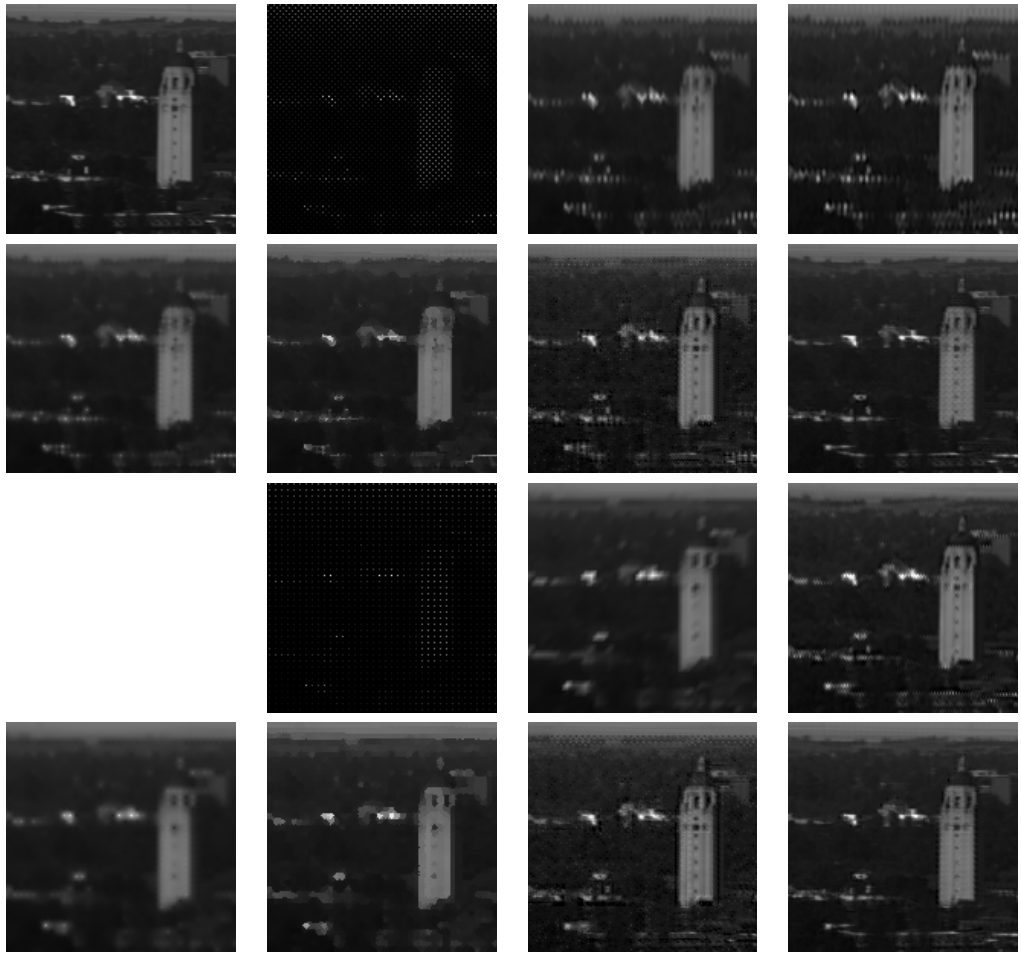

a	b	c	d
e	f	g	h
	i	j	k
l	m	n	o

Figure 11.50: An extraction from band 1 of Scene 4 in the absence of noise. (a) full-resolution image, (b) SFA I mosaicked image, (c) SFA I demosaicked image with BL, (d) SFA I demosaicked image with SH, (e) SFA I demosaicked image with BT, (f) SFA I demosaicked image with VM, (g) SFA I demosaicked image with DWT, (h) SFA I demosaicked image with LMMSE, (i) SFA II mosaicked image, (j) SFA II demosaicked image with BL, (k) SFA II demosaicked image with SH, (l) SFA II demosaicked image with BT, (m) SFA II demosaicked image with VM, (n) SFA II demosaicked image with DWT, (o) SFA II demosaicked image with LMMSE

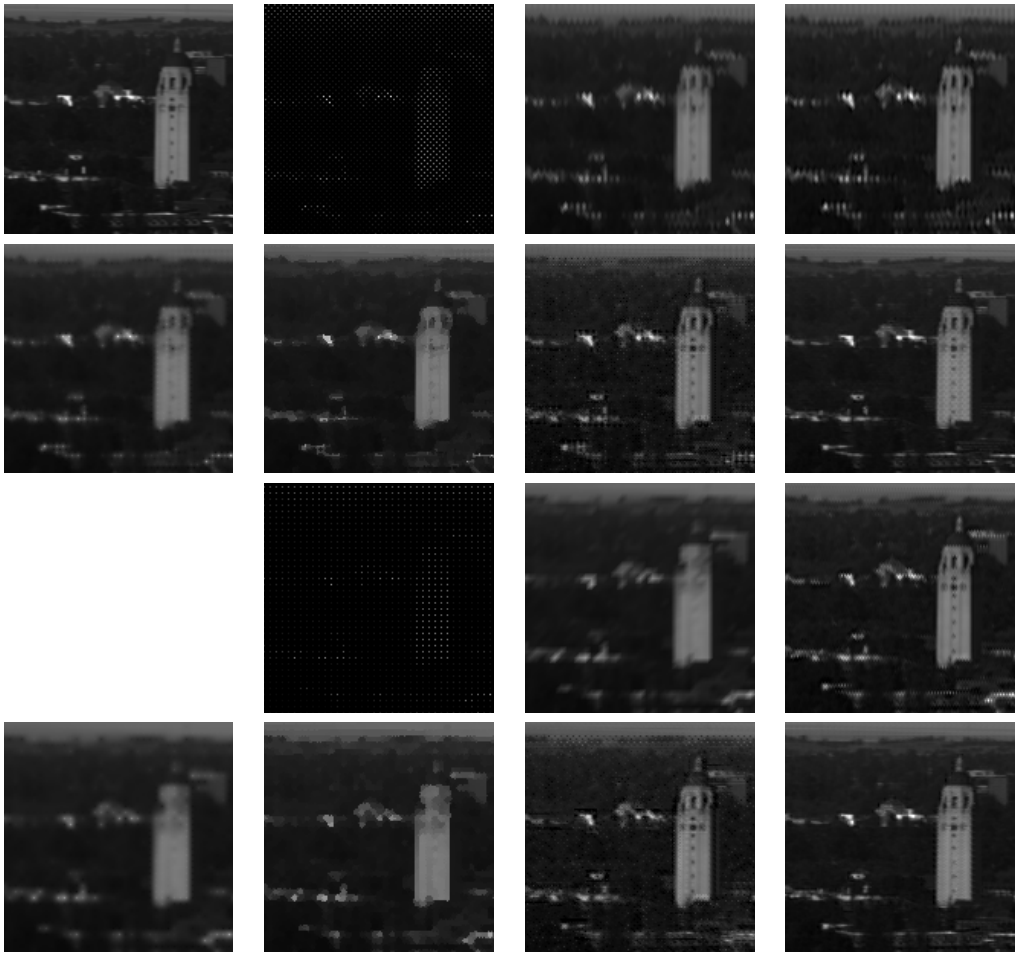

a	b	c	d
e	f	g	h
	i	j	k
l	m	n	o

Figure 11.51: An extraction from band 2 of Scene 4 in the absence of noise. (a) full-resolution image, (b) SFA I mosaicked image, (c) SFA I demosaicked image with BL, (d) SFA I demosaicked image with SH, (e) SFA I demosaicked image with BT, (f) SFA I demosaicked image with VM, (g) SFA I demosaicked image with DWT, (h) SFA I demosaicked image with LMMSE, (i) SFA II mosaicked image, (j) SFA II demosaicked image with BL, (k) SFA II demosaicked image with SH, (l) SFA II demosaicked image with BT, (m) SFA II demosaicked image with VM, (n) SFA II demosaicked image with DWT, (o) SFA II demosaicked image with LMMSE

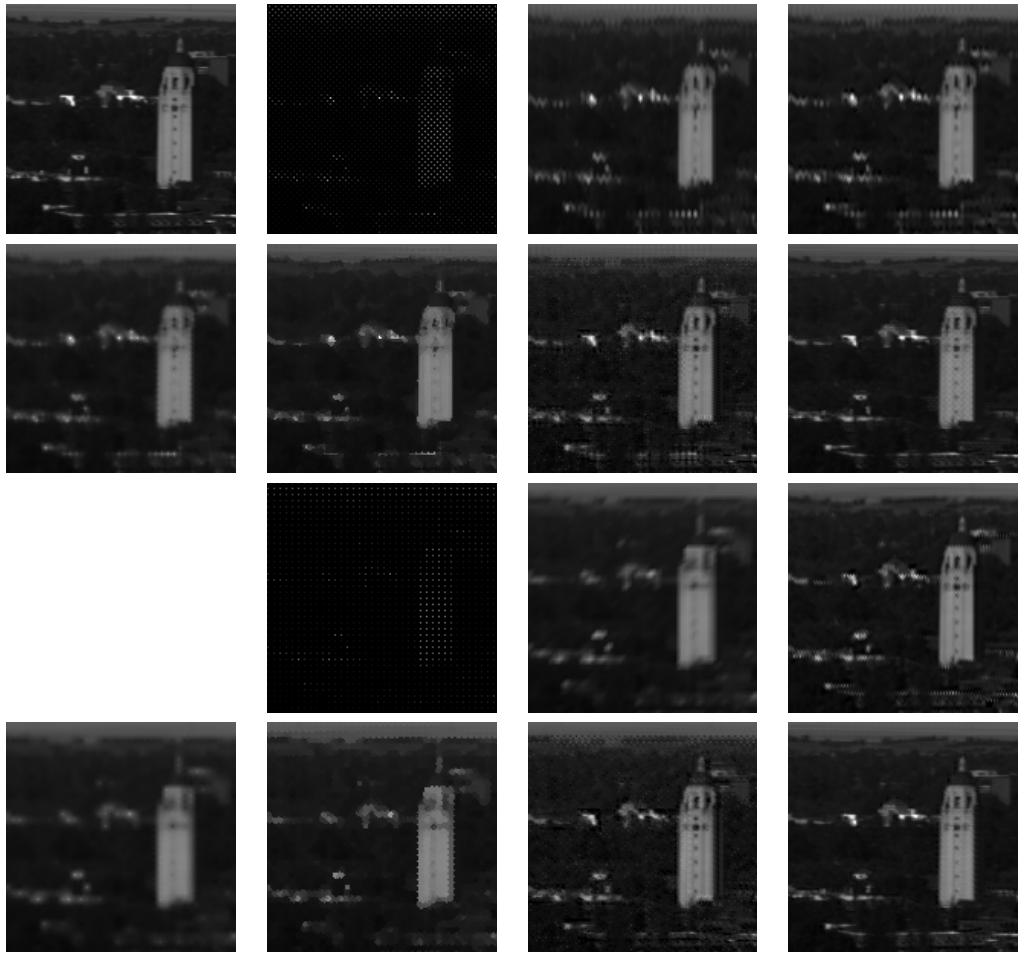

a	b	c	d
e	f	g	h
	i	j	k
l	m	n	o

Figure 11.52: An extraction from band 3 of Scene 4 in the absence of noise. (a) full-resolution image, (b) SFA I mosaicked image, (c) SFA I demosaicked image with BL, (d) SFA I demosaicked image with SH, (e) SFA I demosaicked image with BT, (f) SFA I demosaicked image with VM, (g) SFA I demosaicked image with DWT, (h) SFA I demosaicked image with LMMSE, (i) SFA II mosaicked image, (j) SFA II demosaicked image with BL, (k) SFA II demosaicked image with SH, (l) SFA II demosaicked image with BT, (m) SFA II demosaicked image with VM, (n) SFA II demosaicked image with DWT, (o) SFA II demosaicked image with LMMSE

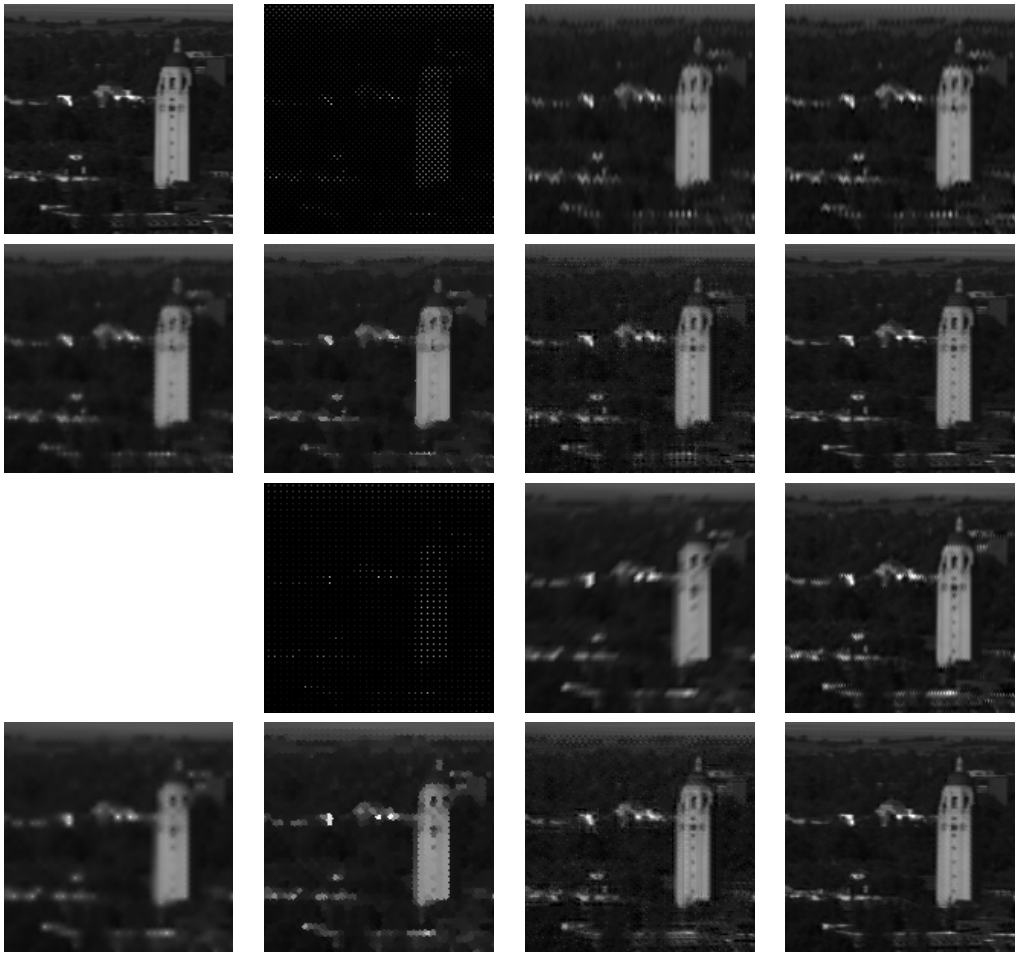

a	b	c	d
e	f	g	h
	i	j	k
l	m	n	o

Figure 11.53: An extraction from band 4 of Scene 4 in the absence of noise. (a) full-resolution image, (b) SFA I mosaicked image, (c) SFA I demosaicked image with BL, (d) SFA I demosaicked image with SH, (e) SFA I demosaicked image with BT, (f) SFA I demosaicked image with VM, (g) SFA I demosaicked image with DWT, (h) SFA I demosaicked image with LMMSE, (i) SFA II mosaicked image, (j) SFA II demosaicked image with BL, (k) SFA II demosaicked image with SH, (l) SFA II demosaicked image with BT, (m) SFA II demosaicked image with VM, (n) SFA II demosaicked image with DWT, (o) SFA II demosaicked image with LMMSE

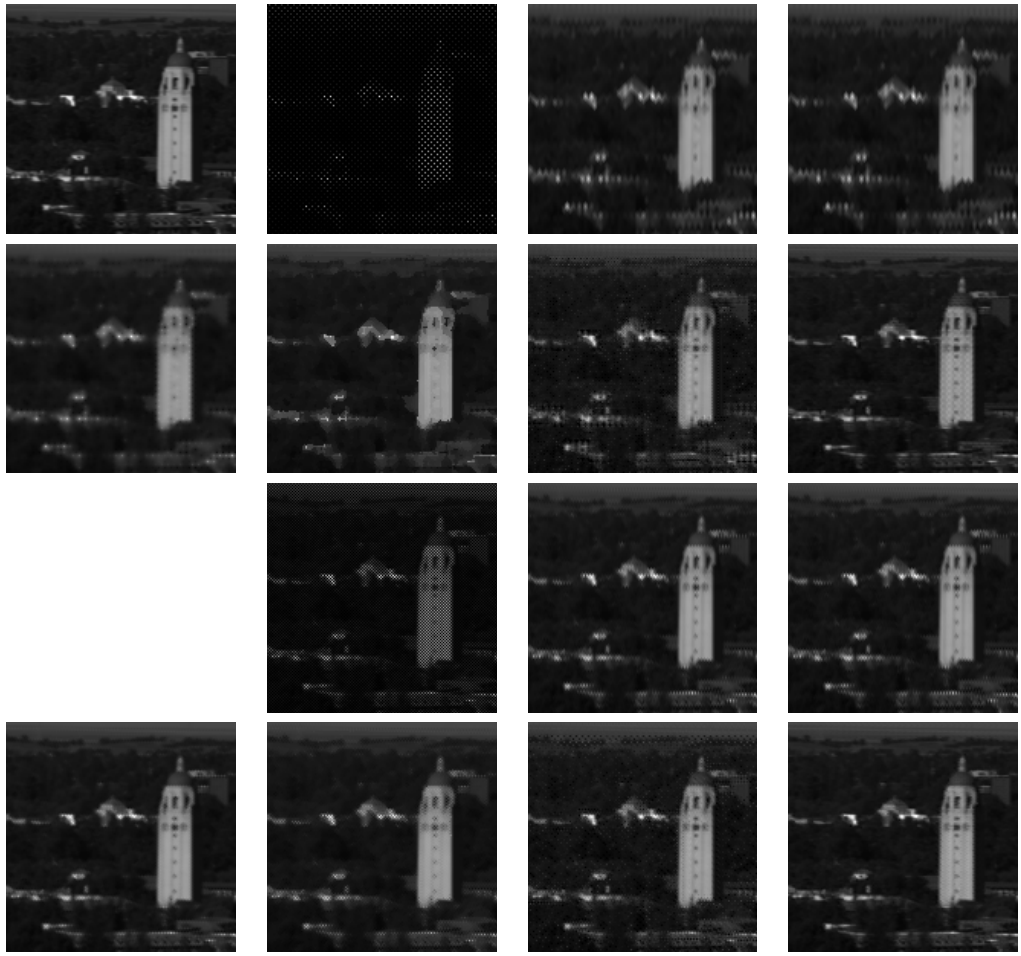

a	b	c	d
e	f	g	h
	i	j	k
l	m	n	o

Figure 11.54: An extraction from band 5 of Scene 4 in the absence of noise. (a) full-resolution image, (b) SFA I mosaicked image, (c) SFA I demosaicked image with BL, (d) SFA I demosaicked image with SH, (e) SFA I demosaicked image with BT, (f) SFA I demosaicked image with VM, (g) SFA I demosaicked image with DWT, (h) SFA I demosaicked image with LMMSE, (i) SFA II mosaicked image, (j) SFA II demosaicked image with BL, (k) SFA II demosaicked image with SH, (l) SFA II demosaicked image with BT, (m) SFA II demosaicked image with VM, (n) SFA II demosaicked image with DWT, (o) SFA II demosaicked image with LMMSE

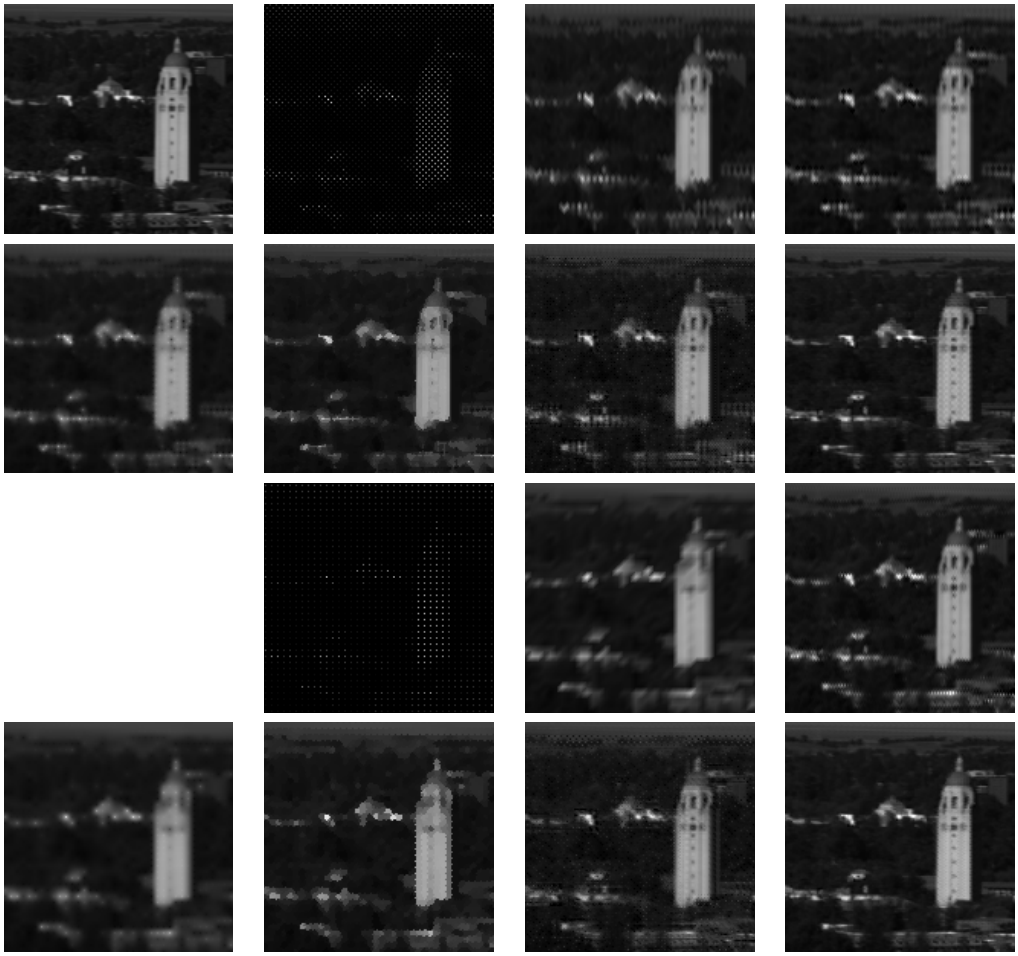

a	b	c	d
e	f	g	h
	i	j	k
l	m	n	o

Figure 11.55: An extraction from band 6 of Scene 4 in the absence of noise. (a) full-resolution image, (b) SFA I mosaicked image, (c) SFA I demosaicked image with BL, (d) SFA I demosaicked image with SH, (e) SFA I demosaicked image with BT, (f) SFA I demosaicked image with VM, (g) SFA I demosaicked image with DWT, (h) SFA I demosaicked image with LMMSE, (i) SFA II mosaicked image, (j) SFA II demosaicked image with BL, (k) SFA II demosaicked image with SH, (l) SFA II demosaicked image with BT, (m) SFA II demosaicked image with VM, (n) SFA II demosaicked image with DWT, (o) SFA II demosaicked image with LMMSE

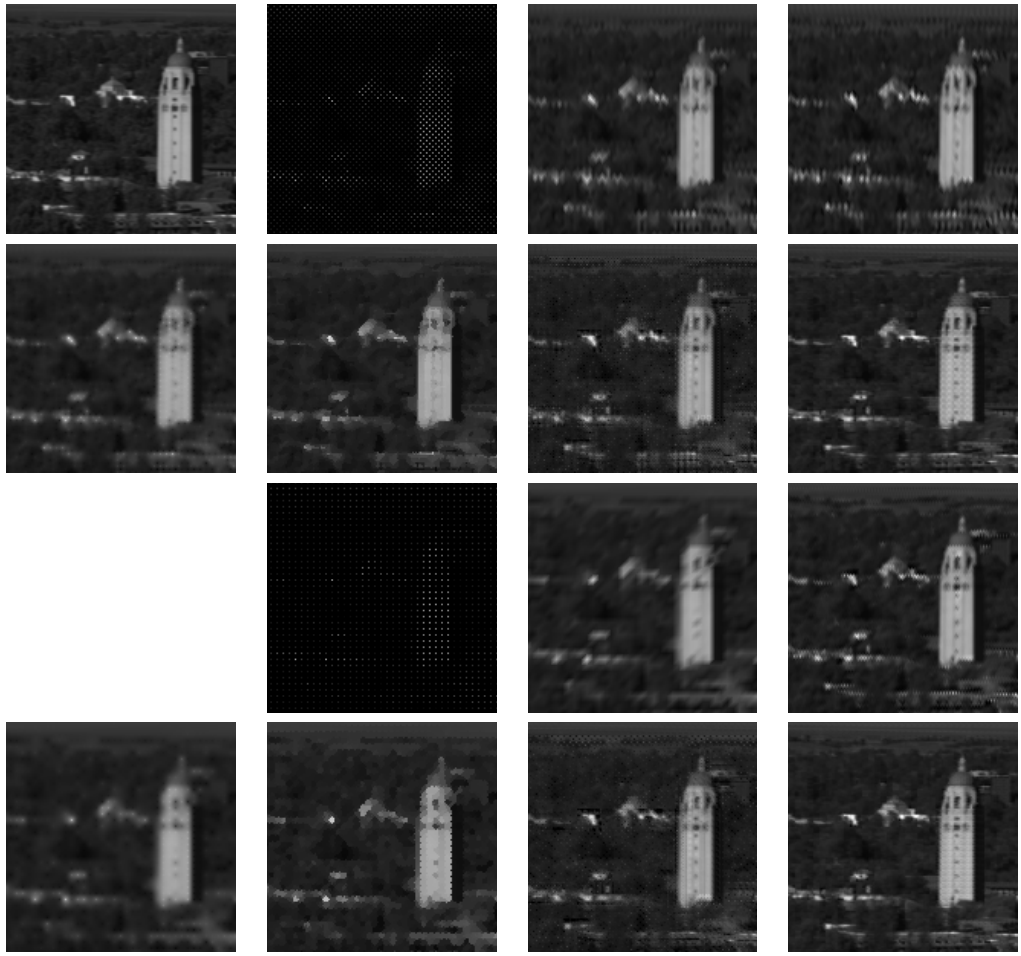

a	b	c	d
e	f	g	h
	i	j	k
l	m	n	o

Figure 11.56: An extraction from band 7 of Scene 4 in the absence of noise. (a) full-resolution image, (b) SFA I mosaicked image, (c) SFA I demosaicked image with BL, (d) SFA I demosaicked image with SH, (e) SFA I demosaicked image with BT, (f) SFA I demosaicked image with VM, (g) SFA I demosaicked image with DWT, (h) SFA I demosaicked image with LMMSE, (i) SFA II mosaicked image, (j) SFA II demosaicked image with BL, (k) SFA II demosaicked image with SH, (l) SFA II demosaicked image with BT, (m) SFA II demosaicked image with VM, (n) SFA II demosaicked image with DWT, (o) SFA II demosaicked image with LMMSE

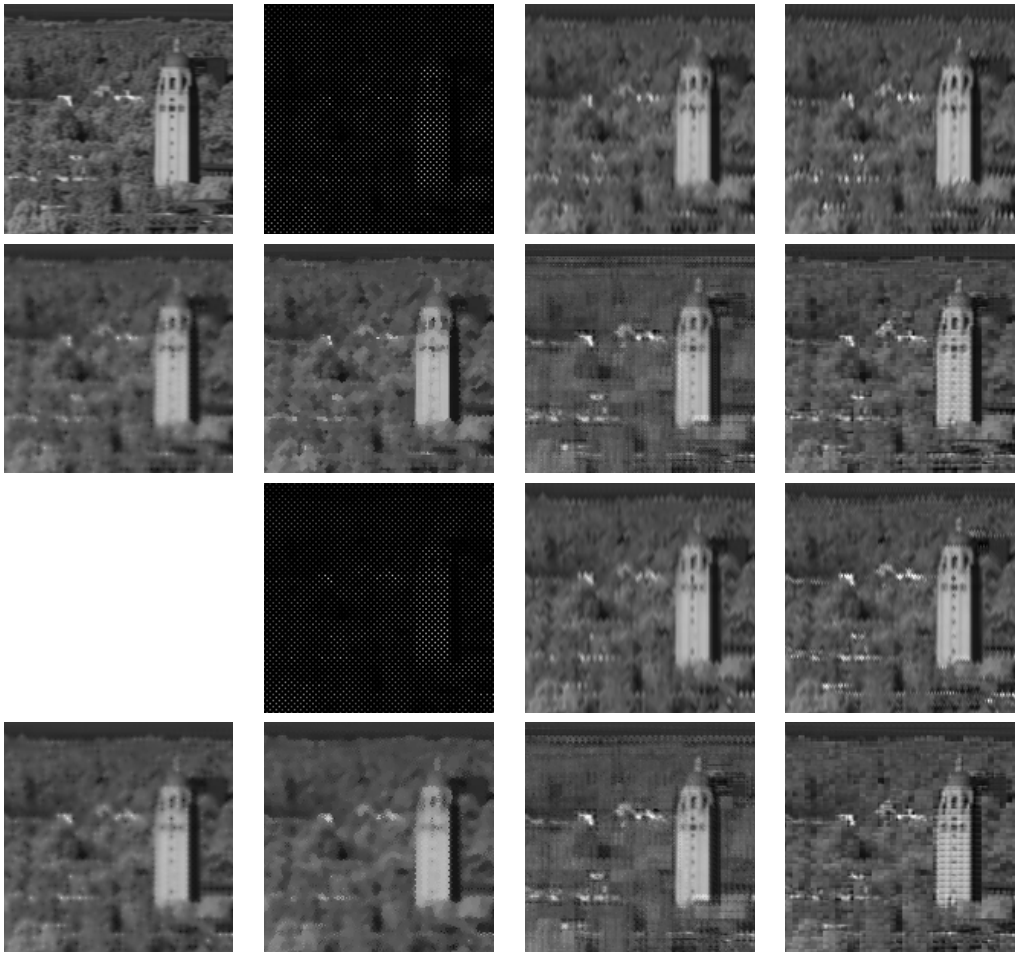

a	b	c	d
e	f	g	h
	i	j	k
l	m	n	o

Figure 11.57: An extraction from band 8 of Scene 4 in the absence of noise. (a) full-resolution image, (b) SFA I mosaicked image, (c) SFA I demosaicked image with BL, (d) SFA I demosaicked image with SH, (e) SFA I demosaicked image with BT, (f) SFA I demosaicked image with VM, (g) SFA I demosaicked image with DWT, (h) SFA I demosaicked image with LMMSE, (i) SFA II mosaicked image, (j) SFA II demosaicked image with BL, (k) SFA II demosaicked image with SH, (l) SFA II demosaicked image with BT, (m) SFA II demosaicked image with VM, (n) SFA II demosaicked image with DWT, (o) SFA II demosaicked image with LMMSE

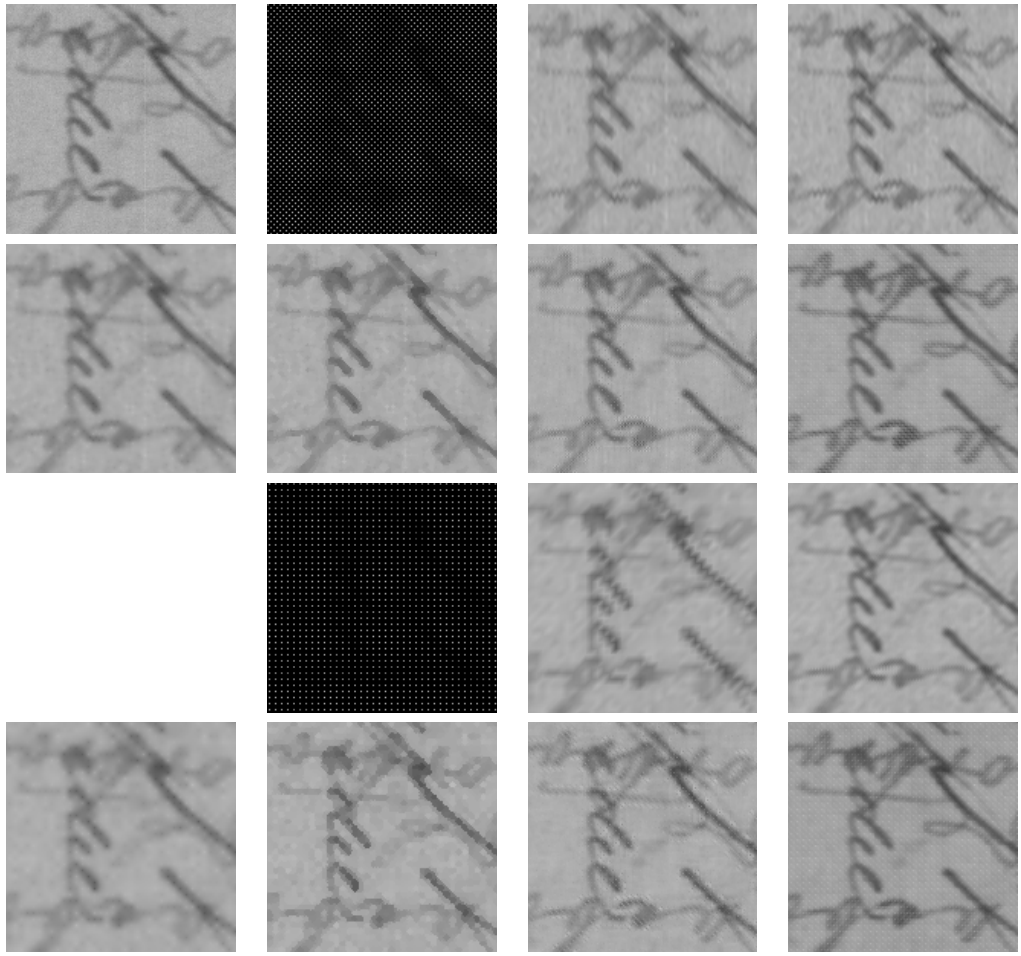

a	b	c	d
e	f	g	h
	i	j	k
l	m	n	o

Figure 11.58: An extraction from band 1 of Scene 5 in the absence of noise. (a) full-resolution image, (b) SFA I mosaicked image, (c) SFA I demosaicked image with BL, (d) SFA I demosaicked image with SH, (e) SFA I demosaicked image with BT, (f) SFA I demosaicked image with VM, (g) SFA I demosaicked image with DWT, (h) SFA I demosaicked image with LMMSE, (i) SFA II mosaicked image, (j) SFA II demosaicked image with BL, (k) SFA II demosaicked image with SH, (l) SFA II demosaicked image with BT, (m) SFA II demosaicked image with VM, (n) SFA II demosaicked image with DWT, (o) SFA II demosaicked image with LMMSE

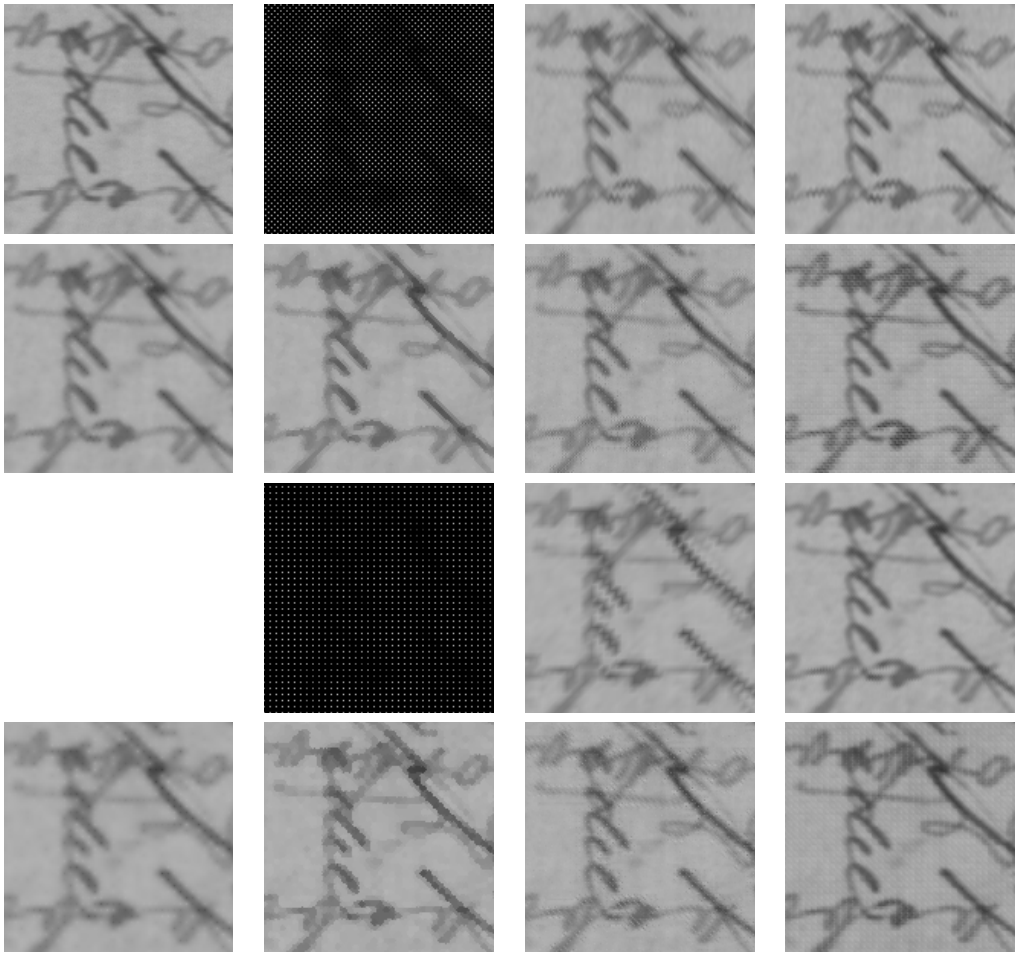

a	b	c	d
e	f	g	h
	i	j	k
l	m	n	o

Figure 11.59: An extraction from band 2 of Scene 5 in the absence of noise. (a) full-resolution image, (b) SFA I mosaicked image, (c) SFA I demosaicked image with BL, (d) SFA I demosaicked image with SH, (e) SFA I demosaicked image with BT, (f) SFA I demosaicked image with VM, (g) SFA I demosaicked image with DWT, (h) SFA I demosaicked image with LMMSE, (i) SFA II mosaicked image, (j) SFA II demosaicked image with BL, (k) SFA II demosaicked image with SH, (l) SFA II demosaicked image with BT, (m) SFA II demosaicked image with VM, (n) SFA II demosaicked image with DWT, (o) SFA II demosaicked image with LMMSE

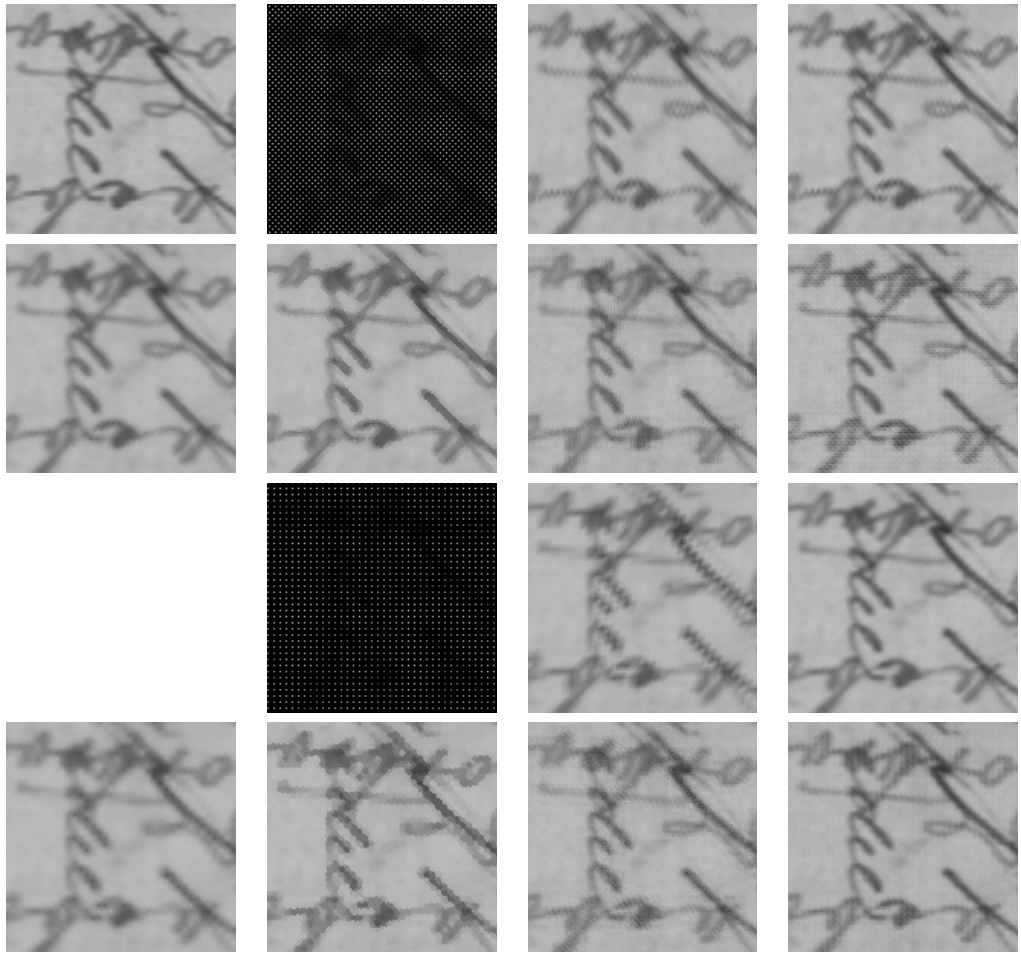

a	b	c	d
e	f	g	h
	i	j	k
l	m	n	o

Figure 11.60: An extraction from band 3 of Scene 5 in the absence of noise. (a) full-resolution image, (b) SFA I mosaicked image, (c) SFA I demosaicked image with BL, (d) SFA I demosaicked image with SH, (e) SFA I demosaicked image with BT, (f) SFA I demosaicked image with VM, (g) SFA I demosaicked image with DWT, (h) SFA I demosaicked image with LMMSE, (i) SFA II mosaicked image, (j) SFA II demosaicked image with BL, (k) SFA II demosaicked image with SH, (l) SFA II demosaicked image with BT, (m) SFA II demosaicked image with VM, (n) SFA II demosaicked image with DWT, (o) SFA II demosaicked image with LMMSE

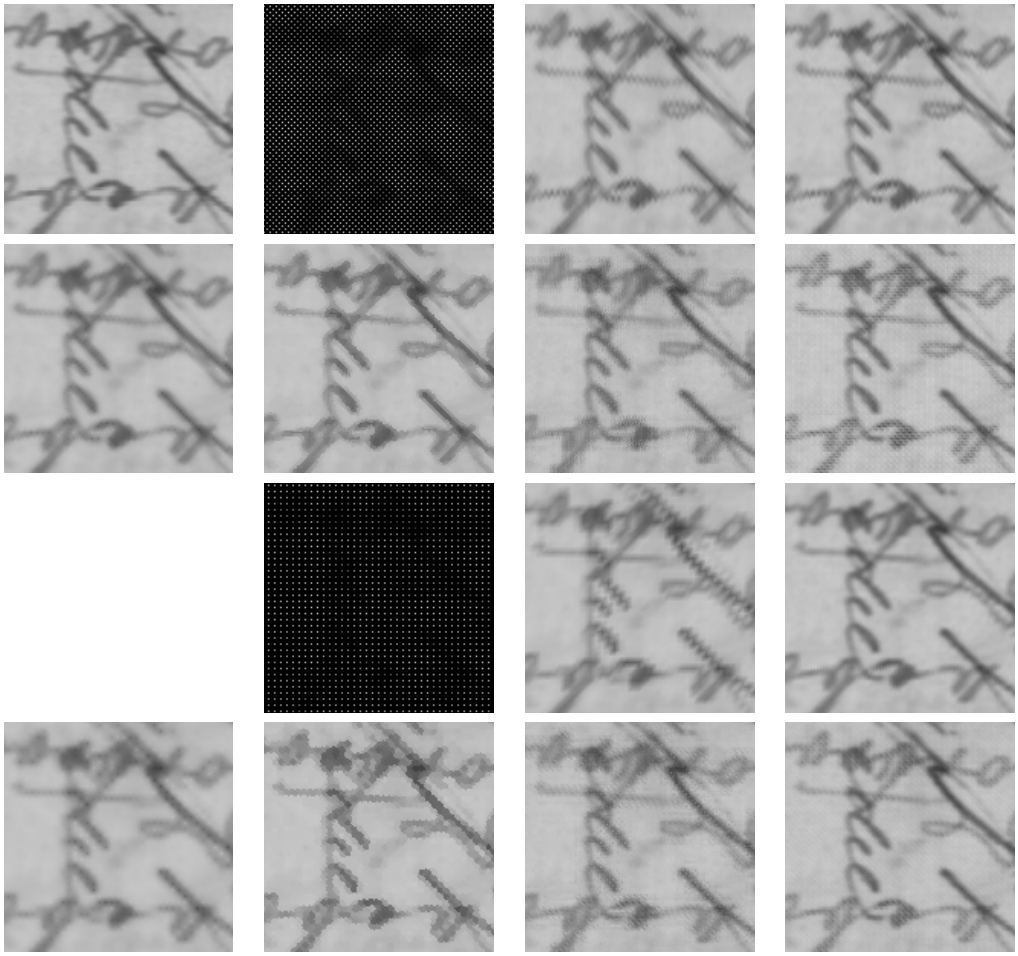

a	b	c	d
e	f	g	h
	i	j	k
l	m	n	o

Figure 11.61: An extraction from band 4 of Scene 5 in the absence of noise. (a) full-resolution image, (b) SFA I mosaicked image, (c) SFA I demosaicked image with BL, (d) SFA I demosaicked image with SH, (e) SFA I demosaicked image with BT, (f) SFA I demosaicked image with VM, (g) SFA I demosaicked image with DWT, (h) SFA I demosaicked image with LMMSE, (i) SFA II mosaicked image, (j) SFA II demosaicked image with BL, (k) SFA II demosaicked image with SH, (l) SFA II demosaicked image with BT, (m) SFA II demosaicked image with VM, (n) SFA II demosaicked image with DWT, (o) SFA II demosaicked image with LMMSE

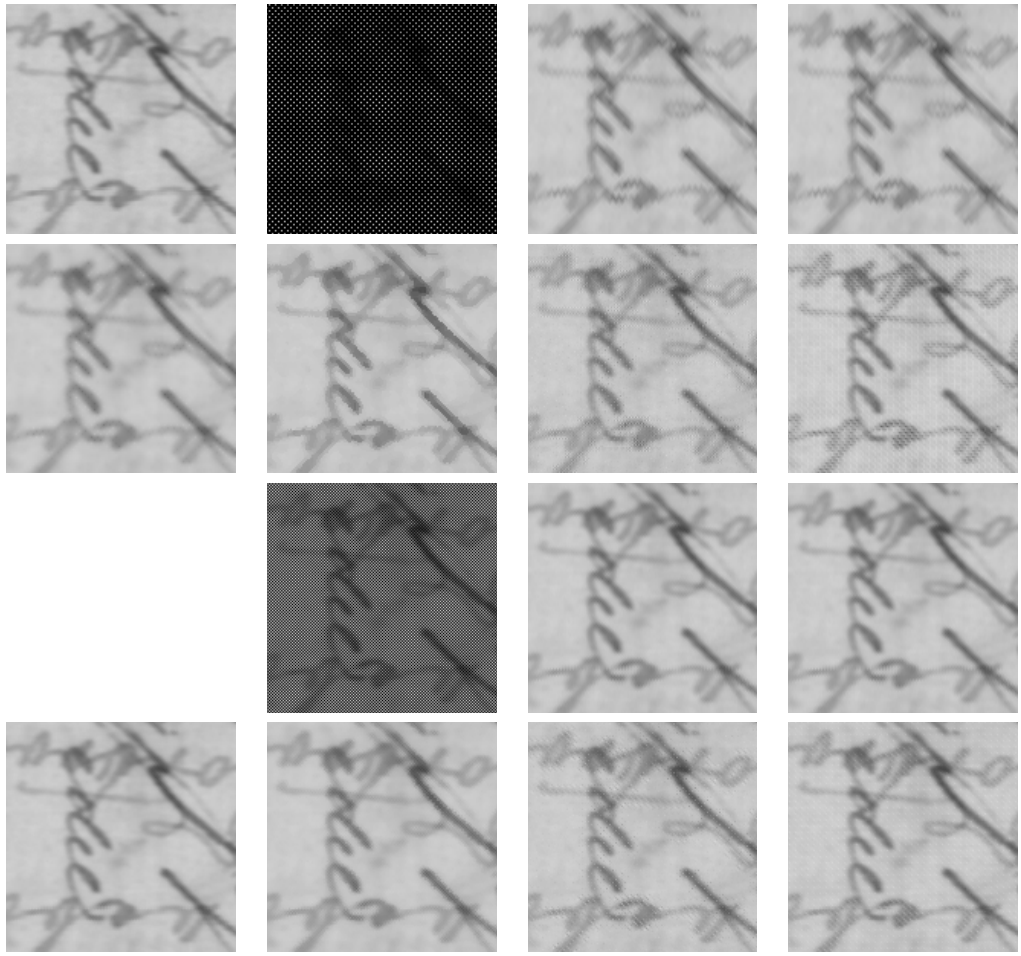

a	b	c	d
e	f	g	h
	i	j	k
l	m	n	o

Figure 11.62: An extraction from band 5 of Scene 5 in the absence of noise. (a) full-resolution image, (b) SFA I mosaicked image, (c) SFA I demosaicked image with BL, (d) SFA I demosaicked image with SH, (e) SFA I demosaicked image with BT, (f) SFA I demosaicked image with VM, (g) SFA I demosaicked image with DWT, (h) SFA I demosaicked image with LMMSE, (i) SFA II mosaicked image, (j) SFA II demosaicked image with BL, (k) SFA II demosaicked image with SH, (l) SFA II demosaicked image with BT, (m) SFA II demosaicked image with VM, (n) SFA II demosaicked image with DWT, (o) SFA II demosaicked image with LMMSE

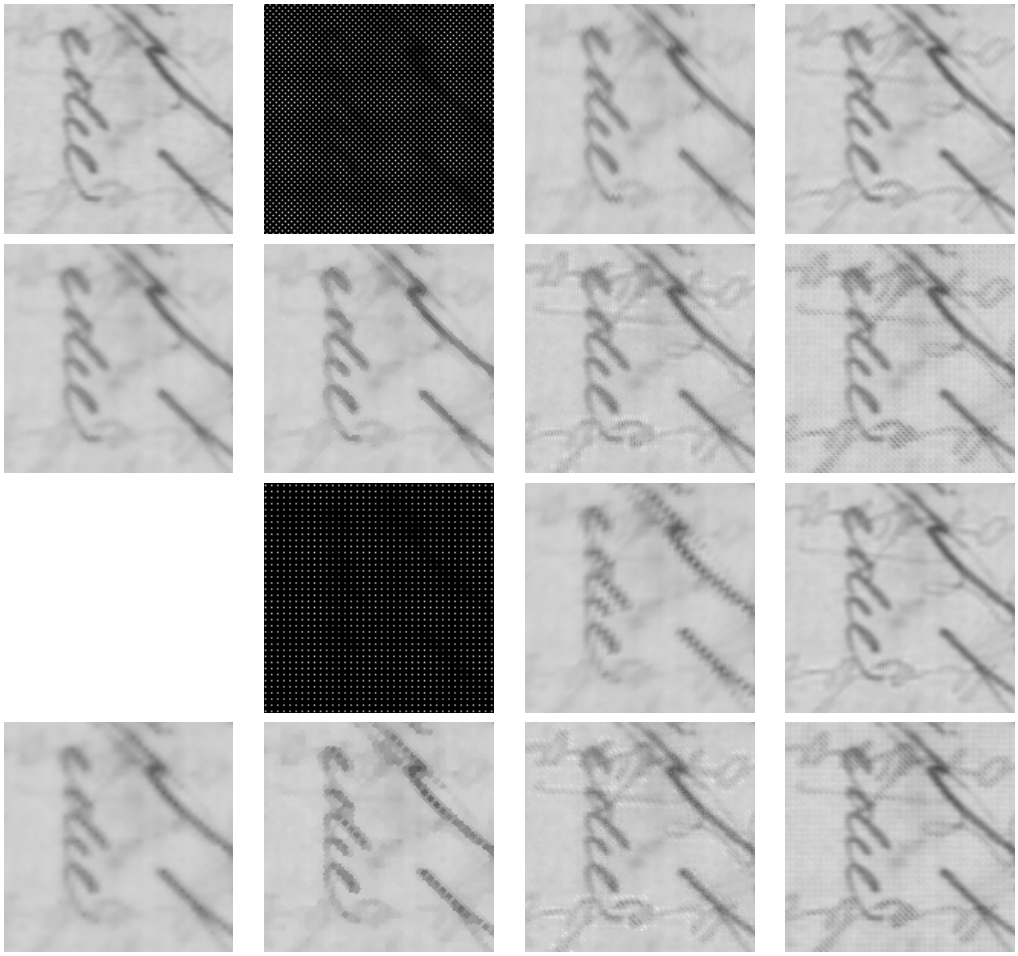

a	b	c	d
e	f	g	h
	i	j	k
l	m	n	o

Figure 11.63: An extraction from band 6 of Scene 5 in the absence of noise. (a) full-resolution image, (b) SFA I mosaicked image, (c) SFA I demosaicked image with BL, (d) SFA I demosaicked image with SH, (e) SFA I demosaicked image with BT, (f) SFA I demosaicked image with VM, (g) SFA I demosaicked image with DWT, (h) SFA I demosaicked image with LMMSE, (i) SFA II mosaicked image, (j) SFA II demosaicked image with BL, (k) SFA II demosaicked image with SH, (l) SFA II demosaicked image with BT, (m) SFA II demosaicked image with VM, (n) SFA II demosaicked image with DWT, (o) SFA II demosaicked image with LMMSE

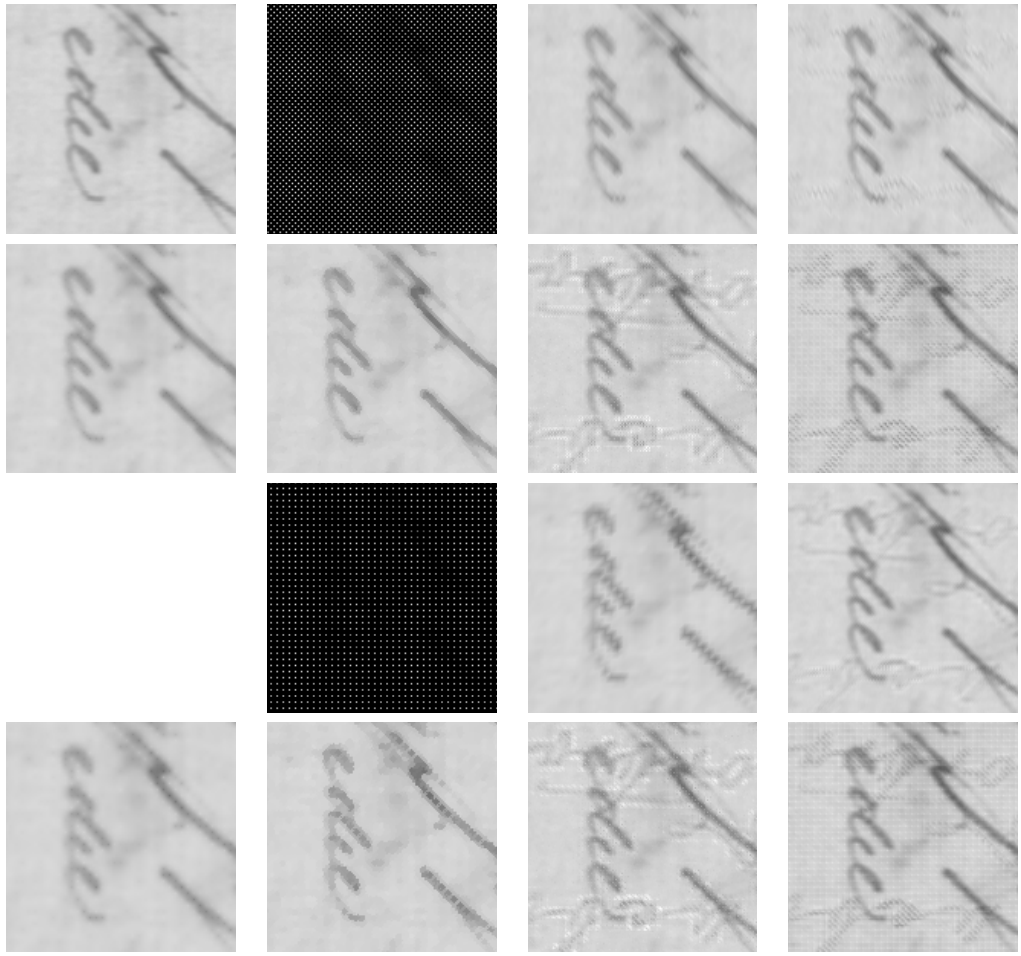

a	b	c	d
e	f	g	h
	i	j	k
l	m	n	o

Figure 11.64: An extraction from band 7 of Scene 5 in the absence of noise. (a) full-resolution image, (b) SFA I mosaicked image, (c) SFA I demosaicked image with BL, (d) SFA I demosaicked image with SH, (e) SFA I demosaicked image with BT, (f) SFA I demosaicked image with VM, (g) SFA I demosaicked image with DWT, (h) SFA I demosaicked image with LMMSE, (i) SFA II mosaicked image, (j) SFA II demosaicked image with BL, (k) SFA II demosaicked image with SH, (l) SFA II demosaicked image with BT, (m) SFA II demosaicked image with VM, (n) SFA II demosaicked image with DWT, (o) SFA II demosaicked image with LMMSE

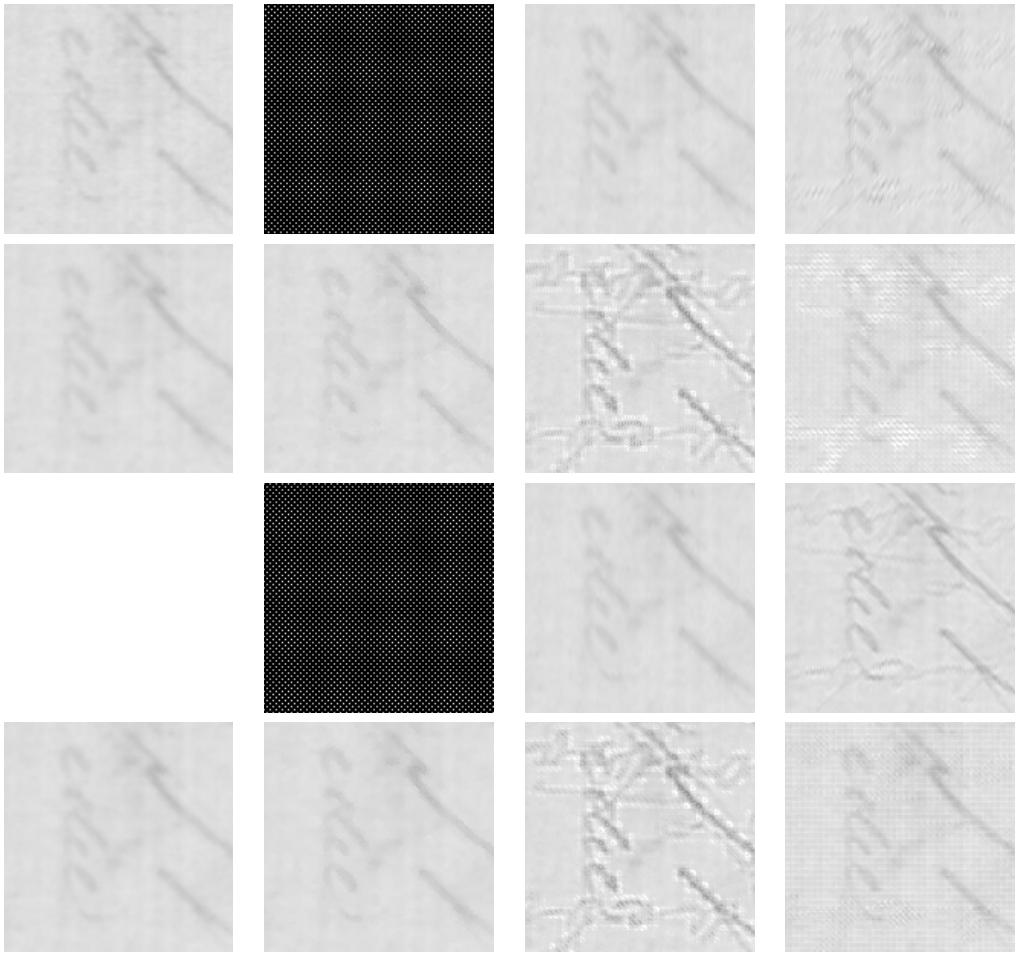

a	b	c	d
e	f	g	h
	i	j	k
l	m	n	o

Figure 11.65: An extraction from band 8 of Scene 5 in the absence of noise. (a) full-resolution image, (b) SFA I mosaicked image, (c) SFA I demosaicked image with BL, (d) SFA I demosaicked image with SH, (e) SFA I demosaicked image with BT, (f) SFA I demosaicked image with VM, (g) SFA I demosaicked image with DWT, (h) SFA I demosaicked image with LMMSE, (i) SFA II mosaicked image, (j) SFA II demosaicked image with BL, (k) SFA II demosaicked image with SH, (l) SFA II demosaicked image with BT, (m) SFA II demosaicked image with VM, (n) SFA II demosaicked image with DWT, (o) SFA II demosaicked image with LMMSE

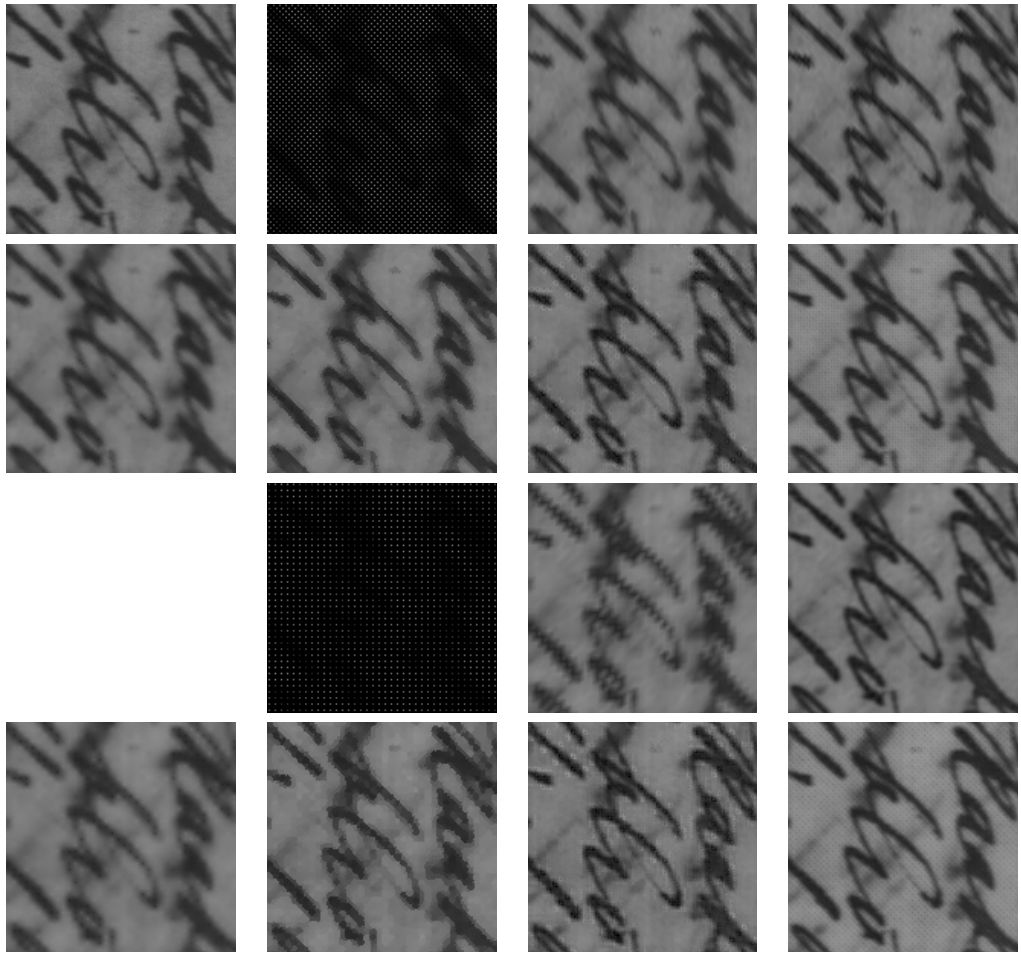

a	b	c	d
e	f	g	h
	i	j	k
l	m	n	o

Figure 11.66: An extraction from band 1 of Scene 6 in the absence of noise. (a) full-resolution image, (b) SFA I mosaicked image, (c) SFA I demosaicked image with BL, (d) SFA I demosaicked image with SH, (e) SFA I demosaicked image with BT, (f) SFA I demosaicked image with VM, (g) SFA I demosaicked image with DWT, (h) SFA I demosaicked image with LMMSE, (i) SFA II mosaicked image, (j) SFA II demosaicked image with BL, (k) SFA II demosaicked image with SH, (l) SFA II demosaicked image with BT, (m) SFA II demosaicked image with VM, (n) SFA II demosaicked image with DWT, (o) SFA II demosaicked image with LMMSE

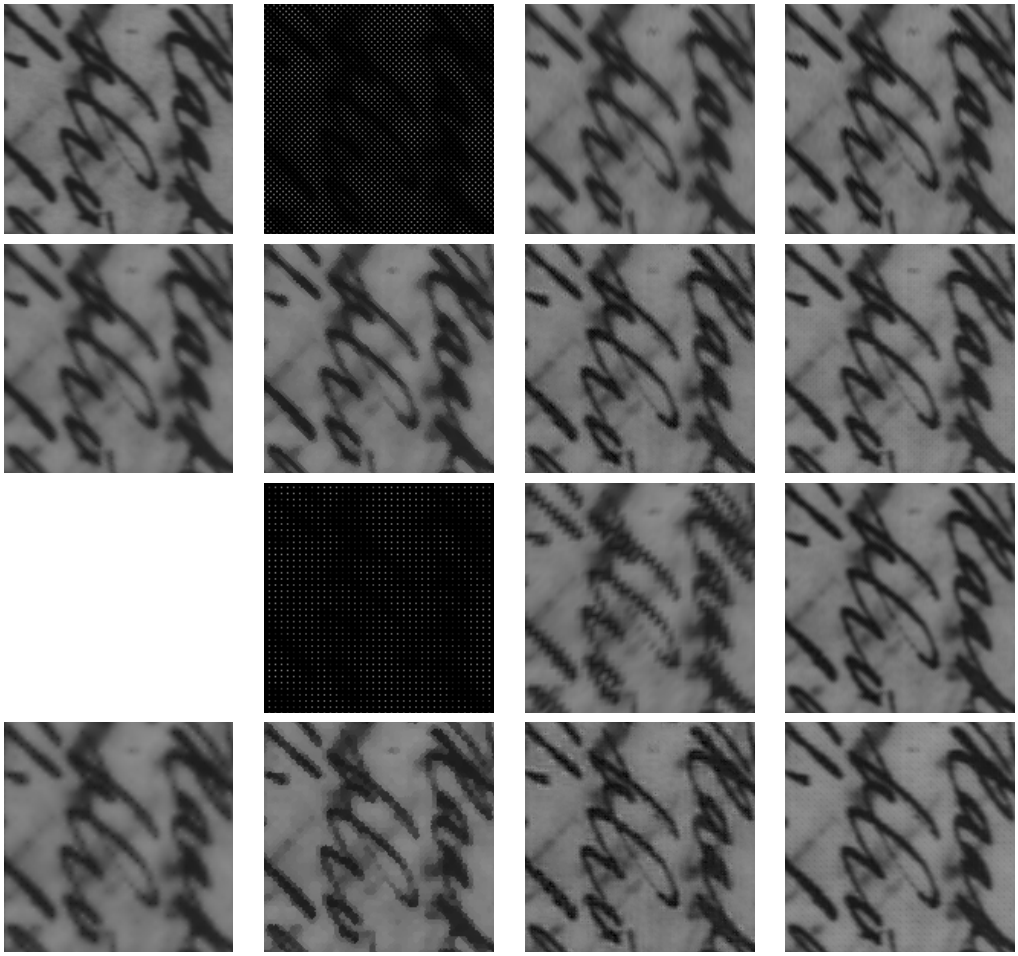

a	b	c	d
e	f	g	h
	i	j	k
l	m	n	o

Figure 11.67: An extraction from band 2 of Scene 6 in the absence of noise. (a) full-resolution image, (b) SFA I mosaicked image, (c) SFA I demosaicked image with BL, (d) SFA I demosaicked image with SH, (e) SFA I demosaicked image with BT, (f) SFA I demosaicked image with VM, (g) SFA I demosaicked image with DWT, (h) SFA I demosaicked image with LMMSE, (i) SFA II mosaicked image, (j) SFA II demosaicked image with BL, (k) SFA II demosaicked image with SH, (l) SFA II demosaicked image with BT, (m) SFA II demosaicked image with VM, (n) SFA II demosaicked image with DWT, (o) SFA II demosaicked image with LMMSE

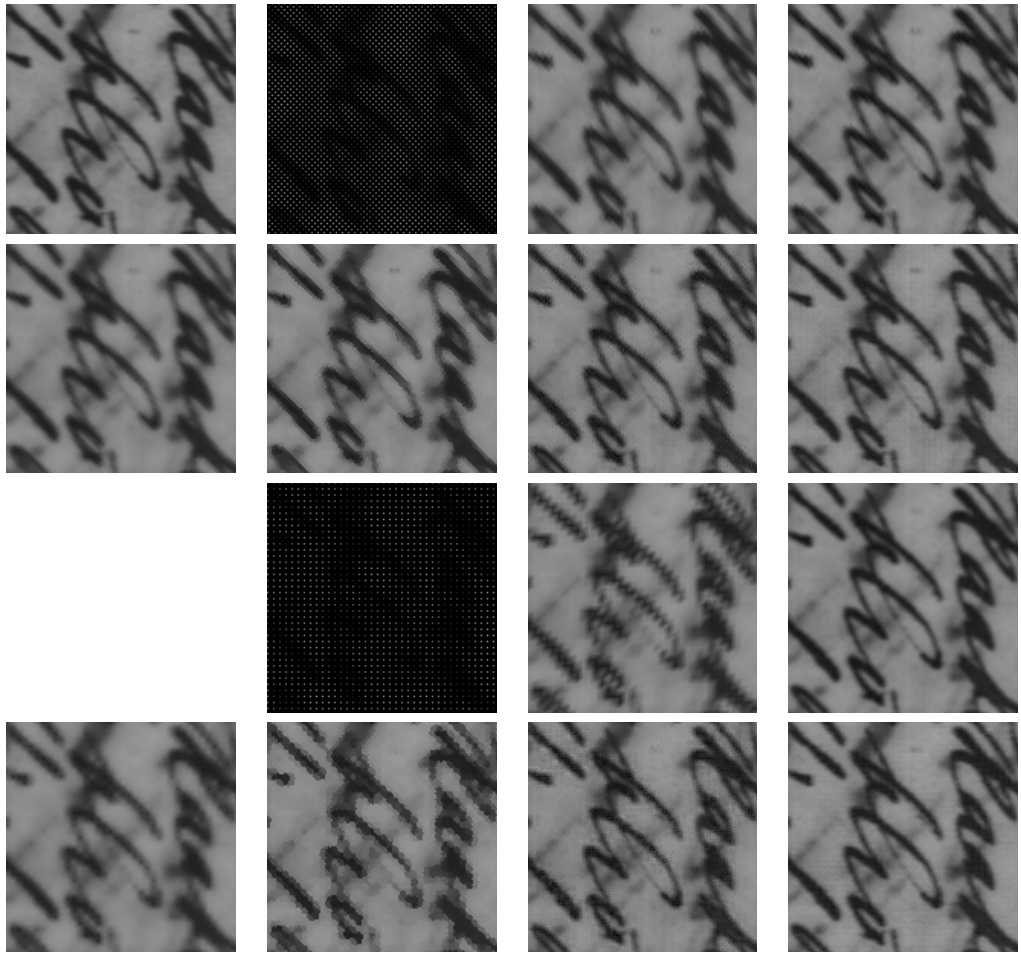

a	b	c	d
e	f	g	h
	i	j	k
l	m	n	o

Figure 11.68: An extraction from band 3 of Scene 6 in the absence of noise. (a) full-resolution image, (b) SFA I mosaicked image, (c) SFA I demosaicked image with BL, (d) SFA I demosaicked image with SH, (e) SFA I demosaicked image with BT, (f) SFA I demosaicked image with VM, (g) SFA I demosaicked image with DWT, (h) SFA I demosaicked image with LMMSE, (i) SFA II mosaicked image, (j) SFA II demosaicked image with BL, (k) SFA II demosaicked image with SH, (l) SFA II demosaicked image with BT, (m) SFA II demosaicked image with VM, (n) SFA II demosaicked image with DWT, (o) SFA II demosaicked image with LMMSE

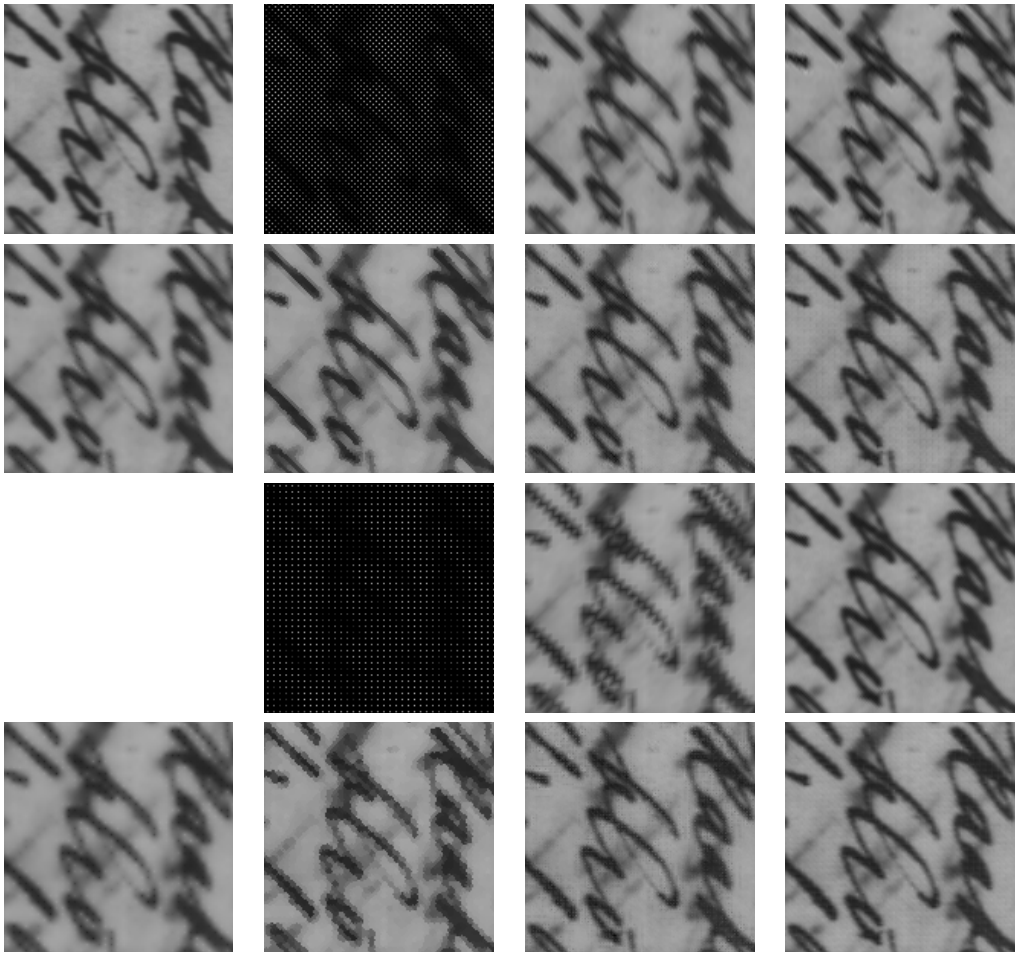

a	b	c	d
e	f	g	h
	i	j	k
l	m	n	o

Figure 11.69: An extraction from band 4 of Scene 6 in the absence of noise. (a) full-resolution image, (b) SFA I mosaicked image, (c) SFA I demosaicked image with BL, (d) SFA I demosaicked image with SH, (e) SFA I demosaicked image with BT, (f) SFA I demosaicked image with VM, (g) SFA I demosaicked image with DWT, (h) SFA I demosaicked image with LMMSE, (i) SFA II mosaicked image, (j) SFA II demosaicked image with BL, (k) SFA II demosaicked image with SH, (l) SFA II demosaicked image with BT, (m) SFA II demosaicked image with VM, (n) SFA II demosaicked image with DWT, (o) SFA II demosaicked image with LMMSE

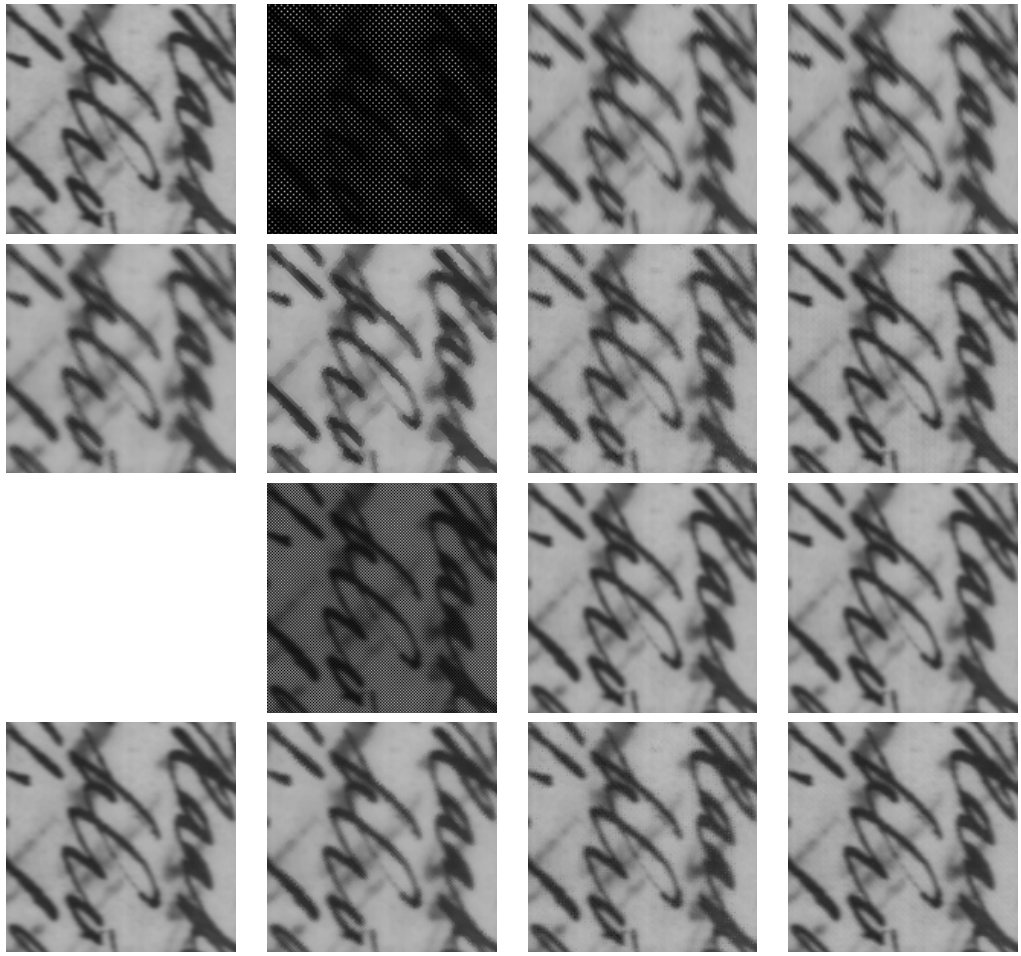

a	b	c	d
e	f	g	h
	i	j	k
l	m	n	o

Figure 11.70: An extraction from band 5 of Scene 6 in the absence of noise. (a) full-resolution image, (b) SFA I mosaicked image, (c) SFA I demosaicked image with BL, (d) SFA I demosaicked image with SH, (e) SFA I demosaicked image with BT, (f) SFA I demosaicked image with VM, (g) SFA I demosaicked image with DWT, (h) SFA I demosaicked image with LMMSE, (i) SFA II mosaicked image, (j) SFA II demosaicked image with BL, (k) SFA II demosaicked image with SH, (l) SFA II demosaicked image with BT, (m) SFA II demosaicked image with VM, (n) SFA II demosaicked image with DWT, (o) SFA II demosaicked image with LMMSE

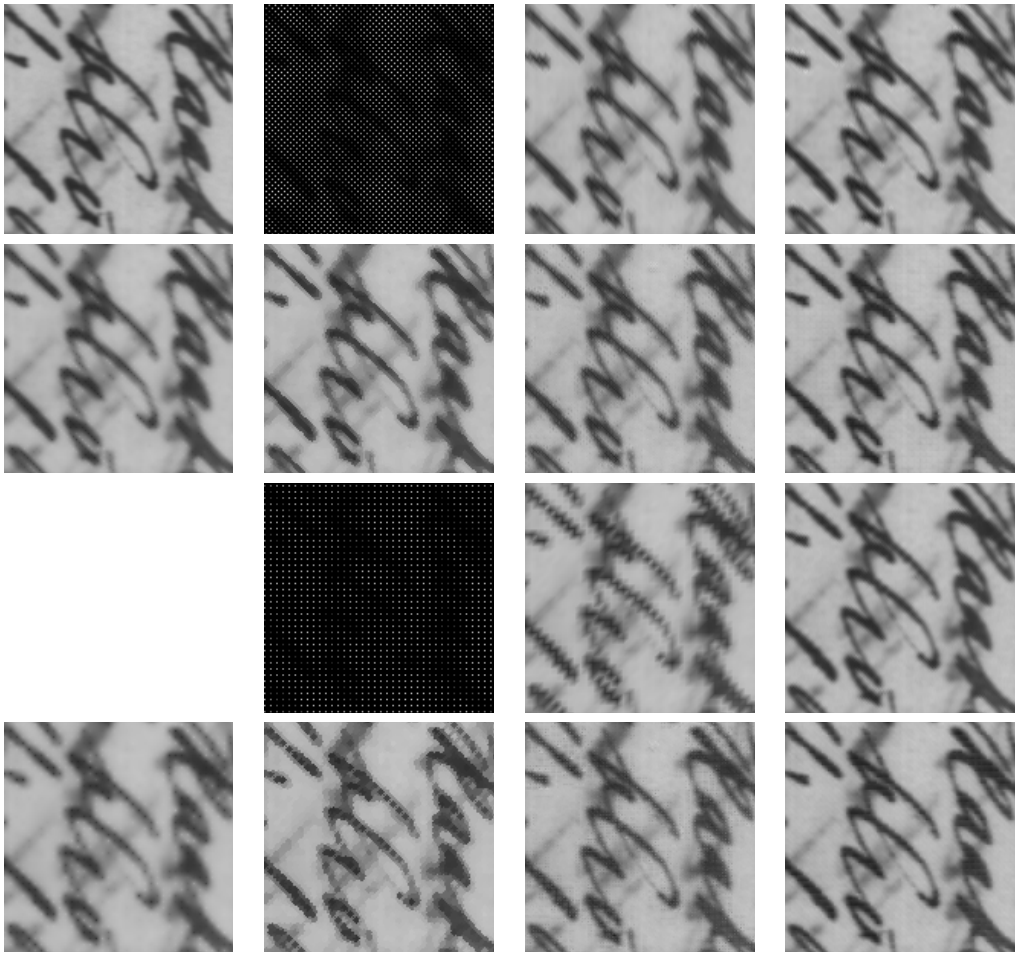

a	b	c	d
e	f	g	h
	i	j	k
l	m	n	o

Figure 11.71: An extraction from band 6 of Scene 6 in the absence of noise. (a) full-resolution image, (b) SFA I mosaicked image, (c) SFA I demosaicked image with BL, (d) SFA I demosaicked image with SH, (e) SFA I demosaicked image with BT, (f) SFA I demosaicked image with VM, (g) SFA I demosaicked image with DWT, (h) SFA I demosaicked image with LMMSE, (i) SFA II mosaicked image, (j) SFA II demosaicked image with BL, (k) SFA II demosaicked image with SH, (l) SFA II demosaicked image with BT, (m) SFA II demosaicked image with VM, (n) SFA II demosaicked image with DWT, (o) SFA II demosaicked image with LMMSE

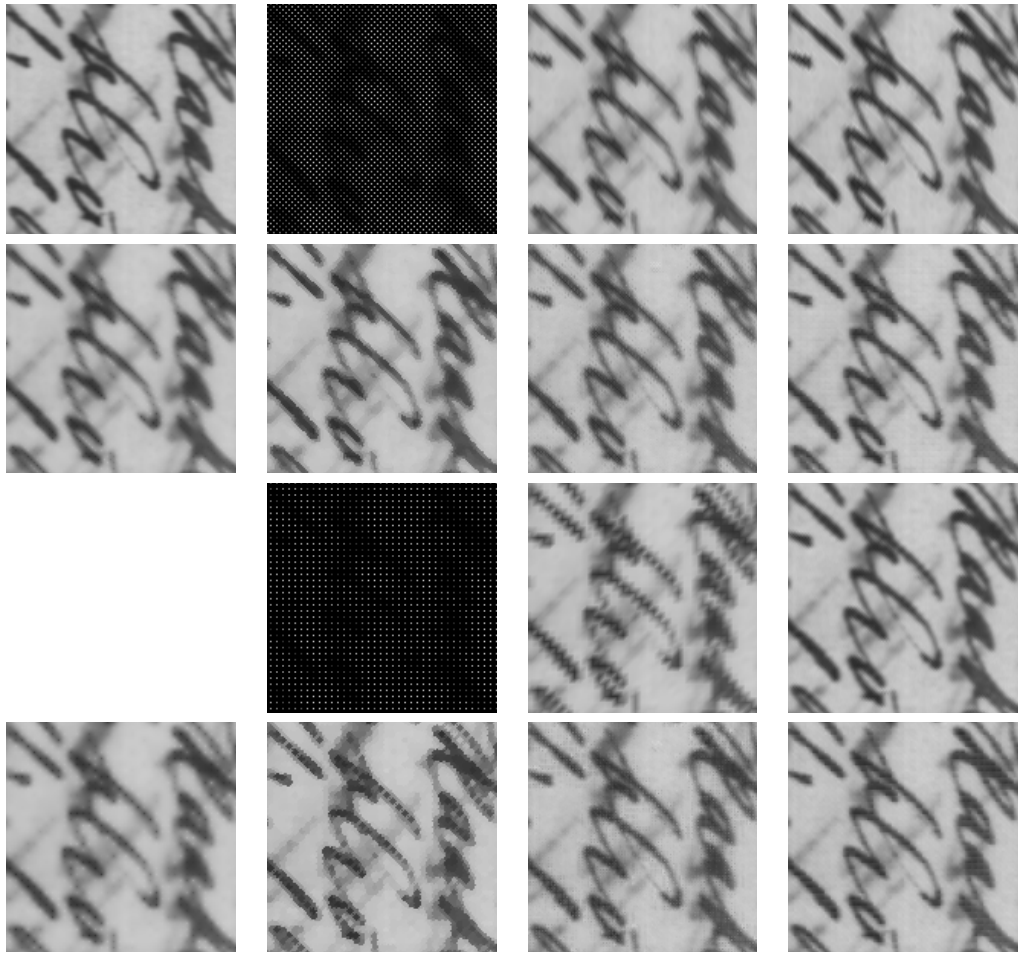

a	b	c	d
e	f	g	h
	i	j	k
l	m	n	o

Figure 11.72: An extraction from band 7 of Scene 6 in the absence of noise. (a) full-resolution image, (b) SFA I mosaicked image, (c) SFA I demosaicked image with BL, (d) SFA I demosaicked image with SH, (e) SFA I demosaicked image with BT, (f) SFA I demosaicked image with VM, (g) SFA I demosaicked image with DWT, (h) SFA I demosaicked image with LMMSE, (i) SFA II mosaicked image, (j) SFA II demosaicked image with BL, (k) SFA II demosaicked image with SH, (l) SFA II demosaicked image with BT, (m) SFA II demosaicked image with VM, (n) SFA II demosaicked image with DWT, (o) SFA II demosaicked image with LMMSE

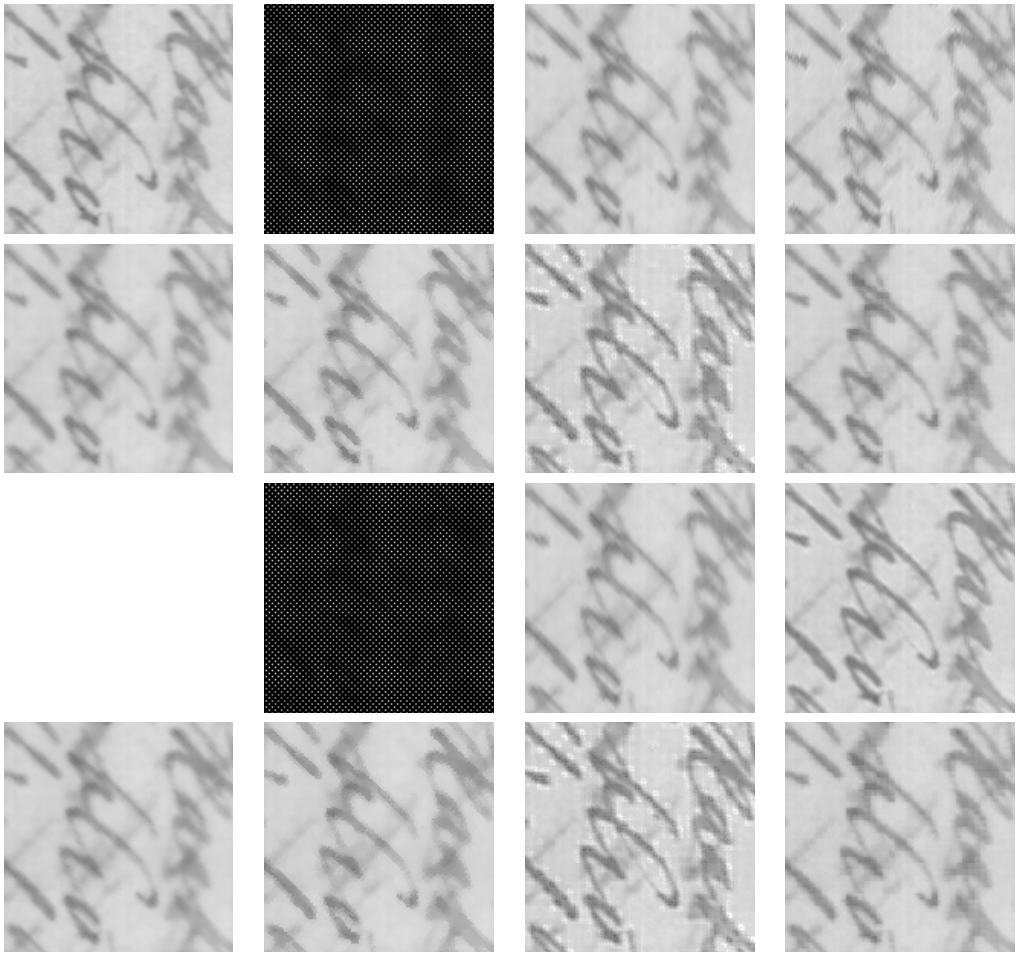

a	b	c	d
e	f	g	h
	i	j	k
l	m	n	o

Figure 11.73: An extraction from band 8 of Scene 6 in the absence of noise. (a) full-resolution image, (b) SFA I mosaicked image, (c) SFA I demosaicked image with BL, (d) SFA I demosaicked image with SH, (e) SFA I demosaicked image with BT, (f) SFA I demosaicked image with VM, (g) SFA I demosaicked image with DWT, (h) SFA I demosaicked image with LMMSE, (i) SFA II mosaicked image, (j) SFA II demosaicked image with BL, (k) SFA II demosaicked image with SH, (l) SFA II demosaicked image with BT, (m) SFA II demosaicked image with VM, (n) SFA II demosaicked image with DWT, (o) SFA II demosaicked image with LMMSE

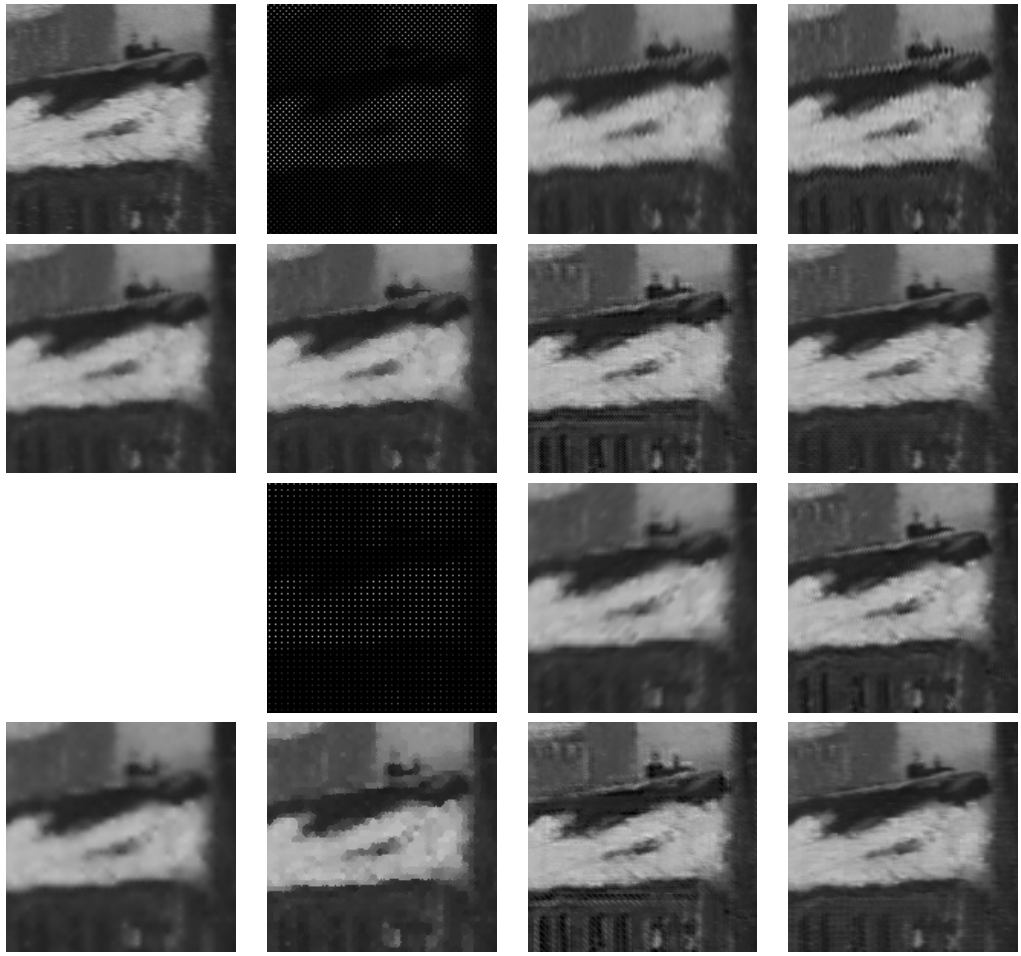

a	b	c	d
e	f	g	h
	i	j	k
l	m	n	o

Figure 11.74: An extraction from band 1 of Scene 7 in the absence of noise. (a) full-resolution image, (b) SFA I mosaicked image, (c) SFA I demosaicked image with BL, (d) SFA I demosaicked image with SH, (e) SFA I demosaicked image with BT, (f) SFA I demosaicked image with VM, (g) SFA I demosaicked image with DWT, (h) SFA I demosaicked image with LMMSE, (i) SFA II mosaicked image, (j) SFA II demosaicked image with BL, (k) SFA II demosaicked image with SH, (l) SFA II demosaicked image with BT, (m) SFA II demosaicked image with VM, (n) SFA II demosaicked image with DWT, (o) SFA II demosaicked image with LMMSE

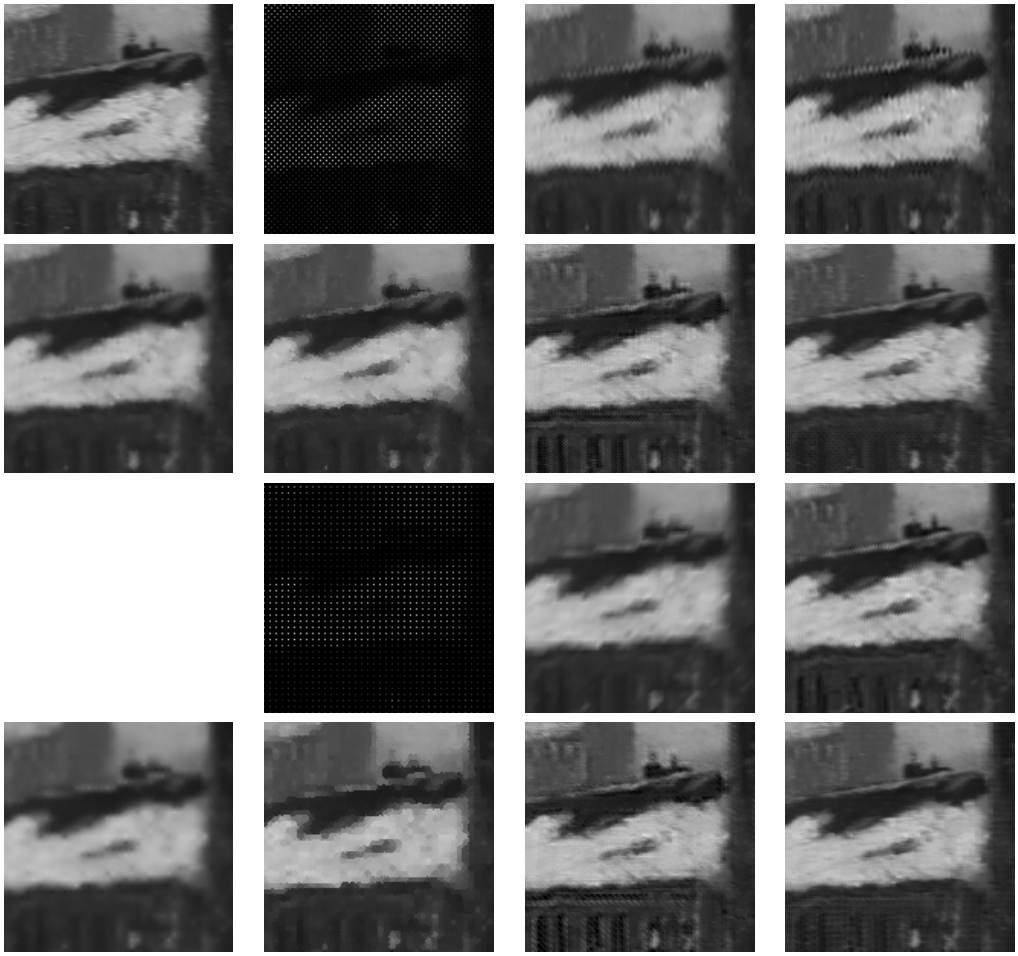

a	b	c	d
e	f	g	h
	i	j	k
l	m	n	o

Figure 11.75: An extraction from band 2 of Scene 7 in the absence of noise. (a) full-resolution image, (b) SFA I mosaicked image, (c) SFA I demosaicked image with BL, (d) SFA I demosaicked image with SH, (e) SFA I demosaicked image with BT, (f) SFA I demosaicked image with VM, (g) SFA I demosaicked image with DWT, (h) SFA I demosaicked image with LMMSE, (i) SFA II mosaicked image, (j) SFA II demosaicked image with BL, (k) SFA II demosaicked image with SH, (l) SFA II demosaicked image with BT, (m) SFA II demosaicked image with VM, (n) SFA II demosaicked image with DWT, (o) SFA II demosaicked image with LMMSE

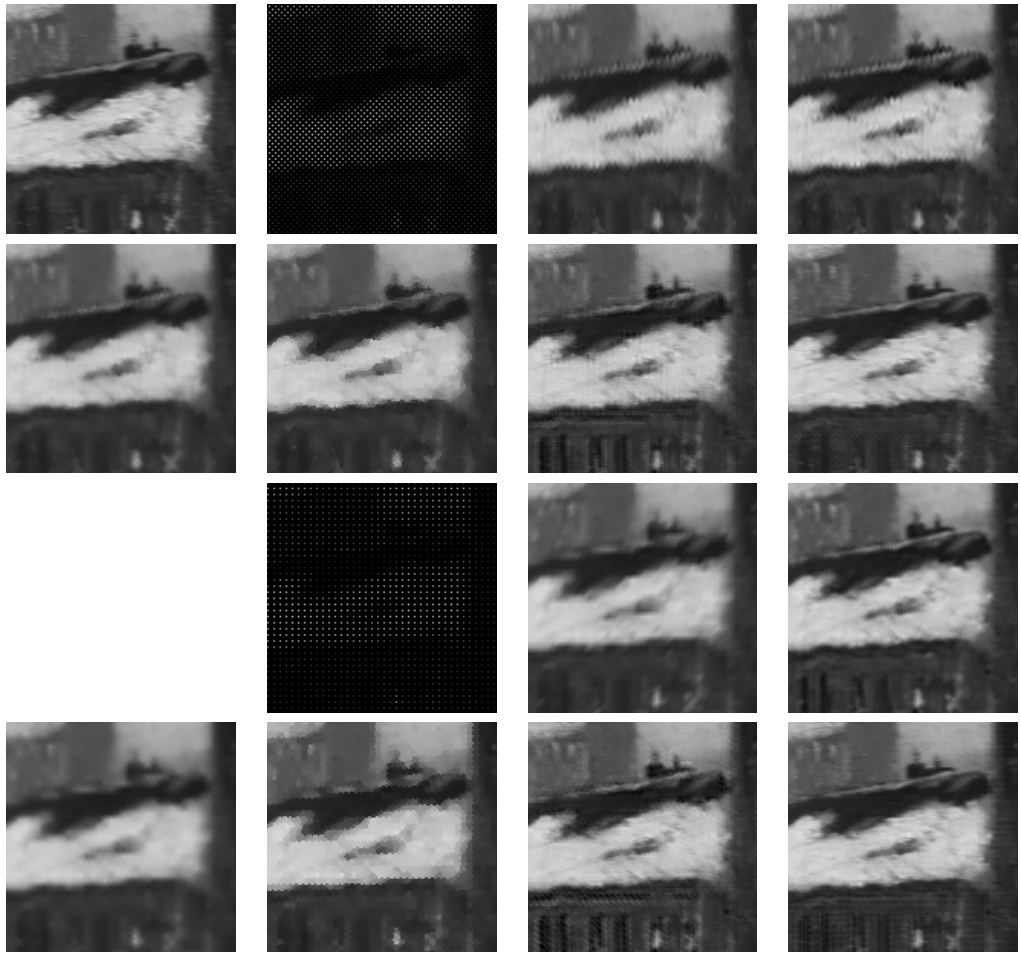

a	b	c	d
e	f	g	h
	i	j	k
l	m	n	o

Figure 11.76: An extraction from band 3 of Scene 7 in the absence of noise. (a) full-resolution image, (b) SFA I mosaicked image, (c) SFA I demosaicked image with BL, (d) SFA I demosaicked image with SH, (e) SFA I demosaicked image with BT, (f) SFA I demosaicked image with VM, (g) SFA I demosaicked image with DWT, (h) SFA I demosaicked image with LMMSE, (i) SFA II mosaicked image, (j) SFA II demosaicked image with BL, (k) SFA II demosaicked image with SH, (l) SFA II demosaicked image with BT, (m) SFA II demosaicked image with VM, (n) SFA II demosaicked image with DWT, (o) SFA II demosaicked image with LMMSE

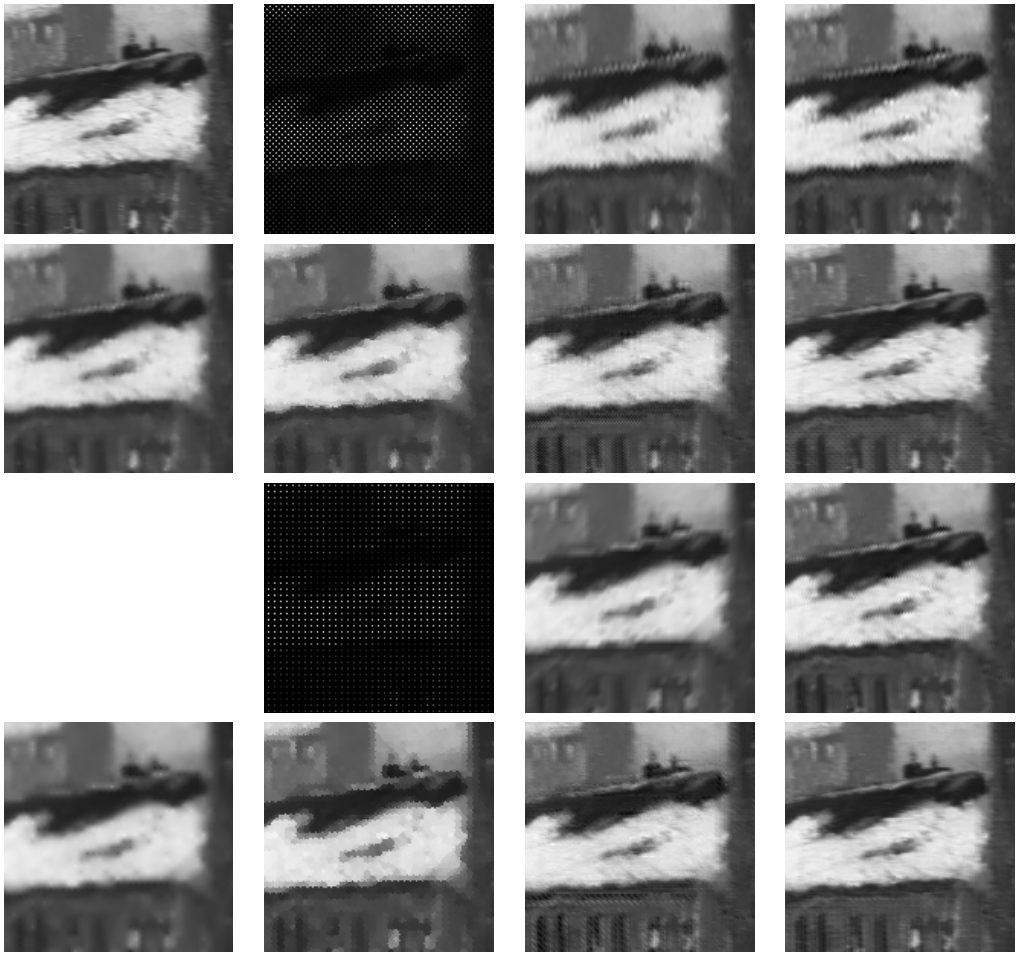

a	b	c	d
e	f	g	h
	i	j	k
l	m	n	o

Figure 11.77: An extraction from band 4 of Scene 7 in the absence of noise. (a) full-resolution image, (b) SFA I mosaicked image, (c) SFA I demosaicked image with BL, (d) SFA I demosaicked image with SH, (e) SFA I demosaicked image with BT, (f) SFA I demosaicked image with VM, (g) SFA I demosaicked image with DWT, (h) SFA I demosaicked image with LMMSE, (i) SFA II mosaicked image, (j) SFA II demosaicked image with BL, (k) SFA II demosaicked image with SH, (l) SFA II demosaicked image with BT, (m) SFA II demosaicked image with VM, (n) SFA II demosaicked image with DWT, (o) SFA II demosaicked image with LMMSE

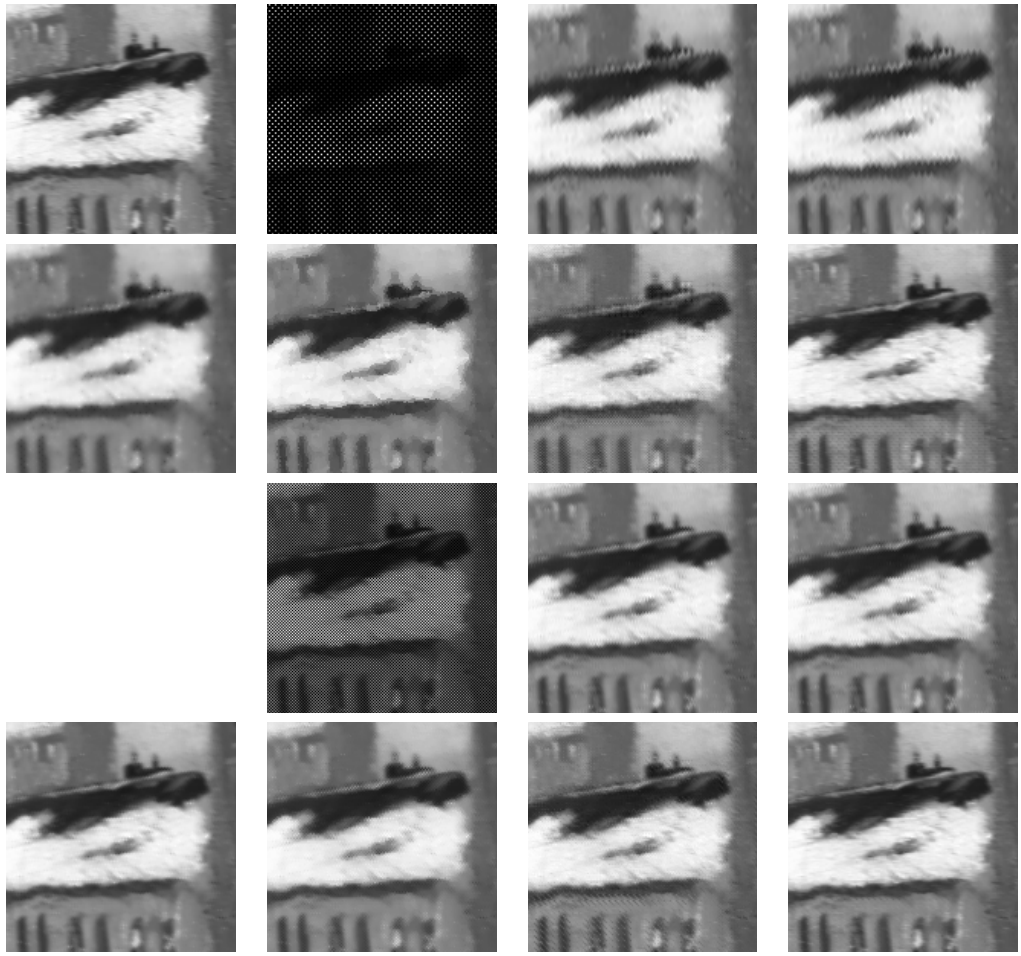

a	b	c	d
e	f	g	h
	i	j	k
l	m	n	o

Figure 11.78: An extraction from band 5 of Scene 7 in the absence of noise. (a) full-resolution image, (b) SFA I mosaicked image, (c) SFA I demosaicked image with BL, (d) SFA I demosaicked image with SH, (e) SFA I demosaicked image with BT, (f) SFA I demosaicked image with VM, (g) SFA I demosaicked image with DWT, (h) SFA I demosaicked image with LMMSE, (i) SFA II mosaicked image, (j) SFA II demosaicked image with BL, (k) SFA II demosaicked image with SH, (l) SFA II demosaicked image with BT, (m) SFA II demosaicked image with VM, (n) SFA II demosaicked image with DWT, (o) SFA II demosaicked image with LMMSE

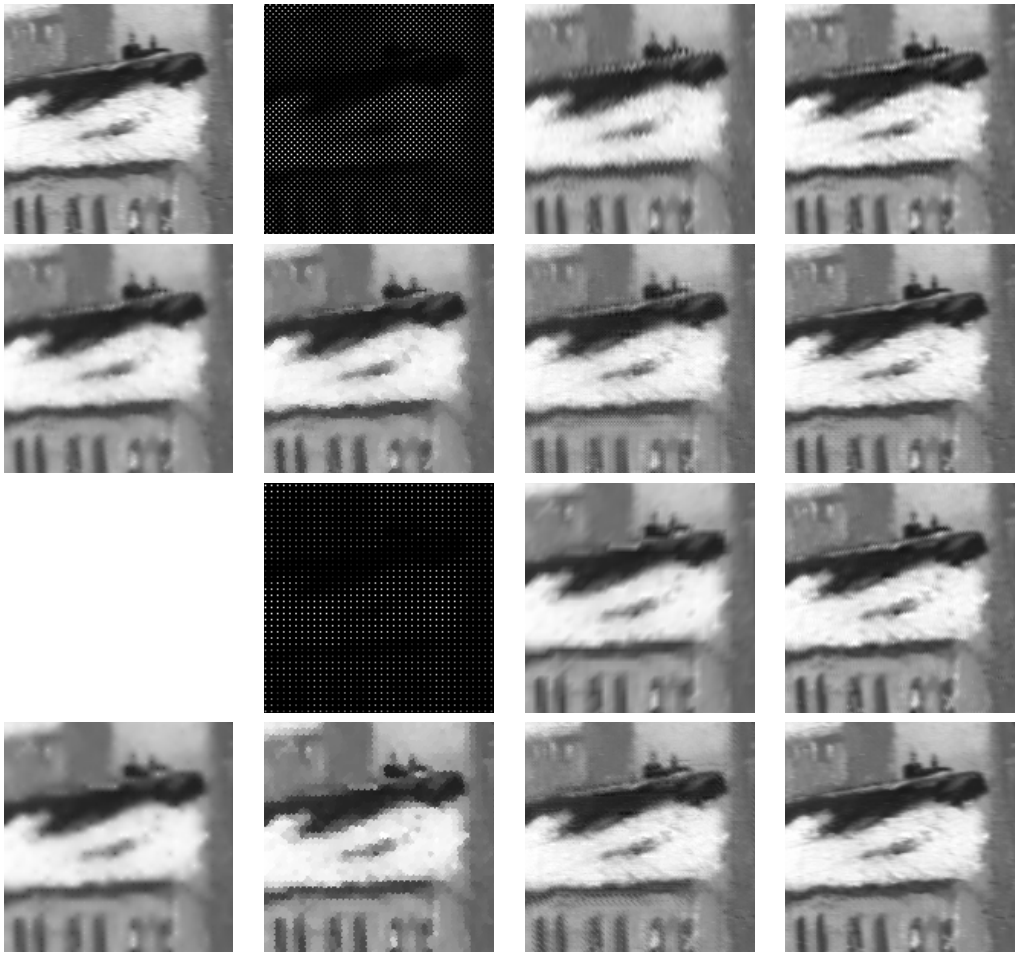

a	b	c	d
e	f	g	h
	i	j	k
l	m	n	o

Figure 11.79: An extraction from band 6 of Scene 7 in the absence of noise. (a) full-resolution image, (b) SFA I mosaicked image, (c) SFA I demosaicked image with BL, (d) SFA I demosaicked image with SH, (e) SFA I demosaicked image with BT, (f) SFA I demosaicked image with VM, (g) SFA I demosaicked image with DWT, (h) SFA I demosaicked image with LMMSE, (i) SFA II mosaicked image, (j) SFA II demosaicked image with BL, (k) SFA II demosaicked image with SH, (l) SFA II demosaicked image with BT, (m) SFA II demosaicked image with VM, (n) SFA II demosaicked image with DWT, (o) SFA II demosaicked image with LMMSE

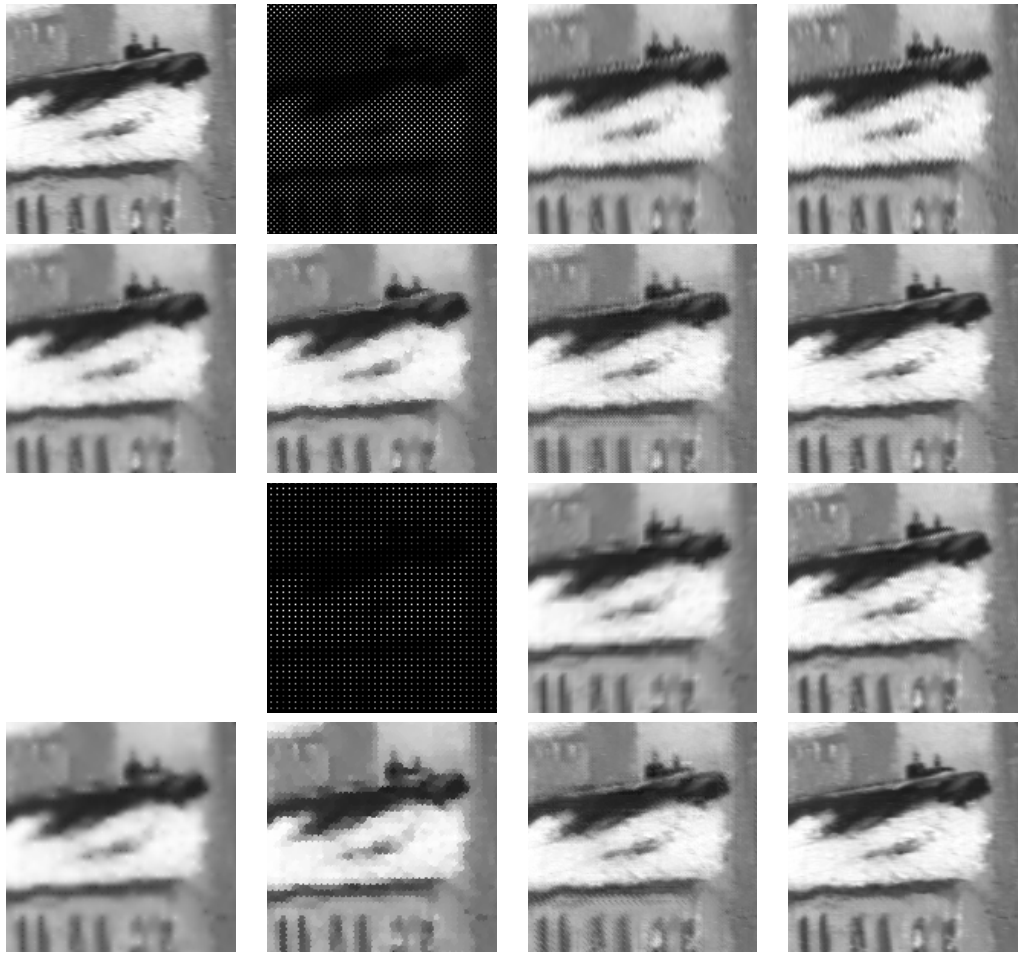

a	b	c	d
e	f	g	h
	i	j	k
l	m	n	o

Figure 11.80: An extraction from band 7 of Scene 7 in the absence of noise. (a) full-resolution image, (b) SFA I mosaicked image, (c) SFA I demosaicked image with BL, (d) SFA I demosaicked image with SH, (e) SFA I demosaicked image with BT, (f) SFA I demosaicked image with VM, (g) SFA I demosaicked image with DWT, (h) SFA I demosaicked image with LMMSE, (i) SFA II mosaicked image, (j) SFA II demosaicked image with BL, (k) SFA II demosaicked image with SH, (l) SFA II demosaicked image with BT, (m) SFA II demosaicked image with VM, (n) SFA II demosaicked image with DWT, (o) SFA II demosaicked image with LMMSE

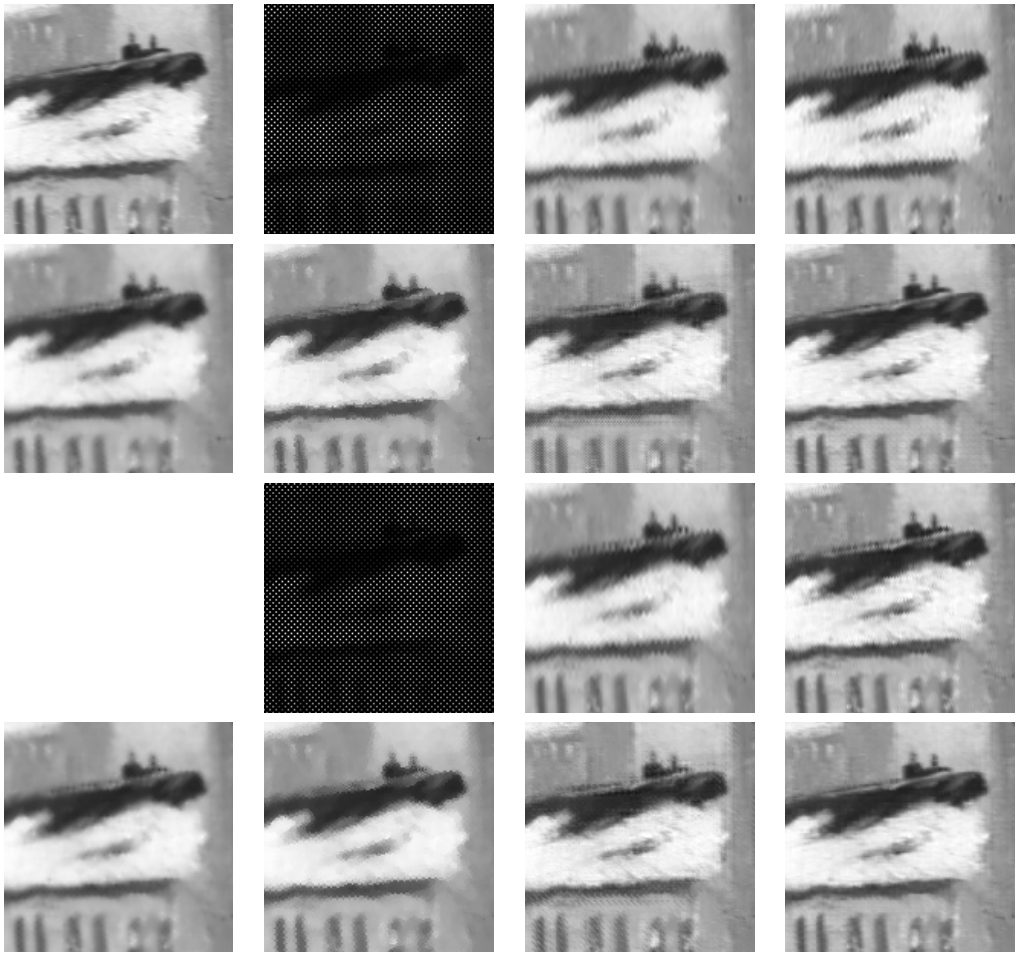

a	b	c	d
e	f	g	h
	i	j	k
l	m	n	o

Figure 11.81: An extraction from band 8 of Scene 7 in the absence of noise. (a) full-resolution image, (b) SFA I mosaicked image, (c) SFA I demosaicked image with BL, (d) SFA I demosaicked image with SH, (e) SFA I demosaicked image with BT, (f) SFA I demosaicked image with VM, (g) SFA I demosaicked image with DWT, (h) SFA I demosaicked image with LMMSE, (i) SFA II mosaicked image, (j) SFA II demosaicked image with BL, (k) SFA II demosaicked image with SH, (l) SFA II demosaicked image with BT, (m) SFA II demosaicked image with VM, (n) SFA II demosaicked image with DWT, (o) SFA II demosaicked image with LMMSE

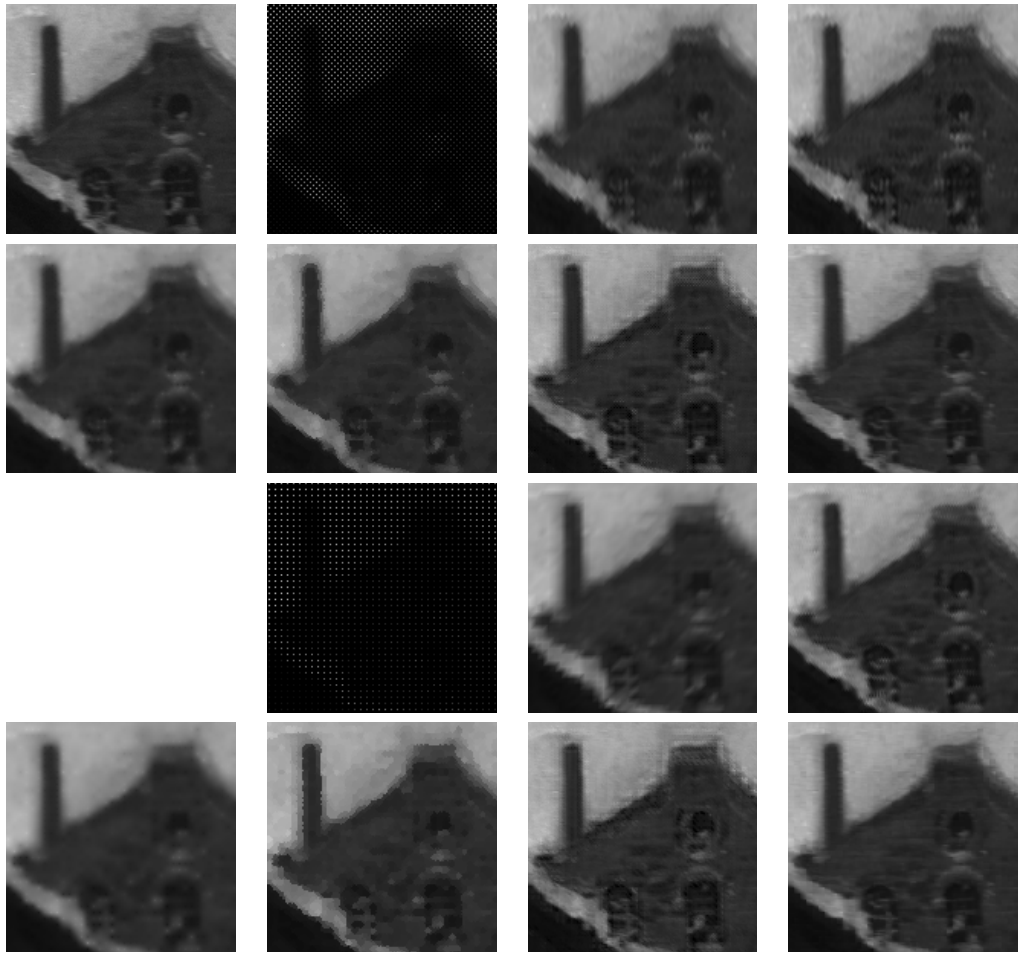

a	b	c	d
e	f	g	h
	i	j	k
l	m	n	o

Figure 11.82: An extraction from band 1 of Scene 8 in the absence of noise. (a) full-resolution image, (b) SFA I mosaicked image, (c) SFA I demosaicked image with BL, (d) SFA I demosaicked image with SH, (e) SFA I demosaicked image with BT, (f) SFA I demosaicked image with VM, (g) SFA I demosaicked image with DWT, (h) SFA I demosaicked image with LMMSE, (i) SFA II mosaicked image, (j) SFA II demosaicked image with BL, (k) SFA II demosaicked image with SH, (l) SFA II demosaicked image with BT, (m) SFA II demosaicked image with VM, (n) SFA II demosaicked image with DWT, (o) SFA II demosaicked image with LMMSE

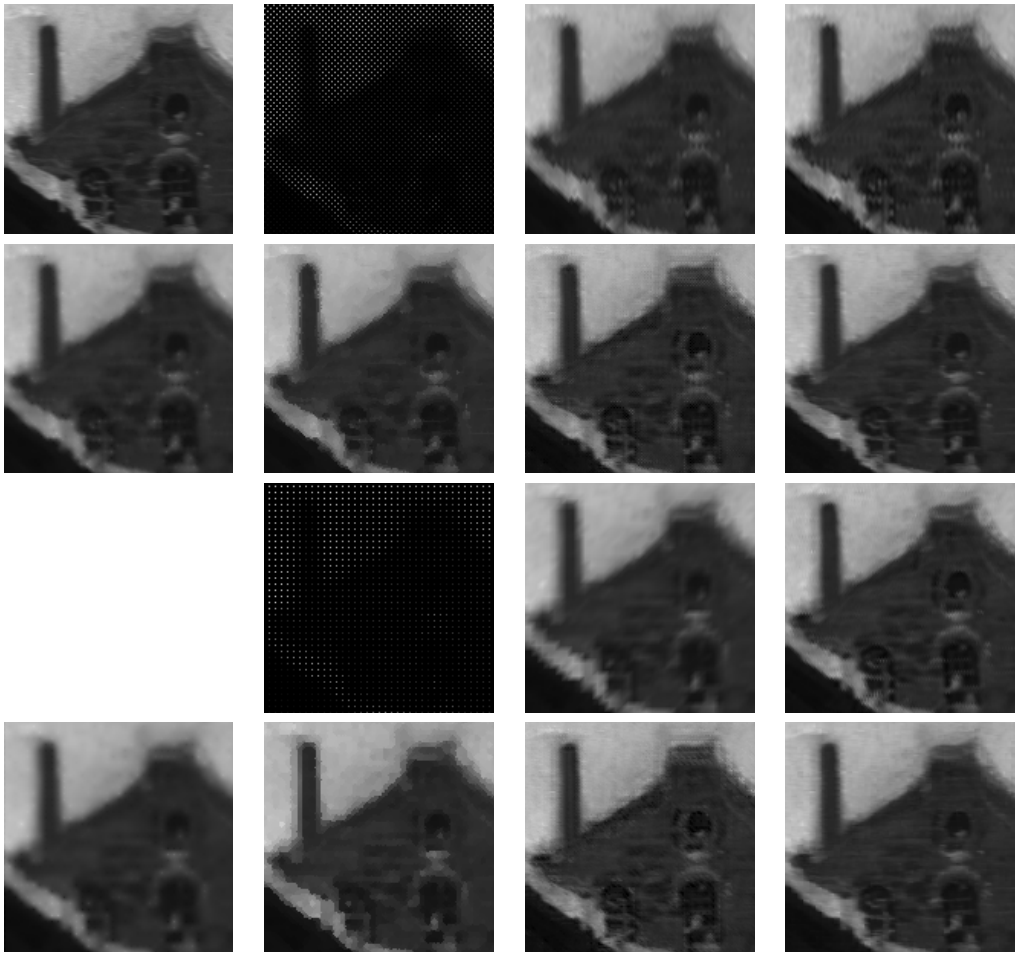

a	b	c	d
e	f	g	h
	i	j	k
l	m	n	o

Figure 11.83: An extraction from band 2 of Scene 8 in the absence of noise. (a) full-resolution image, (b) SFA I mosaicked image, (c) SFA I demosaicked image with BL, (d) SFA I demosaicked image with SH, (e) SFA I demosaicked image with BT, (f) SFA I demosaicked image with VM, (g) SFA I demosaicked image with DWT, (h) SFA I demosaicked image with LMMSE, (i) SFA II mosaicked image, (j) SFA II demosaicked image with BL, (k) SFA II demosaicked image with SH, (l) SFA II demosaicked image with BT, (m) SFA II demosaicked image with VM, (n) SFA II demosaicked image with DWT, (o) SFA II demosaicked image with LMMSE

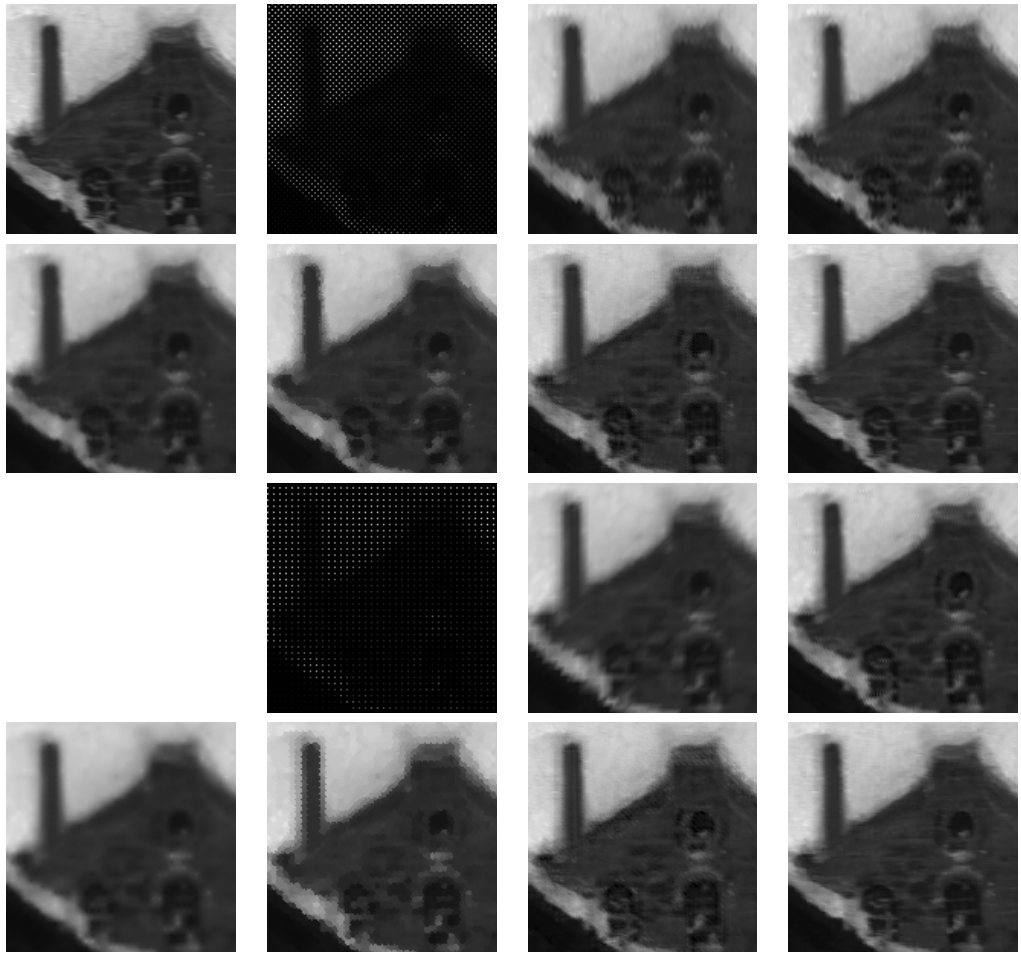

a	b	c	d
e	f	g	h
	i	j	k
l	m	n	o

Figure 11.84: An extraction from band 3 of Scene 8 in the absence of noise. (a) full-resolution image, (b) SFA I mosaicked image, (c) SFA I demosaicked image with BL, (d) SFA I demosaicked image with SH, (e) SFA I demosaicked image with BT, (f) SFA I demosaicked image with VM, (g) SFA I demosaicked image with DWT, (h) SFA I demosaicked image with LMMSE, (i) SFA II mosaicked image, (j) SFA II demosaicked image with BL, (k) SFA II demosaicked image with SH, (l) SFA II demosaicked image with BT, (m) SFA II demosaicked image with VM, (n) SFA II demosaicked image with DWT, (o) SFA II demosaicked image with LMMSE

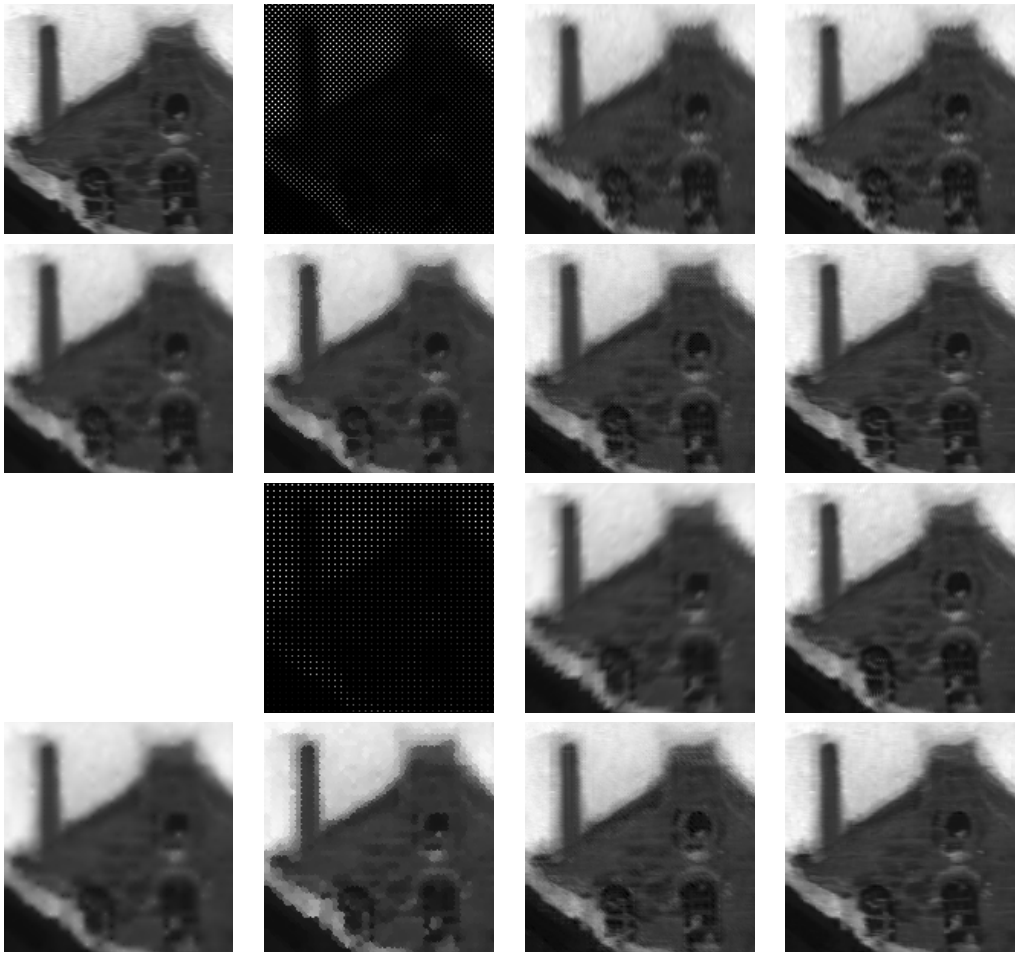

a	b	c	d
e	f	g	h
	i	j	k
l	m	n	o

Figure 11.85: An extraction from band 4 of Scene 8 in the absence of noise. (a) full-resolution image, (b) SFA I mosaicked image, (c) SFA I demosaicked image with BL, (d) SFA I demosaicked image with SH, (e) SFA I demosaicked image with BT, (f) SFA I demosaicked image with VM, (g) SFA I demosaicked image with DWT, (h) SFA I demosaicked image with LMMSE, (i) SFA II mosaicked image, (j) SFA II demosaicked image with BL, (k) SFA II demosaicked image with SH, (l) SFA II demosaicked image with BT, (m) SFA II demosaicked image with VM, (n) SFA II demosaicked image with DWT, (o) SFA II demosaicked image with LMMSE

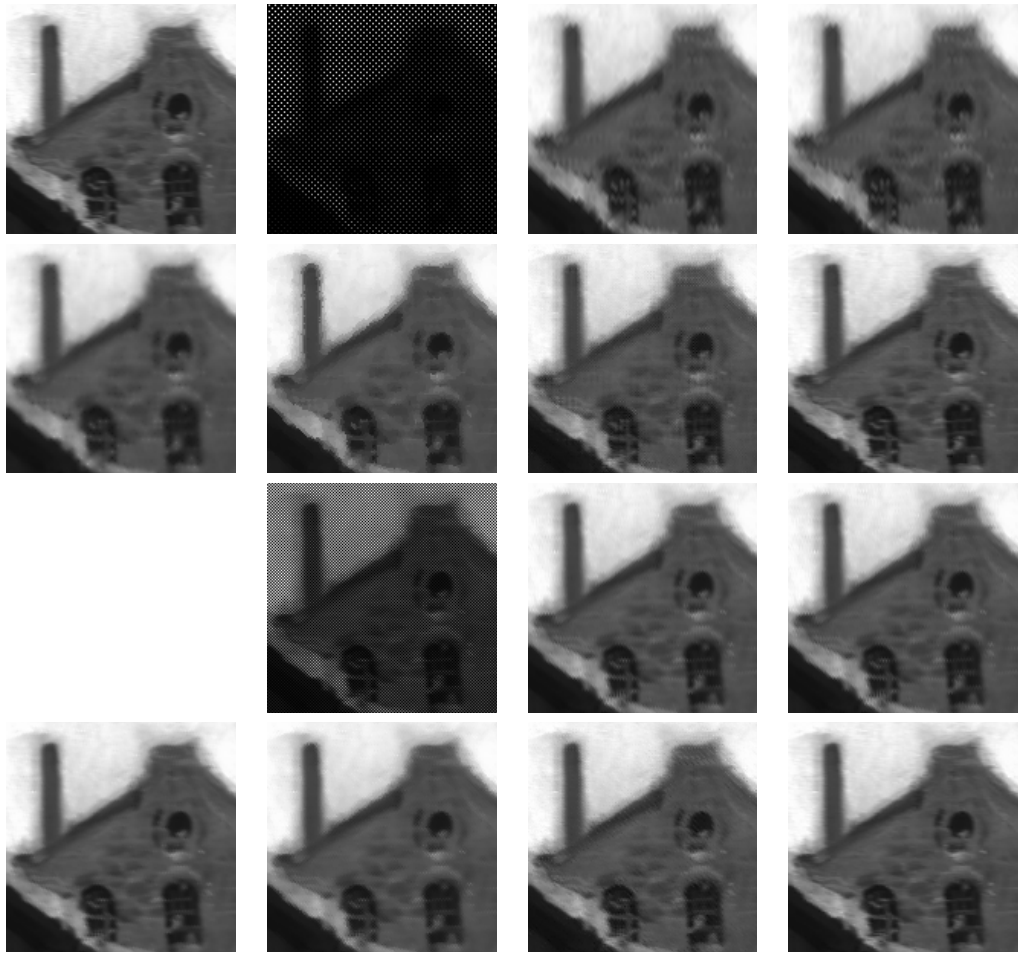

a	b	c	d
e	f	g	h
	i	j	k
l	m	n	o

Figure 11.86: An extraction from band 5 of Scene 8 in the absence of noise. (a) full-resolution image, (b) SFA I mosaicked image, (c) SFA I demosaicked image with BL, (d) SFA I demosaicked image with SH, (e) SFA I demosaicked image with BT, (f) SFA I demosaicked image with VM, (g) SFA I demosaicked image with DWT, (h) SFA I demosaicked image with LMMSE, (i) SFA II mosaicked image, (j) SFA II demosaicked image with BL, (k) SFA II demosaicked image with SH, (l) SFA II demosaicked image with BT, (m) SFA II demosaicked image with VM, (n) SFA II demosaicked image with DWT, (o) SFA II demosaicked image with LMMSE

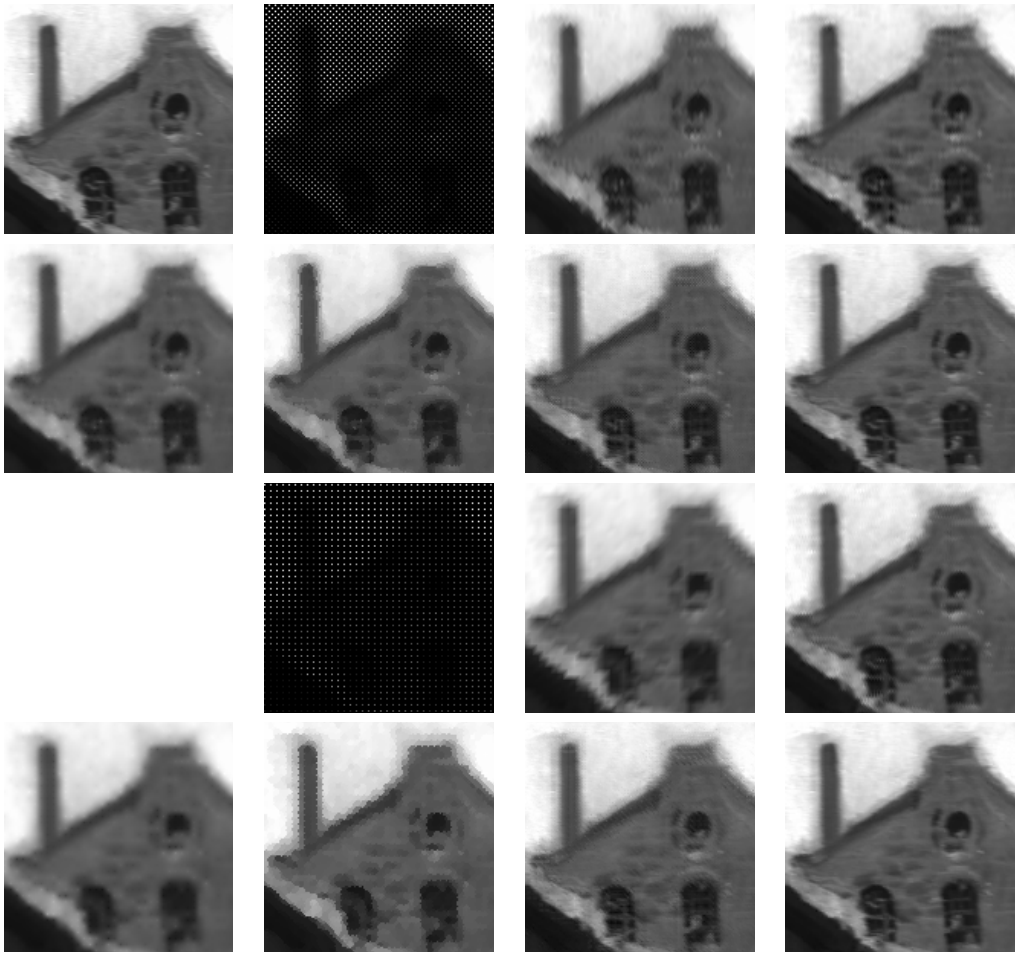

a	b	c	d
e	f	g	h
	i	j	k
l	m	n	o

Figure 11.87: An extraction from band 6 of Scene 8 in the absence of noise. (a) full-resolution image, (b) SFA I mosaicked image, (c) SFA I demosaicked image with BL, (d) SFA I demosaicked image with SH, (e) SFA I demosaicked image with BT, (f) SFA I demosaicked image with VM, (g) SFA I demosaicked image with DWT, (h) SFA I demosaicked image with LMMSE, (i) SFA II mosaicked image, (j) SFA II demosaicked image with BL, (k) SFA II demosaicked image with SH, (l) SFA II demosaicked image with BT, (m) SFA II demosaicked image with VM, (n) SFA II demosaicked image with DWT, (o) SFA II demosaicked image with LMMSE

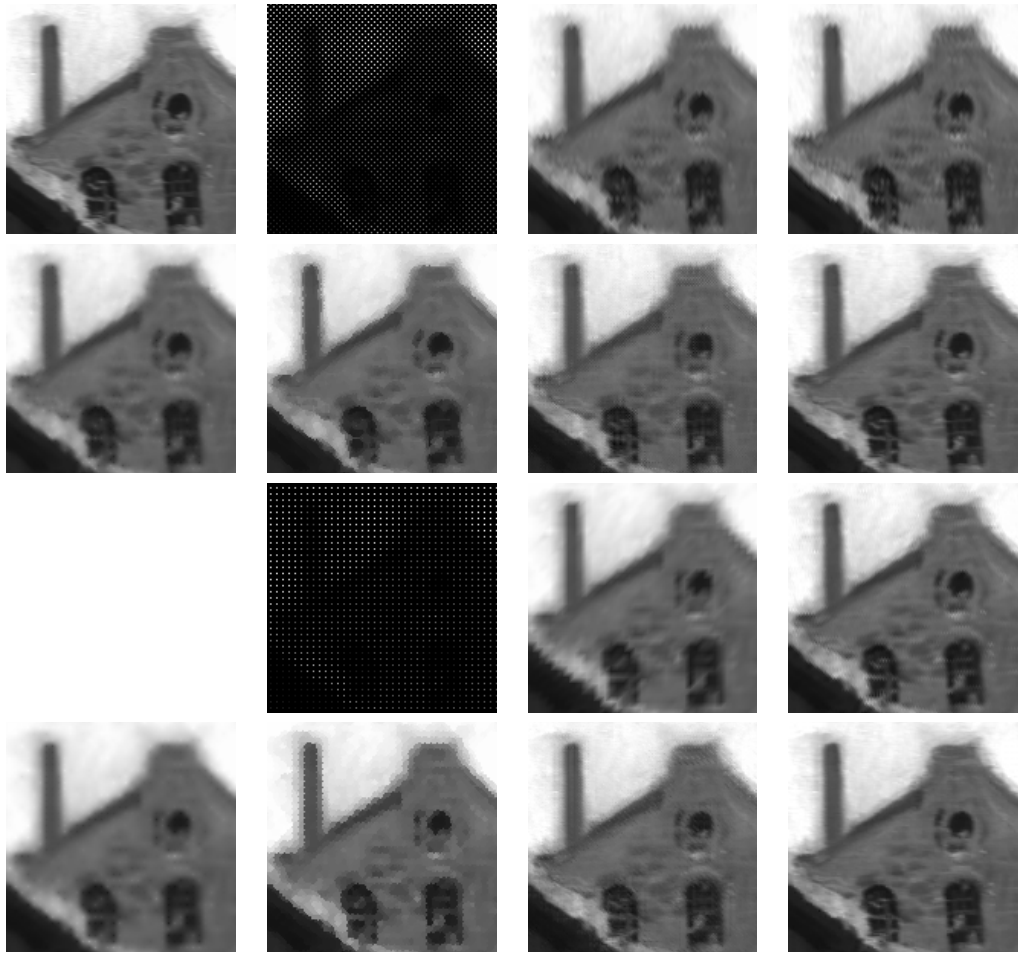

a	b	c	d
e	f	g	h
	i	j	k
l	m	n	o

Figure 11.88: An extraction from band 7 of Scene 8 in the absence of noise. (a) full-resolution image, (b) SFA I mosaicked image, (c) SFA I demosaicked image with BL, (d) SFA I demosaicked image with SH, (e) SFA I demosaicked image with BT, (f) SFA I demosaicked image with VM, (g) SFA I demosaicked image with DWT, (h) SFA I demosaicked image with LMMSE, (i) SFA II mosaicked image, (j) SFA II demosaicked image with BL, (k) SFA II demosaicked image with SH, (l) SFA II demosaicked image with BT, (m) SFA II demosaicked image with VM, (n) SFA II demosaicked image with DWT, (o) SFA II demosaicked image with LMMSE

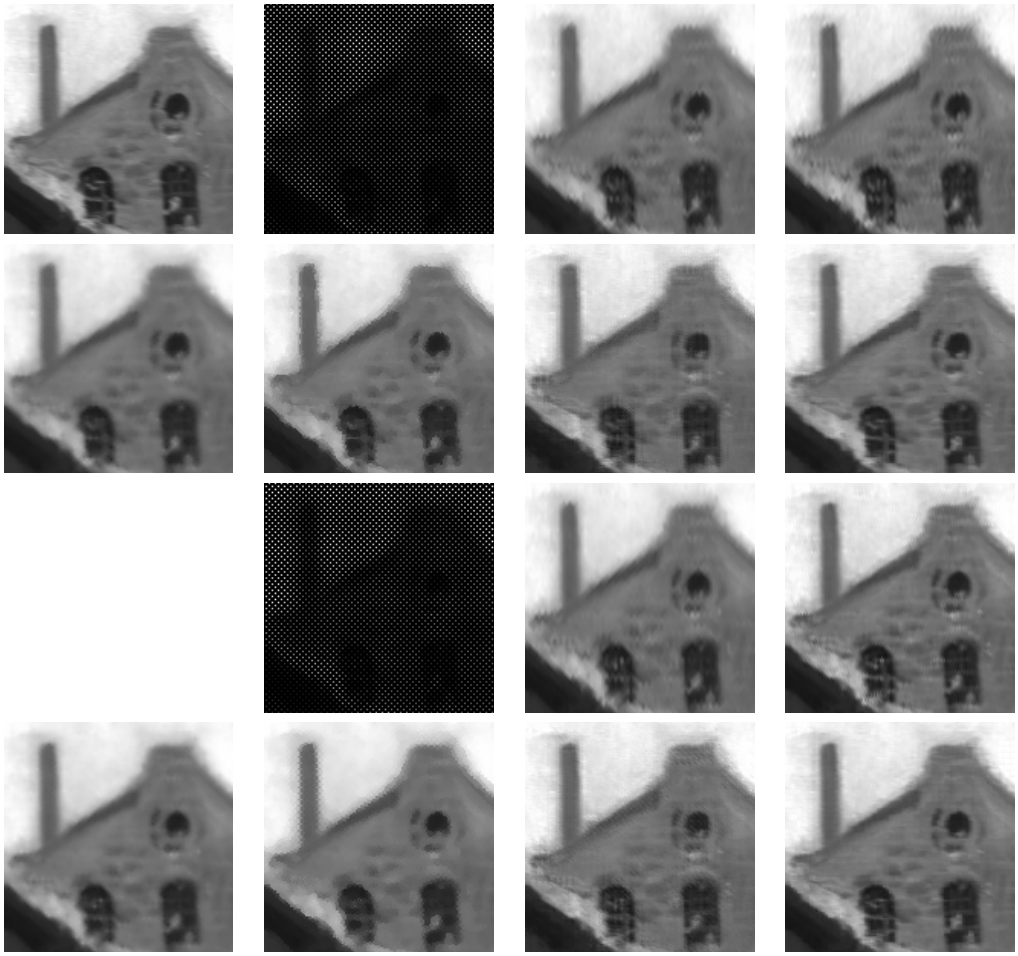

a	b	c	d
e	f	g	h
	i	j	k
l	m	n	o

Figure 11.89: An extraction from band 8 of Scene 8 in the absence of noise. (a) full-resolution image, (b) SFA I mosaicked image, (c) SFA I demosaicked image with BL, (d) SFA I demosaicked image with SH, (e) SFA I demosaicked image with BT, (f) SFA I demosaicked image with VM, (g) SFA I demosaicked image with DWT, (h) SFA I demosaicked image with LMMSE, (i) SFA II mosaicked image, (j) SFA II demosaicked image with BL, (k) SFA II demosaicked image with SH, (l) SFA II demosaicked image with BT, (m) SFA II demosaicked image with VM, (n) SFA II demosaicked image with DWT, (o) SFA II demosaicked image with LMMSE

The differences in the PSNR and SSIM indices indicate distinctions in principles of quality metrics. For imagery, it is always necessary and useful to evaluate visual presentation subjectively. Figure 11.26-11.89 present regions extracted from the resultant images for all scenes mosaicked with SFA I and SFA II and demosaicked with all methods. A glimpse at the extractions show that LMMSE achieves the most satisfactory results almost in all conditions, whereas other methods suffer from the intrinsic artefacts, e.g., blurring, zippering, fringing, etc., which largely degrades the subjective quality.

In principle, Band 5 reflects the distinction between SFA I and SFA II, and the results support this hypothesis. Spatial sampling rate, i.e., probability of appearance of the filter elements in a SFA, is a determining factor in the quality of demosaicked images. In other words, Band 5 in SFA II is superior than that in SFA I, whereas the bands other than Band 5 in SFA II is even worse than that in SFA I.

In addition, images of Band 8, namely the NIR band, differ from the other bands in appearance, however, there seem still high correlations between the NIR band and other bands.

11.4 Conclusion

In this chapter, we performed comparative analyses and evaluations of 6 proposed and basic SFA demosaicking techniques, given characteristics of 2 practical SFA-based imagers and 8 scenes covering both visible and NIR bands.

The objective image quality assessment indicated that the 3 proposed demosaicking techniques based on different assumptions perform differently. Basic techniques, such as bilinear interpolation and the binary-tree approach do not make use of the inter-band correlation, thus suffering from blurring or zippering effects. The smooth-hue interpolation performs well if there exists a band of higher sampling rate. SFA demosaicking on the basis of vector median filtering tends to preserve the edges but smooth the details surrounded by the edges. DWT based SFA demosaicking runs fairly fast but introduces unreal high-frequency information that results in visible noise. The performance of the LMMSE approach relies primarily on the similarity between the training data (a priori information) and the images to be processed.

In addition, tessellation of filter elements in a SFA plays an important role in a SFA-based imaging pipeline, and determines, to a large extent, final image quality. For instance, SFA II sacrifices the sampling rate of other bands for the densely sampled band 5. In the design of a practical system, it is of vital importance to

strike a sensible balance between spatial and spectral resolution, and the way of tessellation also influences the overall performance.

Regarding the computational complexity, the vector median filtering approach is computationally expensive. With suitable trainings, LMMSE is the most efficient method because of its linear property. DWT is in between these two in terms of the complexity.

The presentation of the extractions reveal the disagreements between subjective and objective assessment. More subjective assessments are expected in the future. And the choice of quality metrics should be considered together with the application of a SFA-based imaging system.

Chapter 12

Conclusion

We have presented the main content of this dissertation. In this conclusive chapter, content of the previous chapters are first summarised, before discussions of issues that have been realised. We also list key findings and provide our perspective as suggestions for those interested in spectral filter array based spectral imaging.

12.1 Summary of contribution

The dissertation concerns demosaicking and issues in the design of a SFA based spectral imaging system.

Part I provided the background information in connection with the research. In Chapter 2 we first reviewed the early-stage development of spectral imaging from both roots in spectroscopy and imaging, and traced its evolution and classified a spectrum of approaches according to the fundamental. This illustrates the advantages of filter array based solutions in size, weight, cost and robustness. Subsequently Chapter 3 explored the SFA based solutions of the art by reviewing literature in regard to the design, development and realisation of SFA based systems.

Part II concerned the design, implementation as well as two preliminary studies of the simulation framework in order to facilitate the development of demosaicking. Chapter 4 presented the structure of the simulated pipeline and provided a radiometric analysis on its validity. Also introduced were the assumptions and therefore limitations of the simulation framework. Chapter 5 evaluated the performance of 6 types of filters of varying bandwidths in terms of the accuracy of

spectral reflectance estimation with three linear estimation methods in the context of spectral image acquisition. Chapter 6 investigated the influence of chromatic aberration on demosaicking and proposed a simulation workflow for that purpose. Both axial and transverse types of chromatic aberration and their combination were simulated.

Part III probed into the core design problem by proposing three methods for SFA demosaicking based on vector media filtering, discrete wavelet transform and linear minimum mean square error. In Chapter 7, 8 and 9, these techniques were described in detail and the performance was evaluated with reference to other common methods.

Part IV evaluated the performance of SFA based imaging systems. Chapter 10 compared SFAs with CFAs in terms of colorimetric accuracy by assessing the balance between spatial and spectral resolution that have opposite influence on the colorimetric performance. Chapter 11 scrutinised the proposed demosaicking methods given the characteristics and parameters of a real-world SFA sensor design.

12.2 Discussions

The accuracy of the results obtained in the dissertation is affected by the realisticness of the simulation. The spectral images used as scenes bear limited variety and resolution as well as intrinsic optical and electronic distortions, which makes it difficult to generalise the conclusions. Although the simulation may be improved by more complicated measures, such as optical simulation based on ray tracing analysis of real lenses and the introduction of measured noise, simulation bears intrinsic insufficiencies, inaccuracies and inappropriateness in itself. In a real system, these shortcomings of simulation may very well be overcome. However, real-world systems are not typically flexible for experimental purposes and may not be fully consistent with the theoretical design. Moreover, in a practical system, there would be a lack of ground truth that is essential to objective evaluations of system performance.

In this dissertation, performance is evaluated in terms of objective image or signal quality. Image quality metrics, such as the SSIM, are generally developed to mimic the characteristics of the human visual system, whereas signal quality metrics, such as the RMSE, measure simply the physical differences. Neither of them are entirely appropriate for the assessment of spectral image quality, for spectral

images are not necessarily meant for human observers. Therefore application-specific quality metrics optimised for spectral images would be preferable. Subjective evaluation of image quality may also be useful when the target audience is human.

12.3 Findings

SFA Demosaicking. The assumptions on which a variety of CFA interpolation methods are based are often inapplicable to SFA demosaicking. Among others, the luma/chroma based colour spaces is irrelevant to spectral images. Therefore we proposed and experimented with three adaptive techniques, and compared their performance with some of the common methods as a benchmark.

In SFA demosaicking, median filtering in n-sphere alleviates aliasing numerically that is often resulted from basic interpolation approaches, in particular in regions rich in edges and details. Nevertheless, it introduces non-existent aliasing as a result of its nature of combination, thus reducing the perceptual quality. As an exception, it shows advantages for demosaicking binary images that possess edges and fine details of high-contrast. Parallel computing, e.g., heterogeneous programming, was exploited in implementing these methods to reduce the computational time. The usefulness of this technique is therefore limited by its exceptionally high computational complexity.

The performance of the DWT based SFA demosaicking method depends heavily on the spectral cross-correlation of the mosaic image in question, as a result of the "replace" rule for the high-pass filtered components in the wavelet-transformed images. As a result, it outperforms conventional interpolation techniques for scenes bearing high correlation, achieves worse results for scenes lack of correlation. The use of "replace" rule in DWT based SFA demosaicking is therefore related to the correlation of mosaic images, which is further influenced by scenes themselves and degree of overlap of the filters.

The proposed LMMSE approach is essentially a linear method that combine linear Wiener estimation and an interpolation on residual channels. The latter may overcome the error introduced by the former that is prone to noise. Both steps are of high scalability and computational efficiency, owing to its nature of linear operation. On the other hand, performance of this method is contingent on a priori information, i.e., training. In the experiments, scenes of the same genre were used as training set and testing set, thus yielding good results. In practice, however, real scenes may not be predictable.

Given the same scenes, different SFAs, i.e., varying spectral transmittances of the filters and spatial arrangement of filter elements, would result in filtered images of distinct characters that subsequent demosaicking methods take as input. It is therefore also of great moment to treat SFA and demosaicking as integral parts of a single system.

Selection of filter bandwidth. As demonstrated by the experimental results, bandwidth of filters has a profound impact on the accuracy of spectral reconstruction. Band-pass and band-reject filters of reasonably wide band commonly seen in practice benefit spectral acquisition. Further, band-pass or band-reject filters of extremely narrow or broad bandwidths perform unsatisfactorily or unsteadily. Also the accuracy results also depend on the reconstruction methods used, and noise plays a role as well as the spectral metrics. The experiments were conducted in simulated lighting condition that is sufficient in terms of intensity. In insufficient lighting conditions, however, we assume that the advantages of wider bandwidths would be more visible in the system sensitivity as well as the signal-to-noise ratio.

Chromatic aberration. CA benefits demosaicking to some extent, in particular, blur benefits demosaicking by higher spatial correlation. however any type of CA decreases image quality by means of image blur and mis-registration. In theory, transverse CA in form of mis-registration should reduce correlation, thus decreasing the performance. On the contrary, the figures show opposite results. Perhaps the resampling involved blurs the images to some extent as well. In comparison with intra-channel methods, inter-channel interpolation is more sensitive to the content of the green channel. Axial CA results in higher performance in terms of cross comparison, indicating that blur influences less the signal fidelity and similarity. In comparison, both of the other two types of CA involve transversal CA and lead to significantly worse results. Obviously CA lowers the overall image quality by any means.

Colorimetric performance. In general, the 4-band SFA provides better or comparable performance in comparison with the 3-band setup except for the case of very narrow band-reject and normal bandpass filters. Similarly the 8-band SFA delivers higher colour accuracy expect the case of narrow bandreject filters. Therefore SFA of certain number of bands is not harmful for colorimetric reproduction. Moreover, it is obvious to see that spectral characteristics of a filter set not only make a direct impact on the colour reconstruction, but also influence the spectral correlation of the observed image on which some demosaicking methods depend.

12.4 Perspectives

The simulation based study demonstrates the usefulness, effectiveness and feasibility of a spectral image acquisition system employing a single-sensor covered by a multi-band filter array. The design of a SFA-based imaging framework differs from that of a CFA-based system in the requirements for the spectral range, light sensitivity, spectral and spatial resolution, features of interest as well as observers, etc. As a result, SFA-based systems should be specific to applications in order to narrow down the wide variety to a small number of variables.

A SFA imaging pipeline is composed of several components. The findings reveal that there is significant influence of some components on others. An adjustment of one parameter may impact the subsequent steps and thus the resultant image directly. It is therefore critical to consider the design of the pipeline as a whole by taking into account the interrelationship of the components.

At the moment, there are few commercial spectral imagers based on SFAs, due in part to the technical difficulties and thereby the considerable cost. The lack of supporting data processing further limits their applicability. We hope this work offers valuable information for, and contributes to, further development and wide use of this technology, as a convenient approach to spectral imaging. The dissertation concludes with our fervent hope that the effort will bear fruit in the foreseeable future.

Bibliography

[1] ISETBIO toolbox. https://github.com/isetbio/isetbio. Retrieved 20 Jun 2014.

[2] Kodak lossless true color image suite. http://r0k.us/graphics/kodak/. PhotoCD PCD0992.

[3] The SSIM index for image quality assessment. http://www.cns.nyu.edu/lcv/ssim/. Retrieved 10 Sep 2014.

[4] Hemant Kumar Aggarwal and Angshul Majumdar. Multi-spectral demosaicing technique for single-sensor imaging. In *Fourth National Conference on Computer Vision, Pattern Recognition, Image Processing and Graphics (NCVPRIPG), 2013*, pages 1–4, Dec 2013.

[5] Hemant Kumar Aggarwal and Angshul Majumdar. Compressive sensing multi-spectral demosaicing from single sensor architecture. In *Proceedings of 2nd IEEE China Summit and International Conference on Signal and Information Processing (ChinaSIP), 2014*, July 2014.

[6] Hemant Kumar Aggarwal and Angshul Majumdar. Single-sensor multi-spectral image demosaicing algorithm using learned interpolation weights. In *Proceedings of the International Geoscience and Remote Sensing Symposium (IGARSS), 2014*, July 2014.

[7] Hemant Kumar Aggarwal, Angshul Majumdar, and Rabab Ward. A reconstruction algorithm for multi-spectral image demosaicing. *IASTED Signal and Image Processing*, July 2013.

[8] Mauri Aikio. Hyperspectral prism-grating-prism imaging spectrograph. VTT Publications 435, Technical Research Centre of Finland, Espoo, 2001.

[9] Jaakko Astola, Petri Haavisto, and Yrj´o Neuvo. Vector median filters. *Proceedings of the IEEE*, 78(4):678 –689, April 1990.

[10] I. K. Baldry and J. BlandâĂŘHawthorn. A tunable echelle imager. *Publications of the Astronomical Society of the Pacific*, 112(774):pp. 1112–1120, 2000.

[11] David W. Ball. *Field guide to spectroscopy*, volume FG08 of *SPIE Field Guides*. SPIE Press, Bellingham, WA, US, 2006.

[12] David A. Basiji and William E. Ortyn. Imaging and analyzing parameters of small moving objects such as cells, April 3 2001. US Patent 6,211,955.

[13] Bryce Edward Bayer. Color imaging array, July 20 1976. US Patent 3,971,065.

[14] Andrew Bodkin, A. Sheinis, A. Norton, J. Daly, S. Beaven, and J. Weinheimer. Snapshot hyperspectral imaging: the hyperpixel array camera. In *Algorithms and Technologies for Multispectral, Hyperspectral, and Ultraspectral Imagery XV*, volume 7334 of *Proc. SPIE*, pages 73340H–73340H–11, April 2009.

[15] Matthew B. Bouchard, Brenda R. Chen, Sean A. Burgess, and Elizabeth M. C. Hillman. Ultra-fast multispectral optical imaging of cortical oxygenation, blood flow, and intracellular calcium dynamics. *Opt. Express*, 17(18):15670–15678, Aug 2009.

[16] IS Bowen. The image-slicer a device for reducing loss of light at slit of stellar spectrograph. *The Astrophysical Journal*, 88:113, 1938.

[17] Johannes Brauers and Til Aach. A color filter array based multispectral camera. In German Color Group, editor, *12th Workshop Farbbildverarbeitung*, Ilmenau, October 2006.

[18] James B. Breckinridge. Evolution of imaging spectrometry: past, present, and future. In Michael R. Descour and Jonathan M. Mooney, editors, *Imaging Spectrometry II*, volume 2819 of *Proc. SPIE*, pages 2–6, November 1996.

[19] Encyclopædia Britannica. Spectroheliograph. `http://global.britannica.com/EBchecked/topic/558867/spectroheliograph`. Retrieved 04 Nov 2014.

[20] Philip E. Buchsbaum and Michael J. Morris. Overdeveloping unmasked photoresist layer creating undercut in walls and expose the underlying wafer; for spectroscopic imaging, October 28 2003. US Patent 6,638,668.

[21] Theodor V. Bulygin and Gennady N. Vishnyakov. Spectrotomography: a new method of obtaining spectrograms of two-dimensional objects. In *Analytical Methods for Optical Tomography*, volume 1843 of *Proc. SPIE*, pages 315–322, November 1992.

[22] Emmanuel J. Candès, Justin K. Romberg, and Terence Tao. Stable signal recovery from incomplete and inaccurate measurements. *Communications on Pure and Applied Mathematics*, 59(8):1207–1223, 2006.

[23] Brice Chaix de Lavarène, David Alleysson, and Jeanny Hérault. Practical implementation of lmmse demosaicing using luminance and chrominance spaces. *Computer Vision and Image Understanding*, 107(1):3–13, 2007.

[24] Li Chen, Kim-Hui Yap, and Yu He. Subband synthesis for color filter array demosaicking. *IEEE Transactions on Systems, Man and Cybernetics, Part A: Systems and Humans*, 38(2):485–492, March 2008.

[25] CIE. *The basis of physical photometry*. International Commission on Illumination, 1983. CIE 018.2-1983.

[26] CIE. *International Lighting Vocabulary*. International Commission on Illumination, 1987. CIE 17.4-1987.

[27] CIE. *Colorimetry*. International Commission on Illumination, 2004. CIE 015:2004.

[28] *Colorimetry - Part 6: CIEDE2000 Colour-Difference Formula*. Number CIE Draft Standard DS 014-6/E:2012. CIE, Vienna, Austria, 2012.

[29] Irina Ciortan, Hilda Deborah, Sony George, and Jon Yngve Hardeberg. Color and hyperspectral image segmentation for historical documents. In *2015 Digital Heritage*, volume 1, pages 199–206. IEEE, September 2015.

[30] David R. Cok. Signal processing method and apparatus for producing interpolated chrominance values in a sampled color image signal, February 10 1987. US Patent 4,642,678.

[31] Robert N. Colwell. Some practical applications of multiband spectral reconnaissance. *American Scientist*, 49(1):pp. 9–36, 1961.

[32] Robert N. Colwell. Applications of multispectral sensing. In *Abstracts for 1965: Abstracts of papers submitted for six meetings with which the Society was associated*, number 87 in Geological Society of America Special Paper. Geological Society of America, New York, NY, US, 1966.

[33] Robert N. Colwell. Uses and limitations of multispectral remote sensing. In *Proceedings of the Fourth Symposium on Remote Sensing of Environment*, pages 71–100, 1966.

[34] Sébastien Courroux, Stéphane Guyetant, Stéphane Chevobbe, and Michel Paindavoine. A wavelet-based demosaicking algorithm for embedded applications. In *Conference on Design and Architectures for Signal and Image Processing (DASIP)*, pages 90–96, October 2010.

[35] Georges Courtes. Méthodes d'observation et étude de l'hydrogène interstellaire en émission. 23(2):115–117, 1960. In French.

[36] Georges Courtes. Le télescope spatial et les grands télescope au sol. In *Application de la Photométrie Bidimensionelle à l'Astronomie*, pages 241–269. L'Institut National d'Astronomie et de Géophysique, April 1980. In French.

[37] Hendrik de Lang and Gijsbertus Bouwhuis. Optical system for a color television camera, August 24 1965. US Patent 3,202,039.

[38] Michael R. Descour and Eustace L. Dereniak. Nonscanning no-moving-parts imaging spectrometer. In *Proc. SPIE*, volume 2480, pages 48–64, 1995.

[39] David L. Donoho. Compressed sensing. *IEEE Transactions on Information Theory*, 52(4):1289–1306, April 2006.

[40] John Dougherty, Steve Smith, and Oliver Lischtschenko. Multispectral imaging: Development and applications for snapshot msi instrumentation. In Thomas Längle Jürgen Beyerer, Fernando Puente León, editor, *Proceedings of Optical Characterization of Materials (OCM) 2013*, pages 95–102. KIT Scientific Publishing, March 2013.

[41] Jef Driesen and Paul Scheunders. Wavelet-based color filter array demosaicking. In *International Conference on Image Processing (ICIP)*, volume 5, pages 3311–3314. IEEE, October 2004.

[42] Jason M. Eichenholz. Dichroic filter array multispectral imaging systems. In *Imaging and Applied Optics Congress*, pages A–A4. Optical Society of America, 2010.

[43] Jason M. Eichenholz, Nick Barnett, Yishung Juang, Dave Fish, Steve Spano, Erik Lindsley, and Daniel L. Farkas. Real-time megapixel multispectral bioimaging. In *Imaging, Manipulation, and Analysis of Biomolecules, Cells, and Tissues VIII*, volume 7568 of *Proc. SPIE*, pages 75681L–75681L–10, Jan 2010.

[44] Jason M. Eichenholz and John Dougherty. Ultracompact fully integrated megapixel multispectral imager. In *Integrated Optics: Devices, Materials, and Technologies XIII*, volume 7218 of *Proc. SPIE*, pages 721814–721814–10, 2009.

[45] J. E. Farrell, P. B. Catrysse, and B. A. Wandell. Digital camera simulation. *Appl. Opt.*, 51(4):A80–A90, Feb 2012.

[46] Joyce E. Farrell, Peter B. Catrysse, and Brian A. Wandell. Digital camera simulation. *Applied Optics*, 51(4):A80–A90, February 2012.

[47] Robert D. Fiete. *Modeling the imaging chain of digital cameras*, volume TT92 of *Tutorial Texts in Optical Engineering*. SPIE press, Bellingham, WA, 2010.

[48] David H. Foster, Kinjiro Amano, Sérgio M. C. Nascimento, and Michael J. Foster. Frequency of metamerism in natural scenes. *J. Opt. Soc. Am. A*, 23(10):2359–2372, Oct 2006.

[49] Zane Frentress, L. C. Young, and Howard D. Edwards. Field photometer with nine-element filter wheel. *Appl. Opt.*, 3(2):303–308, Feb 1964.

[50] Liang Gao, Robert T Kester, and Tomasz S Tkaczyk. Compact image slicing spectrometer (iss) for hyperspectral fluorescence microscopy. *Optics express*, 17(15):12293–12308, 2009.

[51] Nahum Gat. Imaging spectroscopy using tunable filters: a review, 2000.

[52] Günter Gauglitz and Tuan Vo-Dinh, editors. *Handbook of spectroscopy*. WILEY-VCH, Weinheim, BW, DE, 2003.

[53] Bert Geelen, Nicolaas Tack, and Andy Lambrechts. A snapshot multispectral imager with integrated tiled filters and optical duplication. In *Advanced Fabrication Technologies for Micro/Nano Optics and Photonics VI*, volume 8613 of *Proc. SPIE*, pages 861314–861314–13, 2013.

[54] Bert Geelen, Nicolaas Tack, and Andy Lambrechts. A compact snapshot multispectral imager with a monolithically integrated per-pixel filter mosaic. In *Advanced Fabrication Technologies for Micro/Nano Optics and Photonics VII*, volume 8974 of *Proc. SPIE*, pages 89740L–89740L–8, 2014.

[55] M. E. Gehm, R. John, D. J. Brady, R. M. Willett, and T. J. Schulz. Single-shot compressive spectral imaging with a dual-disperser architecture. *Opt. Express*, 15(21):14013–14027, Oct 2007.

[56] Sony George and Jon Yngve Hardeberg. Ink classification and visualisation of historical manuscripts: Application of hyperspectral imaging. In *13th International Conference on Document Analysis and Recognition (ICDAR), 2015*, pages 1131–1135. IEEE, August 2015.

[57] Sony George and Jon Yngve Hardeberg. Estimation and correction of geometric distortion in pushbroom hyperspectral system for imaging art paintings. In *Image Sensors and Imaging Systems*, volume 2016 of *Proceedings of Electronic Imaging*, pages 1–4. Society for Imaging Science and Technology, February 2016.

[58] Alexander F. H. Goetz. Imaging spectrometry for remote sensing: vision to reality in 15 years. In Michael R. Descour, Jonathan M. Mooney, David L. Perry, and Luanna R. Illing, editors, *Imaging Spectrometry I*, volume 2480 of *Proc. SPIE*, pages 2–13, June 1995.

[59] Alexander F. H. Goetz. Three decades of hyperspectral remote sensing of the earth: A personal view. *Remote Sensing of Environment*, 113, Supplement 1(0):S5 – S16, September 2009. Imaging Spectroscopy Special Issue.

[60] Alexander F. H. Goetz, Gregg Vane, Jerry E. Solomon, and Barrett N. Rock. Imaging spectrometry for earth remote sensing. *Science*, 228(4704):1147–1153, 1985.

[61] J. W. Goodman. *Introduction to Fourier Optics*. McGraw-Hill physical and quantum electronics series. Roberts & Company, 2005.

[62] Alistair Gorman, David William Fletcher-Holmes, and Andrew Robert Harvey. Generalization of the lyot filter and its application to snapshot spectral imaging. *Opt. Express*, 18(6):5602–5608, Mar 2010.

[63] Robert O. Green. Lessons and key results from 30 years of imaging spectroscopy. In Pantazis Mouroulis and Thomas S. Pagano, editors, *Imaging Spectrometry XIX*, volume 9222 of *Proc. SPIE*, pages 92220B–92220B–12, September 2014.

[64] Bahadir K. Gunturk, Yucel Altunbasak, and Russell Mersereau. Color plane interpolation using alternating projections. In *International Conference on Acoustics, Speech, and Signal Processing (ICASSP)*, volume 4, pages 3333–3336. IEEE, May 2002.

[65] Bahadir K. Gunturk, John Glotzbach, Yucel Altunbasak, Ronald W. Schafer, and Russel M. Mersereau. Demosaicking: color filter array interpolation. *Signal Processing Magazine*, 22(1):44–54, January 2005.

[66] Maya R. Gupta and Ting Chen. Vector color filter array demosaicing. In Morley M. Blouke, John Canosa, and Nitin Sampat, editors, *Sensors and Camera Systems for Scientific, Industrial, and Digital Photography Applications II*, volume 4306 of *Proc. SPIE*, pages 374–382. SPIE, May 2001.

[67] Neelam Gupta, Philip R. Ashe, and Songsheng Tan. Miniature snapshot multispectral imager. *Optical Engineering*, 50(3):033203–033203–9, 2011.

[68] Nathan Hagen and Michael W. Kudenov. Review of snapshot spectral imaging technologies. *Optical Engineering*, 52(9):090901–090901, 2013.

[69] Jon Yngve Hardeberg. *Acquisition and Reproduction of Color Images: Colorimetric and Multispectral Approaches*. dissertation.com., 2001.

[70] Stephen E. Harris and Richard W. WALLACE. Acousto-optic tunable filter. *J. Opt. Soc. Am.*, 59(6):744–747, Jun 1969.

[71] John Hearnshaw. *Astronomical Spectrographs and Their History*. Cambridge University Press, 2009.

[72] John Hershey and Zhengyou Zhang. Multispectral digital camera employing both visible light and non-visible light sensing on a single image sensor, December 2 2008. US Patent 7,460,160.

[73] Mikiya Hironaga and Noriyuki Shimano. Estimating the noise variance in an image acquisition system and its influence on the accuracy of recovered spectral reflectances. *Applied Optics*, 49(31):6140–6148, Nov 2010.

[74] Dicky Howett. *Television Innovations: 50 Technological Developments*. Kelly Publications, 2006.

[75] Emmett J. Ientilucci and Scott D. Brown. Advances in wide-area hyperspectral image simulation. In *AeroSense 2003*, pages 110–121. SPIE, 2003.

[76] Francisco Imai, Lawrence Taplin, David Day, Ellen Day, and Roy Berns. Imaging at the national gallery of art, washington dc. https://ritdml.rit.edu/handle/1850/4355, 2002.

[77] Francisco H. Imai and Roy S. Berns. Spectral estimation using trichromatic digital cameras. In *Proceedings of the International Symposium on Multispectral Imaging and Color Reproduction for Digital Archives*, pages 42–49, Chiba, Japan, 1999.

[78] Francisco H. Imai, Mitchell R. Rosen, and Roy S. Berns. Comparison of spectrally narrow-band capture versus wide-band with a priori sample analysis for spectral reflectance estimation. In *Proceedings of the IS&T/SID Eighth Color Imaging Conference: Color Science and Engineering Systems, Technologies, and Applications*, pages 234–241, Scottsdale, Arizona, November 2000. IS&T.

[79] Thermo Fisher Scientific Inc. Maestro 2 brochure. http://www.thermofisher.com.au/Uploads/file/Scientific/Life-Science-Research-Technologies/In-Vivo-Imaging/In-vivo-Imaging-Systems/Maestro2-Brochure.pdf, 2011. last accessed 8 November 2014.

[80] Pierre Jules César Janssen. Sur la étude spectrale des protubérances solaires [on a spectral study of solar prominences]. *Comptes Rendus Acad. Sci*, 68:93–95, 1869. In French.

[81] Pierre Jules César Janssen. Sur la méthode qui permet de constater la matière protubérantielle sur tout le contour du disque solaire [on a method to see the entire solar corona]. *Comptes Rendus Acad. Sci*, 68:713–715, 1869. In French.

[82] Bo Gyu Jeong, Sueng Hwa Hyun, and Il Kyu Eom. Edge adaptive demosaicking in wavelet domain. In *9th International Conference on Signal Processing (ICSP)*, pages 836–839. IEEE, October 2008.

[83] John B. Johnson. Thermal agitation of electricity in conductors. *Phys. Rev.*, 32:97–109, Jul 1928.

[84] Romuald Jolivot, Pierre Vabres, and Franck Marzani. Reconstruction of hyperspectral cutaneous data from an artificial neural network-based multispectral imaging system. *Computerized Medical Imaging and Graphics*, 35(2):85 – 88, 2011. Advances in Skin Cancer Image Analysis.

[85] Andrey V. Kanaev, Marjorie Rawhouser, Mary R. Kutteruf, Michael K. Yetzbacher, Michael J. DePrenger, Kyle M. Novak, Corey A. Miller, and Christopher W. Miller. Demosaicking for full motion video 9-band swir sensor. In *Spectral Imaging Sensor Technologies: Innovation Driving Advanced Ap-*

plication Capabilities, volume 9104 of *Proc. SPIE*, pages 910407–910407–8, 2014.

[86] Narinder S. Kapany. Fiber optics. In John Strong, editor, *Concepts of Classical Optics*, Dover Books on Physics, chapter Appendix N, pages 553–579. Dover Publications, 2004.

[87] Daniel Keren and Margarita Osadchy. Restoring subsampled color images. *Machine Vision and Applications*, 11(4):197–202, December 1999.

[88] Oleg Khait, Sergev Smirnov, and Chieu D. Tran. Time-resolved multispectral imaging spectrometer. *Appl. Spectrosc.*, 54(12):1734–1742, Dec 2000.

[89] Daisuke Kiku, Yusuke Monno, Masayuki Tanaka, and Masatoshi Okutomi. Simultaneous capturing of rgb and additional band images using hybrid color filter array. In *Digital Photography X*, volume 9023 of *Proc. SPIE*, pages 90230V–90230V–9, 2014.

[90] Hyuk Su Kim, Sang Soo Kim, and Il Kyu Eom. Wavelet-domain demosaicking using linear estimation of interchannel correlation. *Optical Engineering*, 47(6):067002–067002–13, June 2008.

[91] Linghua Kong, Stephen Sprigle, Mark G. Duckworth, Dingrong Yi, Jayme J. Caspall, Jiwu Wang, and Futing Zhao. Handheld erythema and bruise detector. In *Medical Imaging 2008: Computer-Aided Diagnosis*, volume 6915 of *Proc. SPIE*, February 2008.

[92] Linghua Kong, Stephen Sprigle, Dingrong Yi, Fengtao Wang, Chao Wang, and Fuhan Liu. Developing handheld real time multispectral imager to clinically detect erythema in darkly pigmented skin. In *Multimodal Biomedical Imaging V*, volume 7557 of *Proc. SPIE*, January 2010.

[93] D. Krapf, B. Adoram, J. Shappir, A. SaâĂŹar, S. G. Thomas, J. L. Liu, and K. L. Wang. Infrared multispectral detection using Si/Si_xGe_{1-x} quantum well infrared photodetectors. *Applied Physics Letters*, 78(4):495–497, 2001.

[94] Michael W. Kudenov and Eustace L. Dereniak. Compact snapshot birefringent imaging fourier transform spectrometer. In *Imaging Spectrometry XV*, volume 7812 of *Proc. SPIE*, pages 781206–781206–11, August 2010.

[95] Michael W. Kudenov and Eustace L. Dereniak. Compact real-time birefringent imaging spectrometer. *Opt. Express*, 20(16):17973–17986, July 2012.

[96] Michael W. Kudenov, Matthew E. L. Jungwirth, Eustace L. Dereniak, and Grant R. Gerhart. White light sagnac interferometer for snapshot linear polarimetric imaging. *Opt. Express*, 17(25):22520–22534, Dec 2009.

[97] Michael W. Kudenov, Matthew E. L. Jungwirth, Eustace L. Dereniak, and Grant R. Gerhart. White-light sagnac interferometer for snapshot multispectral imaging. *Appl. Opt.*, 49(21):4067–4076, Jul 2010.

[98] Giacomo Langfelder, Antonio Longoni, and Federico Zaraga. The transverse field detector: a cmos active pixel sensor capable of on-line tuning of the spectral response. In *IEEE Sensors, 2009*, pages 1652–1657, Oct 2009.

[99] Jack C. Lansing, Jr. and Richard W. Cline. The four- and five-band multispectral scanners for landsat. *Optical Engineering*, 14(4):144312–144312–, 1975.

[100] Pierre-Jean Lapray, Xingbo Wang, Jean-Baptiste Thomas, and Pierre Gouton. Multispectral filter arrays: Recent advances and practical implementation. *Sensors*, 14(11):21626–21659, 2014.

[101] E. Le Coarer, S. Bensammar, G. Comte, J. L. Gach, and Y. Georgelin. PYTHEAS: A multi-channel fabry-perot spectrometer for astronomical imaging. *Astronomy and Astrophysics Supplement Series*, 111:359, 1995.

[102] H.-C. Lee. *Introduction to Color Imaging Science*. Cambridge University Press, 2005.

[103] Marc Levoy, Ren Ng, Andrew Adams, Matthew Footer, and Mark Horowitz. Light field microscopy. *ACM Transactions on Graphics (TOG)*, 25(3):924–934, 2006.

[104] Xin Li, Bahadir Gunturk, and Lei Zhang. Image demosaicing: a systematic survey. In William A. Pearlman, John W. Woods, and Ligang Lu, editors, *Visual Communications and Image Processing 2008*, volume 6822. SPIE, January 2008.

[105] Andy L Lin and Francisco Imai. Efficient spectral imaging based on imaging systems with scene adaptation using tunable color pixels. In *Color and Imaging Conference*, volume 2011, pages 332–338. Society for Imaging Science and Technology, 2011.

[106] P. Longère, X. Zhang, P. B. Delahunt, and D. H. Brainard. Perceptual assessment of demosaicing algorithm performance. *Proceedings of the IEEE*, 90(1):123–132, Jan 2002.

[107] Philippe Longère and David H. Brainard. Simulation of digital camera images from hyperspectral input. In Christian J. van den Branden Lambrecht, editor, *Vision Models and Applications to Image and Video Processing*, pages 123–150. Springer Science+Business Media Dordrecht, 2001.

[108] Olivier Losson, Ludovic Macaire, and Yanqin Yang. Comparison of color demosaicing methods. In Peter Hawkes, editor, *Advances in Imaging and Electron Physics*, volume 162, chapter 5, pages 173–265. Elsevier, June 2010.

[109] Clément Fredembach Lu, Yue M., Martin Vetterli, and Sabine Süsstrunk. Designing color filter arrays for the joint capture of visible and near-infrared images. In *16th IEEE International Conference on Image Processing (ICIP)*, pages 3797–3800, Nov 2009.

[110] W. Lu and Y.-P. Tan. Color filter array demosaicking: new method and performance measures. *IEEE Transactions on Image Processing*, 12(10):1194–1210, October 2003.

[111] Rastislav Lukac. *Single-Sensor Imaging: Methods and Applications for Digital Cameras*. Image Processing Series. CRC Press, 2008.

[112] P. Y. Maeda. Zernike polynomials and their use in describing the wavefront aberrations of the human eye. `http://scien.stanford.edu/pages/labsite/2003/psych221/projects/03/pmaeda/`, 2003. Retrieved 21 Jun 2014.

[113] H. S. Malvar, L.-W. He, and R. Cutler. High-quality linear interpolation for demosaicing of bayer-patterned color images. In *Proceedings of IEEE International Conference on Acoustics, Speech, and Signal Processing, 2004. (ICASSP '04).*, volume 3, pages 485–488, 2004.

[114] Kirk Martinez, John Cupitt, and David R. Saunders. High-resolution colorimetric imaging of paintings, 1993.

[115] Miguel A. Martínez, Eva M. Valero, Javier Hernández-Andrés, Javier Romero, and Giacomo Langfelder. Combining transverse field detectors and color filter arrays to improve multispectral imaging systems. *Appl. Opt.*, 53(13):C14–C24, May 2014.

[116] Joseph D. Matchett, Richard I. Billmers, Elizabeth J. Billmers, and Mary E. Ludwig. Volume holographic beam splitter for hyperspectral imaging applications. In *Novel Optical Systems Design and Optimization X*, volume 6668 of *Proc. SPIE*, pages 66680K–66680K–8, 2007.

[117] Hideaki Matsuoka, Yuri Kosai, Mikako Saito, Norihide Takeyama, and Hiroshi Suto. Single-cell viability assessment with a novel spectro-imaging system. *Journal of biotechnology*, 94(3):299–308, 2002.

[118] William Ross McCluney. *Introduction to Radiometry and Photometry*. Applied photonics series. Artech House, Norwood, MA, 1994.

[119] Andrew D. Meigs, Eugene W. Butler, Bernard A. Jones, Leonard John Otten III, R. Glenn Sellar, and Bruce Rafert. Airborne visible hyperspectral imaging spectrometer: optical and system-level description. In *Imaging Spectrometry II*, volume 2819 of *Proc. SPIE*, pages 278–284, 1996.

[120] Daniele Menon and Giancarlo Calvagno. Color image demosaicking: An overview. *Image Commun.*, 26(8-9):518–533, October 2011.

[121] Jeffrey Mercier, Toby Townsend, and Robert Sundberg. Utility assessment of a multispectral snapshot lwir imager. In *The 2nd Workshop on Hyperspectral Image and Signal Processing: Evolution in Remote Sensing (WHISPERS), 2010*, pages 1–5, June 2010.

[122] R. Merrill. Vertical color filter detector group and array, February 27 2003. US Patent App. 10/262,809.

[123] Lidan Miao and Hairong Qi. The design and evaluation of a generic method for generating mosaicked multispectral filter arrays. *IEEE Transactions on Image Processing*, 15(9):2780–2791, Sept 2006.

[124] Lidan Miao, Hairong Qi, and Rajeev Ramanath. A generic binary tree-based progressive demosaicking method for multispectral filter array. In *International Conference on Image Processing (ICIP), 2006*, pages 3221–3224. IEEE, Oct 2006.

[125] Lidan Miao, Hairong Qi, and Rajeev Ramanath. Generic msfa mosaicking and demosaicking for multispectral cameras. In *Digital Photography II*, volume 6069 of *Proc. SPIE*, pages 606909–606909–10, 2006.

[126] Lidan Miao, Hairong Qi, Rajeev Ramanath, and Wesley E. Snyder. Binary tree-based generic demosaicking algorithm for multispectral filter arrays. *IEEE Transactions on Image Processing*, 15(11):3550–3558, Nov 2006.

[127] Lidan Miao, Hairong Qi, and Wesley E. Snyder. A generic method for generating multispectral filter arrays. In *International Conference on Image Processing (ICIP)*, volume 5, pages 3343–3346. IEEE, October 2004.

[128] Albert A. Michelson. The relative motion of the earth and the luminiferous ether. *American Journal of Science*, 22(3):120–129, July 1881.

[129] Yusuke Monno, Masayuki Tanaka, and Masatoshi Okutomi. Multispectral demosaicking using adaptive kernel upsampling. In *18th IEEE International Conference on Image Processing (ICIP)*, pages 3157–3160, Brussels, September 2011.

[130] Yusuke Monno, Masayuki Tanakaa, and Masatoshi Okutomia. Multispectral demosaicking using guided filter. In Sebastiano Battiato, Brian G. Rodricks, Nitin Sampat, Francisco H. Imai, and Feng Xiao, editors, *Digital Photography VIII*, volume 8299 of *Proc. of SPIE*, pages 82990O–82990O–7, Burlingame, California, USA, January 2012.

[131] Jonathan M. Mooney. Angularly multiplexed spectral imager. In *Imaging Spectrometry*, volume 2480 of *Proc. SPIE*, pages 65–77, 1995.

[132] Hannah R. Morris, Clifford C. Hoyt, and Patrick J. Treado. Imaging spectrometers for fluorescence and raman microscopy: Acousto-optic and liquid crystal tunable filters. *Appl. Spectrosc.*, 48(7):857–866, Jul 1994.

[133] Yuri Murakami, Masahiro Yamaguchi, and Nagaaki Ohyama. Hybrid-resolution multispectral imaging using color filter array. *Opt. Express*, 20(7):7173–7183, Mar 2012.

[134] Junichi Nakamura. *Image Sensors and Signal Processing for Digital Still Cameras*. Optical Science and Engineering. CRC Press, 2005.

[135] NASA. Landsat 1. `http://landsat.gsfc.nasa.gov/?p=3172`. Retrieved 31 Oct 2014.

[136] NASA. The multispectral scanner system. http://landsat.gsfc.nasa.gov/?p=3227. Retrieved 31 Oct 2014.

[137] Biman B. Nath. *The Story of Helium and the Birth of Astrophysics*. Astronomers' Universe. Springer, 2012.

[138] Harry Nyquist. Thermal agitation of electric charge in conductors. *Phys. Rev.*, 32:110–113, Jul 1928.

[139] Takayuki Okamoto and Ichirou Yamaguchi. Simultaneous acquisition of spectral image information. *Opt. Lett.*, 16(16):1277–1279, Aug 1991.

[140] William E. Ortyn, David A. Basiji, Philip Morrissey, Thaddeus George, Brian Hall, Cathleen Zimmerman, and David Perry. Blood and cell analysis using an imaging flow cytometer, April 12 2011. US Patent 7,925,069.

[141] James M. Palmer and Barbara G. Grant. *The Art of Radiometry*, volume 184 of *SPIE Press monograph*. SPIE Press, Bellingham, WA, 2010.

[142] Panasonic. Primary color and complementary color filters. http://panasonic.jp/support/global/cs/dsc/knowhow/knowhow29.html. last accessed 7 November 2014.

[143] Kenneth A. Parulski. Color filters and processing alternatives for one-chip cameras. *IEEE Transactions on Electron Devices*, 32(8):1381–1389, August 1985.

[144] Hugues Péguillet, Jean-Baptiste Thomas, Pierre Gouton, and Yassine Ruichek. Energy balance in single exposure multispectral sensors. In *Colour and Visual Computing Symposium (CVCS), 2013*, pages 1–6, Sept 2013.

[145] Andrew E. Potter, Jr. Multispectral imaging system, November 14 1972. US Patent 3,702,735.

[146] Hairong Qi, Linghua Kong, Chao Wang, and Lidan Miao. A hand-held mosaicked multispectral imaging device for early stage pressure ulcer detection. *Journal of Medical Systems*, 35(5):895–904, 2011.

[147] Rajeev Ramanath, Wesley E. Snyder, Griff L. Bilbro, and William A. Sander III. Demosaicking methods for bayer color arrays. *Journal of Electronic Imaging*, 11(3):306–315, 2002.

[148] Rajeev Ramanath, Wesley E. Snyder, Griff L. Bilbro, and William A. Sander. Robust multispectral imaging sensors for autonomous robots. Technical report, North Carolina State University, 2001. Retrieved 16 June 2014.

[149] Rajeev Ramanath, Wesley E. Snyder, and Hairong Qi. Mosaic multispectral focal plane array cameras. In *Infrared Technology and Applications XXX*, volume 5406 of *Proc. SPIE*, pages 701–712, 2004.

[150] Javier Romero, Antonio GarciÌĄa-Beltrán, and Javier Hernández-Andrés. Linear bases for representation of natural and artificial illuminants. *Journal of the Optical Society of America A*, 14(5):1007–1014, May 1997.

[151] Zahra Sadeghipoor Kermani, Yue Lu, and Sabine Süsstrunk. Correlation-based joint acquisition and demosaicking of visible and near-infrared images. In *IEEE International Conference on Image Processing (ICIP)*, September 2011.

[152] Hui-Liang Shen, Pu-Qing Cai, Si-Jie Shao, and John H. Xin. Reflectance reconstruction for multispectral imaging by adaptive wiener estimation. *Opt. Express*, 15(23):15545–15554, Nov 2007.

[153] Kazuma Shinoda, Taisuke Hamasaki, Madoka Hasegawa, Shigeo Kato, and Ortega Antonio. Quality metric for filter arrangement in a multispectral filter array. In *Picture Coding Symposium (PCS), 2013*, pages 149–152, Dec 2013.

[154] Rui Shogenji, Yoshiro Kitamura, Kenji Yamada, Shigehiro Miyatake, and Jun Tanida. Multispectral imaging using compact compound optics. *Opt. Express*, 12(8):1643–1655, Apr 2004.

[155] Raju Shrestha, Jon Y. Hardeberg, and Rahat Khan. Spatial arrangement of color filter array for multispectral image acquisition. In *Sensors, Cameras, and Systems for Industrial, Scientific, and Consumer Applications XII*, volume 7875 of *Proc. SPIE*, pages 787503–787503–9, 2011.

[156] Torbjørn Skauli and Joyce Farrell. A collection of hyperspectral images for imaging systems research. In *Digital Photography IX*, volume 8660 of *Proc. SPIE*, pages 86600C–86600C. SPIE, February 2013.

[157] Jerry E. Solomon. Imaging spectrometry: Technology and applications. In *Applications of Electronic Imaging*, volume 1082 of *Proc. SPIE*, pages 126–133, 1989.

[158] Andrew W. Sparks and Michael J. DeWeert. Single camera multi-spectral imager, December 21 2010. US Patent 7,855,786.

[159] Bruce A. Spiering. For generating automatically co-registered images of an object, May 4 1999. US Patent 5,900,942.

[160] Stephen H. Sprigle, Linghua Kong, Jayme J. Caspall, and Mark G. Duckworth. Systems and methods for real time multispectral imaging, June 10 2010. US Patent App. 12/518,824.

[161] Angus Stevenson, editor. *Oxford Dictionary of English*. Oxford University Press, 2 edition, 2005.

[162] Daniel Tamburrino, Jon M. Speigle, Douglas J. Tweet, and Jong-Jan Lee. 2PFC^{TM} (two pixels, full color): Image sensor demosaicing and characterization. *Journal of Electronic Imaging*, 19(2):021103–021103–13, 2010.

[163] David Taubman. Generalized wiener reconstruction of images from colour sensor data using a scale invariant prior. In *International Conference on Image Processing, 2000*, volume 3, pages 801–804. IEEE, Sep 2000.

[164] L. N. Thibos, A. Bradley, and X. Zhang. Effect of ocular chromatic aberration on monocular visual performance. *Optometry & Vision Science*, 68(8):599–607, 1991.

[165] L. N. Thibos, M. Ye, X. Zhang, and A. Bradley. The chromatic eye: a new reduced-eye model of ocular chromatic aberration in humans. *Appl. Opt.*, 31(19):3594–3600, Jul 1992.

[166] H. Joel Trussell and Robert E. Hartwig. Mathematics for demosaicking. *IEEE Transactions on Image Processing*, 11(4):485–492, Apr 2002.

[167] C Vanderriest. A fiber-optics dissector for spectroscopy of nebulosities around quasars and similar objects. *Publications of the Astronomical Society of the Pacific*, 92(550):858–862, December 1980.

[168] Michael J. Vrhel, Ron Gershon, and Lawrence S. Iwan. Measurement and analysis of object reflectance spectra. *Color Research & Application*, 19(1):4–9, 1994.

[169] K. Walls, Q. Chen, J. Grant, S. Collins, D.R.S. Cumming, and T.D. Drysdale. Narrowband multispectral filter set for visible band. *Opt. Express*, 20(20):21917–21923, Sep 2012.

[170] Congcong Wang, Xingbo Wang, and JonYngve Hardeberg. A linear interpolation algorithm for spectral filter array demosaicking. In Abderrahim Elmoataz, Olivier Lezoray, Fathallah Nouboud, and Driss Mammass, editors, *Image and Signal Processing*, volume 8509 of *Lecture Notes in Computer Science*, pages 151–160. Springer International Publishing, July 2014.

[171] S.-W. Wang, M. Li, C.-S. Xia, H.-Q. Wang, X.-S. Chen, and W. Lu. 128 channels of integrated filter array rapidly fabricated by using the combinatorial deposition technique. *Applied Physics B*, 88(2):281–284, 2007.

[172] Shao-Wei Wang, Changsheng Xia, Xiaoshuang Chen, Wei Lu, Ming Li, Haiqian Wang, Weibo Zheng, and Tao Zhang. Concept of a high-resolution miniature spectrometer using an integrated filter array. *Opt. Lett.*, 32(6):632–634, Mar 2007.

[173] Xingbo Wang, Philip John Green, Jean-Baptiste Thomas, Jon Yngve Hardeberg, and Pierre Gouton. Evaluation of the colorimetric performance of single-sensor image acquisition systems employing colour and multispectral filter array. In Alain Trémeau, Raimondo Schettini, and Shoji Tominaga, editors, *Computational Color Imaging*, volume 9016 of *Lecture Notes in Computer Science*, pages 181–191. Springer International Publishing, March 2015.

[174] Xingbo Wang, Marius Pedersen, and Jean-Baptiste Thomas. The influence of chromatic aberration on demosaicking. In *5th European Workshop on Visual Information Processing (EUVIP)*, pages 1–6. IEEE, December 2014.

[175] Xingbo Wang, Jean-Baptiste Thomas, Jon Yngve Hardeberg, and Pierre Gouton. Discrete wavelet transform based multispectral filter array demosaicking. In *Proceedings of Colour and Visual Computing Symposium (CVCS), 2013*, pages 1–6, September 2013.

[176] Xingbo Wang, Jean-Baptiste Thomas, Jon Yngve Hardeberg, and Pierre Gouton. Median filtering in multispectral filter array demosaicking. In *Digital Photography IX*, volume 8660 of *Proc. SPIE*, pages 86600E–86600E–10. SPIE, February 2013.

[177] Xingbo Wang, Jean-Baptiste Thomas, Jon Yngve Hardeberg, and Pierre Gouton. A study on the impact of spectral characteristics of filters on multispectral image acquisition. In *Proceedings of 12th Congress of the International Colour Association*, volume 4, pages 1765–1768, July 2013.

[178] Xingbo Wang, Jean-Baptiste Thomas, Jon Yngve Hardeberg, and Pierre Gouton. Multispectral imaging: narrow or wide band filters? *Journal of the International Colour Association*, 12:44–51, 2014.

[179] Z. Wang, A. C. Bovik, H. R. Sheikh, and E. P. Simoncelli. Image quality assessment: from error visibility to structural similarity. *IEEE Transactions on Image Processing*, 13(4):600–612, 2004.

[180] L Weitzel, A Krabbe, H Kroker, N Thatte, LE Tacconi-Garman, M Cameron, and R Genzel. 3d: The next generation near-infrared imaging spectrometer. *Astronomy and Astrophysics-Supplement Series*, 119(3):531–546, 1996.

[181] C. W. Wells, A. E. Potter, and T. H. Morgan. Near-infrared spectral imaging michelson interferometer for astronomical applications. In *Infrared Imaging Systems Technology*, volume 0226 of *Proc. SPIE*, pages 61–65, 1980.

[182] Y. Yang, O. Losson, and L. Duvieubourg. Quality evaluation of color demosaicing according to image resolution. In *Third International IEEE Conference on Signal-Image Technologies and Internet-Based System, 2007. SITIS '07.*, pages 689–695, Dec 2007.

[183] Fumihito Yasuma, Tomoo Mitsunaga, Daisuke Iso, and Shree K. Nayar. Generalized assorted pixel camera: Post-capture control of resolution, dynamic range and spectrum. Technical report, Department of Computer Science, Columbia University CUCS-061-08, Nov 2008. `http://www1.cs.columbia.edu/CAVE/databases/multispectral/`.

[184] Fumihito Yasuma, Tomoo Mitsunaga, Daisuke Iso, and Shree K. Nayar. Generalized assorted pixel camera: Postcapture control of resolution, dynamic range, and spectrum. *IEEE Transactions on Image Processing*, 19(9):2241–2253, Sept 2010.

[185] Dingrong Yi and Linghua Kong. Novel miniaturized multispectral imaging system for real-time bruise detection. In *3rd International Conference on Biomedical Engineering and Informatics (BMEI)*, volume 1, pages 439–442, Oct 2010.

[186] Dingrong Yi, Linghua Kong, Jiwu Wang, and Futing Zhao. Fabrication of multispectral imaging technology driven mems-based micro-arrayed multichannel optical filter mosaic. In *Advanced Fabrication Technologies for Micro/Nano Optics and Photonics IV*, volume 7927 of *Proc. SPIE*, pages 792711–792711–7. SPIE, 2011.

[187] Dingrong Yi, Chao Wang, Hairong Qi, Linghua Kong, Fengtao Wang, and Ali Adibi. Real-time multispectral imager for home-based health care. In *IEEE Transactions on Biomedical Engineering*, volume 58, pages 736–740, March 2011.

[188] Jianhuan Zhang, Shan Lin, Chentao Zhang, Yanping Chen, Linghua Kong, and Fengxin Chen. An evaluation method of a micro-arrayed multispectral filter mosaic. In *Proceedings of the Eighth International Symposium on Precision Engineering Measurement and Instrumentation*, volume 8759 of *Proc. SPIE*, pages 875908–875908–6, 2013.

[189] X. Zhang and B. A. Wandell. A spatial extension of CIELAB for digital color image reproduction. *Journal of the Society for Information Display*, 5(3):61–63, March 1997.